REPORT DOCUMENTATION PAGE

Form Approved OMB NO. 0704-0188

1. REPORT DATE (DD-MM-YYYY)	2. REPORT TYPE	3. DATES COVERED (From - To)
04-09-2018	Final Report	1-Nov-2010 - 31-Oct-2017

4. TITLE AND SUBTITLE
Final Report: Fundamental Study of Defects and Their Reduction in Type-II Superlattice Materials

5a. CONTRACT NUMBER
W911NF-10-1-0524

5b. GRANT NUMBER

5c. PROGRAM ELEMENT NUMBER
611103

6. AUTHORS

5d. PROJECT NUMBER

5e. TASK NUMBER

5f. WORK UNIT NUMBER

7. PERFORMING ORGANIZATION NAMES AND ADDRESSES
University of Illinois - Urbana - Champaign
c/o Office of Sponsored Programs
1901 S. First Street, Suite A
Champaign, IL 61820 -7406

8. PERFORMING ORGANIZATION REPORT NUMBER

9. SPONSORING/MONITORING AGENCY NAME(S) AND ADDRESS (ES)
U.S. Army Research Office
P.O. Box 12211
Research Triangle Park, NC 27709-2211

10. SPONSOR/MONITOR'S ACRONYM(S)
ARO

11. SPONSOR/MONITOR'S REPORT NUMBER(S)
58141-EL-MUR.117

12. DISTRIBUTION AVAILIBILITY STATEMENT
Approved for public release; distribution is unlimited.

13. SUPPLEMENTARY NOTES
The views, opinions and/or findings contained in this report are those of the author(s) and should not contrued as an official Department of the Army position, policy or decision, unless so designated by other documentation.

14. ABSTRACT

15. SUBJECT TERMS

16. SECURITY CLASSIFICATION OF:			17. LIMITATION OF ABSTRACT	15. NUMBER OF PAGES	19a. NAME OF RESPONSIBLE PERSON
a. REPORT	b. ABSTRACT	c. THIS PAGE			Jian-Min Zuo
UU	UU	UU	UU		19b. TELEPHONE NUMBER 217-244-6504

Standard Form 298 (Rev 8/98)
Prescribed by ANSI Std. Z39.18

RPPR Final Report
as of 05-Sep-2018

Agency Code:

Proposal Number: 58141ELMUR **Agreement Number: W911NF-10-1-0524**
INVESTIGATOR(S):

Name: PhD David John Smith
Email: david.smith@asu.edu
Phone Number: 4809654540
Principal: N

Name: Jian-Min Zuo
Email: jianzuo@illinois.edu
Phone Number: 2172446504
Principal: Y

Name: Kuang-Chien Hsieh Phd
Email: khsieh@illinois.edu
Phone Number: 2172441806
Principal: N

Name: Russell Dean Dupuis Phd
Email: russell.dupuis@ece.gatech.edu
Phone Number: 4043856094
Principal: N

Name: Yong-Hang Zhang
Email: yhzhang@asu.edu
Phone Number: 4807272795
Principal: N

Name: Yong Zhang
Email: yong.zhang@uncc.edu
Phone Number: 7046878652
Principal: N

Organization: **University of Illinois - Urbana - Champaign**
Address: c/o Office of Sponsored Programs, Champaign, IL 618207406
Country: USA

DUNS Number: 041544081 EIN: 376000511
Report Date: 31-Jan-2018 Date Received: 04-Sep-2018
Final Report for Period Beginning 01-Nov-2010 and Ending 31-Oct-2017
Title: Fundamental Study of Defects and Their Reduction in Type-II Superlattice Materials
Begin Performance Period: 01-Nov-2010 **End Performance Period:** 31-Oct-2017
Report Term: 0-Other

Submitted By: Russell Dupuis Email: russell.dupuis@ece.gatech.edu
Phone: (404) 385-6094

STEM Degrees: 25 **STEM Participants:** 50

Major Goals: GaSb-based Type-II superlattices (T2SLs) offer advantages for MWIR and LWIR detector applications due to their broad bandgap tunability, material uniformity, and predicted superior performance compared to traditional MCT (HgCdTe) IR photodetectors, which is mainly due to the suppressed Auger recombination in T2SLs through band-structure engineering. However, this predicted high performance has yet to be realized as T2SL IR detectors are still limited by defects and interface-related traps. A thorough understanding of detector theory, materials growth processes, and defect physics is crucial for suppression of defect formation and their adverse effects. Our team will develop a more accurate theory for the fundamental limits of T2SL detectors and study the physical origin of the defects as well as their structural, electrical, and optical properties.

RPPR Final Report
as of 05-Sep-2018

Novel growth methods and new materials and T2SL designs will be tested and utilized to drastically reduce the defect density and to improve IR detector performance. Our main objectives are:
1. Identify and understand the origin of various defects in superlattice materials through experimental studies coupled to theoretical calculations. Correlate defect properties with minority carrier lifetime and device performance as a function of operating temperature.
2. Examine novel MBE and MOCVD growth methods and passivation that eliminate or mitigate defects in InAs/GaSb, InAs/InGaSb, and InAs/InAsSb T2SLs.
3. Fabricate and characterize T2SL structures and devices, and develop models for understanding the device physics.

Accomplishments: See report in Upload Section

Training Opportunities: The University of Illinois led Army MURI project on "Fundamental Study of Defects and Their Reduction in Type-II Superlattice Materials" ran from Oct., 2010, through Oct. 2017. The program supported a group of ten prominent university researchers along with 20 PhD students, 3 Masters, 2 undergraduate students, and 2 postdoctoral fellows across five participating universities.

Specifically:

- Two PhD graduate students and one Post Doc worked on this program at Georgia Tech during the course of this program. The research at Georgia Tech was focused on the MOCVD growth of GaSb-InAsSb Type II superlattices. X-ray and atomic force microscopy (AFM) characterization of grown layers was also performed at Georgia Tech. Other characterization measurements were performed by out collaborators.
- Eleven PhD graduate students, two Masters graduate students and one BS degree student were trained and contributed to this program at Arizona State University (ASU). The research at ASU focused on MBE growth, device characterization and transmission electron microscopy.
- Four PhD graduate students worked on this program at University of North Carolina at Charlotte (UNCC). The research at UNCC focused on theory and Raman Spectroscopy.
- One PhD graduate student, one BS undergraduate student and one Professional Staff were trained and contributed to this program at Texas A&M University (TAMU). Research at TAMU focused on scanning tunneling microscopy.
- Three PhD graduate students, one Masters graduate student and one Post Doc worked on this program at University of Illinois, Urbana-Champaign (UIUC). Research at UIUC focused on device characterization, theory and transmission electron microscopy.

Results Dissemination: See Uploaded List of publications and presentations in Final Report

Honors and Awards: Over the course of the project period, our team members were recognized by a number of highly prestigious honors and awards, including
- Russell Dean Dupuis, Alexander von Humboldt Research Award, Alexander von Humboldt Foundation, Germany, 2013
- Yong-Hang Zhang: Elected Fellow, OSA, 2013
- David J. Smith: Elected Fellow, Microscopy Society of America, 2013
- Russell Dean Dupuis, Elected Fellow of the National Academy of Inventors, 2014
- David J. Smith, 2014 Distinguished Physical Scientist Award, Microscopy Society of America
- David J. Smith, 2014 Helmholtz International Fellow Award, Helmholtz Association
- Jian-Min Zuo, Elected Fellow of American Physical Society, 2014
- Russell Dean Dupuis, The Institute of Electrical and Electronics Engineers IEEE Life Fellow Award, 2015
- Russell Dean Dupuis, National Academy of Engineering Charles Stark Draper Engineering Award, 2015. With I. Akasaki, M. G. Craford, N. Holonyak, Jr., and S. Nakamura
- Yong-Hang Zhang: Elected Fellow IEEE, 2015
- Jian-Min Zuo, Ernst Ruska Prize of the German Society for Electron Microscopy, 2015
- Russell Dean Dupuis, International SSL Alliance Award of Outstanding Achievement for Global Solid State Lighting Development, 2016
- Jian-Min Zuo, Racheff Professorship, Engineering College, UIUC, 2016-present
- Jian-Min Zuo, Lars Onsager Professorship, Norwegian University of Science and Technology, 2017
- Yong Zhang, Elected Fellow of American Physical Society, 2017

RPPR Final Report
as of 05-Sep-2018

Protocol Activity Status:

Technology Transfer: Nothing to Report

PARTICIPANTS:

Participant Type: Co PD/PI
Participant: Russell D Dupuis
Person Months Worked: 6.00 **Funding Support:**
Project Contribution:
International Collaboration:
International Travel:
National Academy Member: Y
Other Collaborators:

Participant Type: Co-Investigator
Participant: Theeradetch Detchprohm
Person Months Worked: 15.00 **Funding Support:**
Project Contribution:
International Collaboration:
International Travel:
National Academy Member: N
Other Collaborators:

Participant Type: Co-Investigator
Participant: Jae-Hyun Ryou
Person Months Worked: 12.00 **Funding Support:**
Project Contribution:
International Collaboration:
International Travel:
National Academy Member: N
Other Collaborators:

Participant Type: Postdoctoral (scholar, fellow or other postdoctoral position)
Participant: Xuebing Zhang
Person Months Worked: 8.00 **Funding Support:**
Project Contribution:
International Collaboration:
International Travel:
National Academy Member: N
Other Collaborators:

Participant Type: PD/PI
Participant: Jian-Min Zuo
Person Months Worked: 3.00 **Funding Support:**
Project Contribution:
International Collaboration:
International Travel:
National Academy Member: N
Other Collaborators:

Participant Type: PD/PI
Participant: Shun-Lien Chuan
Person Months Worked: 2.00 **Funding Support:**

Project Contribution:
International Collaboration:
International Travel:
National Academy Member: N
Other Collaborators:

Participant Type: Co PD/PI
Participant: Yong Zhang
Person Months Worked: 3.00 **Funding Support:**
Project Contribution:
International Collaboration:
International Travel:
National Academy Member: N
Other Collaborators:

Participant Type: Co PD/PI
Participant: David J Smith
Person Months Worked: 6.00 **Funding Support:**
Project Contribution:
International Collaboration:
International Travel:
National Academy Member: N
Other Collaborators:

Participant Type: Co PD/PI
Participant: Shane R. Johnson
Person Months Worked: 6.00 **Funding Support:**
Project Contribution:
International Collaboration:
International Travel:
National Academy Member: N
Other Collaborators:

Participant Type: Co PD/PI
Participant: Yong-Hang Zhang
Person Months Worked: 10.00 **Funding Support:**
Project Contribution:
International Collaboration:
International Travel:
National Academy Member: N
Other Collaborators:

Participant Type: Co PD/PI
Participant: Michael Weimer
Person Months Worked: 2.00 **Funding Support:**
Project Contribution:
International Collaboration:
International Travel:
National Academy Member: N
Other Collaborators:

Participant Type: Graduate Student (research assistant)
Participant: Qiong Chen

Person Months Worked: 14.00 **Funding Support:**
Project Contribution:
International Collaboration:
International Travel:
National Academy Member: N
Other Collaborators:

Participant Type: Graduate Student (research assistant)
Participant: Yong Huang
Person Months Worked: 12.00 **Funding Support:**
Project Contribution:
International Collaboration:
International Travel:
National Academy Member: N
Other Collaborators:

Participant Type: Graduate Student (research assistant)
Participant: Honggyu Kim
Person Months Worked: 15.00 **Funding Support:**
Project Contribution:
International Collaboration:
International Travel:
National Academy Member: N
Other Collaborators:

Participant Type: Graduate Student (research assistant)
Participant: Jingjing Li
Person Months Worked: 1.00 **Funding Support:**
Project Contribution:
International Collaboration:
International Travel:
National Academy Member: N
Other Collaborators:

Participant Type: Postdoctoral (scholar, fellow or other postdoctoral position)
Participant: Jianwei Wang
Person Months Worked: 15.00 **Funding Support:**
Project Contribution:
International Collaboration:
International Travel:
National Academy Member: N
Other Collaborators:

Participant Type: Postdoctoral (scholar, fellow or other postdoctoral position)
Participant: Quan Zhang
Person Months Worked: 1.00 **Funding Support:**
Project Contribution:
International Collaboration:
International Travel:
National Academy Member: N
Other Collaborators:

Participant Type: Postdoctoral (scholar, fellow or other postdoctoral position)

RPPR Final Report
as of 05-Sep-2018

Participant: Hua Li
Person Months Worked: 1.00 **Funding Support:**
Project Contribution:
International Collaboration:
International Travel:
National Academy Member: N
Other Collaborators:

Participant Type: Postdoctoral (scholar, fellow or other postdoctoral position)
Participant: Hal-Su Kim
Person Months Worked: 4.00 **Funding Support:**
Project Contribution:
International Collaboration:
International Travel:
National Academy Member: N
Other Collaborators:

Participant Type: Postdoctoral (scholar, fellow or other postdoctoral position)
Participant: Stuart Farrell
Person Months Worked: 3.00 **Funding Support:**
Project Contribution:
International Collaboration:
International Travel:
National Academy Member: N
Other Collaborators:

Participant Type: Postdoctoral (scholar, fellow or other postdoctoral position)
Participant: Ding Ding
Person Months Worked: 1.00 **Funding Support:**
Project Contribution:
International Collaboration:
International Travel:
National Academy Member: N
Other Collaborators:

Participant Type: Postdoctoral (scholar, fellow or other postdoctoral position)
Participant: Oray Cellek
Person Months Worked: 10.00 **Funding Support:**
Project Contribution:
International Collaboration:
International Travel:
National Academy Member: N
Other Collaborators:

Participant Type: Graduate Student (research assistant)
Participant: Naili Yue
Person Months Worked: 8.00 **Funding Support:**
Project Contribution:
International Collaboration:
International Travel:
National Academy Member: N
Other Collaborators:

RPPR Final Report
as of 05-Sep-2018

Participant Type: Graduate Student (research assistant)
Participant: Henan Liu
Person Months Worked: 15.00 **Funding Support:**
Project Contribution:
International Collaboration:
International Travel:
National Academy Member: N
Other Collaborators:

Participant Type: Graduate Student (research assistant)
Participant: James Devin Justice
Person Months Worked: 15.00 **Funding Support:**
Project Contribution:
International Collaboration:
International Travel:
National Academy Member: N
Other Collaborators:

Participant Type: Graduate Student (research assistant)
Participant: Xinhao Zhao
Person Months Worked: 7.00 **Funding Support:**
Project Contribution:
International Collaboration:
International Travel:
National Academy Member: N
Other Collaborators:

Participant Type: Graduate Student (research assistant)
Participant: Preston Webster
Person Months Worked: 15.00 **Funding Support:**
Project Contribution:
International Collaboration:
International Travel:
National Academy Member: N
Other Collaborators:

Participant Type: Graduate Student (research assistant)
Participant: Dinghao Tang
Person Months Worked: 2.00 **Funding Support:**
Project Contribution:
International Collaboration:
International Travel:
National Academy Member: N
Other Collaborators:

Participant Type: Graduate Student (research assistant)
Participant: Xiaomeng Shen
Person Months Worked: 15.00 **Funding Support:**
Project Contribution:
International Collaboration:
International Travel:
National Academy Member: N
Other Collaborators:

RPPR Final Report
as of 05-Sep-2018

Participant Type: Graduate Student (research assistant)
Participant: Nathaniel Riordan
Person Months Worked: 1.00 **Funding Support:**
Project Contribution:
International Collaboration:
International Travel:
National Academy Member: N
Other Collaborators:

Participant Type: Graduate Student (research assistant)
Participant: Lu Ouyang
Person Months Worked: 11.00 **Funding Support:**
Project Contribution:
International Collaboration:
International Travel:
National Academy Member: N
Other Collaborators:

Participant Type: Graduate Student (research assistant)
Participant: Jing Lu
Person Months Worked: 15.00 **Funding Support:**
Project Contribution:
International Collaboration:
International Travel:
National Academy Member: N
Other Collaborators:

Participant Type: Graduate Student (research assistant)
Participant: Zhiyuan Lin
Person Months Worked: 15.00 **Funding Support:**
Project Contribution:
International Collaboration:
International Travel:
National Academy Member: N
Other Collaborators:

Participant Type: Graduate Student (research assistant)
Participant: Huan Liang
Person Months Worked: 5.00 **Funding Support:**
Project Contribution:
International Collaboration:
International Travel:
National Academy Member: N
Other Collaborators:

Participant Type: Graduate Student (research assistant)
Participant: Zhaoyu He
Person Months Worked: 15.00 **Funding Support:**
Project Contribution:
International Collaboration:
International Travel:
National Academy Member: N
Other Collaborators:

Participant Type: Graduate Student (research assistant)
Participant: Pengfei Qiao
Person Months Worked: 11.00 **Funding Support:**
Project Contribution:
International Collaboration:
International Travel:
National Academy Member: N
Other Collaborators:

Participant Type: Graduate Student (research assistant)
Participant: Benjamin Kesler
Person Months Worked: 11.00 **Funding Support:**
Project Contribution:
International Collaboration:
International Travel:
National Academy Member: N
Other Collaborators:

Participant Type: Postdoctoral (scholar, fellow or other postdoctoral position)
Participant: Jin Fang
Person Months Worked: 1.00 **Funding Support:**
Project Contribution:
International Collaboration:
International Travel:
National Academy Member: N
Other Collaborators:

Participant Type: Graduate Student (research assistant)
Participant: Shyamala Malagari
Person Months Worked: 6.00 **Funding Support:**
Project Contribution:
International Collaboration:
International Travel:
National Academy Member: N
Other Collaborators:

Participant Type: Graduate Student (research assistant)
Participant: Ankur Sharma
Person Months Worked: 4.00 **Funding Support:**
Project Contribution:
International Collaboration:
International Travel:
National Academy Member: N
Other Collaborators:

Participant Type: Graduate Student (research assistant)
Participant: Ankur Sharma
Person Months Worked: 1.00 **Funding Support:**
Project Contribution:
International Collaboration:
International Travel:
National Academy Member: N

Other Collaborators:

Participant Type: Graduate Student (research assistant)
Participant: Shi Liu
Person Months Worked: 3.00 **Funding Support:**
Project Contribution:
International Collaboration:
International Travel:
National Academy Member: N
Other Collaborators:

Participant Type: Graduate Student (research assistant)
Participant: Premkumar Pugalenthi
Person Months Worked: 4.00 **Funding Support:**
Project Contribution:
International Collaboration:
International Travel:
National Academy Member: N
Other Collaborators:

Participant Type: Graduate Student (research assistant)
Participant: Guan-Lin Su
Person Months Worked: 5.00 **Funding Support:**
Project Contribution:
International Collaboration:
International Travel:
National Academy Member: N
Other Collaborators:

Participant Type: Graduate Student (research assistant)
Participant: Yifei Meng
Person Months Worked: 15.00 **Funding Support:**
Project Contribution:
International Collaboration:
International Travel:
National Academy Member: N
Other Collaborators:

Participant Type: Graduate Student (research assistant)
Participant: Maxwell Lassise
Person Months Worked: 1.00 **Funding Support:**
Project Contribution:
International Collaboration:
International Travel:
National Academy Member: N
Other Collaborators:

Participant Type: Graduate Student (research assistant)
Participant: Zhaofeng Gan
Person Months Worked: 2.00 **Funding Support:**
Project Contribution:
International Collaboration:
International Travel:

National Academy Member: N
Other Collaborators:

Participant Type: Graduate Student (research assistant)
Participant: Liqin Su
Person Months Worked: 12.00 **Funding Support:**
Project Contribution:
International Collaboration:
International Travel:
National Academy Member: N
Other Collaborators:

Participant Type: Graduate Student (research assistant)
Participant: Yang Hu
Person Months Worked: 1.00 **Funding Support:**
Project Contribution:
International Collaboration:
International Travel:
National Academy Member: N
Other Collaborators:

Participant Type: Postdoctoral (scholar, fellow or other postdoctoral position)
Participant: Qiang Zhang
Person Months Worked: 3.00 **Funding Support:**
Project Contribution:
International Collaboration:
International Travel:
National Academy Member: N
Other Collaborators:

Participant Type: Postdoctoral (scholar, fellow or other postdoctoral position)
Participant: Hee Jin Kim
Person Months Worked: 12.00 **Funding Support:**
Project Contribution:
International Collaboration:
International Travel:
National Academy Member: N
Other Collaborators:

Participant Type: Graduate Student (research assistant)
Participant: Jason Marmon
Person Months Worked: 5.00 **Funding Support:**
Project Contribution:
International Collaboration:
International Travel:
National Academy Member: N
Other Collaborators:

Participant Type: Graduate Student (research assistant)
Participant: Yen-Ting Lu
Person Months Worked: 1.00 **Funding Support:**
Project Contribution:
International Collaboration:

International Travel:
National Academy Member: N
Other Collaborators:

Participant Type: Postdoctoral (scholar, fellow or other postdoctoral position)
Participant: Jeomoh Kim
Person Months Worked: 12.00 **Funding Support:**
Project Contribution:
International Collaboration:
International Travel:
National Academy Member: N
Other Collaborators:

Participant Type: Postdoctoral (scholar, fellow or other postdoctoral position)
Participant: Martyn James Fisher
Person Months Worked: 3.00 **Funding Support:**
Project Contribution:
International Collaboration:
International Travel:
National Academy Member: N
Other Collaborators:

Participant Type: Graduate Student (research assistant)
Participant: Narae Yoon
Person Months Worked: 8.00 **Funding Support:**
Project Contribution:
International Collaboration:
International Travel:
National Academy Member: N
Other Collaborators:

Participant Type: Graduate Student (research assistant)
Participant: Yuan Zhao
Person Months Worked: 3.00 **Funding Support:**
Project Contribution:
International Collaboration:
International Travel:
National Academy Member: N
Other Collaborators:

Participant Type: Graduate Student (research assistant)
Participant: Ying-Shen Kuo
Person Months Worked: 3.00 **Funding Support:**
Project Contribution:
International Collaboration:
International Travel:
National Academy Member: N
Other Collaborators:

Participant Type: Graduate Student (research assistant)
Participant: Calli Michele Campbell
Person Months Worked: 2.00 **Funding Support:**
Project Contribution:

International Collaboration:
International Travel:
National Academy Member: N
Other Collaborators:

Participant Type: Graduate Student (research assistant)
Participant: Jacob John Becker
Person Months Worked: 1.00 **Funding Support:**
Project Contribution:
International Collaboration:
International Travel:
National Academy Member: N
Other Collaborators:

Participant Type: PD/PI
Participant: Daniel Wasserman
Person Months Worked: 9.00 **Funding Support:**
Project Contribution:
International Collaboration:
International Travel:
National Academy Member: N
Other Collaborators:

Participant Type: Graduate Student (research assistant)
Participant: Mathew R Wood
Person Months Worked: 6.00 **Funding Support:**
Project Contribution:
International Collaboration:
International Travel:
National Academy Member: N
Other Collaborators:

Participant Type: Undergraduate Student
Participant: Matthew T Breen
Person Months Worked: 1.00 **Funding Support:**
Project Contribution:
International Collaboration:
International Travel:
National Academy Member: N
Other Collaborators:

Participant Type: Graduate Student (research assistant)
Participant: Jose Castaneda
Person Months Worked: 3.00 **Funding Support:**
Project Contribution:
International Collaboration:
International Travel:
National Academy Member: N
Other Collaborators:

Participant Type: Graduate Student (research assistant)
Participant: Tim Mode
Person Months Worked: 6.00 **Funding Support:**

Project Contribution:
International Collaboration:
International Travel:
National Academy Member: N
Other Collaborators:

Participant Type: Postdoctoral (scholar, fellow or other postdoctoral position)
Participant: Qiong Chen
Person Months Worked: 6.00 **Funding Support:**
Project Contribution:
International Collaboration:
International Travel:
National Academy Member: N
Other Collaborators:

Participant Type: Postdoctoral (scholar, fellow or other postdoctoral position)
Participant: Liqin Su
Person Months Worked: 6.00 **Funding Support:**
Project Contribution:
International Collaboration:
International Travel:
National Academy Member: N
Other Collaborators:

Participant Type: Graduate Student (research assistant)
Participant: Rajeev Reddy Kosireddy
Person Months Worked: 2.00 **Funding Support:**
Project Contribution:
International Collaboration:
International Travel:
National Academy Member: N
Other Collaborators:

Participant Type: Graduate Student (research assistant)
Participant: Majid Vaghayenegar
Person Months Worked: 1.00 **Funding Support:**
Project Contribution:
International Collaboration:
International Travel:
National Academy Member: N
Other Collaborators:

Participant Type: Graduate Student (research assistant)
Participant: Daniel Yuan Zuo
Person Months Worked: 15.00 **Funding Support:**
Project Contribution:
International Collaboration:
International Travel:
National Academy Member: N
Other Collaborators:

Participant Type: Graduate Student (research assistant)
Participant: Progna Banerjee

Person Months Worked: 1.00 **Funding Support:**
Project Contribution:
International Collaboration:
International Travel:
National Academy Member: N
Other Collaborators:

Participant Type: Graduate Student (research assistant)
Participant: Chien-Chia Cheng
Person Months Worked: 4.00 **Funding Support:**
Project Contribution:
International Collaboration:
International Travel:
National Academy Member: N
Other Collaborators:

Participant Type: Graduate Student (research assistant)
Participant: Sukrith Dev
Person Months Worked: 4.00 **Funding Support:**
Project Contribution:
International Collaboration:
International Travel:
National Academy Member: N
Other Collaborators:

Participant Type: Postdoctoral (scholar, fellow or other postdoctoral position)
Participant: Qun Yang
Person Months Worked: 15.00 **Funding Support:**
Project Contribution:
International Collaboration:
International Travel:
National Academy Member: N
Other Collaborators:

Participant Type: Undergraduate Student
Participant: Yizhe Qin
Person Months Worked: 2.00 **Funding Support:**
Project Contribution:
International Collaboration:
International Travel:
National Academy Member: N
Other Collaborators:

Participant Type: Undergraduate Student
Participant: Hengyu Zhou
Person Months Worked: 1.00 **Funding Support:**
Project Contribution:
International Collaboration:
International Travel:
National Academy Member: N
Other Collaborators:

Participant Type: Graduate Student (research assistant)

RPPR Final Report
as of 05-Sep-2018

Participant: Kyou Hyun Kim
Person Months Worked: 2.00 **Funding Support:**
Project Contribution:
International Collaboration:
International Travel:
National Academy Member: N
Other Collaborators:

Participant Type: Co-Investigator
Participant: Michael Wood
Person Months Worked: 2.00 **Funding Support:**
Project Contribution:
International Collaboration:
International Travel:
National Academy Member: N
Other Collaborators:

ARTICLES:

Publication Type: Journal Article Peer Reviewed: Y **Publication Status:** 1-Published
Journal: Applied Physics Letters
Publication Identifier Type: DOI Publication Identifier: 10.1063/1.3625429
Volume: 99 Issue: 7 First Page #: 71111
Date Submitted: Date Published:
Publication Location:
Article Title: Structural and optical characterization of type-II InAs/InAs1?xSbx superlattices grown by metalorganic chemical vapor deposition
Authors:
Keywords: arsenic compounds, III-V semiconductors, indium compounds, MOCVD, photoluminescence, semiconductor growth, semiconductor superlattices, transmission electron microscopy, X-ray diffraction
Abstract: Strain-balanced type-II InAs/InAs1–xSbx superlattices with various compositions (x?=?0.22, 0.23, 0.37) and different layer thicknesses (t_InAs?=?7 nm, t_InAsSb?=?3.3, 2.3, 2.0 nm, respectively) have been grown by metalorganic chemical vapor deposition on GaSb substrates. X-ray diffraction revealed narrow satellite peaks (full-width-half-maximum of <100 arc sec), indicative of uniform superlattice periodicity and excellent crystallinity, which was also corroborated by cross-sectional transmission electron microscopy observations. Despite relaxation, low-temperature photoluminescence measurements showed peaks at 6.7 ?m and 5.8 ?m, while photoconductance results showed strong spectral response up to 200 K, when the photoresponse onset was 8.6 ?m.
Distribution Statement: 1-Approved for public release; distribution is unlimited.
Acknowledged Federal Support:

RPPR Final Report
as of 05-Sep-2018

Publication Type: Journal Article Peer Reviewed: Y **Publication Status:** 1-Published
Journal: Applied Physics Letters
Publication Identifier Type: DOI Publication Identifier: 10.1063/1.3456386
Volume: 96 Issue: 25 First Page #: 251107
Date Submitted: Date Published:
Publication Location:
Article Title: InAs/GaSb type-II superlattice structures and photodiodes grown by metalorganic chemical vapor deposition
Authors:
Keywords: gallium compounds, III-V semiconductors, indium compounds, interface structure, internal stresses, MOCVD, p-i-n photodiodes, semiconductor epitaxial layers, semiconductor growth, semiconductor superlattices
Abstract: We report on the characterization and performance of epitaxial structures and photodiodes based on InAs/GaSb type-II superlattices grown by metalorganic chemical vapor deposition. Interfacial layers were introduced at the superlattice interfaces to compensate the tensile strain and hence to improve the overall material quality of the superlattice structures. The optimal morphology and low strain was achieved via a combined interfacial layer scheme with InAsSb+InGaSb layers. Using this scheme, a p-i-n photodiode structure with a 360-period InAs/GaSb superlattice was grown on a GaSb substrate, which operates at 78 K with a cut-off wavelength of ? 8??m and a peak responsivity of 0.6 A/W at ? 6??m.
Distribution Statement: 1-Approved for public release; distribution is unlimited.
Acknowledged Federal Support:

Publication Type: Journal Article Peer Reviewed: Y **Publication Status:** 1-Published
Journal: Journal of Crystal Growth
Publication Identifier Type: DOI Publication Identifier: 10.1016/j.jcrysgro.2010.11.003
Volume: 314 Issue: 1 First Page #: 92
Date Submitted: Date Published:
Publication Location:
Article Title: Epitaxial growth and characterization of InAs/GaSb and InAs/InAsSb type-II superlattices on GaSb substrates by metalorganic chemical vapor deposition for long wavelength infrared photodetectors
Authors:
Keywords: Low dimensional structures, Metalorganic vapor phase epitaxy, Semiconducting III–V materials, Infrared devices
Abstract: We report on the epitaxial growth and characterization of InAs/GaSb and InAs/InAsSb type-?? superlattices (T2SLs) on GaSb substrates by metalorganic chemical vapor deposition. For InAs/GaSb strained T2SLs, interfacial layers were introduced at the superlattice interfaces to compensate the tensile strain and hence to improve the overall material quality of the superlattice structures. The optimal morphology and low strain was achieved via a combined interfacial layer scheme with 1 monolayer (ML) InAsSb+1 ML InGaSb layers. In contrast, the InAs/InAsSb strain-balanced T2SLs allow for a relatively easy strain management and simple precursor flow switching scheme while maintaining device-quality materials. Surface root mean square roughness of 0.108 nm and a nearly zero net strain were obtained, with effective bandgaps of 147 and 94 meV determined for two sets of InAs/InAsSb strain-balanced T2SLs.
Distribution Statement: 1-Approved for public release; distribution is unlimited.
Acknowledged Federal Support:

RPPR Final Report
as of 05-Sep-2018

Publication Type: Journal Article Peer Reviewed: Y **Publication Status:** 1-Published
Journal: Applied Physics Letters
Publication Identifier Type: DOI Publication Identifier: 10.1063/1.3609240
Volume: 99 Issue: 1 First Page #: 11109
Date Submitted: Date Published:
Publication Location:
Article Title: Strain-balanced InAs/GaSb type-II superlattice structures and photodiodes grown on InAs substrates by metalorganic chemical vapor deposition
Authors:
Keywords: absorption coefficients, buffer layers, compressive strength, gallium compounds, III-V semiconductors, indium compounds, infrared spectra, ion exchange, MOCVD, p-i-n photodiodes, semiconductor growth, semiconductor superlattices
Abstract: We propose and demonstrate strain-balanced InAs/GaSb type-II superlattices (T2SLs) grown on InAs substrates employing GaAs-like interfacial (IF) layers by metalorganic chemical vapor deposition (MOCVD) for effective strain management, simplified growth scheme, improved materials crystalline quality, and reduced substrate absorption. The in-plane compressive strain from the GaSb layers in the T2SLs on the InAs was completely balanced by the GaAs-like IF layers formed by controlled precursor carry-over and anion exchange effects, avoiding the use of complicated IF layers and precursor switching schemes that were used for the MOCVD growth of T2SLs on GaSb. An infrared (IR) p-i-n photodiode structure with 320-period InAs/GaSb T2SLs on InAs was grown and the fabricated devices show improved performance characteristics with a peak responsivity of ?1.9 A/W and a detectivity of ?6.78?×?10^9 Jones at 8 ?m at 78 K. In addition, the InAs buffer layer and substrate show a lower IR absorption coeff
Distribution Statement: 1-Approved for public release; distribution is unlimited.
Acknowledged Federal Support:

Publication Type: Journal Article Peer Reviewed: Y **Publication Status:** 1-Published
Journal: Journal of Vacuum Science & Technology B: Microelectronics and Nanometer Structures
Publication Identifier Type: DOI Publication Identifier: 10.1116/1.3672028
Volume: 30 Issue: 2 First Page #: 107
Date Submitted: Date Published:
Publication Location:
Article Title: Strain-balanced InAs/InAs1-xSbx type-II superlattices grown by molecular beam epitaxy on GaSb substrates
Authors:
Keywords: antimony alloys, energy gap, gallium alloys, III-V semiconductors, molecular beam epitaxial growth, photoluminescence, semiconductor superlattices, X-ray diffraction
Abstract: Strain-balanced InAs/InAs1?xSbx type-II superlattices (SLs) on GaSb substrates with 0.27???x??0.33 were grown by molecular beam epitaxy and demonstrated photoluminescence (PL) up to 11.1??m. The calculated SL bandgap energies agree with the PL peaks to within 5?meV for long-wavelength infrared samples (9.5, 9.9, and 11.1??m) and to within 9?meV for a mid-wavelength infrared sample (5.9??m). X-ray diffraction measurements reveal average SL mismatches of less than 0.2%, and the PL full-width-at-half-maximums increase with the mismatch, confirming the importance of strain-balancing for material quality.
Distribution Statement: 1-Approved for public release; distribution is unlimited.
Acknowledged Federal Support:

RPPR Final Report
as of 05-Sep-2018

Publication Type: Journal Article Peer Reviewed: Y **Publication Status:** 1-Published
Journal: Optics Express
Publication Identifier Type: DOI Publication Identifier: 10.1364/OE.20.002319
Volume: 20 Issue: 3 First Page #: 2319
Date Submitted: Date Published:
Publication Location:
Article Title: Electronic band structures and optical properties of type-II superlattice photodetectors with interfacial effect
Authors:
Keywords: Multiple quantum well, Photodetectors, Detector materials
Abstract: The electronic band structures and optical properties of type-II superlattice (T2SL) photodetectors in the mid-infrared (IR) range are investigated. We formulate a rigorous band structure model using the 8-band k · p method to include the conduction and valence band mixing. After solving the 8 × 8 Hamiltonian and deriving explicitly the new momentum matrix elements in terms of envelope functions, optical transition rates are obtained through the Fermi's golden rule under various doping and injection conditions. Optical measurements on T2SL photodetectors are compared with our model and show good agreement. Our modeling results of quantum structures connect directly to the device-level design and simulation. The predicted doping effect is readily applicable to the optimization of photodetectors. We further include interfacial (IF) layers to study the significance of their effect. Optical properties of T2SLs are expected to have a large tunable range by controlling the thickness and mate
Distribution Statement: 1-Approved for public release; distribution is unlimited.
Acknowledged Federal Support:

Publication Type: Journal Article Peer Reviewed: Y **Publication Status:** 1-Published
Journal: Journal of Vacuum Science & Technology B: Microelectronics and Nanometer Structures
Publication Identifier Type: DOI Publication Identifier: 10.1116/1.3672026
Volume: 30 Issue: 2 First Page #: 106
Date Submitted: Date Published:
Publication Location:
Article Title: Structural properties of InAs/InAs1–xSbx type-II superlattices grown by molecular beam epitaxy
Authors:
Keywords: III-V semiconductors , X-ray diffraction , indium compounds , molecular beam epitaxial growth , segregation , semiconductor growth , semiconductor superlattices , surfactants , transmission electron microscopy
Abstract: Strain-balanced InAs/InAs1?xSbx type-II superlattices (SLs) have been proposed for possible long-wavelength infrared applications. This paper reports a detailed structural characterization study of InAs/InAs1?xSbx SLs with varied Sb composition grown on GaSb (001) substrates by modulated and conventional molecular beam epitaxy (MBE). X-ray diffraction was used to determine the SL periods and the average composition of the InAs1?xSbx alloy layers. Cross-section transmission electron micrographs revealed the separate In(As)Sb/InAs(Sb) ordered-alloy layers within individual InAs1?xSbx layers for SLs grown by modulated MBE. For the SLs grown by conventional MBE, examination by high-resolution electron microscopy revealed that interfaces for InAs1?xSbx deposited on InAs were more abrupt, relative to InAs deposited on InAs1?xSbx: this feature was attributed to Sb surfactant segregation occurring during the SL growth. Overall, these results establish that strain-balanced SL structures with ex
Distribution Statement: 1-Approved for public release; distribution is unlimited.
Acknowledged Federal Support:

RPPR Final Report
as of 05-Sep-2018

Publication Type: Journal Article Peer Reviewed: Y **Publication Status:** 1-Published
Journal: Applied Physics Letters
Publication Identifier Type: DOI Publication Identifier: 10.1063/1.3671398
Volume: 99 Issue: 25 First Page #: 251110
Date Submitted: Date Published:
Publication Location:
Article Title: Significantly improved minority carrier lifetime observed in a long-wavelength infrared III-V type-II superlattice comprised of InAs/InAsSb
Authors:
Keywords: III-V semiconductors , carrier lifetime , indium compounds , minority carriers , photoluminescence , semiconductor superlattices , time resolved spectra
Abstract: Time-resolved photoluminescence measurements reveal a minority carrier lifetime of >412?ns at 77?K under low excitation for a long-wavelength infrared InAs/InAs0.72Sb0.28 type-II superlattice (T2SL). This lifetime represents an order-of-magnitude increase in the minority carrier lifetime over previously reported lifetimes in long-wavelength infrared InAs/Ga1-xInxSb T2SLs. The considerably longer lifetime is attributed to a reduction of non-radiative recombination centers with the removal of Ga from the superlattice structure. This lifetime improvement may enable background limited T2SL long-wavelength infrared photodetectors at higher operating temperatures.
Distribution Statement: 1-Approved for public release; distribution is unlimited.
Acknowledged Federal Support:

Publication Type: Journal Article Peer Reviewed: Y **Publication Status:** 1-Published
Journal: Ultramicroscopy
Publication Identifier Type: Publication Identifier:
Volume: 136 Issue: 0 First Page #: 50
Date Submitted: Date Published:
Publication Location:
Article Title: Lattice and Strain Analysis of atomic resolution Z-contrast images based on template matching
Authors:
Keywords: Strain, Modeling
Abstract: A real space approach is developed based on template matching for quantitative lattice analysis using atomic resolution Z-contrast images. The method, called TeMA, uses the template of an atomic column, or a group of atomic columns, to transform the image into a lattice of correlation peaks. This is helped by using a local intensity adjusted correlation and by the design of templates. Lattice analysis is performed on the correlation peaks. A reference lattice is used to correct for scan noise and scan distortions in the recorded images. Using these methods, we demonstrate that a precision of few picometers is achievable in lattice measurement using aberration corrected Z-contrast images. For application, we apply the methods to strain analysis of a molecular beam epitaxy (MBE) grown LaMnO3 and SrMnO3 superlattice. The results show alternating epitaxial strain inside the superlattice and its variations across interfaces at the spatial resolution of a single perovskite unit cell. Our met
Distribution Statement: 1-Approved for public release; distribution is unlimited.
Acknowledged Federal Support:

CONFERENCE PAPERS:

Publication Type: Conference Paper or Presentation **Publication Status:** 1-Published
Conference Name: International Nano-Optoelectronics Workshop
Date Received: Conference Date: 24-Jul-2011 Date Published:
Conference Location:
Paper Title: Demonstration of the first MOCVD grown InAs/GaSb type-II superlattice photodetectors on an InAs substrate
Authors:
Acknowledged Federal Support:

RPPR Final Report
as of 05-Sep-2018

Publication Type: Conference Paper or Presentation **Publication Status:** 1-Published
Conference Name: 15th International Conference on Narrow Gap Systems
Date Received: Conference Date: 01-Aug-2011 Date Published:
Conference Location:
Paper Title: Optical properties of strain balanced InAs/InxAs1-xSb type-II superlattices
Authors:
Acknowledged Federal Support:

Publication Type: Conference Paper or Presentation **Publication Status:** 1-Published
Conference Name: 15th International Conference on II-VI Compounds
Date Received: Conference Date: 20-Aug-0211 Date Published:
Conference Location:
Paper Title: 6.1 Å II-VI and III-V materials: A platform for photovoltaic and IR device applications
Authors:
Acknowledged Federal Support:

Publication Type: Conference Paper or Presentation **Publication Status:** 1-Published
Conference Name: Advanced Concepts in Semiconductor Materials and Devices for Energy Conversion
Date Received: Conference Date: Date Published:
Conference Location:
Paper Title: 6.1 Å II-VI and III-V materials: A platform for photovoltaic, thermophotovoltaic, and thermoelectric device applications
Authors:
Acknowledged Federal Support:

Publication Type: Conference Paper or Presentation **Publication Status:** 1-Published
Conference Name: Int. Nano-Optoelectronics Workshop
Date Received: Conference Date: 08-Aug-2012 Date Published:
Conference Location:
Paper Title: Improved performance of InAs/GaSb type-II superlattice infrared photodetectors by interface control
Authors:
Acknowledged Federal Support:

Publication Type: Conference Paper or Presentation **Publication Status:** 1-Published
Conference Name: Proceedings of SPIE 8268
Date Received: Conference Date: 21-Jan-2012 Date Published:
Conference Location:
Paper Title: Valance band offset study for InAs/InAsSb superlattice infrared photodetectors
Authors:
Acknowledged Federal Support:

Publication Type: Conference Paper or Presentation **Publication Status:** 1-Published
Conference Name: Quantum Sensing and Nanophotonic Devices IX
Date Received: Conference Date: 20-Jan-2012 Date Published:
Conference Location: San Francisco, California, USA
Paper Title: Optically addressed multiband photodetector for infrared imaging applications
Authors:
Acknowledged Federal Support:

RPPR Final Report
as of 05-Sep-2018

Publication Type: Conference Paper or Presentation **Publication Status:** 1-Published
Conference Name: Quantum Sensing and Nanophotonic Devices IX
Date Received: Conference Date: 20-Jan-2012 Date Published:
Conference Location: San Francisco, California, USA
Paper Title: Structural properties of InAs/InAs1-xSbx type-II superlattices
Authors:
Acknowledged Federal Support:

Publication Type: Conference Paper or Presentation **Publication Status:** 1-Published
Conference Name: Proceedings of the 15th International Conference on Narrow Gap Systems
Date Received: Conference Date: 01-Aug-2011 Date Published:
Conference Location:
Paper Title: Optical properties of strain balanced InAs/InxAs1-xSb type-II superlattices
Authors:
Acknowledged Federal Support:

Publication Type: Conference Paper or Presentation **Publication Status:** 1-Published
Conference Name: SPIE Optics + Photonics 2012
Date Received: Conference Date: 14-Aug-2012 Date Published:
Conference Location:
Paper Title: Temperature-dependent minority carrier lifetimesof InAs/InAs1-xSbx type-II superlattices
Authors:
Acknowledged Federal Support:

Publication Type: Conference Paper or Presentation **Publication Status:** 1-Published
Conference Name: SPIE Defense, Security, and Sensing
Date Received: Conference Date: 23-Apr-2012 Date Published:
Conference Location:
Paper Title: InAs/InAsSb Type-II Superlattice: A Promising Material for Long Wavelength Infrared Applications
Authors:
Acknowledged Federal Support:

Publication Type: Conference Paper or Presentation **Publication Status:** 1-Published
Conference Name: Quantum Sensing and Nanophotonic Devices IX
Date Received: 11-Jul-2018 Conference Date: 21-Jan-2012 Date Published: 21-Jan-2012
Conference Location: San Francisco, California
Paper Title: Structural properties of InAs/InAs1-xSbx type-II superlattices
Authors: Lu Ouyang, Elizabeth H. Steenbergen, O. Orkun Cellek, Yong-Hang Zhang, David J. Smith, Manijeh Ra
Acknowledged Federal Support: **N**

Publication Type: Conference Paper or Presentation **Publication Status:** 1-Published
Conference Name: Internation Nanooptoelectronics Workshop
Date Received: 11-Jul-2018 Conference Date: 19-Aug-2013 Date Published: 19-Aug-2013
Conference Location: Cargèse, France
Paper Title: Modeling and extraction of minority carrier diffusion lengths in superlatticephotodiodes using electron beam induced current
Authors: Daniel Zuo, Shun Lien Chuang
Acknowledged Federal Support: **N**

Publication Type: Conference Paper or Presentation **Publication Status:** 1-Published
Conference Name: Electronic Materials Conference
Date Received: 11-Jul-2018 Conference Date: 25-Jun-2014 Date Published: 25-Jun-2014
Conference Location: Santa Barbara, California USA
Paper Title: Properties of InAs/InAsSb type-II superlattices grown on GaSb by MOCVD
Authors: James D. Justice, Xiaohang Li, Theeradetch Detchprohm, Russell D. Dupuis, Honggyu Kim, Jian-Min Zu
Acknowledged Federal Support: **Y**

Publication Type: Conference Paper or Presentation **Publication Status:** 1-Published
Conference Name: Intl. Conf. on Metal Organic Vapor Phase Epitaxy XVII
Date Received: 11-Jul-2018 Conference Date: 14-Jul-2014 Date Published: 14-Jul-2014
Conference Location: Lausanne, Switzerland
Paper Title: Properties of InAs/InAsSb Type-II superlattices Grown on GaSb by MOCVD
Authors: James D. Justice, Xiaohang Li, Theeradetch Detchprohm, Russell D. Dupuis, Honggyu Kim, Jian-Min Zu
Acknowledged Federal Support: **Y**

Publication Type: Conference Paper or Presentation **Publication Status:** 1-Published
Conference Name: MICROSCOPY AND MICROANALYSIS
Date Received: 11-Jul-2018 Conference Date: 04-Aug-2013 Date Published: 04-Aug-2013
Conference Location: Indianapolis, IN
Paper Title: Atom-Probe Tomographic Study of Interfacial Intermixing and Segregation in InAs/GaSb Superlattices
Authors: Yifei Meng, Honggyu Kim, Dieter Isheim, David N. Seidman, Jian-Min Zuo
Acknowledged Federal Support: **Y**

Publication Type: Conference Paper or Presentation **Publication Status:** 1-Published
Conference Name: Microscopy and Microanalysis
Date Received: Conference Date: 04-Aug-2013 Date Published:
Conference Location:
Paper Title: Atom Scale Analysis of Chemical Intermixing in MBE-grown GaSb/InAs Superlattices Based on Z-contrast Imaing
Authors:
Acknowledged Federal Support:

Publication Type: Conference Paper or Presentation **Publication Status:** 1-Published
Conference Name: Microscopy and Microanalysis
Date Received: Conference Date: 04-Aug-2013 Date Published:
Conference Location:
Paper Title: Atom Scale Analysis of Chemical Intermixing in MBE-grown GaSb/InAs Superlattices Based on Z-contrast Imaing
Authors:
Acknowledged Federal Support:

Publication Type: Conference Paper or Presentation **Publication Status:** 1-Published
Conference Name: Microscopy and Microanalysis
Date Received: Conference Date: 04-Aug-2013 Date Published:
Conference Location:
Paper Title: Atom Scale Analysis of Chemical Intermixing in MBE-grown GaSb/InAs Superlattices Based on Z-contrast Imaing
Authors:
Acknowledged Federal Support:

RPPR Final Report
as of 05-Sep-2018

Publication Type: Conference Paper or Presentation **Publication Status:** 1-Published
Conference Name: Electrochemical Society
Date Received: Conference Date: 11-May-2014 Date Published:
Conference Location:
Paper Title: Spatially Resolved Study of the EQE Droop in InGaN QW LEDs: Interplay of Point Defects, Extended Defects, and Carrier Localization
Authors:
Acknowledged Federal Support:

Publication Type: Conference Paper or Presentation **Publication Status:** 1-Published
Conference Name: SPIE Defense + Security
Date Received: Conference Date: 20-Apr-2015 Date Published:
Conference Location: Baltimore, Maryland, United States
Paper Title: Photoluminescence study of carrier recombination processes in InAs/InAsSb type-II superlattices
Authors:
Acknowledged Federal Support:

Publication Type: Conference Paper or Presentation **Publication Status:** 1-Published
Conference Name: Proceeding of SPIE
Date Received: Conference Date: 20-Apr-2015 Date Published:
Conference Location: Baltimore, Maryland, United States
Paper Title: Effects of AlSb interfaces on InAs/InAsSb type-II infrared superlattice material properties
Authors:
Acknowledged Federal Support:

Publication Type: Conference Paper or Presentation **Publication Status:** 1-Published
Conference Name: The 57th Electronic Material Conference, Ohio State University, Columbus, OH, USA
Date Received: 11-Jul-2018 Conference Date: 24-Jun-2015 Date Published: 24-Jun-2015
Conference Location: OSU, Ohio, USA
Paper Title: "Study of MOCVD growth of InAs/InAsSb type-II superlattices using a LayTec EpiTT in-situ optical monitoring system"
Authors: James D. Justice, Jeomoh Kim, Theeradetch Detchprohm, Russell D. Dupuis, Honggyu Kim, Jian-Min Z
Acknowledged Federal Support: **Y**

Publication Type: Conference Paper or Presentation **Publication Status:** 1-Published
Conference Name: Conference on Lasers and Electro-Optics
Date Received: Conference Date: 10-May-2015 Date Published:
Conference Location:
Paper Title: Diffusion Characterization Using Electron Beam Induced Current and Time-Resolved Photoluminescence of InAs/InAsSb Type-II Superlattices
Authors:
Acknowledged Federal Support:

Publication Type: Conference Paper or Presentation **Publication Status:** 1-Published
Conference Name: Electronic Materials Conference
Date Received: 11-Jul-2018 Conference Date: 24-Jun-2015 Date Published: 24-Jun-2015
Conference Location: OSU, Ohio, USA
Paper Title: Diffusion Characterization Using Electron Beam Induced Current and Time-Resolved Photoluminescence of InAs/InAsSb Type-II Superlattices
Authors: Daniel Zuo, Narae Yoon, Runyu Liu, James Mabon, Zhao-Yu He, Shi Liu, Yong-Hang Zhang, Emil A. Ka
Acknowledged Federal Support: **N**

RPPR Final Report
as of 05-Sep-2018

Publication Type: Conference Paper or Presentation **Publication Status:** 1-Published
Conference Name: Lasers and Electro-Optics (CLEO)
Date Received: 11-Jul-2018 Conference Date: 10-May-2015 Date Published: 10-May-2015
Conference Location: San Jose, CA
Paper Title: Diffusion Characterization Using Electron Beam Induced Current and Time-Resolved Photoluminescence of InAs/InAsSb Type-II Superlattices
Authors: D. Zuo, R. Liu, J. Mabon, Z.-Y. He, S. Liu, Y.-H. Zhang, E. A. Kadlec, B. Olson, E. A. Shaner, D. Wasse
Acknowledged Federal Support: **Y**

Publication Type: Conference Paper or Presentation **Publication Status:** 1-Published
Conference Name: 16th International Conference of Metalorganic Vapor Phase Epitaxy (ICMOVPE XVI)
Date Received: 04-Apr-2018 Conference Date: 20-May-2012 Date Published: 25-May-2012
Conference Location: Busan, Korea,
Paper Title: Growth of InAs/GaSb and InAs/InAsSb type-II superlattice photodiodes on GaSb and InAs substrates by metalorganic chemical vapor deposition
Authors: Y. Huang, J.-H. Ryou, R. D. Dupuis, E. H. Steenbergen, J. Fan, Y.-H. Zhang, D. Zuo, B. Kesler, S.-L. Ch
Acknowledged Federal Support: **Y**

Publication Type: Conference Paper or Presentation **Publication Status:** 1-Published
Conference Name: Quantum Sensing and Nano Electronics and Photonics XV
Date Received: Conference Date: 27-Jan-2018 Date Published: 27-Jan-2018
Conference Location: San Francisco, United States
Paper Title: Optical quality in strain-balanced InAs/InAsSb superlattices grown with and without Bi surfactant
Authors: Preston T. Webster, Stephen T. Schaefer, Elizabeth H. Steenbergen, Shane R. Johnson
Acknowledged Federal Support: **N**

DISSERTATIONS:

Publication Type: Thesis or Dissertation
Institution:
Date Received: 04-Sep-2011 Completion Date:
Title: Antimony-based type-II superlattice infrered detectors based on InAs Substrates
Authors:
Acknowledged Federal Support:

Publication Type: Thesis or Dissertation
Institution:
Date Received: 30-Aug-2012 Completion Date:
Title: Antimonide-based type-II superlattices for infrared detection
Authors:
Acknowledged Federal Support:

Publication Type: Thesis or Dissertation
Institution:
Date Received: 30-Aug-2012 Completion Date:
Title: Theory and experiment of type-II superlattice infrared photodetectors
Authors:
Acknowledged Federal Support:

RPPR Final Report
as of 05-Sep-2018

Publication Type: Thesis or Dissertation
Institution: Arizona State University
Date Received: 11-Jul-2018 Completion Date: 4/1/12 5:00AM
Title: Conversion of a Molecular Beam Epitaxy System for the Growth of 6.1 Angstrom Semiconductors
Authors: W. Hank G., Dettlaff
Acknowledged Federal Support: **N**

Publication Type: Thesis or Dissertation
Institution: Arizona State University
Date Received: 11-Jul-2018 Completion Date: 2/1/13 6:00AM
Title: High-Quality Extended-Wavelength Materials for Optoelectronic Applications
Authors: Ankur, Sharma
Acknowledged Federal Support: **N**

Publication Type: Thesis or Dissertation
Institution: Texas A&M University
Date Received: 08-Jul-2018 Completion Date: 12/1/17 6:10PM
Title: ORDER AND DISORDER IN TYPE–II InAs/InAsSb SUPERLATTICES
Authors: MATTHEW ROBERT WOOD
Acknowledged Federal Support: **Y**

Publication Type: Thesis or Dissertation
Institution: Arizona State University
Date Received: 11-Jul-2018 Completion Date: 10/1/15 10:00AM
Title: Study of Structural, Optical and Electrical Properties of InAs/InAsSb Superlattices Using Multiple Characterization Techniques
Authors: Xiaomeng, Shen
Acknowledged Federal Support: **Y**

Publication Type: Thesis or Dissertation
Institution: Arizona State University
Date Received: 11-Jul-2018 Completion Date: 4/1/12 10:00AM
Title: Structural characterization of II-VI and III-V compound semiconductor heterostructures and superlattices
Authors: Lu, Ouyang
Acknowledged Federal Support: **N**

Publication Type: Thesis or Dissertation
Institution: Arizona State University
Date Received: 11-Jul-2018 Completion Date: 4/1/12 5:00AM
Title: Structural characterization of II-VI and III-V compound semiconductor heterostructures and superlattices
Authors: Lu, Ouyang
Acknowledged Federal Support: **N**

Publication Type: Thesis or Dissertation
Institution: Arizona State University
Date Received: 11-Jul-2018 Completion Date: 3/1/12 6:00AM
Title: Strain-balanced InAs-InAsSb Type-II Superlattices on GaSb Substrates for Infrared Photodetector Applications
Authors: Elizabeth H., Steenbergen
Acknowledged Federal Support: **Y**

RPPR Final Report
as of 05-Sep-2018

Publication Type: Thesis or Dissertation
Institution: Arizona State University
Date Received: 11-Jul-2018 Completion Date: 3/1/12 12:00PM
Title: Strain-balanced InAs-InAsSb Type-II Superlattices on GaSb Substrates for Infrared Photodetector Applications
Authors: Elizabeth H., Steenbergen
Acknowledged Federal Support: **Y**

Publication Type: Thesis or Dissertation
Institution: Arizona State University
Date Received: 11-Jul-2018 Completion Date: 3/1/17 6:00AM
Title: Evaluation of Compound Semiconductors for Infrared Photo-Detection Applications
Authors: Jing, Lu
Acknowledged Federal Support: **Y**

Publication Type: Thesis or Dissertation
Institution: Arizona State University
Date Received: 11-Jul-2018 Completion Date: 5/1/16 5:00AM
Title: Growth, Optical Properties, and Optimization of Infrared Optoelectronic Materials
Authors: Preston Thomas, Webster
Acknowledged Federal Support: **Y**

Publication Type: Thesis or Dissertation
Institution: University of Illinois at Urbana-Champaign
Date Received: 11-Jul-2018 Completion Date: 12/1/16 12:00PM
Title: DIFFUSION CHARACTERIZATION OF ANTIMONY-BASED TYPE-II SUPERLATTICES USING ELECTRON BEAM INDUCED CURRENT AND TIME-RESOLVED PHOTOLUMINESCENCE
Authors: NARAE YOON
Acknowledged Federal Support: **Y**

Publication Type: Thesis or Dissertation
Institution: University of Illinois at Urbana-Champaign
Date Received: 11-Jul-2018 Completion Date: 7/1/15 5:00AM
Title: ATOMIC STRUCTURE AND DEFECTS OF III-V COMPOUND SEMICONDUCTOR STRAINED-LAYER-SUPERLATTICES FOR INFRARED DETECTION
Authors: HONGGYU KIM
Acknowledged Federal Support: **Y**

Publication Type: Thesis or Dissertation
Institution: University of Illinois at Urbana-Champaign
Date Received: 11-Jul-2018 Completion Date: 7/1/15 10:00AM
Title: DEFECT CHARACTERIZATION OF ANTIMONIDE-BASED TYPE-II SUPERLATTICES FOR INFRARED DETECTION
Authors: Daniel, Zuo
Acknowledged Federal Support: **Y**

Publication Type: Thesis or Dissertation
Institution: University of North Carolina at Charlotte
Date Received: 11-Jul-2018 Completion Date: 12/1/15 6:00AM
Title: Micro-Raman/PL Investigation sof Materials for IR and PV Applications
Authors: Henan, Liu
Acknowledged Federal Support: **Y**

RPPR Final Report
as of 05-Sep-2018

Army Research Office, MURI Program

Project Title: Fundamental study of defects and their reduction in type-II superlattice materials

Principal Investigators:

UIUC (Lead): J. M. Zuo (PI), S.L Chuang (Deceased)

UTA: D. Wasserman (Also UIUC)

Georgia Tech (GT): R. D. Dupuis

ASU: S. R. Johnson, D. J. Smith, Y.-H. Zhang

UNCC: Y. Zhang

TAMU: M. Weimer

Report Period: Final Report

1. Introduction:

The University of Illinois led Army MURI project on "Fundamental Study of Defects and Their Reduction in Type-II Superlattice Materials" ran from Oct., 2010, through Oct. 2017. The program supported a group of ten prominent university researchers along with 47 graduate students, 3 undergraduate students, and 16 postdoctoral fellows across five participating universities over the seven years period.

Together, the group published 52 papers in the peer-reviewed literature, with direct acknowledgement of the support from this award, including publications in top archival science and engineering journals.

Over the course of the project period, our team members were recognized by a number of highly prestigious honors and awards, including

- Russell Dean Dupuis, Alexander von Humboldt Research Award, Alexander von Humboldt Foundation, Germany, 2013
- Yong-Hang Zhang: Elected Fellow, OSA, 2013
- David J. Smith: Elected Fellow, Microscopy Society of America, 2013
- Russell Dean Dupuis, Elected Fellow of the National Academy of Inventors, 2014
- David J. Smith, 2014 Distinguished Physical Scientist Award, Microscopy Society of America
- David J. Smith, 2014 Helmholtz International Fellow Award, Helmholtz Association
- Jian-Min Zuo, Elected Fellow of American Physical Society, 2014
- Russell Dean Dupuis, The Institute of Electrical and Electronics Engineers IEEE Life Fellow Award, 2015
- Russell Dean Dupuis, National Academy of Engineering Charles Stark Draper Engineering Award, 2015. With I. Akasaki, M. G. Craford, N. Holonyak, Jr., and S. Nakamura
- Yong-Hang Zhang: Elected Fellow IEEE, 2015
- Jian-Min Zuo, Ernst Ruska Prize of the German Society for Electron Microscopy, 2015
- Russell Dean Dupuis, International SSL Alliance Award of Outstanding Achievement for Global Solid State Lighting Development, 2016
- Jian-Min Zuo, Racheff Professorship, Engineering College, UIUC, 2016-present
- Jian-Min Zuo, Lars Onsager Professorship, Norwegian University of Science and Technology, 2017
- Yong Zhang, Elected Fellow of American Physical Society, 2017

The project was motivated by the advantages offered by antimony-based type-II superlattice (T2SLs) for MWIR (Midwave Infrared) and LWIR (Long-Wave Infrared) laser and detector applications due to their broad bandgap tunability and material uniformity. The performance of T2SL IR detectors is predicted to be superior to that of MCT (HgCdTe) IR detectors. Previous research on novel T2SL structures has demonstrated significant progress and interesting device physics, but the predicted high performance has yet to be realized as T2SL IR detectors are still limited by defects and

interface-related traps. A thorough understanding of defect physics, growth processes, and detector theory is thus crucial for the suppression of defect formation and their adverse effects. To achieve this, the project brought together a team of experts in MBE and MOCVD growth, device theory device fabrication and characterization, Raman spectroscopy, X-ray diffraction, transmission electron microscopy.

The main objectives of the project are to:

1) Identify and understand the origin of point defects, line defects, interfacial traps, and surface states in T2SL structures through experimental studies closely coupled to theoretical modeling.
2) Correlate defect properties with device performance as a function of operating temperature, including minority carrier lifetime, detector noise, dark current, breakdown voltage, shunt resistance, and surface recombination.
3) Examine novel MBE and MOCVD growth methods and passivation techniques that eliminate and or mitigate defects in InAs/GaSb, InAs/InGaSb, and InAs/InAsSb T2SLs.
4) Develop a comprehensive device physics model that includes extrinsic material properties to accurately predict device performance and provide vital device design rules.

A broad range of research activities were carried out by the team in following three task areas. Major achievements in each area include the followings.

Task 1: Theoretical and Experimental Study of Defects

- Developed 8 band **k.p** model for type-II superlattice materials
    - Leveraged model to design GaSb/InAs, Ga-free, and interface controlled T2SL absorbers.
- Identified Ga vacancy as the major point defect in InAs/GaSb T2SLs
    - Developed an atomic resolution strain mapping based method for the location and identification of vacancy defects.
    - Demonstrated the large strain from vacancy defects and obtained good agreement with the first principles calculations.
- Developed a digital model for high resolution X-ray diffraction of T2SLs and the model fitting method. Applied the method successfully for characterization of superlattice period, period fluctuations, interfacial intermixing and strain in the InAs/GaSb and InAs/InAsSb T2SLs.
- Determined interfacial intermixing in InAs/GaSb T2SLs using X-ray diffraction, atom probe tomography (APT) and scanning transmission electron microscopy (STEM). Compared results with kinetic growth model and identify the segregation of Sb and As as the mechanism for interfacial intermixing.
- Demonstrated Sb induced strain fluctuations in an InAs/InAsSb T2SL.
- Identified GaAs interfacial bonds as the major cause of large strain fluctuations in InAs/GaSb T2SLs, and demonstrated the effectiveness of InSb interfacial treatment for the reduction of GaAs interfacial bonds.

- Established the connection between period fluctuations and interface roughness in the InAs/InAsSb T2SLs using cross-sectional scanning tunnelling microscopy (STM).
- Identified short-range, atomic-alloy, order in the InAs/InAsSb T2SLs.
- Systematic examination of different DFT based methods for computing defect states in a semiconductor, using anti-site defect Ga on Sb as a prototype, allowing for correct comparison between experiment and theory.
- Observation of new Raman modes in InAs/GaSb T2SLs.

Task 2: Innovative Growth and Fabrication Processes for Defect Reduction

- Demonstration of record long minority carrier lifetimes in Ga-free InAs/InAsSb type-II superlattice.
- Demonstration of record low dark current in LWIR nBn photodetectors made of Ga-free InAs/InAsSb type-II superlattice.
- Demonstrated high PL efficiency MOCVD-grown MWIR "Ga-free" InAs-InAsSb. Type II superlattices (T2SLs) emitting at various wavelengths from 5-8 um.
- Good interface control established between MOCVD-grown InAs and InAsSb with accurate composition control.
- Band structure investigation of nBn photodetectors, and development of state-of-the-art nBn devices with InAs/InAsSb T2SLs.
- Developed MOCVD growth conditions and strain management schemes that can minimize the strain accumulation in InAs/GaSb and InAs/InAsSb T2SLs on GaSb substrates.
- Demonstrated the first MOCVD-grown InAs/GaSb and InAs/InAsSb T2SL structure and devices.

Task 3: Evaluation of Defect Reduction Approaches and Device Applications

- Design, growth, fabrication and characterization of interface-controlled T2SL absorbers demonstrating improved absorption coefficient, smaller effective bandgap, and longer diffusion lengths
- Development of electron-beam induced current measurement for type-II superlattice materials
    - Demonstration of EBIC technique for p+-pi-n diode architecture T2SL detectors
    - Application of EBIC to Ga-free T2SL nBn detectors
- Development of new approach to EBIC measurements with improved spatial resolution, increased parameter extraction accuracy, and the potential for integrating carrier concentration dependent effects into EBIC parameter extraction.

- Characterization of InAsSb/InGaAs T2SL materials using EBIC and TRPL. Comparison of EQE and EBIC approaches for determination of vertical carrier mobility.

Our final report is organized in five sections, according to the three research tasks, with Sections 2 and 3 on Task I of experimental and theoretical study of defects and Sections 4 and 5 on Task II and III, respectively. During the course of project, to address the research challenges faced by the team, team members also undertook efforts to develop new characterization techniques and methodologies. These methods are described together with the resulted major findings.

2. Experimental Study of Defects

2.1. Evaluation of minority carrier lifetimes in InAs/InAsSb superlattices (Zhang, ASU)

The III-V type-II superlattice (T2SL) is predicted to have a number of advantages over bulk HgCdTe infrared (IR) photodetectors including a decreased dependence of the bandgap on compositional non-uniformity, the ability to wavelength tune by changing layer thicknesses and alloy composition, the lower cost of III-V semiconductor substrates, a higher electron effective mass leading to smaller tunneling currents and band-engineered lower Auger recombination rates and thus lower dark currents, as predicted theoretically.[1, 2] The widely studied InAs/GaInSb T2SLs have very short carrier lifetimes, on the order of 30 ns[3] because the energy levels of intrinsic point defects in bulk GaSb are near the valence band edge or in the middle of the energy gap,[4, 5] leaving the trap states available for Shockley-Read-Hall (SRH) recombination. The other alternative approach, i.e. "Ga-free" InAs/InSbAs T2SLs[6] has demonstrated a broad wavelength coverage from 4 μm to 12 μm,[7, 8] and superior material performance, especially minority carrier lifetimes longer than 400 ns[9] in the long-wave IR range and 10 μs in the mid-wave IR range[10] as recently demonstrated. Such a dramatic improvement in minority carrier lifetime is believed to be due to the fact that in bulk InAs and As-rich InAsSb alloys the "stabilized Fermi level" is above the conduction band edge,[5] rendering any mid-gap defect states inactive for SRH processes as demonstrated by relatively high photoluminescence efficiencies even when grown on highly mismatched GaAs substrates.[11] Furthermore, Eastman *et al*[12] showed that empty surface states may exist within the bandgap of GaSb and above the conduction band edge of InAs. These observations have led us to investigate the intrinsic point defect energy levels in Ga-free T2SL structures to better understand why InAs/InAsSb T2SLs have significantly longer minority carrier lifetimes.

In this program, we set out to find experimental evidence to confirm that the defect energy states are above the conduction band edge of Ga-free T2SLs. Applying hydrostatic pressure to III-V semiconductors causes a strong and reversible change in their electronic band-structure[13] and is a perfect tool to investigate the fundamental properties of semiconductor systems and heterostructures as well as to probe recombination mechanisms in semiconductor devices.[13] Of most relevance to this study, the conduction band edge moves upwards in energy at a typical rate of ≈100 meV·GPa^{-1} for III-V semiconductors. This manifests itself very clearly through an increase in bandgap and consequently, an increase in the optical transition energy with increasing pressure. In contrast, localized states such as defect energy states, are typically pressure insensitive owing to the fact that they are strongly localized and decoupled from the periodicity of the crystal.[14] It is therefore possible to use high pressure to probe the interaction between the band edges and defect energy states, which for example, may be seen through the quenching of photoluminescence or in an abrupt increase in the dark current of a photodetector due to increased non-radiative recombination. The experimental approach is similar to that used to find nitrogen complex levels above the conduction band edge of GaAs[15] with high pressure, low temperature photoluminescence (PL). *Figure 2.1*(a) shows a schematic representation of a Ga-free InAs/InAsSb T2SL band edge diagram and the suspected

localized defect states at ambient pressure. The optical transition is shown as an arrow from the electron miniband above the conduction band edge of InAs to the hole miniband below the valence band edge of InAsSb. In *Figure 2.1*(a) the bandgap of InAs is 0.417 eV,[16] for $InAs_{0.86}Sb_{0.14}$ a value of 0.311 eV is determined based on parameters from Vurgaftman *et al*[15] and a bowing parameter of 0.65 eV[17]. A fractional valence band offset, $Q_v = \Delta E_v/\Delta E_g$, of 1.75 ± 0.03 is used[17] giving electron and hole well depths of 80 and 186 meV respectively. The electron and hole minibands have confinement energies of 18 meV and 65 meV respectively. The effect of applying pressure increases the effective bandgap of the T2SL, namely the separation of the electron and the hole minibands. Most of the increase of the effective bandgap is due to the upward shift in energy of the conduction band edge and thus the electron miniband. It is anticipated that the PL intensity will decrease dramatically when the electron miniband moves above the defect energy level as shown in *Figure 2.1*(b), due to increased nonradiative recombination through the trap states of the defects.

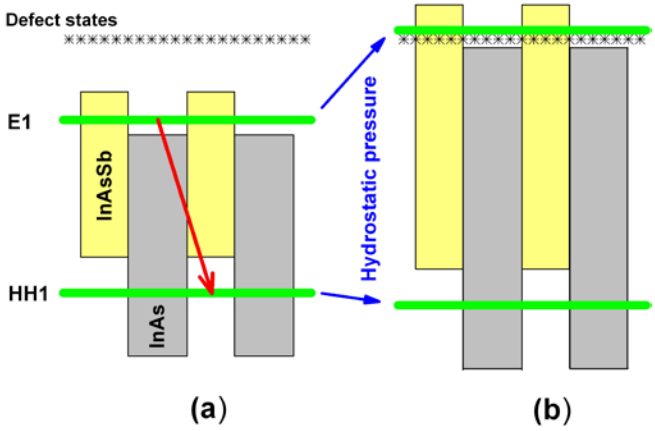

Figure 2.1. (a) A schematic band edge diagram for a Ga-free InAs/InAsSb T2SL showing a defect state above the conduction band edge; (b) Under hydrostatic pressure the effective bandgap energy increases, mainly due to an upward shift in the conduction band edge, while the defect states remain at the same energy. Quenching of the photoluminescence happens when the electron miniband edge moves close to the defect energy level.

The $InAs/InAs_{0.86}Sb_{0.14}$ T2SL sample studied in this work was grown by molecular beam epitaxy on an n-type GaSb (100) substrate and contained a nominally undoped T2SL layer consisting of 48 periods of 8.1 nm InAs and 2.5 nm $InAs_{0.86}Sb_{0.14}$ (see *Figure 2.1*(a)) with a lattice mismatch of 0.4%. The background doping density in this sample is estimated to be in the order of 1.0×10^{16} cm^{-3} n-type. The growth details (sample B1761) and full optical and structural properties are reported elsewhere.[8, 18] PL experiments were performed at 10K under pressure in a backscattering geometry in a clamp style sapphire ball cell (SBC).[19] Methanol-ethanol (4:1) was used as the pressure transmitting media with pressure changes being carried out at room temperature before cooling down. PL was excited with a chopped 100 mW 1064nm ND:YVO_4 laser with neutral density filters being placed in the beam to vary the pump power incident on the sample. PL measurements were carried out in a closed-cycle helium cryostat using a Triax 320 spectrometer with a liquid nitrogen cooled InSb detector and CaF_2 lenses. The pressure calibrant was a InGaAsP quantum well structure with a known linear pressure coefficient ($86 meV \cdot GPa^{-1}$)[20] which gave strong PL with peaks at 0.8145 eV and 0.8651 eV at room and low temperature respectively, but without any possible overlap with the T2SLs emission (0.3147 eV at 10K). Both samples were thinned and loaded into the SBC after confirming that the thinning process resulted in no change to their PL. The system spectral response (Triax grating, InSb detector, quartz cryostat window, two CaF_2 lenses and a sapphire ball) was

determined before and after the experimental runs using a Bentham traceable broadband light source to correct the measured PL spectra.

Four separate pressure runs were carried out with most of the data being taken with increasing pressure (several decreasing pressure cycle points were checked and gave good agreement). *Figure 2.2*(a) shows corrected PL spectra from one pressure run up to 2.16 GPa. Increased noise in the PL signal was seen over the range from 0.34 eV to 0.44 eV due to the absorption of the pressure medium over this wavelength range as shown in *Figure 2.2*(b). The interpolated transmission data[21] from liquid methanol and ethanol based on the 4:1 mixture ratio at 300K (solid line) and the data from ethanol under pressure and frozen methanol spectra are used to estimate the shift and transmission behavior up to 2.16 GPa (dashed line). Based on this evidence it is clear that the transmission data changes with pressure, but whilst it was not possible for us to carry out a dynamic correction at each pressure and temperature we are able to show that the absorption should have little effect above 0.46 eV; this is confirmed by PL spectra from the InGaAsP pressure gauge.

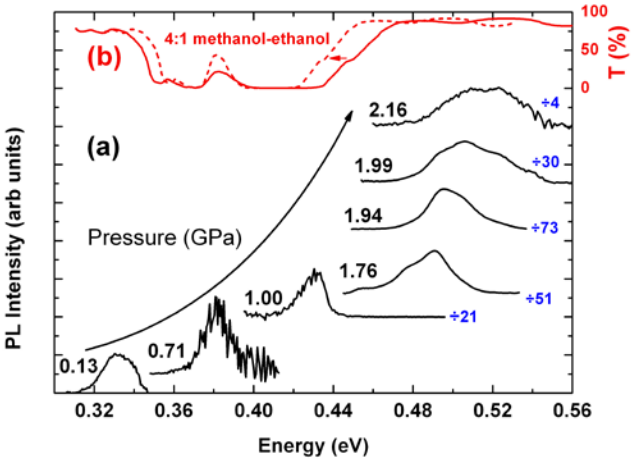

Figure 2.2 (a) Photoluminescence spectra acquired from one run at different hydrostatic pressures up to 2.16 GPa. (b) On the same energy axis the optical transmission "T" (from 0 to 100%) of the methanol-ethanol pressure transmitting media calculated from literature data at 0 GPa (solid line), the arrow indicates the shift to the estimated transmission at 2.16 GPa (dashed line).

The PL full width half maximum (FWHM) of the T2SL peak was 20 meV at an estimated excitation density of 13 $W \cdot cm^{-2}$ and decreased approximately linearly to around 15 meV at 1.5 GPa, above this it increased approximately linearly reaching 40 meV at 2.16 GPa. Figure 3(a) shows the collected peak emission energy data against pressure, which when fitted gives a pressure coefficient of 93 ± 4 $meV \cdot GPa^{-1}$. This value is close to the quoted value of 96-108 $meV \cdot GPa^{-1}$ for InAs[23] and 128-155 $meV \cdot GPa^{-1}$ for InSb.[22] Calculations based on this structure using Nextnano software and taking into account bandgap and effective mass changes, show that the confinement energy of the electron states changes by as little as 1 meV up to 2.16 GPa. The change in strain is negligible as the two constituent layers of the T2SL have similar elastic constants. The initial electron confinement is calculated as 18 meV in the superlattice well of depths of 80 meV. This well depth deepens slightly with pressure but importantly the electron miniband is expected to shift at the same rate as the InAs layer.

Figure 2.3(b) shows all of the integrated PL intensity data corrected for the system response and optical collection efficiency from the four pressure runs as a function of pressure and peak energy shift. An energy level crossover between a defect energy level (or another conduction band minima) and a conduction band edge state is normally accompanied by a strong decrease in the integrated PL intensity as seen in InAs/GaAs

quantum dots undergoing a Γ- X crossover[23] and may also give rise to new radiative peaks moving with different or negative pressure coefficients.[15, 23] Figure 2.3(b) shows such a decrease in PL intensity but we report no change in the pressure coefficient of the PL peak energy associated with this quenching nor any new radiative peaks above the crossover pressure. All these characteristics are expected in the case of a crossover with a non-radiative defect level. PL was not observed above the pressures shown in Figure 2.3(b) as the defect energy levels move below the conduction band edge and into the InAs bandgap becoming SRH recombination centers.

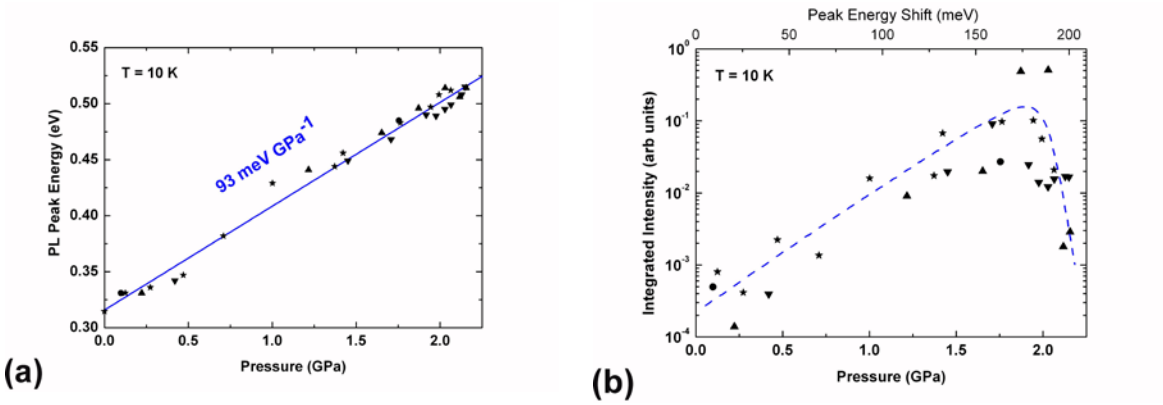

Figure 2.3 (a) A linear fit of the photoluminescence peak energy data obtained for the T2SL sample from the four pressure runs indicated using four different symbols. (b) The integrated photoluminescence intensity of the T2SL sample plotted as a function of pressure and also peak energy shift from ambient pressure on the top axis. The dashed line is drawn as a guide to the eye.

A careful comparison of the energy and intensity data shown in Figure 2.3(b) and those reported by Itskevich *et al*[23] and elsewhere indicates a crossover at 2 GPa. This corresponds to a PL energy shift of 0.186 eV (onset at 1.92 GPa with the true crossover close to 2 GPa, giving 1.96 ± 0.04 GPa or an energy shift of ~0.18 ± 0.01 eV). According to Daunov *et al*[24] the ratio of the pressure coefficients of the conduction and valence band edges for many III-V semiconductors (including InSb) are equal to ~7. For our structure this would mean that 82 meV·GPa^{-1} of the determined pressure coefficient of our sample would go into the conduction band edge with the valence band edge moving down at a rate of -11 meV·GPa^{-1}. Assuming that the defect energy level does not move with pressure, as shown in *Figure 2.1*, using the above conduction band edge shift over 2 GPa and adding the 17 meV confinement energy at 2 GPa leads to a determined defect level ~0.18 eV above the InAs conduction band edge at ambient pressure. More details about this assignment will be discussed further below.

The PL intensity data as a function of laser excitation power and temperature under pressure are plotted in Figure 2.4 and examined to confirm that the PL quenching at 2 GPa is indeed due to a change from a radiative dominant recombination process to a non-radiative dominant recombination mechanism. Figure 2.4(a) shows the excitation power dependence of the T2SL integrated PL intensity data at 0, 0.42, 1.87 and 2.16 GPa at 10K.

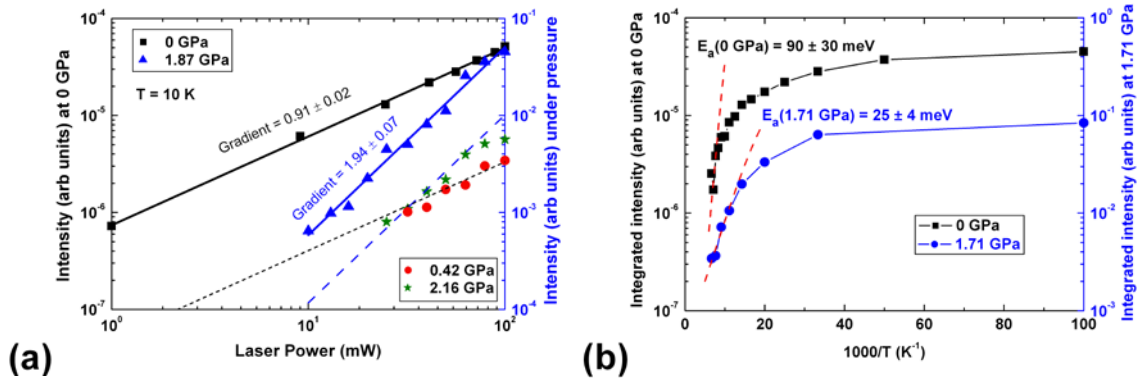

Figure 2.4 (a) Power dependent PL measurements taken at 0 GPa (intensity axis on left), and 0.42, 1.87 and 2.16 GPa (intensity axis on right). Solid lines show linear fits of the PL intensity at 0 and 1.87 GPa. Dotted and broken lines are the same fits offset as a guide to the eye at 0.42 GPa and 2.16 GPa respectively. (b) Arrhenius plots of data at 0 GPa (left intensity axis) and 1.71 GPa (right intensity axis). Dashed lines in the high temperature range are marked with the determined activation energy (E_a) in meV.

The observed PL intensity as a function of excitation power density is easily described by a power law with a fitted power exponent at 0 GPa of 0.91, close to 1, which, for an undoped sample, such as that discussed here, clearly indicates a dominant radiative recombination process.[25, 26] A similar gradient is seen at 0.42 GPa, confirming that the recombination is radiative in nature and that mid gap SRH recombination is negligible at low pressure. At 1.87 GPa (the onset of the high pressure PL intensity decline) the measured gradient is 1.94. This value is close to 2, which indicates a dominant non-radiative, defect-related recombination path is now involved. Finally at 2.16 GPa a gradient close to 1.94 is seen but with possible evidence of saturation at the highest laser power. All the data in Figure 2.4(a) confirm our expectation that the PL quenching at 2 GPa is the result of a transition from dominant radiative recombination to dominant non-radiative recombination.

Assuming that the non-radiative recombination can also be thermally activated we studied the integrated PL intensity quenching from 10K to 150 K at 0 GPa and 1.71 GPa and the measured results are shown in Figure 2.4(b). At high pressure and over this low temperature range it should be noted that the pressure medium remains solid and the pressure is constant within the SBC.

From Figure 2.4(b) it can be seen that the higher temperature behavior of each data set follows an exponential dependence,[27] from which activation energies have been calculated. The 0 GPa data gives an activation energy of 90 ± 30 meV, but at 1.71 GPa a much lower value of 25 ± 4 meV is obtained. Our measured activation energy of 90 meV at 0 GPa may be related to the depth of the electron well (80 meV). At 1.71 GPa it is 0.29 GPa from our determined crossover pressure (2 GPa) and using our conduction band edge pressure coefficient of 82 meV·GPa^{-1} we estimate that the energy level associated with the quenching is ~24 meV away. This data confirms our assumptions of the pressure-dependent energy shifts of the valence band and conduction band edges. It also points to the fact that the defect level is indeed not moving with pressure, as if it were then the

activation energy obtained at 1.71 GPa would not be consistent with our results as the rate at which the confined electron state approached the defect would depend on both pressure coefficients. We note here that the nature and exact identification of these defect states is outside of the scope of this present work, but will be investigated in the future studies.

In summary, we have performed pressure-dependent PL measurements on an InAs/$InAs_{0.86}Sb_{0.14}$ T2SL structure. By fitting the measured peak energy shift and observing a quenching of the PL intensity we have determined a crossover pressure at which we believe the T2SL electron confined state reaches that of a defect level in the superlattice. This change in nature from a radiative to non-radiative recombination mechanism with pressure is confirmed from power dependent PL measurements. We also examine the thermal activation energies at ambient pressure and close to the crossover pressure which support and are consistent with the determined values for the pressure coefficients of the valence and conduction band edges of the structure and the defect level. As a result, these experiments provide strong evidence that the defect level is approximately 180 meV above the conduction band edge of InAs. Consequently, these findings explain why Ga-free T2SL structures have much longer minority carrier lifetimes, a highly desirable advantage for both mid-wave and long-wave IR photodetector applications.

2.2. Structural properties of InAs/GaSb superlattices determined by high resolution X-ray diffraction (Zuo, UIUC)

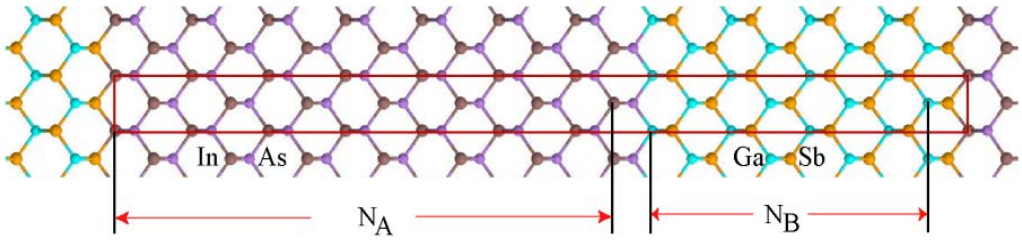

Figure 2.5 The structure model of a perfect (ideal) superlattice of InAs/GaSb with a 14 monolayers (ML) slab of InAs and 8 ML slab of GaSb with two atoms in each ML.

An ideal InAs/GaSb superlattice (SL) consists of alternating layers of strained InAs and GaSb (Figure 2.5). However, real SLs are far from the ideal SL structure and characterization of their structure is important for the study of defects. Here, we used high-resolution X-ray diffraction (HRXRD) to measure the average structure of the MBE grown InAs/GaSb SLs.

The HRXRD measurements were performed on a PANalytical MRD System with a radiation wavelength of 1.5406Å ($CuK_{\alpha 1}$). The instrument is equipped with 2-bounce Ge (220) monochromator integrated with an X-ray mirror and a high speed line detector, PIXcel, with the scatter slit placed in front of the detector. The 2θ-ω high-angle scans are taken with a step size of 0.01 degree and the time per step is 3 seconds.

To improve modelling of the superlattice diffraction peaks from high quality MBE grown samples, we developed the so-called "digital model".[28] The model is built with bilayers consisting of varying thickness of *A* and *B* layers and uniform interfacial distances between the layers. Sharp diffraction peaks with minimal width broadening are the characteristics of high quality superlattices. Thus, in the digital model, variations in

interfacial distance (interlayer continuous disorder) are not considered. For the discrete fluctuation of superlattice period Λ, we follow the Hendricks-Teller[29] approach. We assume different types of bilayers with different number of monolayers in A or B. Each type of bilayer has a finite probability of occurrence, but their stacking sequence is assumed random. For each bilayer, we calculate its structure factor F_i and the structure factor of the superlattice F_{SL} is a sum of the structure factors of all bilayers and their phases. The calculated peak intensities of different stacking configurations are similar, but fluctuate for each configuration. So the calculated spectra from a large number of configurations are averaged to achieve a converging result, which is used for fitting the experimental data.

The parameters used to fit the experimental X-ray diffraction data are strain and composition. Chemical intermixing is modelled as an exponential decay from the interface for three monolayers and their structure factors are modified accordingly.[30] We treat anion and cation separately since previous studies show that they have different levels of intermixing during the MBE growth.[31] Two methods were used to construct the local strain in SLs. One is the composition-correlated strain model (CCSM) and the other is the free strain model (FSM). In the CCSM, the local strain inside the superlattice is directly correlated with the local composition. Two neighbouring atomic layers are considered as an alloy structure and the distance between them is calculated using Vegard's law. In the FSM, however, the strain is not constrained with the composition. To limit the number of parameters, in the FSM, we consider strain deviations of all GaSb monolayers 3 InAs monolayers near each interface. The 8 mono-layers in the middle of the InAs layer are assumed to have zero deviation from their ideal positions. Our study shows that the CCSM is more suitable for extracting composition information and the FSM is better for extracting strain variations.

Five InAs/GaSb T2SLs grown by MBE on GaSb (001) substrate were studied by HRXRD. The samples were kindly provided by Dr. Amy Liu of IQE. The T2SLs were designed with the thickness of InAs and GaSb in a single period at 44Å and 21Å respectively. There are a total of 80 periods for all five samples. A barrier layer of AlSb of 10 nm thick was grown between the GaSb and T2SL. The InAs-on-GaSb interface has been treated in different ways as shown in Table 2.1.

Table 2.1 InAs/GaSb T2SLs measured by HR-XRD. These samples contain different interfacial control as listed below.

Sample No.	Interface control	ε	Modulation wavelength Å	Standard deviation Å
A (2300534)	Neutral	-0.26%	63.29	0.30
B (2300537)	InSb-like (Sb soak)	-0.18%	67.09	0.22
C (2300536)	Forced thin InSb on GaSb	-0.13%	67.18	0.50
D (2300538)	Forced thick InSb on GaSb	~0 (<±0.015%)	66.09	0.45

E (2300540)	Thin InSb-like (Sb soak)	0.04%	65.38	0.28

Table 2.1 lists the measured out of plane lattice strain and the Modulation wavelength for the five InAs/GaSb T2SLs grown by MBE. The out-of-plane average strain is calculated by $\varepsilon = (a_z - a_0)/a_0$, where a_z represents the average out-of-plane lattice constant and a_0 represents the substrate lattice constant. The average out of plane strain is negative at -0.26% for sample A without any interfacial control.

The modulation wavelength is obtained directly from HRXRD data using the satellite peaks observed around the substrate (004) diffraction peak, the peak position of the nth SL satellite reflection is given by

$$q_n = \frac{4\pi n \sin\theta}{\lambda} = \frac{2\pi n}{\Lambda}. \quad (1)$$

Here, Λ is the SL modulation wavelength or SL period. We used a linear fit to the peak position as function of the order of satellite peaks to determine the SL period. Fluctuations in the thickness of the slabs contribute to the standard deviation in the modulation wavelength. They can be analysed using the FWHM of the satellite peaks according to [5].

$$w_n = w_0 + (\ln 2)^{1/2} \cdot \Delta\theta \cdot \frac{\sigma}{\Lambda} \cdot n \qquad (2)$$

where w_n is FWHM of peak of order n, w_0 is the intrinsic FWHM, $\Delta\theta$ is the space between satellite peaks in the 2θ scale, and σ represents the fluctuation in the modulation wavelength.

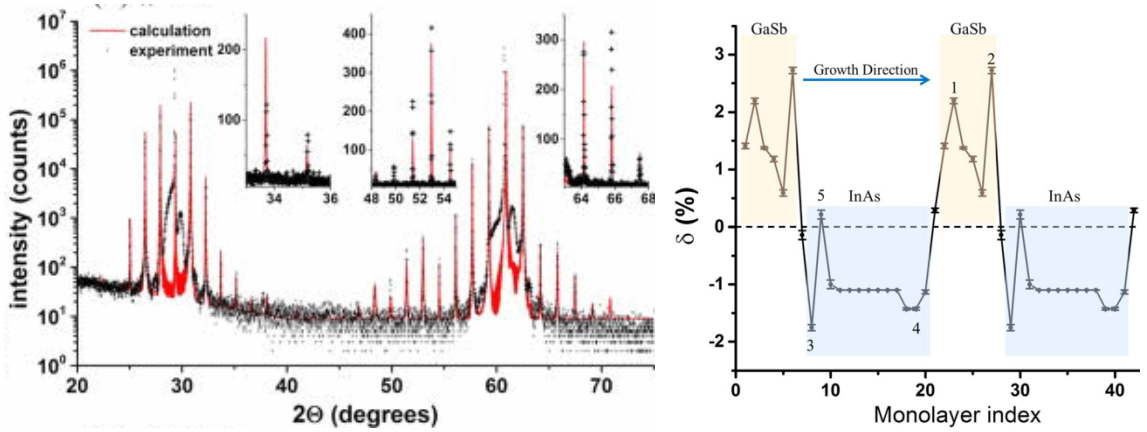

Figure 2.6 Left) Comparison between HRXRD experimental data (black cross) and calculated spectrum (red line) using FSM. Right) FSM strain profile along the out-of-plane direction. Error bars represent the standard deviations of strain sampled from 10 parallel refinements. The growth direction goes from left to right.

Figure 2.6 shows the strain profile acquired form the FSM for the IQE InAs/GaSb superlattice sample 2300534 (see Table 2.1). Two positive peaks in the nominal GaSb layer

(Label 1 and 2 in Figure 2.6, right) indicate InSb type bonding and two negative peaks (Label 3 and 4 in Figure 2.6, right) in the InAs layer indicate GaAs type bonding. These features can result from the Ga-In exchange process at interfaces. They were also identified in latest studies using strain mapping techniques.[32, 33] The abrupt positive peak near the InAs-on-GaSb interface (Label 5 in Figure 2.6, right) is possibly caused by the substitution of Sb for In in the InAs layer. These results show that the GaSb layers experience compressive strain with In incorporation, and there are interfacial strain associated with InSb-like bonds in GaSb and GaAs-like bonds in InAs.

2.3.Interfacial Intermixing and kinetic growth model (Zuo, UIUC)

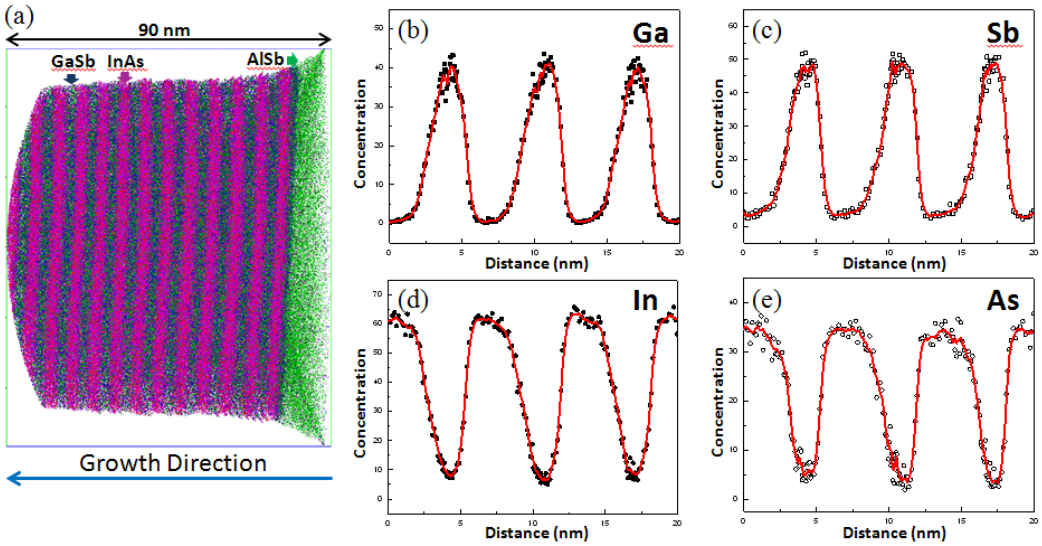

Figure 2.7 (a) 3D reconstruction of GaSb/InAs superlattice near the substrate region. Concentration profiles for (b) Ga, (c) Sb, (d) In, and (e) As across the interfaces, showing asymmetric interfacial sharpness.

Interfacial intermixing is critical to device performance. To address this, we studied interfacial composition using three different techniques: 1) 3D atom probe (3DAP), 2) atomic resolution Z-contrast imaging and 3) X-ray diffraction. We demonstrated all three techniques for the IQE InAs/GaSb superlattice sample D (2300538).

The 3DAP experiment was performed at Northwestern University on a Cameca LEAP 4000X Si at a base temperature of 25K and under ultra-high vacuum ($<8\times10^{-9}$ Pa). The measurement was performed using laser assisted field evaporation under the conditions of 1.4 pJ laser pulse energy, repetition rate of 250 kHz, specimen voltage at 6.5-8.0 kV and evaporation rates of 0.01 ions per pulse. The 3DAP data was reconstructed by using IVAS 3.6.2 software of Cameca. Figure 2.79(a) shows a 3D reconstruction of the atomic distribution in InAs/GaSb SL near the AlSb barrier layer. The GaSb and InAs layers are labelled. They appear to have similar layer thickness in the reconstruction. The InAs layer appears thinner than they should be according to STEM results because InAs has a lower evaporation field than GaSb[34]. From the reconstruction, we created atomic concentration profiles using a small box (20×20×30nm) selected from the center of the 3D cylindrical tip where the spatial resolution of atom-probe appears the best. The profile was density-corrected[35] and the z-direction was rescaled based on the STEM results to compensate the

distortion caused by lower evaporation field of InAs layer[36]. The results for each element are shown in Figure 2.7(b) to (e). The largest concentrations measured are approximately 40, 50, 60 and 35 in percentage for Ga, Sb, In and As respectively. The measured concentration deviates from the ideal concentration of 50/50 at%. Some of the difference can be attributed to the difference in evaporation rates of different atoms. Using the definition for interfacial width as the distance between 10% and 90% relative concentration, the average widths of cations (Ga, In) for InAs-on-GaSb and GaSb-on-InAs interface are 1.99nm (6.5 MLs) and 0.79nm (2.6 MLs), respectively. The average anion widths for Sb and As are 1.65nm (5.4 MLs) and 0.59nm (2.0 MLs) for InAs-on-GaSb and GaSb-on-InAs interface, respectively. Both cation and anion profiles show that the GaSb-on-InAs interface is sharper than the InAs-on-GaSb one.

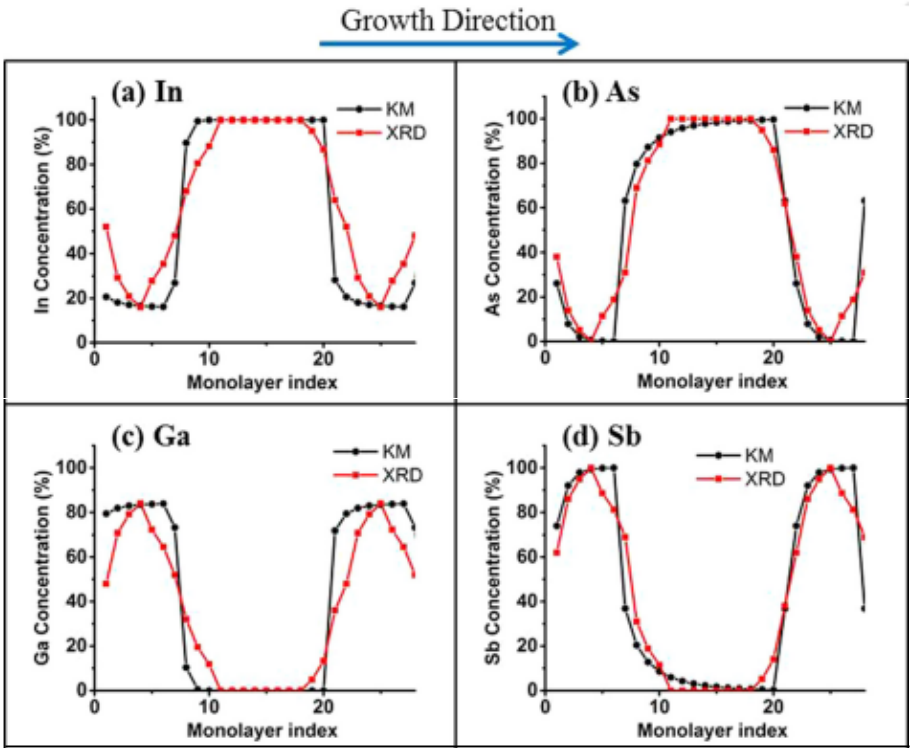

Figure 2.8 Comparison of concentration profiles from XRD simulation (CCSM), APT data, and kinetic model (KM) prediction: (a) In; (b) As; (c) Ga; and (d) Sb. The growth direction goes from left to right.

Figure 2.8 displays the composition profiles as determined by X-ray diffraction using the CCSM model discussed in Section 2.2. Using the same definition of the interfacial width as the distance between the 10% and 90% of the maximum plateau values, we obtained the cation widths for InAs-on-GaSb and GaSb-on-InAs interface as 1.69 nm and 1.27 nm, respectively. The anion widths for InAs-on-GaSb and GaSb-on-InAs interface are 1.60 nm and 1.20 nm.

Further, we simulated the segregation of elements during MBE growth using the kinetic model proposed by Dehaese et al.[37] and data from Ref.[38]. The model simulates layer-by-layer growth by taking into account of the effects of segregation, and diffusion during film

growth. Surface segregation is determined by atomic exchange rate at the surface. The model describes the anion and cation sub-lattice separately using

$$\frac{dx_A{}^s(t)}{dt} = \Phi_A + P_1 x_A{}^b(t) x_B{}^s(t) - P_2 x_A{}^s(t) x_B{}^b(t) \qquad (3)$$

With

$$P_i = \nu_i \exp\left[-E^i_{A/B} / k_B T\right], \qquad (4)$$

where $x_A{}^{s,b}(t)$, $x_B{}^{s,b}(t)$ are time-dependent concentrations of A and B at the surface or bulk, Φ_A is the deposition rate of A atoms. P_1 is the rate of A atoms arriving from subsurface to the surface after exchanging with surface B atoms, and P_2 is the rate of A atoms leaving the surface after exchanging with bulk B atoms. Figure 2.8 presents the composition profiles generated by this kinetic model and the comparison to CCSM results. The anion profiles are in relatively good agreement with each other, especially that the kinetic model successfully recreates the Sb incorporation into InAs near the InAs-on-GaSb interface.

Overall, the GaSb-on-InAs interface is chemically sharper than the InAs-on-GaSb interface, and Sb substitutes a significant amount of As inside InAs layer near the InAs-on-GaSb interface. The anion profiles are in good agreement with the kinetic Monte Carlo model predictions.

2.4. Atomic vacancies in InAs/GaSb superlattices (Zuo, UIUC)

Here, we identify atomic vacancies as the major point defect and the source of large strain fluctuations observed in the InAs/GaSb LSs. The strain analysis is performed on the anion and cation sublattices at a high spatial resolution using the method described by [39]. The InAs/GaSb SLS studied here was grown by molecular beam epitaxy (MBE) (IQE, Bethlehem, PA, Sample A in Table 2.1) at 480 °C on a GaSb substrate with 80 periods on top of a 10 nm AlSb bottom barrier and a 500 nm GaSb buffer layer. Then, a 10 nm AlSb top barrier was deposited on top of SLS, followed by an InAs capping layer. The thicknesses of InAs and GaSb are 4.4 nm and 2.1 nm, respectively. This SLS is an undoped and grown for photoluminescence and absorption studies for the target cut-off wavelength of 11 μm at the temperature of 77 K.

For HAADF imaging, cross-section samples were prepared by mechanical polishing, followed by Ar ion milling using liquid nitrogen to minimize the ion-induced structural damage. Atomic resolution HAADF images for strain mapping were recorded using a probe-corrected FEI Ultimate STEM, operating at 300 kV (MINATEC, Grenoble, France). The HAADF images were recorded at highest spatial resolution and image contrast. Such contrast is obtained when the electron probe is channeled by the atomic column at a distance below the sample entrance surface. The electron beam was scanned parallel to the growth direction, so that the primary direction (out-of-plane direction) for strain measurements is not affected by the so-called scan fly-back error (which induces systematic errors in the measured strain normal to the scan direction)[40, 41]. For analysis, experimental images were carefully selected to avoid any change in contrast due to the electron beam knock-on damage. HAADF image simulation was performed with the Zmult simulation package based on the multislice algorithm with a pixel resolution of 13.25

pm/pixel[42]. This simulation utilizes the absorptive potential method for electron scattering into the HAADF detector. The thickness of the TEM sample, from which the HAADF images were recorded, was estimated to be 20.1 ± 4.2 nm using position averaged convergent beam electron diffraction (PACBED).

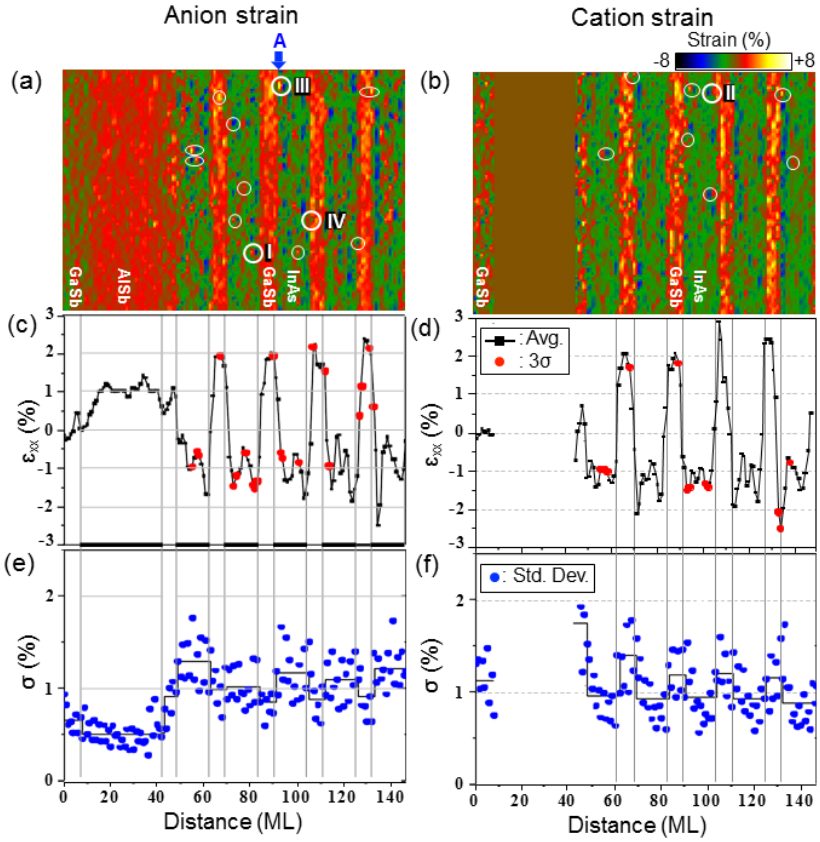

Figure 2.9 Strain maps of (a) anion and (b) cation sublattices. (c) and (d) Strain profiles averaged over 52 unit cells for the anion and cation lattices respectively, showing the compressive strained GaSb and tensile strained InAs. (e) and (f) Standard deviations of the measured strain in each monolayer are drawn in blue solid circles. Lines in (e) and (f) indicate the averaged standard deviation of strain in each layer of the InAs/GaSb SLS. The red circles in (c) and (d) and white circles in (a) and (b) locate where large strain deviations from the mean are observed. The AlSb barrier is not shown in (b) because the intensity of Al (Z=13) columns is too weak to locate its position.

The HAADF images of the InAs/GaSb SL were recorded along the [$\bar{1}$10] zone axis, including GaSb buffer, AlSb barrier and 5 periods of superlattices. In this projection, atomically resolved dumbbell-like features, which consists of a pair of cation and anion atomic columns, are observed for both InAs and GaSb layers. Since the distance between cation and anion atomic columns is close (~1.5 Å), the intensity of atomic columns overlaps, which makes the precise determination of atomic column positions difficult [43]. To overcome this issue, we developed the peak separation method [39]. The method uses Gaussian peak fitting to construct two fitted images of cations and anions, respectively. By subtracting one of the two fitted images from the recorded HAADF image, two sublattice images with the experimental noise intact are obtained, one for anions and another for

cations. From these separated images, atomic column positions can be measured and used to calculate strain using the template matching method [41]. For the GaSb buffer layer, which was used as a measurement reference, we measured the standard deviations, σ_{anion} =7 × 10^{-3} and σ_{cation} =1 × 10^{-2} for the anion and cation lattices respectively, corresponding to a change in distance at 2 and 3 pm of the atomic column, representing the measurement precision. The difference in the σ values here arises from the different signal-to-noise ratios in the anion and cation sublattice images.

Figure 2.9(a) and (b) shows the ε_{xx} (out-of-plane direction) maps for the anion and cation sublattices over an area of 46 x 24 nm^2, The measured strain is defined by $\varepsilon_{xx} = \varepsilon^{\perp} = (a_f^{\perp} - a_{GaSb}^{bulk})/a_{GaSb}^{bulk}$, which can be related to the material strain $\varepsilon_m = (a_f^{\perp} - a_f^{bulk})/a_f^{bulk}$ ($a_f^{\perp}$ is the local lattice parameter of the film, a_{GaSb}^{bulk} and a_f^{bulk} are the bulk lattice constants of GaSb and the film, see the Supporting Information). The HAADF image of the GaSb buffer layer, which was recorded simultaneously with the film, was used as the reference lattice to calibrate the measured strain. The major features of two strain maps are similar; both strain maps show that the ε_{xx} inside the nominal GaSb layers in the SLS is positive with the maximum strain reaching >2 %, which are attributed to In incorporation into the GaSb layer [28]. The averaged strain in the nominal InAs is -1.06 %. At interfaces, the strain ranges from -1.5 to -2.5 %. This is more negative than the stoichiometric InAs (-1.29 %) but less negative than the stoichiometric GaAs (-13.99 %), showing intermixing present at the interface, which is in agreement with the reported composition characterization[44].

To detect point defects, we examined strain variations inside each monolayer of the T2SL. The strain distribution in each monolayer follows approximately the Gaussian distribution with the width σ, which are plotted in Figure 2.9(e) and (f). Next, we searched for strain values lying beyond 3σ from the mean. The locations of large strain deviations are determined and marked by white circles in Figure 2.9(a) and (b). Within the 46 x 24 nm^2 area of the T2SL examined, 12 are identified on the anion lattice and 8 on the cation lattice. Among these, 3 in the anion and cation lattices are located close to each other and can be attributed to the same defect. The majority (> 80 %) is located near the local maxima or minima in the strain profile, marked as red dots in Figure 2.9(c) and (d). We selected four locations for further examination. They are marked as I, II, III, and IV in Figure 2.9(a) and (b). Here, the emphasis is placed on region I located inside the nominal InAs layer.

Figure 2.10(a) shows the atomic resolution image and the atomic model drawn using the measured atomic column positions from region I in Figure 2.9(a). Among the three dumbbells labeled as A, B, and C, the anion atomic column in dumbbell B (marked by a yellow arrow) is located where large strain deviation (>3σ) is measured. The As atomic column is displaced toward the In atomic column, giving rise to a short As-In distance of 1.35 Å in the dumbbell B, which is about 15 pm shorter than As-In distances of neighbouring dumbbells, A and C [Figure 2.10(b)], while both anion and cation atomic column intensities of dumbbell B are comparable to those of dumbbells A and C. Locations II and III were also found inside the nominal InAs layer, as is location I. Similar to location I, we observed local bond length changes close to 15 pm at those two locations. Locations with large displacements were also observed inside the nominal GaSb layer. Location IV

is an example where the Sb atomic column is displaced toward the neighboring Ga atomic column, resulting in distinctly shorter bond length compared to neighboring dumbbells.

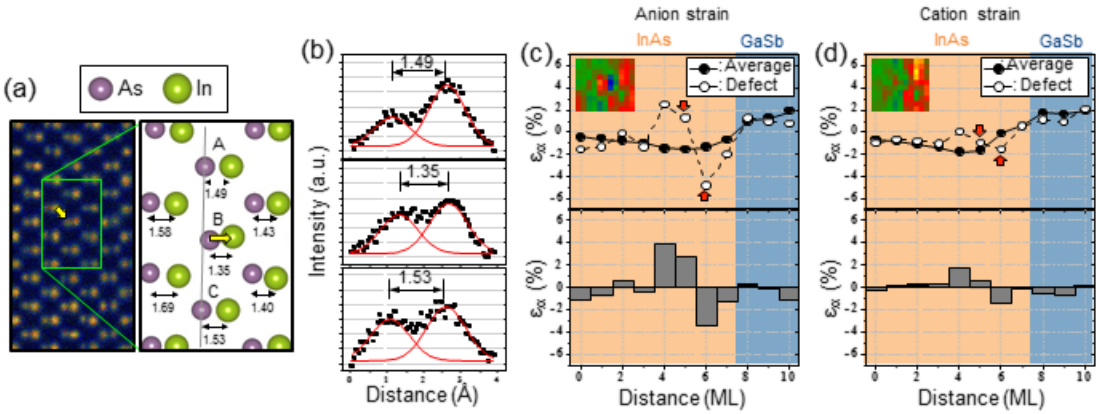

Figure 2.10 Defect atomic structure and strain distribution. (a) Magnified HAADF image and atomic model from location I in Fig.2. A single atomic column, marked by the yellow arrow, shows a large displacement with respect to the averaged position of the monolayer indicated by the dotted line. The atomic distances of dumbbells labeled in the model are gradually changed along the growth direction due to the chemical intermixing near the interface. (b) Gaussian peak fitting of three dumbbells (A, B and C) showing the measured atomic distances. (c) and (d) Strain profiles from the anion and cation lattices across dumbbell B compared to the average strain profile. The difference between the two shows characteristic positive and negative strain differences associated with the defect.

On average, the observed displacements beyond 3σ give rise to 3 % deviations from the mean strain value in each monolayer, thus represent a change of >10 pm in the projected bond distances. The size of defects extends to 1 nm. Thus, both the amount of strain and size are much smaller than what is expected from large defects, such as a misfit dislocation. The defects observed here likely involve a few atoms along the atomic column since the depth of focus (DoF) for our observation is about 6 nm (DoF $\approx 1.772\lambda/\alpha^2$, where λ =1.97 pm at 300 keV and α =23.5 mrad is the semi-convergence angle of the electron probe) [45, 46].

Local defects with small changes in bond distances have been predicted for point defects in compound semiconductors [47]. Thus, to identify the defects, we modeled point defects in InAs, where several defects are detected, using density functional theory (DFT). The following types of point defects are considered: As vacancy (V_{As}); In vacancy (V_{In}); As antisite defect located on a In site (As_{In}); In antisite defect on a As site (In_{As}); Ga substitutional atom on a In site (Ga_{In}). DFT calculations show that vacancy-type point defects induce a large displacement of their nearest neighboring atoms by 48 and 50 pm for V_{As} and V_{In}, respectively. In addition, the nearest neighboring atoms move toward the vacancy position for both V_{As} and V_{In}. In case of antisite defects, the nearest neighboring atoms around As_{In} and In_{As} are displaced by 3 and 12 pm, while a Ga substitutional atom displaces the nearest neighboring atoms by 13 pm. The observed change in dumbbell distance from above analysis is >10 pm. To induce such displacements by either antisite defects or compositional changes, most of atoms in a relevant atomic column would have to be replaced by those defects, which are energetically unfavorable. In addition, those

extended defects, i.e. a cluster of antisite defects or substitutional atoms, should be evidenced by image contrast changes, which is not observable in our experiment. Therefore, vacancy-type defects are most likely sources responsible for both large changes in dumbbell distance and inward displacements of neighboring atoms.

To further investigate the image characteristic of atomic scale defects, we performed HAADF image simulations using the constructed models with different number of displaced atoms in an atomic column. The results show that an As atom displaced by 30 pm along the [001] directionin a column leads to a 0.66 pm shift of the atomic column position in the simulated HAADF image. As the number of displaced As atoms increases, the measured atomic column displacement in the simulated HAADF image also increases, eventually exceeding 10 pm with four displaced As atoms. Overall, the image simulation study supports that the observed displacement (>10 pm) of atomic column could result from a number of vacancy-type point defects within the depth of focus.

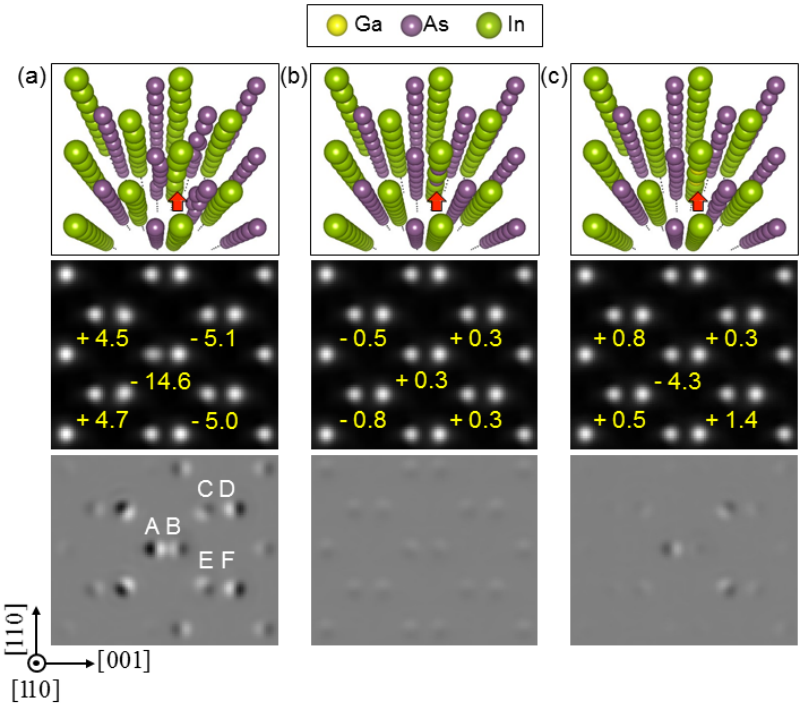

Figure 2.11 Image simulation for different type of point defects. Top row shows the structure models for (a) vacancy, (b) anti-site, and (c) substitutional defects as marked by red arrows. Middle displays the simulated Z-contrast images where the atomic distances are compared to the original structure without defects. The bottom row shows the difference images between the ones with and without defects. The numbers in the middle row indicate the change in bond lengths due to point defects.

Figure 2.11 shows the simulated HAADF images using the relaxed structure obtained from DFT calculations for following models: (a) two In vacancies; (b) two As_{In} anti-site defects; (c) two Ga_{In} substitution, which are all located in the In column. The two In vacancies are separated by an In atom. Four As atoms in the neighboring column of A are displayed along [001], while two As atoms each in columns of C and E are displaced toward the In column of B. The HAADF simulation results show that the displacement of

four As atoms in column A leads to a 9.9 pm displacement in the simulated HAADF image for a sample of 20 nm thick, which is estimated by PACBED, while the In column (B) is displaced by 4.7 pm. Thus, the atomic dumbbell distance in the image is shorten by 14.6 pm in a good agreement with the experiment. Other atomic columns show much smaller displacements in the simulated image as indicated in Figure 2.11. The atomic model in Figure 2.11(b) represents the structure with two As_{In} anti-site defects in which the measured atomic column position changes very little, less than 1 pm. In case of two Ga_{In} substitutional atoms in Figure 2.11(c), the measured distance of the dumbbell with Ga_{In} atoms changes by 4.3 pm. All in all, the match between the DFT models and image simulation results suggests that the origin of short bond lengths is vacancy-type defects, and we can also rule out anti-site defects.

Lastly, we examined local strain variations near defect locations. Figure 2.10(c) and (d) plot the strain profiles of the anion and cation lattices across the defect at location I (open dots), before (top) and after (bottom) subtracting the average strain (solid dots, averaged over 52 unit cells along the in-plane direction). Both profiles show characteristic negative and positive differences in strain that appear as a pair as seen in the strain map [See the cutout strain map in Figure 2.10 (c)]. The extent of strain modification is over 3~4 monolayers (1 nm). Compared to the simulation results obtained from the DFT models, the amount of deviation from the averaged strain measured in the cation lattice [Figure 2.10 (d)] is smaller than that in the anion lattice [Figure 2.10 (c)], while the two vacancies model predicts similar strain for both cations and anions. The cation strain cannot be attributed to Ga substitution alone since the theory predicts almost no change in this case. Experimentally, at the location of the defect, there is 10 % of Ga substitutions in the In atomic column [28], which amounts to 2 Ga atoms within the DoF. Thus, our results can be explained by the presence of 1~2 vacancies in the Ga substituted In atomic column.

Among the observed locations (20 in total) having large atomic displacements, three occurs in the Ga-rich columns inside the nominal GaSb layer. Among those, location IV shows similar strain characteristic as that of location I, which can be attributed to Ga vacancy. Cation vacancies introduce deep defect levels in InAs or GaSb as they create T_2-derived discrete energy levels just below the valence band of bulk crystals, which act as electron acceptors [48]. However, in an InAs/GaSb superlattice, the valence band edge of the effective bandgap is lower in energy than the valence band edge of the bulk GaSb due to the quantum confinement effects. Defect levels created by Ga vacancies are thus in the proximity of the effective bandgap, while In vacancies only create acceptor levels. We emphasize that our results here infer that Ga plays an important role in defects in the InAs/GaSb superlattice depending on whether it is vacancy formed in the Ga substituted In atomic columns or the Ga vacancy formed in the nominal Ga atomic columns.

2.5. Evaluation of Sb segregation in the MBE grown InAs/InAsSb superlattices (Smith, ASU)

Compositional profiles across the interfaces of InAs/$InAs_{1-x}Sb_x$ T2SL caused by Sb segregation would likely induce undesirable effects on band-gap engineering, such as blue-shift or broadening of the optical response, as well as weakened absorption. Our previous reciprocal-space image analysis used the geometric phase method to reveal asymmetric interfacial misfit strain profiles at the InAs-on-InAsSb interface. Moreover, measurement

of local Sb concentrations across the superlattices using electron energy-loss spectroscopy (EELS) and (002) dark-field imaging confirmed asymmetric Sb distribution, with the InAs-on-InAsSb interface being chemically graded. Thus, our recent attention has been primarily directed towards obtaining a more quantitative evaluation of the interface chemical diffusion, including interface width and segregation probability. More detailed information can be found elsewhere.[49]

The major challenge for EELS investigations of the InAs/$InAs_{1-x}Sb_x$ T2SL samples lies in the fact that the core-loss edges of interest, namely Sb and In $M_{4,5}$ edges (edge onsets at 528 eV and 443 eV, respectively), are two closely-positioned delayed edges with significant overlap. As a result, regular EELS quantification routines using background subtraction and peak integrals would likely fail due to unreliable extraction of individual signals. In this study, multiple-linear-least-squares (MLLS) fitting was implemented to achieve reliable separation of the Sb $M_{4,5}$ edge from the In $M_{4,5}$ edge. The Sb and In reference spectra were taken from the AlSb barrier layer and from the InAs capping layer, respectively. Thus, the reference and target spectra were acquired from the same TEM specimen with identical acquisition parameters under similar chemical environment (same valence state). Zero-loss spectra were also recorded to calculate the relative sample thickness (in unit of λ, the mean free path for inelastic scattering) in order to select suitably thin regions of the TEM specimens, so that both two-dimensional spectrum images and reference spectra could be acquired from relatively thin regions with similar thicknesses, eliminating the need for deconvolution of plural scattering.

A representative STEM-EELS analysis is summarized in Figure 2.12. The EELS spectrum image was recorded from the region indicated by the solid blue rectangle in Figure 2.12 (a), and a closely adjacent region, indicated by the dashed yellow square, was used for drift correction. The core-loss spectrum image was acquired with both In and Sb $M_{4,5}$ edges included to enable MLLS fitting. The relative thickness map shown in Figure 2.12 (d) indicates that the thickness in this region was relatively uniform and considerably less than one inelastic mean free path (average thickness of 0.7 λ), implying that plural scattering was negligible. This was also true for the reference spectra (not shown here). Under this single inelastic-scattering condition, the ratio of MLLS fitting coefficients for the corresponding Sb/In 2D map in Figure 2.12 (b) and the extracted averaged line profile in Figure 2.12 (c) (averaged over two pixels) give the projected areal density of Sb compared with In in the scanned region. Thus, since the In composition is presumed to be constant and 100 % throughout growth of the InAs/$InAs_{1-x}Sb_x$ SL stack, the Sb composition can be extracted directly from the ratio of MLLS fitting coefficients of Sb versus In. Note that the Sb composition is the average for the examined region projected along the electron beam direction.

Closer examination of Figure 2.12(c), which is the averaged projected line profile of Sb composition, confirmed the asymmetric interfaces in the superlattices, as previously indicated by the geometrical phase analysis (GPA)[50]. The InAsSb-on-InAs interface was relatively sharp, while the graded InAs-on-InAsSb interface demonstrated a typical segregational feature of an exponential-like tail with Sb atoms migrating from the InAsSb layer into the following InAs layer. The maximum Sb composition in the InAsSb layers here is about 35 %.

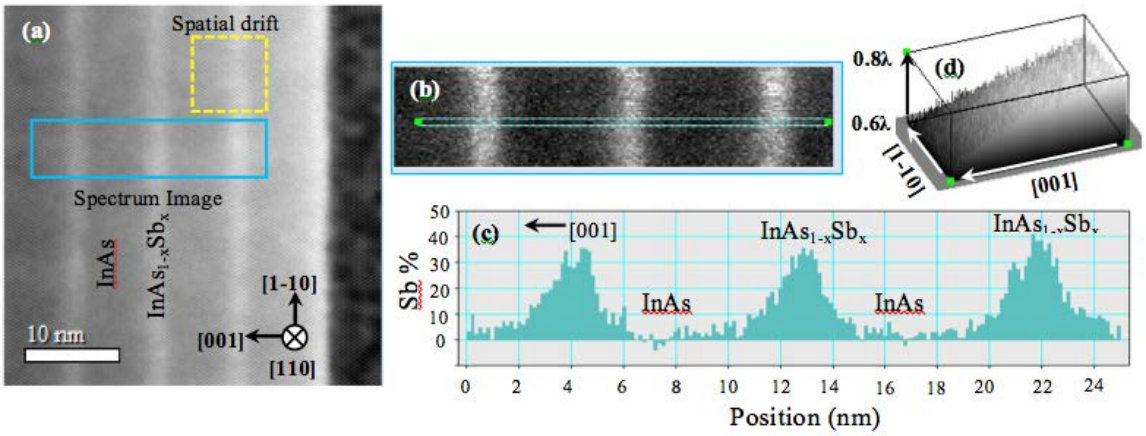

Figure 2.12 (a) Survey image for spectrum image acquisition, defining region of interest with solid blue rectangle, and area for spatial drift correction with dashed yellow square; (b) ratio map of MLLS fitting coefficients of Sb versus In; (c) Sb composition profile extracted from dashed blue rectangle in (b) averaged over two pixels; (d) relative thickness map of region of interest calculated from zero-loss spectrum image.

A typical {002} dark-field (DF) image of the superlattices is shown in Figure 2.13(a), while Figure 2.13(b) shows the averaged Sb composition profile extracted from the region marked by the white dashed rectangle (averaged over 30 pixels, which corresponds to about 4 nm). The averaged intensity line profile was initially calibrated using a characteristic dark-line feature (minimum-intensity line) at the AlSb/InAsSb interface. Quantitative chemical determination was then carried out by analyzing the (002) diffracted intensity assuming the kinematical scattering approximation (with atomic-scattering factors adapted from Doyle and Turner[51]). The influence of electron redistribution due to the bonding of atoms, local structural distortions and thin-foil surface relaxation is not considered here. Note that the layer contrast in the {002} DF images is not the same as for the HAADF images used in GPA analysis, i.e., the InAsSb layers appear darker than the InAs layers because of different contrast mechanisms for the two techniques. The maximum Sb content of about 35 % estimated by {002} DF analysis is in remarkable agreement with the value obtained from EELS. Furthermore, the presence of asymmetric Sb profiles on either side of the InAsSb layers is confirmed; in agreement with the information revealed previously by GPA and EELS analysis. The {002} DF imaging results corroborate that the InAsSb-on-InAs interface is relatively sharp while the InAs-on-InAsSb interface is graded and resembles a typical segregation profile with a decreasing exponential-like tail penetrating into the next InAs layer.

The main challenge associated with implementation of {002} DF imaging is to tilt the specimen with the 002 beam at or close to the Bragg diffraction condition while imaging the interface closely edge-on. We estimate a small tilting offset of the interface from the exact edge-on condition, which would broaden the projected interface by 0.5 ~ 1 monolayer (ML) for a specimen thickness of 50 ~ 100 nm. Such broadening is negligible provided that careful choices of specimen/beam tilting and specimen thickness are made, and is much smaller than the interface width measured here and for other MBE-grown III-V heterostructures (typical interface width (10% ~ 90% criterion) ranges between 4.4 and 7.5 ML). In addition, although this imaging method is aperture-limited, it was already shown

that detailed analysis of the composition profiles, supported by structural modeling, allows information retrieval beyond the experimental spatial resolution: i.e., it is possible to extract quantitative fine-scale information such as interface widths and layer thicknesses, and to detect subtle variations as small as 0.1 ML.

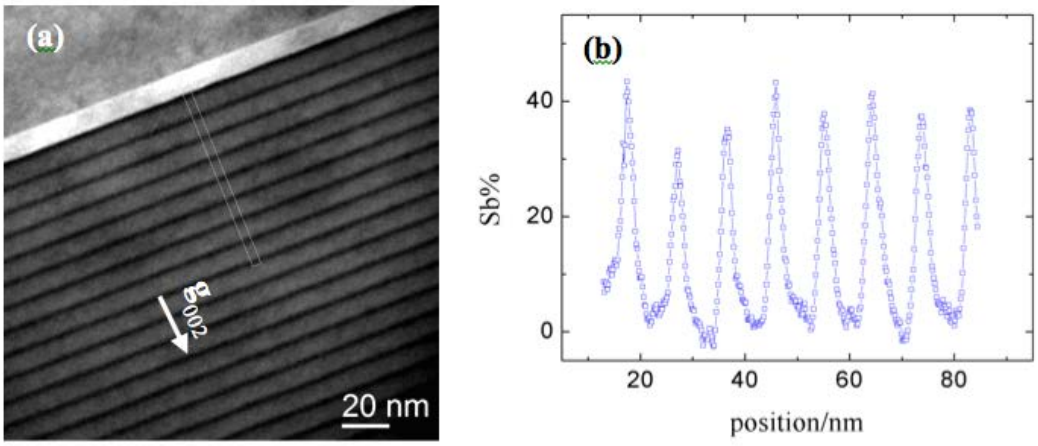

Figure 2.13 (a) Representative chemically-sensitive (002) DF image, with white dashed rectangle defining region of interest; (b) Experimental Sb composition profile obtained through analysis of diffracted intensity.

The graded/broadened InAs-on-InAsSb interface demonstrated an exponential-like descending tail characteristic of surface segregation. Thus, the Sb composition profiles across this interface obtained from {002} DF and EELS measurements were evaluated using Muraki's phenomenological segregation model, which initially assumes a step-like interface.[52]

The segregation probability R defines the fraction of Sb atoms in the topmost layer that segregate into the next layer, N is the thickness of the InAsSb layer, and x_0 is the Sb composition within the InAsSb layer. The analysis was performed by evaluating the profile fitting in the vicinity of the InAs-on-InAsSb interface by adjusting the parameters R, N and x_0. It was found that regardless of the technique used to obtain the Sb composition profiles or their particular location within the 58-period stack, the decay at the graded InAs-on-InAsSb interface was well reproduced by the segregation model with the same parameters. Figure 2.14(a) and (c) list representative experimental Sb composition profiles and corresponding segregation fitting curves for the {002} DF imaging and STEM EELS study. The segregation probability R obtained from multiple fittings of data with both techniques agree well within experimental error and yield 0.81 ± 0.01, which represents strong segregation when compared to values reported in the literature. In particular, R = 0.81 indicates that 81 % of the Sb atoms in the topmost layer on average have segregated into the next monolayer during growth. The interface width due to segregation broadening, defined as the length over which the Sb composition changes from 90 % to 10 % of the plateau value, can also be obtained. The interface width was found to be about 10 ML, which corresponds to a broadened width of about 3 nm (using a lattice constant of 0.62 nm for $InAs_{0.66}Sb_{0.34}$ following Vegard's law). This unexpectedly strong segregation significantly altered the composition profile and the consequent strain evolution across the

InAs-on-InAsSb interface and beyond, from the ideal, step-like interface usually assumed during T2SL structure design to one that is a rather broadened.

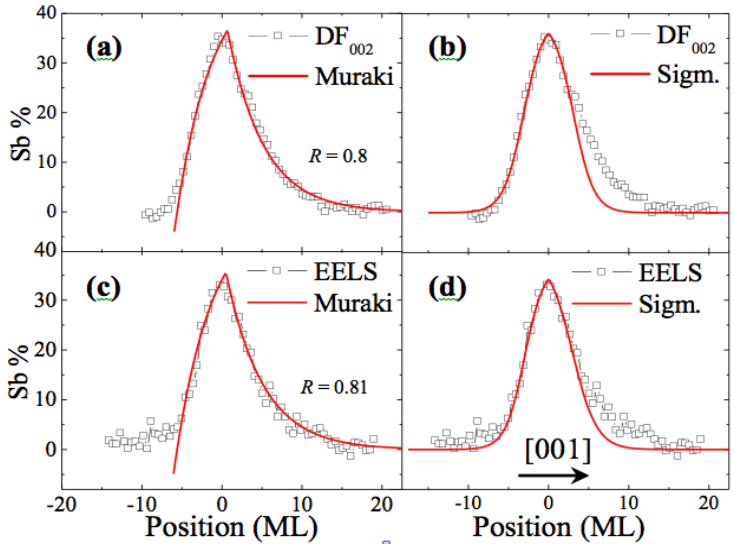

Figure 2.14 Experimental Sb composition profiles and corresponding segregation and sigmoidal fitting curves obtained from: (a) & (b) (002) DF imaging; and (c) & (d) STEM EELS.

The InAsSb-on-InAs interface, although relatively abrupt, also deviated from the ideal, step-like shape assumed in the segregation model, as evident from the slight discrepancy between the Sb composition profiles and the segregation fitting at this interface. This is unlikely to be due to Sb segregation; rather, this non-ideal interface is due to an intrinsic minimum interface width that is dictated by the molecules-surface interaction potential during growth, and can be approximated with a set of sigmoidal functions. This sigmoidal-type interface exists naturally at both interfaces in this T2SL system. However, the segregation effect across the InAs-on-InAsSb interface is so strong that it dominates over the intrinsic sigmoidal profile (Figure 2.14 (b) and (d)), and the Sb composition evolution can be reasonably reproduced using only the segregation model (Figure 2.14 (a) and (c)). Hence, the Sb composition profile across a three-layer structure of InAs/InAsSb/InAs was better described using a piecewise function, using the sigmoidal model for the InAsSb-on-InAs interface, and Muraki's segregation model for the InAs-on-InAsSb interface. The connecting point of the two models is marked with an arrow, as indicated in Figure 2.15 for profiles obtained from {002} DF imaging and EELS analysis. Experimental Sb composition profiles obtained from these two independent microscopy techniques were very well reproduced using the combined models with the same fitting parameters. In addition to the segregation probability of 81 %, an intrinsic interface width of 1.2 ML was obtained for the InAsSb-on-InAs interfaces, which is relatively small compared to the broad InAs-on-InAsSb interface, confirming segregation as the dominant mechanism.

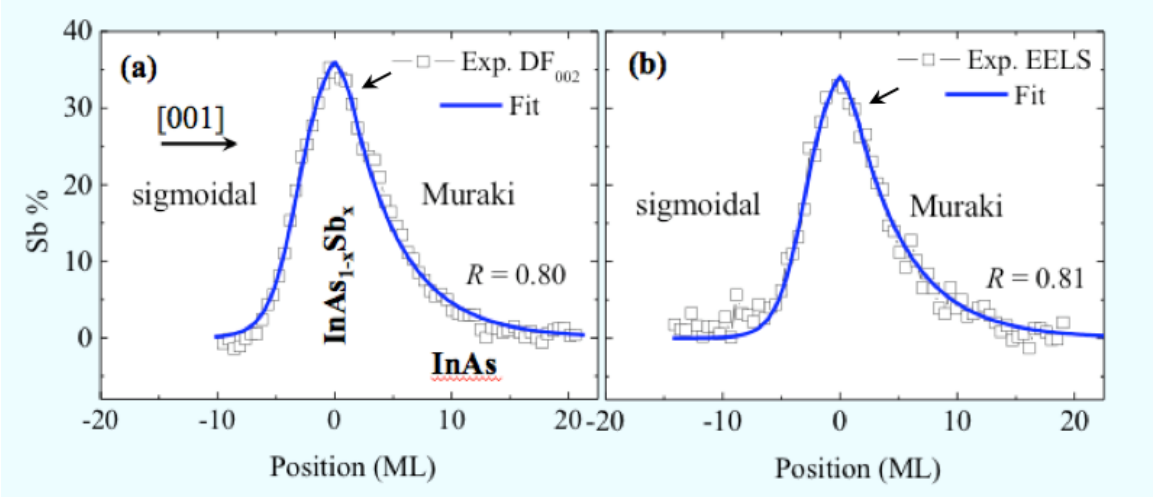

Figure 2.15 Experimental Sb composition profiles and corresponding fitting curves using combination of sigmoidal function for InAsSb-on-InAs interface and Muraki's segregation model for InAs-on-InAsSb interface, as obtained from: (a) {002} DF imaging; and (b) STEM EELS. Arrows indicate connection points of the fitting curves.

Thus, quantitative evaluation of the Sb composition profiles that has been obtained from these two independent microscopy techniques, with the aid of segregation and sigmoidal models, demonstrates remarkable agreement: both yield Sb segregation probability of 81% and a segregation broadening length of about 3 nm. This Sb segregation will result in: a) interfaces that are graded rather than abrupt, as assumed during structure design; b) lower maximum Sb incorporation in the InAsSb layers, which would induce blue shift of the optical response; c) effectively thicker InAsSb layers due to segregated Sb, which would reduce the overlap of electron and hole wavefunctions and thus lead to weakened absorption; d) smaller maximum compressive strain in the InAsSb layers and reduced tensile strain in the first half of each InAs layer, which would mean reduced effect of strain on band-gap engineering. All of these effects must be taken into account during structure design to avoid any undesirable or even detrimental impact on device performance.

2.6. Sb-induced strain fluctuations in a MBE grown strained layer superlattice of InAs/InAsSb (Zuo, UIUC)

We demonstrated that Sb substitution for As in an MBE grown InAs/InAsSb strained layer superlattice (SLS) is accompanied by significant strain fluctuations. The Ga-free SL was observed using STEM along the [100] zone axis, where the cation and anion atomic columns are separately resolved. Strain analysis based on atomic column positions revealed asymmetrical strain profile across the InAs and InAsSb interfaces. The averaged strain profile is quantitatively fitted to the Sb segregation model, which yielded a distribution of Sb in agreement with the scanning tunnelling microscopy (STM) result. The subtraction of the calculated strain reveals an increase in strain fluctuations with the Sb concentration, as well as isolated regions with large strain deviations extending over ~ 1 nm, which suggest the presence of point defects.

In the InAs/InAsSb SL, the strain is directly related to the Sb composition. During MBE growth, the Sb distribution is determined by surface segregation and exchange reaction between anions at high growth temperatures.[38] In case of the InAs/InAsSb SLs, it has been shown that a small variation in Sb content significantly affects the photoluminescence (PL) transition energies that are related to the cut-off wavelength of the device.[53] Thus, the determination of strain and composition is essential for understanding their electronic properties.

The InAs/InAsSb T2SL studied here was grown on a GaSb substrate by solid-source molecular beam epitaxy (MBE) at Sandia National Laboratories. The constituent layers were deposited on a (001)–oriented GaSb substrate under an anion overpressure of ~1.5:1 and growth rate of 0.9 monolayers/s (ML/s). The substrate was held at approximately 420 °C and rotated continuously throughout deposition. The T2SL consists of 100 periods of 4.6 nm thick InAs and 1.7 nm thick $InAs_{1-x}Sb_x$ with the targeted composition of x = 33.3 %. A separate layer of GaSb (buffer layer) was grown between the T2SL and the GaSb substrate. The same sample was previously measured by STM on a monolayer-by-monolayer basis following wafer cleavage in ultra-high vacuum (UHV).[54]

The cross-sectional TEM sample used for HAADF imaging was prepared by mechanical wedge polishing, which was followed by ion milling using 3.0 kV and 1.0 kV Ar ions at the glancing angle of 6º. During ion milling, the sample was kept at the liquid nitrogen temperature to minimize the ion-induced surface damage.[55] Atomic resolution HAADF imaging was performed using a Nion UltraSTEM (Kirkland, WA), which is equipped with a cold field emission gun and a probe aberration corrector. The microscope was operated at the accelerating voltage of 100 kV to minimize structural damage caused by the high-energy electron knock-on effect (under the imaging conditions used in this work, no visible structural damage was observed). The convergence semi-angle for the incident electron probe and a HAADF detector range were set to be 31 mrad and 86-200 mrad, respectively. The depth of focus (DoF $\approx 1.772\lambda/\alpha^2$)[46] for our STEM observation is about 6.8 nm. During HAADF imaging, the electron probe was scanned parallel to the film growth direction, thus the out-of-plane direction for strain measurement is not affected by the so-called “fly-back” error, which involves a systematic error along the perpendicular direction to the scan direction.[40, 42, 56] Using the recorded HAADF images, strain was measured by TeMA at atomic resolution.[56] High-resolution XRD (HRXRD) spectra were acquired using a PANalytical Materials Research Diffractometer system with a radiation wavelength of 1.5406 Å (Cu $K_{\alpha 1}$). The averaged out-of-lattice constant (d) and the modulation period (Λ) were measured at 6.0966 Å and 6.28 nm, respectively, which are close to the original design of d = 6.0959 Å and Λ = 6.30 nm. Details of the fitting procedure are presented elsewhere.[28]

For HAADF imaging, TEM samples were prepared along the crystallographic direction of [100]. Figure 2 (a) and (b) show a schematic and the HAADF image of GaSb viewed along the [100] zone axis, respectively. Most (S)TEM observations of III-V semiconductors have been performed along the <110> zone axes, which gives the well separated dumbbells made of two atomic columns.[57] When observed along [100], on the other hand, the projected unit cell consists of one atomic column (Ga or In) at the center and another atomic column (Sb or As) at the corner; those atomic columns are equally spaced from each other.

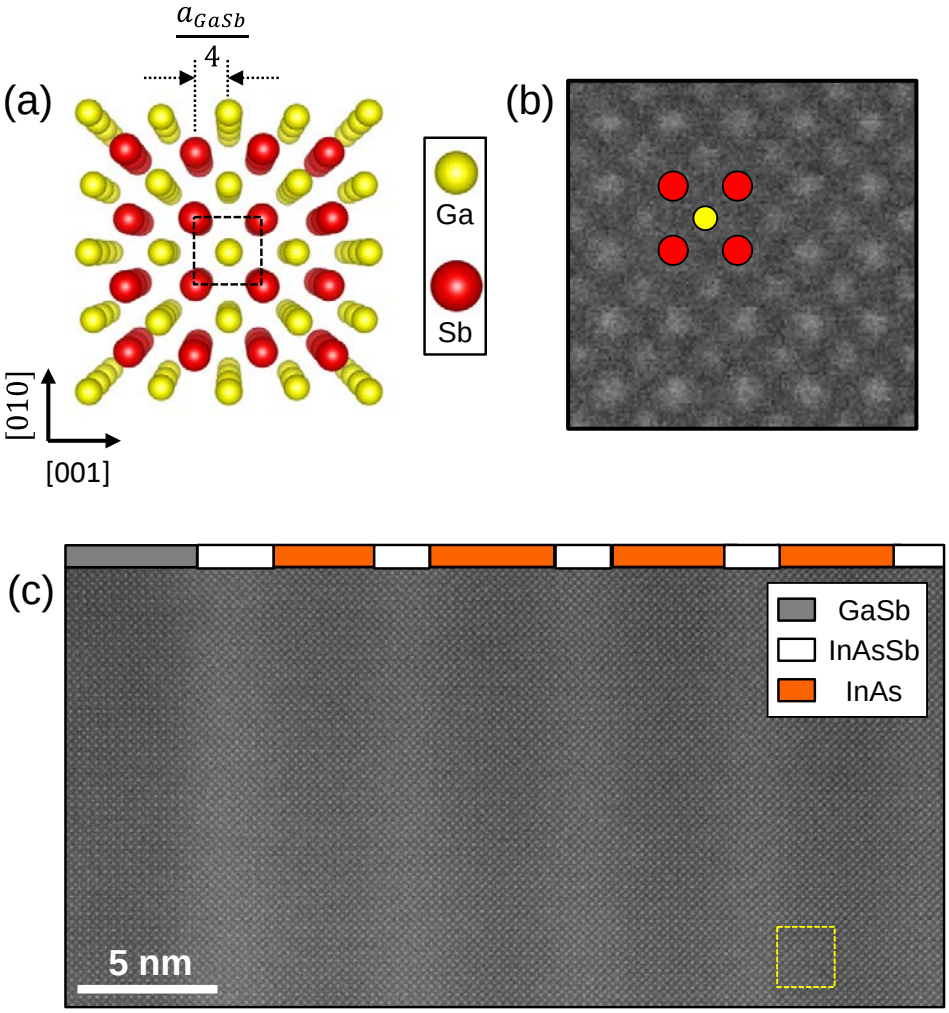

Figure 2.16 (a) Schematic and (b) HAADF image of GaSb along the [100] zone axis. The yellow and red circles in (b) represent Ga and Sb atomic columns respectively. (c) Atomic resolution HAADF image of an MBE-grown InAs/InAsSb T2SL imaged along the [100] zone axis. The growth direction is from left to right.

Figure 2.16 (c) displays an atomic resolution HAADF image of the InAs/InAsSb T2SL from a sample region near the GaSb buffer layer. The image shows the excellent crystallinity of the T2SL with no visible structural defects. Since the atomic number of Sb (Z=51) is larger than that of As (Z=33), the InAsSb layers appear brighter than the InAs layers, resulting in alternating bright and dark contrast. Each atomic column provides a sampling point for strain mapping. The unit distance for strain calculation is *a/4* as denoted in Figure 2.16(a).

Figure 2.17(a) shows the strain map along the growth direction (out-of-plane) obtained from the HAADF image by using a template image containing a single atomic column and TeMA.[56] The strain value measured here is based on the out-of-plane lattice constant difference between the GaSb buffer layer and the film ($\varepsilon^{\perp} = (a_f^{\perp} - a_{GaSb}) / a_{GaSb}$ with $a_f^{\perp}$ the local film out-of-plane lattice constant). This is different from the mismatch strain ($\varepsilon_m = (a_f - a_{GaSb}) / a_{GaSb}$ with a_f the lattice constant of the film material) arising from the

lattice constant difference in bulk materials, which is typically used in the field of material mechanics.[58] The GaSb buffer layer, where the lattice mismatch with the GaSb substrate is minimal, is used to measure a_{GaSb}.

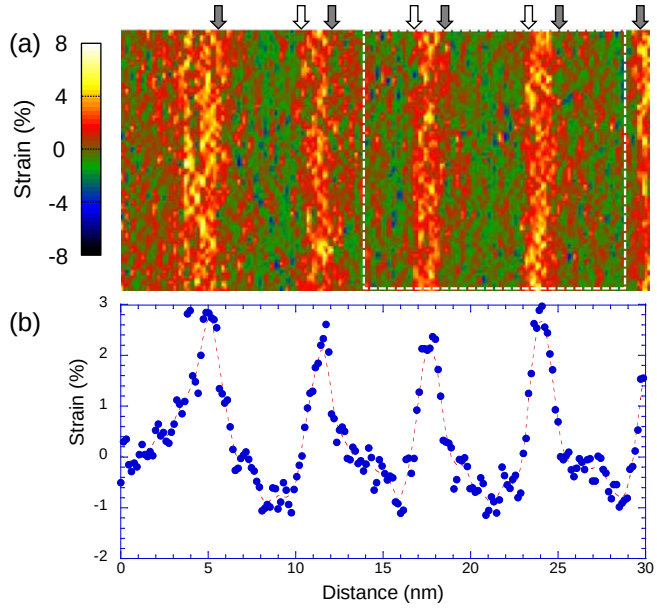

Figure 2.17 (a) Strain map and (b) line profile along the growth direction obtained using the HAADF image in Fig. 2 (c). The white and gray arrows on top of strain map indicate InAsSb-on-InAs and InAs-on-InAsSb interfaces, respectively.

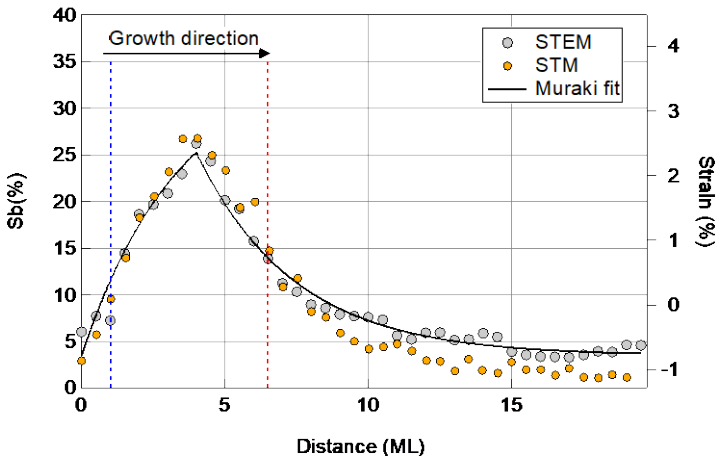

Figure 2.18 Average Sb composition profiles obtained using STEM (gray color) and STM (orange color). Muraki's segregation model is fitted to the STEM result. The blue and red dashed lines indicate the InAsSb-on-InAs and InAs-InAsSb interfaces, respectively.

The InAs and InAsSb layers in the T2SL are clearly distinguished in the strain map due to their lattice constant difference. The nominal composition of Sb in InAsSb is 33.3 % and 0 % in InAs, which leads to a_{InAsSb} =6.199 Å and a_{InAs} =6.0583, respectively, according to the Vegard's law, while the lattice constant of stoichiometric GaSb is 6.0959 Å.[59] In the T2SL, the InAs layer is under tensile in-plane strain and thus the out-of-plane strain has a negative value, while the InAsSb layer is under compressive in-plane strain and the out-of-plane strain has a positive value in the strain map. Using the Poisson's ratios of 0.35 and 0.31 for InAs and GaSb, respectively[59], the epitaxially grown InAs on GaSb should have an $\varepsilon^{\perp}$ of -1.28% and ε_m of -0.62%. Similarly, the $\varepsilon^{\perp}$ of $InAs_{0.67}Sb_{0.33}$ on GaSb is calculated at 3.52%. Figure 2.17(b) plots the measured $\varepsilon^{\perp}$ in the InAs/InAsSb T2SL along the growth direction. The positive and negative strain modulation is clearly seen in the

profile across the four periods of alternating InAs and InAsSb layers. The measured $\varepsilon^{\perp}$ ranges from -1% in the nominal InAs to +3% in the nominal InAsSb layer.

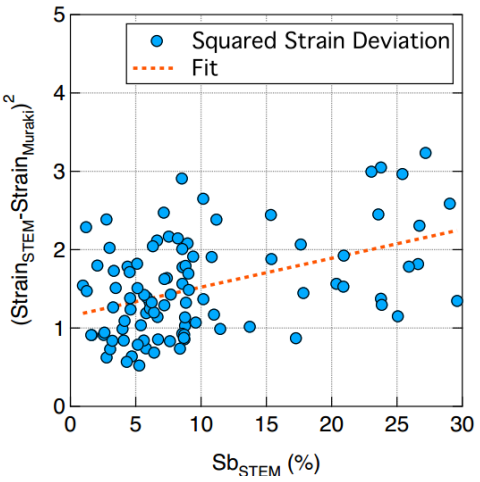

Figure 2.19 The squared strain deviation (SDD), which is calculated by $(\text{Strain}_{\text{STEM}}\text{-Strain}_{\text{Muraki}})^2$*, as function of Sb concentration.*

Figure 2.18 displays the averaged $\varepsilon^{\perp}$ across a single superlattice period of 20 monolayers and the calculated Sb contents. The average was performed over 7 periods from a sample area of 98.47 nm^2. The strain profile at the InAs-on-InAsSb interface is more extended than that at the InAsSb-on-InAs interface. This finding is consistent with the previously reported STM and TEM studies.[54, 60] The asymmetric anion segregation at interfaces was previously attributed to the surfactant nature of Sb, which has a tendency to segregate to the growth front.[61, 62] Segregation of atomic species during film growth is a common feature in the synthesis of heterojunctions.[62] To further evaluate chemical intermixing at interfaces between the InAs and InAsSb layers, we utilized the phenomenological segregation model first suggested by Muraki et al.[52] We also compared the Sb composition profile obtained from the STM measurement.[54] Good agreement was observed for the anion intermixing at both InAs-on-InAsSb and InAsSb-on-InAs interfaces, while the measured Sb concentration in the nominal InAs is somewhat higher than the STM result.

The strain map in Figure 2.17(a) shows significant strain fluctuations. To further investigate the fluctuations, we compared the experimentally measured strain with the strain calculated using the Muraki's model and Vegard's law. Figure 2.19 plots the squared strain deviation (SDD), which is calculated by $(Strain_{STEM}\text{-}Strain_{Muraki})^2$. The SDD is averaged over each monolayer and plotted as a function of the monolayer-averaged Sb content measured from the strain map. The increase in the SDD with Sb content indicates that the substitution of As with Sb in the InAsSb induces larger strain fluctuations in the InAsSb layers.

Figure 2.20 identifies the two-dimensional (2D) distribution of the strain fluctuations. Figure 2.20(a) and (b) show the strain map of two superlattice periods taken from the white dotted box region in Figure 2.17(a) and the calculated strain map based on the Muraki's model and Vegard's law. The difference between the two, i.e. $Strain_{STEM}\text{-}Strain_{Muraki}$, serves as a measure of strain fluctuation (Figure 2.20(c)). Local strain fluctuations with a spatial extent on the order of ~1 nm are seen in the difference map. For example, in Figure 2.20(c), a large *positive* difference value of 3.7 % is found at location I, while a large

negative SD value of -3.9 % is found at location II. The large difference values in the nominal InAsSb layer can be attributed to the local high and low concentrations of Sb in the anion atomic columns, i.e. Sb and As segregations.

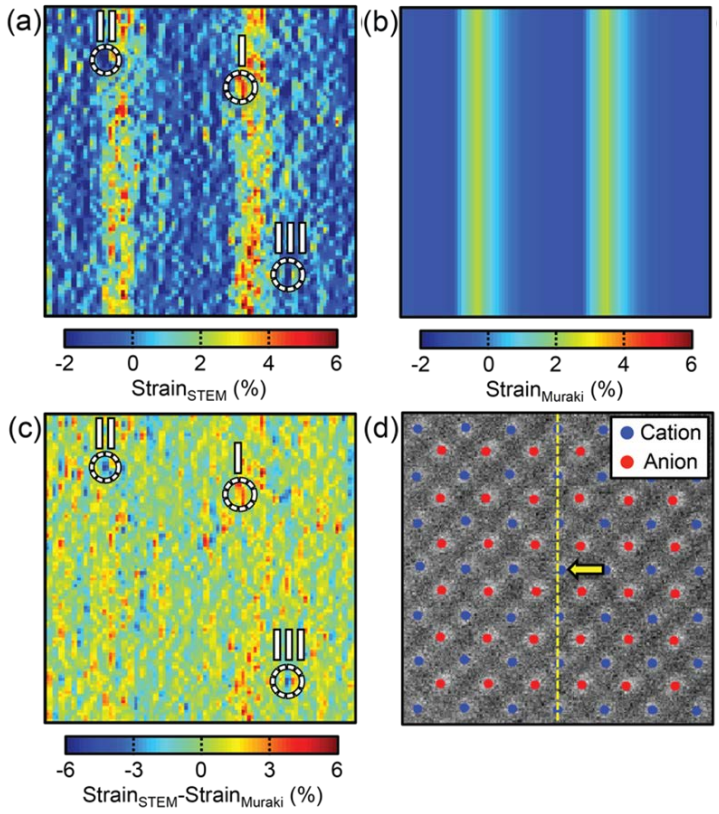

Figure 2.20 Strain maps obtained from (a) STEM and (b) Muraki's segregation model, respectively. Using these maps, (c) a strain difference map is obtained, revealing locations with a large deviation (see white arrows) from the ideal composition profile. (d) Magnified HAADF image near location III (dotted box in Fig. 2 (c)) with red and blue dots representing cation and anion atomic columns. The anion column marked by the yellow arrow is associated with large strain deviation values at location III. The yellow dashed line in (d) represents the average position of the cation layer.

Figure 2.20 (c) also identifies several locations (as indicated by the white arrows) with the unexpectedly small or large strain values. The strain values at these locations deviate from the Muraki model by an amount of equal to, or greater than, 3σ. Here, the σ represents the standard deviation of strain values in the monolayer. The measured σ in the GaSb substrate is 0.86 %, corresponding to a change in distance of 1.3 pm. The location III in Figure 2.20(c) is an example where a difference of -4.2 % is observed in the strain value, while the Muraki model predicts a strain value of -0.71 %. The σ of for the monolayer is 1.39 %. The anion atomic column marked by the yellow arrow in the magnified image in Figure 2.20(d) is associated with a large difference value at location III. The marked atomic column shows a distinct displacement with respect to the average atomic plane position (yellow dashed line). The spatial extent of strain fluctuation (~ 1 nm) rules out extended defects and suggests a point defect at this location. According to reported theoretical studies, vacancy-type defects in III-V semiconductors induce an inward relaxation of the nearest atoms by 10-20%, depending on the chemical species and charge states, which is largest among point defects.[63, 64] Previously, the measurement of atomic column positions in the HAADF images of oxides was successfully used to detect point defects in these materials.[65, 66] The atomic relaxation around a vacancy defect could explain the large local

strain fluctuation observed here; it would be of further interest to verify this hypothesis with modeling. Especially, point defects such as vacancies and antisite defects are important in the T2SLs since the minority carrier lifetime is mainly limited by SRH recombination.[67] [68]

With the above method, we identified 8 locations in the 15 x 15 nm^2 area of the T2SL where the strain values deviate beyond 3σ, leading to the defect density of ~5×10^{18} cm^{-3} by taking the depth of focus into account. The smaller strain fluctuations are correlated with the Sb contents. The significance of local strain can be estimated based on the impact on the deformation potentials. The deformation potentials for InAs and InSb are a_c= -5.08 eV, -6.94 eV, a_v= 1 eV, 0.36 eV and b = -1.8 eV and -2 eV, corresponding to the shift in conduction and valence band energies and the split of hole energy, respectively.[59] On average, the amount of strain variations inside the InAsSb layer is about 1.35%, which amounts to the change in the deformation potentials from ~5 to 94 meV with the largest impact on the conduction band energy shift. Additionally, the variation in local compositions also introduces a change in the energy gap, which can be estimated using $E_{g(InAsSb)} = (1-x)E_{g(InAs)} + xE_{g(InSb)} - x(1-x)C$ with C = 0.67 eV.[69] The 1.35 % change in strain amounts to 9.46 % change in anion compositions (x) and 50 meV change in the energy gap.

In summary, strain measurement on atomic column basis of the Ga-free T2SL has been performed using the [100] projected HAADF image, where intensity overlap effects between the nearest cation and anion atomic columns are mitigated. Thus, this approach enables precise determination of individual atomic columns and removes artifacts in strain maps. Atomic resolution strain mapping revealed asymmetric interface anion segregation. The averaged strain profile can be quantitatively fitted to the Muraki's segregation model and Vegard's law, and the results are in quantitative agreement with the scanning tunneling microscopy measurements. Further, we have shown that correlation with the segregation model can be used to examine strain fluctuations in T2SLs for the study of local anion segregation and point defects. A comprehensive analysis on strain and composition quantifications at atomic scale would provide new opportunities for studying the kinetics of chemical intermixing in heterostructures and allow for further optimization of process and material properties.

2.7. Quantitative Characterization of Order and Disorder in MBE grown InAs / InAsSb Strained–layer Superlattices with Cross–sectional STM (Weimer Group, TAMU)

Innovative methods for the characterization of order and disorder in strained–layer superlattices have been brought to maturity and applied to the previously overlooked problems of (i) period fluctuations, and their relationship with correlated interface roughness, in InAs / InAsSb superlattices; and (ii) short–range, atomic–alloy order in these same structures. The results so obtained illustrate the remarkable power of cross–sectional Scanning Tunneling Microscopy (STM) to provide new insights relevant to an informed understanding of carrier transport, and the kinetics of antimony incorporation, in device structures built from these materials.

2.7.1. Period fluctuations and long–range structural disorder

Period fluctuations are a frequently overlooked source of disorder in strained–layer superlattices. High resolution x-ray diffraction (HRXRD)[70, 71] and transmission electron microscopy (TEM)[72, 73] are the long–established standards for assessing the period fidelity in these, and similar, structures. We have developed, and applied, a new STM–based technique that enables accurate mapping of the period fluctuations throughout epitaxial structures comprised of alternating layers of InAs and InAsSb, or other, similar, materials[74]. The method relies on an analysis of [001]–convolved reciprocal–space satellite peaks obtained from discrete Fourier transforms of individual STM images, and, as such, represents an analagous implementation of Bragg's law as routinely used in x–ray diffraction. While not as accurate as x–ray, the inherent, single–image measurement error associated with this approach may be made as small as 0.1%, allowing both vertical and lateral period fluctuations contributing to carrier localization[75] and inhomogeneous energy broadening[76] in these, and related, structures to be pinpointed and quantified.

Previous advances have made the acquisition of micron–long, atomic–resolution STM surveys over deliberately–targeted subsets of superlattice repeats anywhere within a multi–layer stack routine[77]. Figure 2.21 presents one such example, Figure 2.22 illustrates the standard crop window adopted for computing a discrete Fourier transform (DFT) from each image of the survey, and Figure 2.23 demonstrates the reciprocal–space maps so generated exhibit reproducibly–situated superlattice satellites, and reciprocal lattice spots, in both (–1–10) and (1–10) cross section.

Referencing the image–by–image satellite–peak spacing to the image–by–image [001] reciprocal–lattice vector yields the dimensionless, survey–averaged Bragg plot shown in Figure 2.24, whose inverse slope (superlattice period in monolayers) is identical with that of the correspondingly–analyzed x–ray data from the same sample.

Figure 2.25, where the laterally–averaged period measurements from STM surveys over six, disjoint, vertical subsets of superlattice repeats (early on, midway through, and late in the growth) are assembled, offers a more incisive comparison. The small, but reproducible period drift noted for similar vertical repeats in orthogonal cross-sections on different dies is independently corroborated by least–squares fits to the spatially–coincident, laterally–averaged, [001] antimony profiles[78], whose reconstruction via atomic counting is facilitated by the robust impurity discrimination in Figure 2.22, as well as the subsequent discovery of multi–period, minority components buried within the dominant x–ray satellites[78] identified in Figure 2.24.

Analysis of the corresponding image–to–image period fluctuations along any subset of superlattice repeats in this system demonstrates the period variance so obtained exceeds expectations based on a naive assumption of uncorrelated interface roughness by a factor of 70[74]. Such surprisingly large, lateral fluctuations, which have so far been observed only with STM, are nevertheless consistent with interface roughness that is correlated over nanometer length scales; reasonable estimates place that correlation length, here, at ~ 7 nm.

2.7.2. Short–range alloy order

The specific structure chosen to test the more general analysis techniques respecting alloy order we have brought to maturity under MURI support is a nominally 33% antimony InAs / InAsSb superlattice grown by molecular beam epitaxy (MBE) at Sandia National Laboratory. The monolayer–by–monolayer antimony distribution in the growth direction

throughout this sample has been previously characterized with STM, so that its physical origins and accurate modeling are both well understood[79]. As we shall see, that detailed understanding facilitates a ready partitioning of the population of antimony–for–arsenic replacement sites into statistical subpopulations representative of direct incorporation versus segregation, as well as compressive versus tensile strain or high versus low antimony fraction.

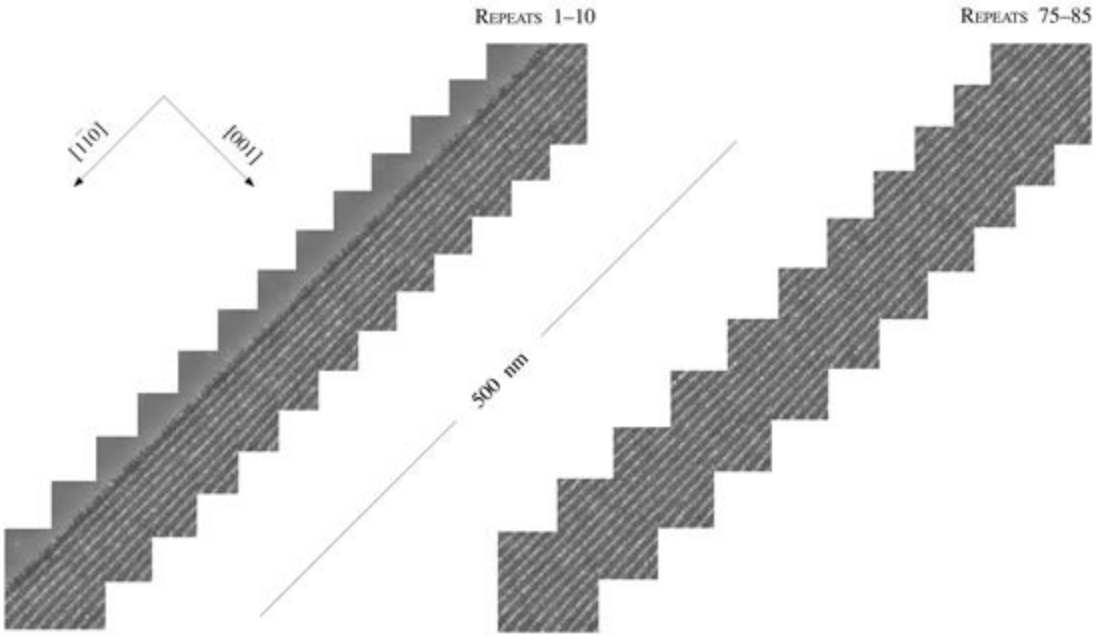

Figure 2.21 Device–scale surveys across a (–1–10) cleavage plane through an InAs / InAsSb superlattice illustrating early and late superlattice repeats. Bright regions are InAsSb and [001] growth direction is from top–left to bottom–right.

The underlying data on which these analyses build is essentially that already shown in Figure 2.21 and Figure 2.22: device–scale atomic–resolution surveys in complementary (–1–10) and (1–10) cross–sections, followed by identification of all antimony–for–arsenic replacement sites — together with their relative [001] lattice coordinates within a single, cleavage–exposed atomic plane — in non-overlapping counting windows encompassing fixed sets of superlattice repeats. The bulk–density profiles reconstructed with these data (Figure 2.26) illustrate the signature compositional grading that results from antimony segregation during, as well as following, antimony exposure.

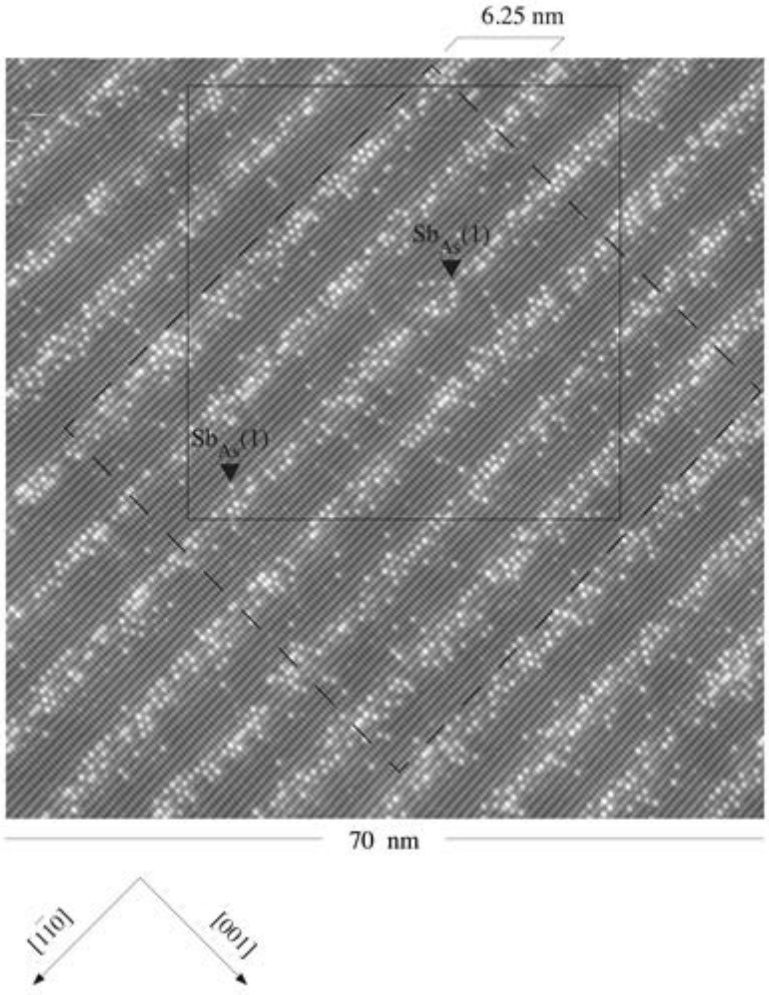

Figure 2.22 Individual atomic–resolution image, with top–layer, antimony–for–arsenic substitution indicated with carets. Solid outline identifies a standard DFT crop window, dashed outline a representative counting window used to compile the antimony fraction in successive [001] monolayers.

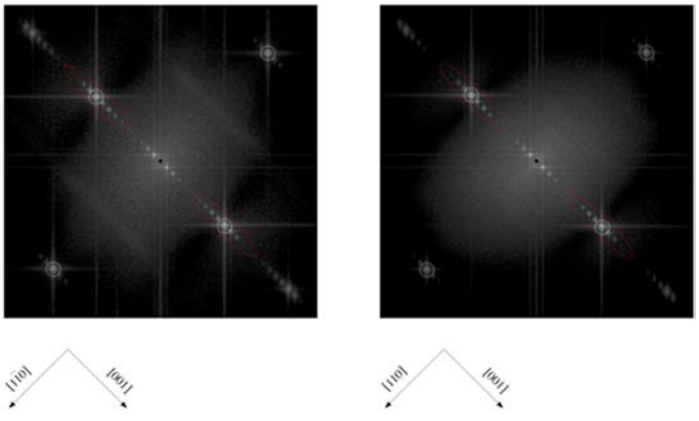

Figure 2.23 Two–dimensional reciprocal space maps from complementary 40 nm x 40 nm crops in (–1–10) and (1–10) cross section (left and right respectively). Reciprocal lattice spots encircled in white, [001]–convolved superlattice satellites encircled in red. Satellite peaks and reciprocal lattice vectors are similarly situated in both cross sections.

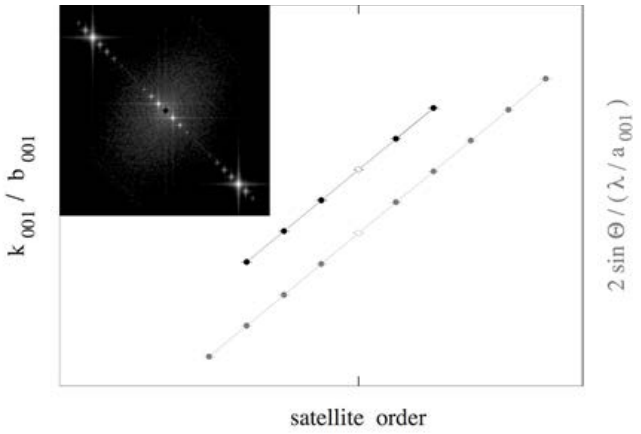

Figure 2.24 DFT reciprocal–space map (inset) together with dimensionless Bragg plots and linear fits for (–4, + 5) HRXRD (grey, right axis) and (–3, + 2) STM satellites (black, left axis, vertically offset for clarity). Direct– and reciprocal–space lattice constants are for the superlattice.

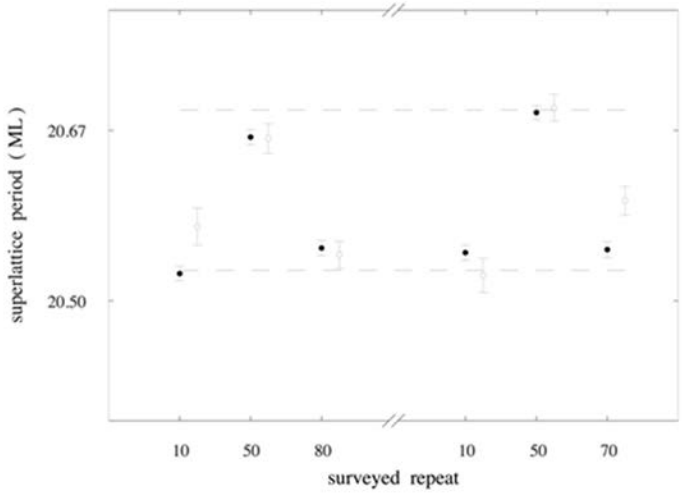

Figure 2.25 Discrete Fourier Transform periods (closed circles) over like repeats exhibit similar vertical period drifts in either cross section; DFT periods are independently validated by real–space fits to the antimony segregation profiles (open circles) reconstructed from spatially–coincident counts (Figure 2.22). Minority Gaussian components embedded in the HRXRD satellite spectrum (dashed lines) agree with the STM measurements.

This natural focus on the monolayer–by–monolayer dependence of the laterally–averaged antimony fraction throughout the structure necessarily overlooks potentially interesting correlations in the way these antimony atoms are incorporated at the (001) growth surface itself. The new course adopted here is to examine the < 110 > distribution of antimony–for–arsenic replacement sites in successive growth planes directly, employing the pair–correlation function[80]

$$g_2\left(\mathbf{r}_2-\mathbf{r}_1\right)=\frac{1}{x_{Sb}^2}\left\{\frac{N_{Sb-Sb\ pairs}\left(\mathbf{r}_2-\mathbf{r}_1\right)}{N_{anion\ pairs}\left(\mathbf{r}_2-\mathbf{r}_1\right)}\right\} \quad (5)$$

as a quantitative metric for assessing the deviations (if any) from random incorporation.

The mathematical structure of $g_2\left(\mathbf{r}_2-\mathbf{r}_1\right)$ is most easily surveyed by appealing, first, to a bulk alloy, where $\mathbf{r}_2-\mathbf{r}_1$ designates any member of the set of available lattice vectors that connect two anion–sublattice sites in a given {110} plane. If antimony–for–arsenic replacement is truly random, the number of antimony pairs with given $\mathbf{r}_2-\mathbf{r}_1$ will be independent of the lattice–separation vector involved, and therefore the same for each and every $\mathbf{r}_2-\mathbf{r}_1$. Normalization to the square of the mean antimony fraction then ensures a spatially–uniform, limiting value of one as the number of surveyed sites approaches infinity[81].

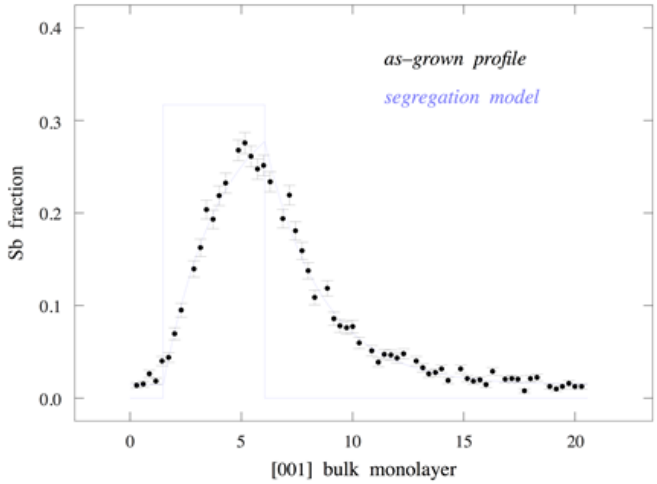

Figure 2.26 Monolayer–by–monolayer composition profile reconstructed from STM. Fits to a single–source segregation model facilitate a reliable partitioning of the growth sequence into source–on (antimony shutter open) and source–off (antimony shutter closed) components.

The corresponding situation for a compositionally–graded superlattice is simpler, in one regard, but more complex in another. Here, the spatially–modulated, bulk–density profile evident in Figure 2.26 suggests a natural specialization to one– versus two–dimensional lattice vectors, each of which is parallel to the applicable <110> direction. This observation prompts the following definition[82] for an analogous, monolayer–resolved, pair correlation function

$$g_2^i\left(\left|\mathbf{r}_2-\mathbf{r}_1\right|\right)=\frac{1}{x_i^2}\left\{\frac{N_{Sb-Sb\ pairs}^i\left(\left|\mathbf{r}_2-\mathbf{r}_1\right|\right)}{N_{anion\ pairs}\left(\left|\mathbf{r}_2-\mathbf{r}_1\right|\right)}\right\} \quad (6)$$

where i is now an [001] monolayer index, and x_i the equivalent local antimony fraction. An appropriate generalization for $g_2\left(\left|\mathbf{r}_2-\mathbf{r}_1\right|\right)$ then follows as the expectation value of this monolayer–resolved correlation function with respect to the actual population of squared antimony fractions[82], viz.

$$g_2\left(\left|\mathbf{r}_2-\mathbf{r}_1\right|\right)=\frac{1}{\Sigma_i x_i^2}\left\{\Sigma_i g_2^i\left(\left|\mathbf{r}_2-\mathbf{r}_1\right|\right)x_i^2\right\} \qquad (7)$$

a physically–sensible ansatz that explicitly reduces to the [001]–translation invariant bulk form, above, whenever $x_i = x_{Sb}$ for all i.

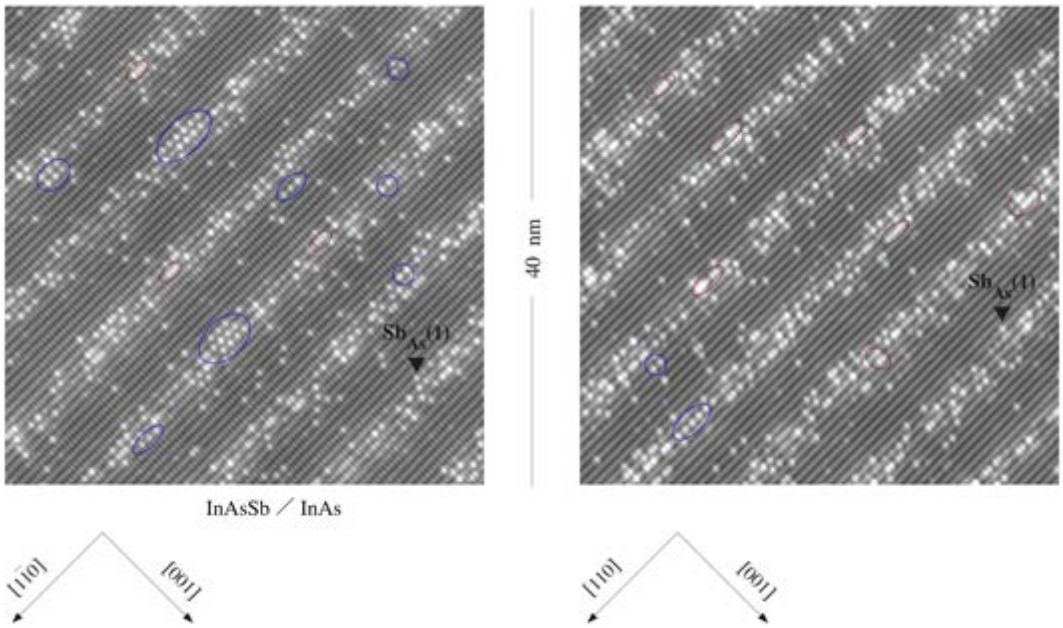

Figure 2.27 Representative survey crops, in (–1–10) cross section (left), and (1–10) cross section (right). Antimony–for–arsenic replacement preferentially occurs at next–nearest–neighbor anion sites (encircled in blue) in (–1–10) cross section and nearest–neighbor anion sites (encircled in red) in (1–10) cross section.

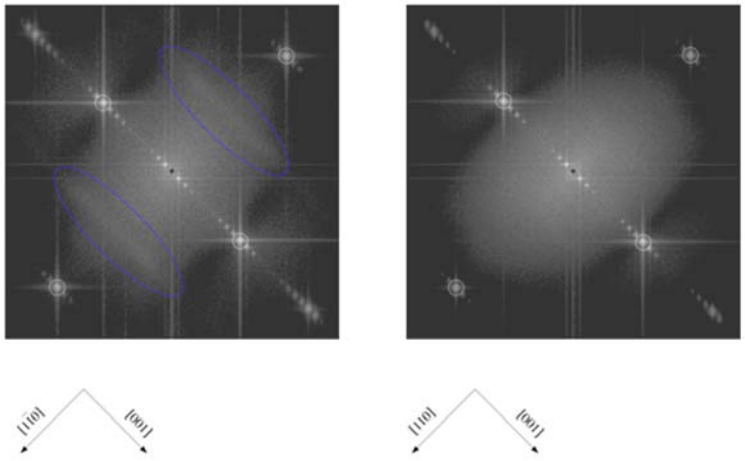

Figure 2.28 Ensemble reciprocal–space maps generated from cropped (–1–10) and (1–10) images (left, right respectively), with growth– and in–plane reciprocal lattice vectors (encircled in white) indicating the surface atomic mesh. Excess power (encircled in blue) at one–half the in–plane reciprocal lattice vector in (–1–10) cross section reflects

the every–other–atom separation observed in Figure 2.26 (left); this power is missing from the (1–10) reciprocal–space map, consistent with Figure 2.26 (right).

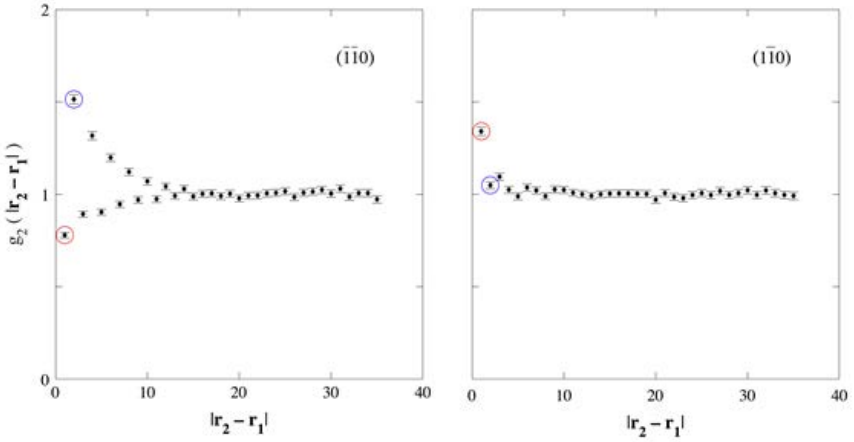

Figure 2.30 All–inclusive, antimony pair correlation functions in (–1–10) and (1–10) cross section (left, right respectively). Next–nearest–neighbor (blue) correlations are predominate in (–1–10) cross section, whereas the correlations in (1–10) cross section are (almost) exclusively nearest–neighbor (red). Colors conventions are those of Figure 2.26.

The phenomena to be so quantified and understood are best appreciated by referring to

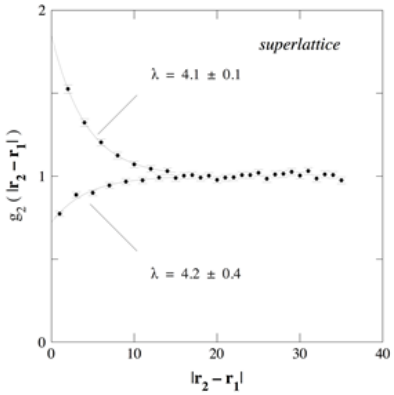

Figure 2.29 FIGURE 10. Antimony pair correlation function in (–1–10) cross section reproduced from Figure 2.28. The first fifteen points in upper (more likely than random) and lower (less likely than random) branches are independently fit by exponential functions with a common decay length of 4 lattice constants.

Figure 2.27 and Figure 2.28, respectively. Figure 2.27 contrasts representative, small–area crops from the atomic–resolution STM surveys on orthogonal cleavage faces, thereby highlighting a key distinction in the short–range correlations between antimony atoms along one or the other <110> direction: preferential antimony–for–arsenic replacement at next–nearest–neighbor sites in (–1–10) cross section, versus a greater propensity for like replacement at nearest–neighbor sites in (1–10) cross section. The global nature of this dissimilarity is confirmed by universally–noted, mirroring features in the accompanying (digitally–generated) survey–averaged, reciprocal–space maps (Figure 2.28). The associated ensemble–averaged pair correlation functions, $g_2\left(\left|\mathbf{r}_2-\mathbf{r}_1\right|\right)$, constructed from these (real–space) STM data (Figure 2.30) serve to underscore the quantitative significance of the qualitative differences just described.

Figure 2.30 makes several important points. First, the pair correlation function in (–1–10) cross section exhibits damped oscillations about unity, at small pair separations, that

ultimately converge on the anticipated asymptotic value (one) at larger separations, and exponential fits to this correlated behavior yield a decay length of the order of 4 lattice constants (Figure 2.29). Conversely, the pair correlation function in (1–10) cross section is essentially unipolar with respect to its deviation from unity (i.e., random behavior), and these deviations are largely quenched at separations exceeding one lattice constant.

Second, the smoothly–decaying oscillations about unity seen in (–1–10) cross section have the following physically transparent interpretation: since the pair–correlation function at odd–integer <110> lattice separations (nearest neighbor sites, and so on) falls short of one, these pairings occur less frequently than expected for a random alloy with the same mean–squared antimony fraction; likewise, because the pair correlation function at even–integer <110> lattice separations (next–nearest neighbor sites, and so on) exceeds unity, these pairings occur more frequently than otherwise expected for a random distribution.

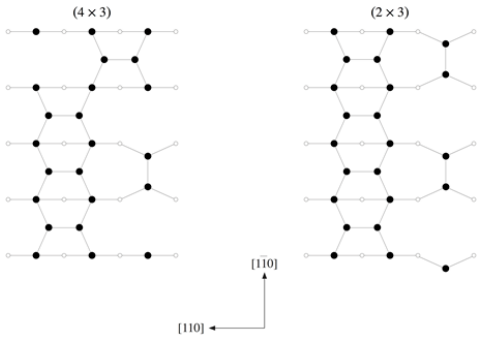

Figure 2.31 Prevailing (001) surface reconstructions during antimonide growth; [001] direction is out of the page. A single surface cell is shown for the (4x3) case, and two consecutive (in the [1–10] direction) surface cells shown for the (2x3) case, respectively. Top–layer antimony dimers preferentially align with the [110] direction in both reconstructions. The dimers situated between [110] rows form a 2/3 ML "floating layer" of unincorporated antimony atoms.

This logic formalizes and extends many of the conclusions already clear from Figure 2.27, but the magnitude of the pair–correlation function also has direct physical meaning: the observed value of 3/2 at next–nearest–neighbor sites, for example, indicates such (–1–10) antimony pairs are 50% more likely, here, than in the corresponding random alloy; the value of 2/3 that obtains at nearest–neighbor sites, on the other hand, signals those pairs are 50% more likely in a random alloy than they are here. So weighing the prevalence of nearest–neighbor antimony–antimony pairs on one cross section against those on the other (Figure 2.30), we notice something quite extraordinary: the excess frequency of (1–10) pairs quantitatively compensates for the deficit in (–1–10) pairs in the sense that the product of the two correlation functions equals one — the expected result for a random distribution — within experimental error; put more simply, the nearest–neighbor antimony pairs missing from one cross section show up on the other, but the analogous effect clearly does not hold at next–nearest–neighbor separations (Figure 2.30).

This initially surprising finding, that a (–1–10) nearest–neighbor pair deficit originates from a complementary (1–10) pair surplus, suggests antimony atoms are preferentially incorporated into the bulk from surface dimers oriented along a [110] direction. That guess is both consistent with, and motivated by, our accepted understanding of the antimony–rich surface reconstructions prevailing under common growth conditions (Figure 2.31); these reconstructions support a (maximum) two–thirds monolayer over–layer of antimony situated in [110]–aligned surface dimers [see [83], [84], and references therein].

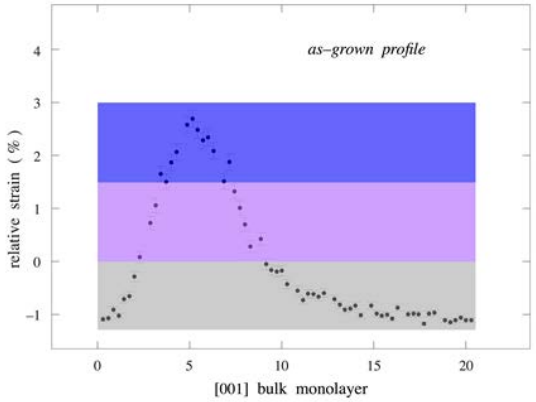

Figure 2.32 Partition of the as–grown antimony profile into source–on and source–off components following the fit in Figure 2.25. Monolayers deposited while the antimony vapor source is on are highlighted in blue, those deposited with the source off are highlighted in grey.

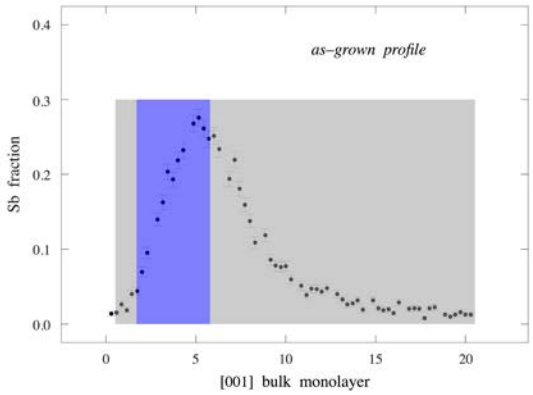

Figure 2.33 The one–to–one correspondence between composition and coherent strain permits direct translation of the monolayer–by–monolayer composition profile (Figure 2.25) into a corresponding [001] strain profile, illustrated here. This strain profile can then be partitioned into tensile (grey, strain < 0.0 %), weakly–compressive (magenta, 0.0 % < strain < 1.5%), and strongly–compressive (blue, 1.5% < strain) ensembles. The division between weakly and strongly compressive ensembles is set, here, at one–half the maximum observed strain.

In view of the long–established connection between antimony segregation and the overlayer stoichiometry[52, 84] of these surfaceFigure 2.33 reconstructions, it seems natural to consider the following question: what difference, if any, is there in the pair correlations between antimony atoms nominally incorporated from an incoming vapor stream (antimony shutter open / source on) and those incorporated from a previously–established floating layer that seeds subsequent antimony segregation (antimony shutter closed / source off)[52, 84]. Our quantitative understanding of the relationship between the as–grown [001] antimony profile and the externally–imposed, antimony–shutter–sequencing cycle[79] fortunately facilitates just such a division (Figure 2.32).

The pair correlations exhibited by source–on and source–off sub–ensembles, thus obtained, are so similar to one another, and to the all–inclusive ensemble in Figure 2.30, that one can come to no other conclusion but that the presence (or absence) of an incoming vapor stream has no significant bearing. And although changes in the magnitude of the nearest–neighbor correlations within these subpopulations are, indeed, observed, those changes strictly adhere to the compensation rule already described. Both facts directly support the hypothesis that short–range order originates with the floating layer of antimony dimers atop the surface reconstructions in *Figure 2.31*.

The one–to–one correspondence between alloy composition and [001] strain in coherently–strained structures permits an alternative, and potentially relevant, partitioning of the pair correlations in this system (Figure 2.33) motivated by the identification of long–range order in epitaxial InAsSb alloy films[85] together with evidence this order is sensitive to the overall [001] strain in the film[86]. A natural dividing line for any strain–balanced sample, as is the case here, is the distinction between tensile (negative strain) and compressive (positive strain) regimes; pair statistics, in this instance, support a further subdivision (Figure 2.33) into weakly– and strongly–compressive ensembles.

The correlation functions for these strain–resolved ensembles are, again, qualitatively similar to each other, as well as the all–inclusive ensemble (Figure 2.30) from which they were drawn, and evidence quantitatively similar decay lengths (Figure 2.29). The quantitative variations between populations are most pronounced for nearest–neighbor pairs, but these variations, once again, strictly comply with the compensation rule.

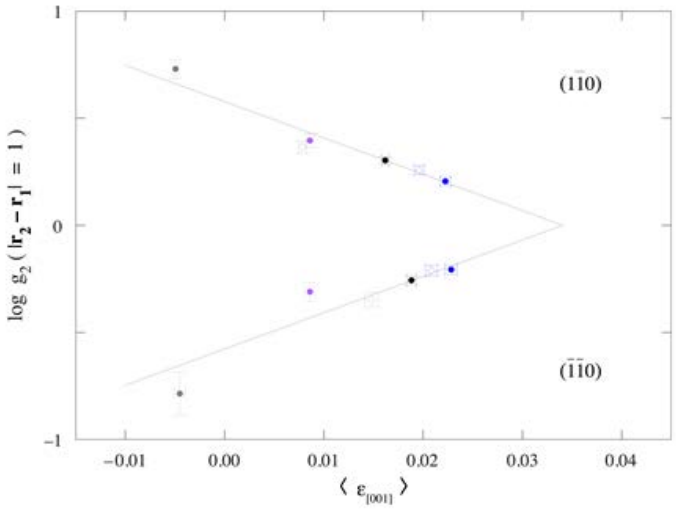

Figure 2.34 Logarithm of nearest–neighbor correlations versus mean ensemble strain in orthogonal cleavage directions; values in (1–10) and (–1–10) cross section sum to zero in all cases, reflecting an ensemble–invariant compensation rule where a nearest–neighbor pair excess on one face is mirrored by a complementary deficit on the other. Simultaneous, straight–line fits to the populations on each face convincingly describe all six ensembles. Solid, colored points are strain–resolved, open points source–resolved, and solid black points all–inclusive data, respectively.

One may now survey the compensating behavior of nearest–neighbor correlations on orthogonal cross sections over the full set of experimental ensembles in either of two ways: if we consider, first, ensemble–mean strain, defined via

$$\langle \varepsilon \rangle = \frac{\Sigma_i \, \varepsilon_i \, N^i_{Sb-Sb\ pairs}\left(\left|\mathbf{r}_2 - \mathbf{r}_1\right| = 1\right)}{\Sigma_i \, N^i_{Sb-Sb\ pairs}\left(\left|\mathbf{r}_2 - \mathbf{r}_1\right| = 1\right)} \qquad (8)$$

as the controlling variable, we arrive at the plot shown in Figure 2.34. We note the near–linear dependence of the logarithm of $g_2\left(\left|\mathbf{r}_2 - \mathbf{r}_1\right| = 1\right)$ on $\langle \varepsilon \rangle$, with unmistakable reflection

symmetry about $g_2\left(\left|\mathbf{r}_2-\mathbf{r}_1\right|=1\right)=1$. The common horizontal intercept that signals random behavior for large compressive strain engenders skepticism, however, as does the corollary prediction of strong nearest–neighbor correlations at vanishing strain.

If we consider, instead, ensemble–mean antimony fraction, analogously defined via

$$\left\langle x\right\rangle=\frac{\Sigma_i\, x_i\, N^i_{Sb-Sb\ pairs}\left(\left|\mathbf{r}_2-\mathbf{r}_1\right|=1\right)}{\Sigma_i\, N^i_{Sb-Sb\ pairs}\left(\left|\mathbf{r}_2-\mathbf{r}_1\right|=1\right)} \qquad (9)$$

as the controlling variable, we obtain the qualitatively similar plot shown in Figure 2.34, where the common intercept of $g_2\left(\left|\mathbf{r}_2-\mathbf{r}_1\right|=1\right)=1$ now occurs at a bulk antimony fraction equal to the intended 33%.

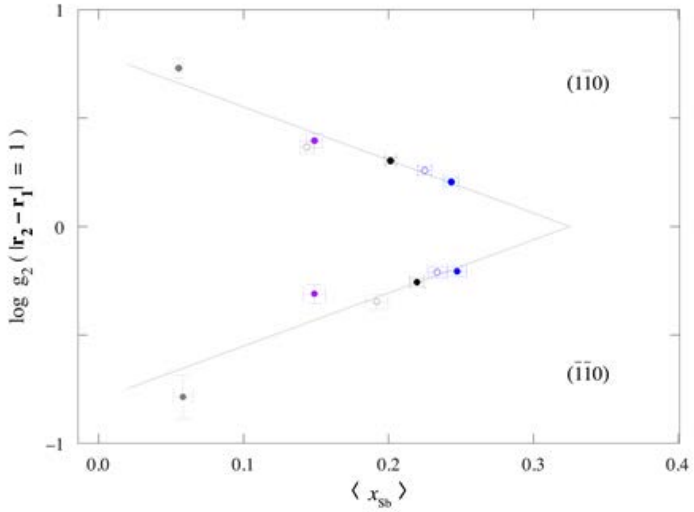

Figure 2.35 Logarithm of nearest–neighbor correlations in Figure 2.34 plotted versus mean antimony fraction for the corresponding ensemble. Solid, colored points are strain–resolved, open points source–resolved, and solid black points all–inclusive data, respectively.

For a binary system evidencing segregation, surface and bulk impurity fractions will be related to each other through a segregation coefficient[52], *R*, that is accurately determined by fits to the compositional grading observed with STM[84]. The value of that parameter in InAs / InAsSb is very close to two–thirds[78], implying a fixed, monolayer–by–monolayer ratio between surface– and bulk–incorporated antimony fractions of 2:1. The common horizontal intercept in Figure 2.35 may thus be equivalently interpreted as a surface antimony fraction of 66%, the maximum that can be accommodated by either of the surface–dimer reconstructions in *Figure 2.31*.

All experimental findings therefore point to the number of [110]–oriented antimony dimers on the growth surface as the starting point for short–range order in the bulk.

2.8.Raman spectroscopy of Type-II Superlattices (Zhang, NCSU)

Heterostructures like InAs/GaSb superlattices (SLs) are distinctly different from well-studied ones like GaAs/AlAs SLs in terms of band alignment, common interface atom, and phonon spectrum overlapping of the constituents, which manifests as stark differences in

their electronic and vibrational properties. We performed the first comprehensive examination of all four types of phonon modes (confined, quasiconfined, extended, and interface) that have long been predicted for the InAs/GaSb SL. In the past besides the two interface modes (InSb and GaAs like) have been reported, only one LO like supplatice mode was observed from the (001) backscattering studies. It was unclear that this mode belongs to which of the three possible types of phonon modes: confined, quasiconfined, and extended. By performing polarized μ-Raman study on (110) cleaved edges, and using the superlattice samples grown on both GaSb and InAs substrate and bulk reference samples, we observed multiple new phonon modes and attributed them to different types of superlattice modes[87]. Achieved detailed understanding of the superlattice phonon spectrum makes it feasible to use Raman spectroscopy as a nondestructive tool for material quality analysis.

The InAs/$InAs_{1-x}Sb_x$ superlattice system distinctly differs from two well-studied superlattice systems GaAs/AlAs and InAs/GaSb in terms of electronic band alignment, common elements at the interface, and phonon spectrum overlapping of the constituents. This fact leads to the unique electronic and vibrational properties of the InAs/$InAs_{1-x}Sb_x$ system when compared to the other two systems. InAs/$InAs_{1-x}Sb_x$ superlattices have rarely been studied. We preformed a polarized Raman study of the vibrational properties of the InAs/$InAs_{1-x}Sb_x$ superlattices as well as selected $InAs_{1-x}Sb_x$ alloys, all grown on GaSb substrates by either MBE or MOCVD, from both the growth surface and cleaved edge. In the SL, from the (001) backscattering geometry, an InAs-like longitudinal optical (LO) mode is observed as the primary feature, and its intensity is found to increase with increasing Sb composition. From the (110) cleaved-edge backscattering geometry, an InAs-like transverse optical (TO) mode is observed as the main feature in two cross-polarization configurations, but an additional InAs-like "forbidden" LO mode is observed in two parallel-polarization configurations. The $InAs_{1-x}Sb_x$ alloys lattice matched to the substrate ($x_{Sb} \sim 0.09$) grown by MBE are also found to exhibit the forbidden LO mode, implying the existence of some unexpected [001] modulation. However, the strained samples ($x_{Sb} \sim 0.35$) grown by MOCVD are found to behave like a disordered alloy. The primary conclusions are (1) the InAs-like LO or TO mode can be either a confined or quasi-confined mode in the InAs layers of the SL or extended mode of the whole structure depending on the Sb composition. (2) InAs/$InAs_{1-x}Sb_x$ and InAs/GaSb SLs exhibit significantly different behaviours in the cleaved-edge geometry but qualitatively similar in the (001) geometry. (3) The appearance of the forbidden LO-like mode is a universal signature for SLs and bulk systems resulting from the mixing of phonon modes due to structural modulation or symmetry reduction. The results of MBE and MOCVD samples with nominally identical structures are considerable different in details. This study provides the ground work for further careful examination of the structural difference between the two growth techniques[88].

3. Theoretical study of defects

3.1. First-principles density functional theory (DFT) based modeling (Zhang, UNCC)

On the theoretical modeling part, we intended to carry out the modeling using first-principles density functional theory (DFT) based techniques. The defects of interest include point defects, line defects, and interfacial imperfection. Although other techniques, such as k.p method, empirical pseudopotential method (EPM), have been used in the past, the accuracy of those methods were uncertain. The DFT method would have its own challenges: Firstly, the well-known bandgap error in the commonly adopted local density approximation (LDA), which leads to error in the defect state energy level, because a localized defect state does not follow the band edge, therefore, we cannot simply shift the DFT band edge to expect the defect state does the same. Secondly, to obtain the accurate defect energy level with respect to the band edge a fairly large supercell is required (typically at least a few thousand atoms). The conventional DFT method cannot easily handle the required supercell size. We are able to overcome these two challenges by applying a new LDA correction scheme[89] to address the first challenge, and a charge patching method to address the second challenge[90]. Specifically, our modeling work focused on these areas:

1) We calculated the band structure of InAs/GaSb T2SLs using DFT, achieving better agreement with experimental results than previous EPM results [91].
2) We performed a systematic investigation, using Ga on Sb (Ga_{Sb}) anti-site defect in GaSb as a prototype system, to examine the defect calculation results with different DFT approaches, because this defect was considered as an acceptor like defect that has significant impact on the device performance. A paper is under preparation for publication.
3) We calculated four point defects in InAs: In vacancy (V_{In}), As vacancy (V_{As}), and antisite of In on As (In_{As}) and antisite of As on In (As_{In}), attempting to explain why InAs tends to have higher mobility than other low bandgap materials, and confirm the suggestion that the InAs defect states are above the conduction band edge according to a pressure study by co-PI Y.-H. Zhang's group[92]. A paper is under preparation for publication.
4) We proposed a new understanding of the acceptor electronic states, a bound exciton model[93], which can be generalized to donors as well. This model is distinctly different from the conventional model initially proposed by Mott et al. in 1940's[94] and used thereafter with some modifications [95]. A review paper [arXiv:1709.04058 (2017)] has been written to offer more detailed discussions between different theoretical models.
5) We performed preliminary calculation of the Ga_{sb} defect in InAs/GaSb SLs with mid-wave IR and long-wave IR wavelengths, assuming the defect the center of the GaSb layer and at the interface of InAs/GaSb.

3.2.Type II Superlattice Modeling, Effects of Interface Layers (Chuang, UIUC)

Early in the program, the 8-band k.p model[96] is re-developed with updated material parameters on a more user-friendly platform. The convergence of the model is examined by using two different boundary conditions and by changing the numerical parameters such as the finite-difference grid size, the number of periods, and the summation interval and range. The accuracy of the model is verified by the experimental data.

Figure 3.1 and *Figure 3.2* show good agreement between our theoretical model and the experimental data. Small variations in material parameters and layer structure become critical when modeling optical properties at long wavelengths. Slight fluctuations in the input parameters, such as the layer thicknesses and the valence band offset (VBO), can cause a large percentage change with respect to the small transition energy. One major difficulty of modeling semiconductor nanostructures with hetero-junctions is the determination of the band alignment and the VBO. One commonly used method is the model-solid theory, where the unstrained valence bandedges for all materials are measured from an absolute reference. However, large variation exists among reported experimental VBO values, obtained through different measuring techniques or by different researchers. Besides experimental error, one of the major reasons is the imperfectness of the hetero-junction formed in practice. Interfacial layers are formed unintentionally at the hetero-junction and will affect the measurement of VBO and other optical properties.

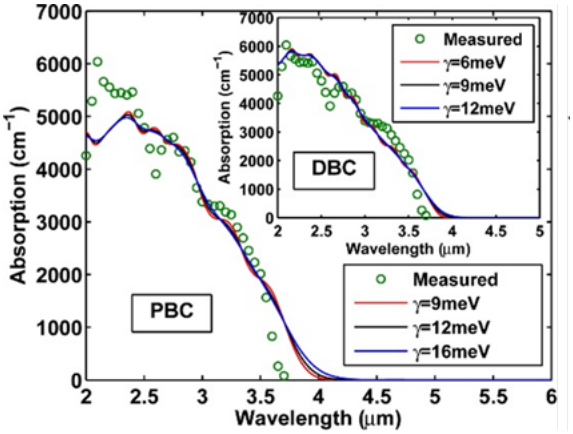

Figure 3.1 Comparison between theoretical model and experimental data[97] for an InAs/GaSb 18 Å/22 Å superlattice on GaSb substrate. Both the periodic boundary condition (PBC) and Dirichlet boundary condition (DBC) (inset) are used, along with different linewidths, γ.

Figure 3.2 Comparison between theoretical model and experimental data[97] for an InAs/GaSb 48 Å/22 Å superlattice on GaSb substrate. Both the periodic boundary condition (PBC) and Dirichlet boundary condition (DBC) are used and different valence band offset values take into account the interfacial effect if actual interfacial layers are not included.

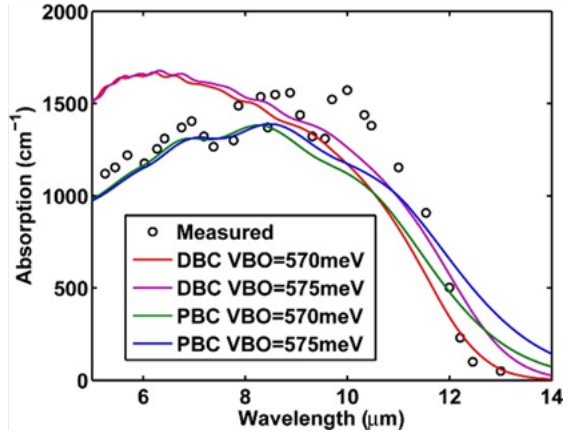

3.3.Modeling Ga-Free T2SLs (Chuang, UIUC)

The UIUC team applied the developed **k.p** method to model the absorption spectrum of Ga-free T2SLs grown by the ASU team. The absorption spectrum for the T2SL sample was extracted from spectroscopic ellipsometry (SE), by fitting the measured curve with optical model shown in Fig. 3. Excellent matching between experimental SE parameters, Δ and Ψ, and the fitting, produced the refractive index (n) and extinction coefficient (κ) of the T2SL sample from around 0.05 eV to 0.7 eV. The extracted absorption spectrum

(Figure 3.4b) was fitted by our 8 band **k·p** model, with the degree of freedom to adjust alloy and material parameters. An unusual singularity was seen around 3.8 μm, and thus we basically focused on wavelengths above 4 μm.

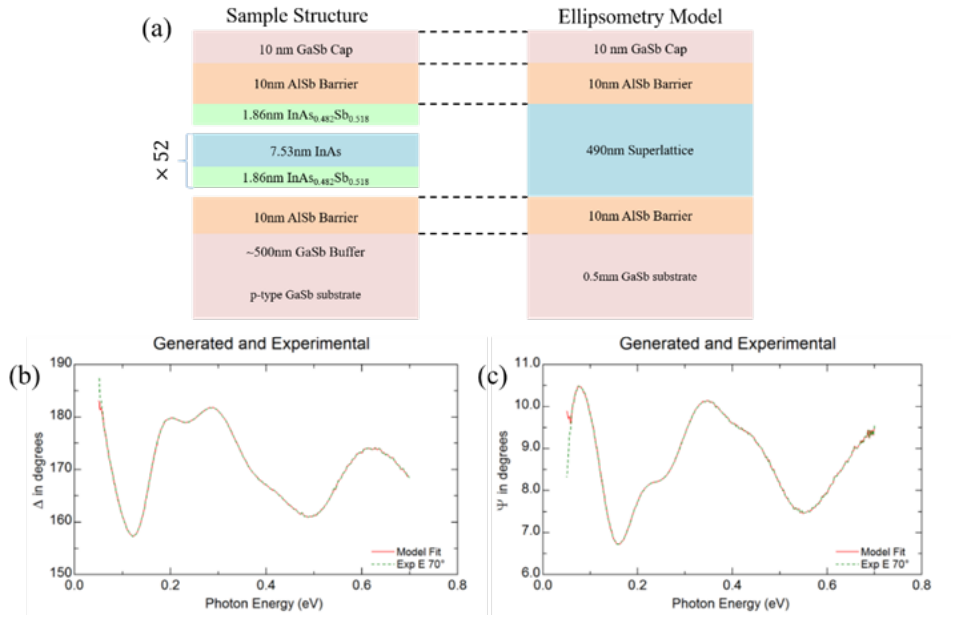

Figure 3.3 (a) Sample structure and optical model used for ellipsometry measurement. Measured ellipsometry parameters (b) Δ and (c) Ψ and fitting.

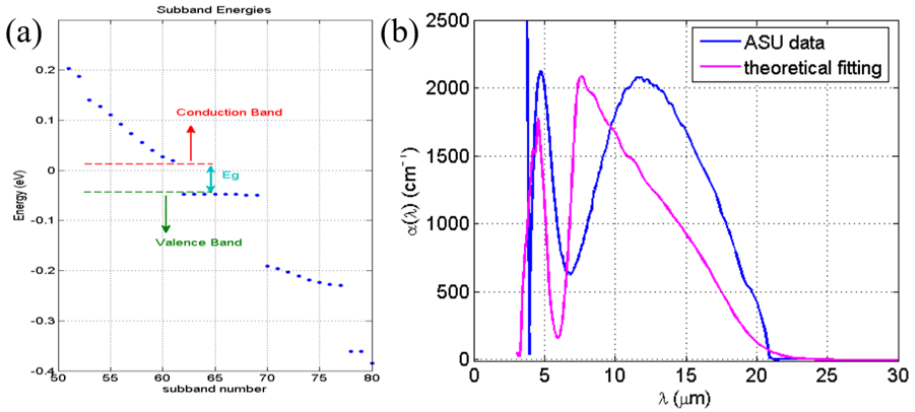

Figure 3.4 (a) T2SL Bandstructure. The cut-off wavelength is defined by E_g. (b) The best fitting of the absorption spectra from our theoretical calculation

By changing the material parameters of each constituent material, such as VBO, deformation potential, Luttinger parameter potential, and bandgap, as functions of alloy composition, the cutoff wavelength could be matched. In addition to the material aspect, the cutoff wavelength is also determined by the superlattice period. Instead of modeling with the nominal 1.86 nm / 7.53 nm growth period, our work suggested an "effective InAs well width" of 7.83 nm. This could be explained as due to either the fluctuation in alloy composition across the interface or to the extension of hole wavefunctions in the InAs

quantum wells. Although the fitting agreed well with the experimental data in the onset behavior and the overall profile, the sharp slope could not be simultaneously matched by varying material parameters within reasonable range.

4. Innovative Growth and Fabrication Processes for Defect Reduction

4.1. Study of Ga-free InAs/$InAs_{1-x}Sb_x$ T2SLs (Y.-H. Zhang, Johnson, Smith ASU)

The InAs/$Ga_{1-x}In_xSb$ type-II superlattice (T2SL) is the most investigated III-V T2SL material for mid- and long-wavelength infrared (MWIR and LWIR) photodetectors. T2SLs are predicted to have a number of advantages over the currently used bulk HgCdTe, including a decreased dependence of the bandgap on compositional non-uniformity, the ability to leverage III-V manufacturing capabilities, the lower cost of substrates, a higher electron effective mass leading to smaller tunneling currents, and band-engineered lower Auger recombination rates and thus lower dark currents.[98] However, reported minority carrier lifetimes at 77 K are 50 – 80 ns for MWIR InAs/$Ga_{1-x}In_xSb$ T2SLs[99, 100] and 10 – 40 ns for LWIR InAs/$Ga_{1-x}In_xSb$ T2SLs[3, 99, 101] as compared to 1 μs for $Hg_{0.78}Cd_{0.22}Te$ (~ 10 μm bandgap).[99] The short minority carrier lifetime has been attributed to Shockley-Read-Hall (SRH) recombination and is detrimental to the device dark current and quantum efficiency.[102] Calculations show that a 350-ns lifetime must be reached for a LWIR T2SL *pn* homojunction photodiode to achieve background limited operation (BLIP) at 80 K with F/6.5 optics in a 300 K background.[4, 5]

Campaigns to improve the minority carrier lifetime have led to investigations of the InAs/$Ga_{1-x}In_xSb$ T2SL interface type[103] and density,[104, 105] as well as doping concentration,[99, 106] but have thus far resulted in minor or no improvements to the carrier lifetime. It is hypothesized that a native defect associated with InAs or GaSb limits the carrier lifetime.[105] The measured lifetimes of bulk InAs (~ 325 ns)[105] and bulk $InAs_{0.80}Sb_{0.20}$ (250 ns)[99] are longer than that of bulk GaSb (~ 100 ns),[105] suggesting that defects associated with GaSb and other Ga-related bonds limit the lifetime of InAs/$Ga_{1-x}In_xSb$ T2SLs and that InAs/$InAs_{1-x}Sb_x$ T2SLs should have a longer minority carrier lifetime than InAs/$Ga_{1-x}In_xSb$ T2SLs. Furthermore, InAs/$InAs_{1-x}Sb_x$ T2SLs have been successfully demonstrated for MWIR lasers and proposed for LWIR photodetectors.[42] A theoretical comparison between LWIR InAs/$InAs_{1-x}Sb_x$ and InAs/$Ga_{1-x}In_xSb$ T2SLs, which excludes SRH recombination, found that the ideal detectivities of the two types of T2SL devices are comparable and are both greater than that of HgCdTe devices.[2] This letter reports an order-of-magnitude improvement of the minority carrier lifetime for a LWIR InAs/$InAs_{1-x}Sb_x$ T2SL over that of a LWIR InAs/$Ga_{1-x}In_xSb$ T2SL. We observe a carrier lifetime of > 412 ns at 77 K under low-excitation for an InAs/$InAs_{0.72}Sb_{0.28}$ T2SL as determined by time-resolved photoluminescence (TRPL) measurements. This improvement in minority carrier lifetime could now enable LWIR T2SL BLIPs at higher operating temperatures.

The InAs/$InAs_{1-x}Sb_x$ T2SL was designed with AlSb barriers for TRPL measurements. The AlSb barriers ensure that the measured PL decay time is due to carrier recombination in the T2SL and the influence of carrier transport, surface recombination, or any junction fields within the sample is minimized. Studies of a T2SL homojunction have shown that the restoring current in a narrow-bandgap junction results in an ostensibly long PL lifetime.[103] The sample was grown by molecular beam epitaxy on an undoped 2-inch GaSb

substrate with a 500-nm GaSb buffer layer. The T2SL consists of 20 periods of InAs (173 Å) and $InAs_{0.72}Sb_{0.28}$ (72 Å), with a total thickness of 500 nm. The T2SL is unintentionally doped *n*-type (~ $3x10^{16}$ cm^{-3} at 10 K) as determined by Hall measurements. AlSb barrier layers (100 Å), above and below the T2SL, are used to confine the electrons to the superlattice as well as to provide an adequate heavy hole barrier of over 100 meV. The entire structure is capped with 100 Å of p^+ InAs. Photoluminescence (PL) measurements show peak emission at 8.2 μm (150 meV) at 77 K.

TRPL measurements were performed on the InAs/$InAs_{0.72}Sb_{0.28}$ T2SL sample at 11, 40, 77, 110, 150, 200, and 250 K. An ultrafast laser with ~ 100 fs pulses at a 250 kHz repetition rate with 2 μm (0.62 eV) emission was used to excite carriers in only the T2SL region to excess carrier densities between 10^{15} and 10^{17} cm^{-3}. The carrier concentrations were calculated using an absorption coefficient of 10^4 cm^{-1} from published *n*-type InAs room-temperature absorption data at 0.62 eV.[107] This is a reasonable absorption coefficient value given that the laser pump energy is well above the SL band edge energy. The PL was detected with an HgCdTe detector operating at 200 K with a 3 ns temporal resolution and a 1 x 1 mm^2 detector area. A 3.6 μm longpass filter isolated the PL signal from the pump laser scattering. Further details of the experimental technique can be found in Ref. [3].

The TRPL signal at 77 K is shown in for a sampling of initial excess carrier densities, $\delta p_{t=0}$, between $4.0x10^{15}$ and $1.0x10^{17}$ cm^{-3}. For the highest $\delta p_{t=0}$, $1.0x10^{17}$ cm^{-3}, a fast initial decay is observed in the PL signal, and the instantaneous PL lifetime increases significantly as the signal decays. At the lowest initial excess carrier density of $4.0x10^{15}$ cm^{-3}, the PL signal approaches a single exponential decay, indicating excitation levels are much lower than the background doping density (at least an order of magnitude lower) and we are approaching the low-excitation regime. As described in Ref. [3], at a given temperature the PL intensity is only a function of the excess carrier density, δp. Therefore, the PL data taken at lower $\delta p_{t=0}$ can be shifted in time to overlap with the data taken at higher $\delta p_{t=0}$. This shifting process provides a combined PL decay signal with an improved signal-to-noise ratio. At each temperature, the decay rate of the PL signal shows a strong dependence on δp, evolving from a faster decay in the first 100 ns, which corresponds to excess carrier densities > $5x10^{16}$ cm^{-3}, to a slower, almost single exponential decay at the tail end of the decay, which corresponds to excess carrier densities < $5x10^{15}$ cm^{-3}. This strong dependence of the carrier lifetime on the excess carrier density cannot be explained by SRH recombination alone. Contributions from radiative or Auger recombination, which vary strongly with excess carrier density, must also be considered.

Under typical detector operating conditions, only very small excess carrier densities on the order of 10^{12} cm^{-3} are expected,[108] so it is important to determine the carrier lifetime in the low-excitation regime where the lifetime is independent of the excess carrier density to predict device performance. We therefore fit the tail of the TRPL data, where the excitation level is low (~ 10^{15} cm^{-3}) compared to the background doping density (~ 10^{16} cm^{-3}), with a single exponential decay to obtain the lifetime, τ, at each temperature. When the PL decay rate reaches a single exponential decay in the low-excitation regime, the PL lifetime is equivalent to the minority carrier lifetime. At higher excitation levels, however, the PL lifetime is shorter than the minority carrier lifetime. Since the lowest excitation levels used

in this study are just approaching the low-excitation regime, the measured PL lifetime represents a lower limit of the minority carrier lifetime.

The PL lifetime is observed to increase from low temperature (11 K) to a maximum of 412 ns at 77 K. This lifetime is an order-of-magnitude longer than the SRH-limited lifetime of ~30 ns that was previously observed in LWIR InAs/$Ga_{1-x}In_xSb$ T2SL absorber layers at 77 K.[3, 99, 101] The temperature dependence of the lifetime can be attributed to a combination of both SRH and radiative recombination. At temperatures below 77 K, the PL lifetime increases with increasing temperature, indicating that the lifetime is dominated by radiative recombination and that the radiative lifetime is shorter than the non-radiative (SRH) lifetime. At temperatures above 77 K, the PL lifetime decreases with increasing temperature, signifying that the PL lifetime is dominated by SRH recombination and the radiative lifetime is longer than the SRH lifetime. Around 77 K, both radiative and SRH recombination contribute significantly to the lifetime.

The improved lifetime observed in this InAs/$InAs_{0.72}Sb_{0.28}$ T2SL sample offers evidence that the constituent InAs and InAsSb layers have excellent crystalline properties and the sample possesses a low density of non-radiative recombination centers at the interfaces and in the layers. It is important to note that this sample gives a strong PL signal and has excellent structural properties with an x-ray diffraction zero-order satellite peak FWHM of 40 arcsec, ruling out the possibility of a long carrier lifetime due to strong localization of photogenerated carriers by interface roughness or layer thickness fluctuations. The InAs/$InAs_{0.72}Sb_{0.28}$ T2SL has a longer lifetime than even bulk InAs at 77 K due to the decreased radiative transition probability compared to that of a direct bandgap bulk material resulting from a decrease in the wave function overlap in the type-II structure. These results also shine some light on the origin of the relatively short carrier lifetime (~30 ns) in LWIR InAs/$Ga_{1-x}In_xSb$ T2SLs, which could be due to the non-radiative recombination centers associated with Ga atoms. Furthermore, the "stabilized Fermi level" due to intrinsic point defects in bulk GaSb and GaAs are near the valence band edge or the midgap, respectively,[4] leaving mid-gap trap states available for SRH recombination. In comparison, in bulk InAs, the stabilized Fermi level is above the conduction band edge,[4] rendering any mid-gap defect states inactive for SRH processes, as demonstrated by relatively high photoluminescence efficiencies in As-rich InAs/InAsSb T2SLs.[109]

We observe an order-of-magnitude longer minority carrier lifetime (> 412 ns at 77 K) in the LWIR InAs/$InAs_{0.72}Sb_{0.28}$ T2SL sample studied compared to that observed in LWIR InAs/$Ga_{1-x}In_xSb$ T2SLs. In addition, the observed carrier lifetime in InAs/$InAs_{0.72}Sb_{0.28}$ is longer across all temperatures than that previously reported in InAs/$Ga_{1-x}In_xSb$ T2SLs. Measurements on several other InAs/InAsSb T2SLs similar to the sample presented here also show substantially longer minority carrier lifetimes (100's of ns). We attribute the recombination mechanism to both SRH and radiative recombination, with comparable contributions from both near 77 K. This minority carrier lifetime improvement may now enable background limited T2SL LWIR *pn* photodetectors at higher operating temperatures. It should be noted that the InAs/$InAs_{0.72}Sb_{0.28}$ T2SL sample growth and material properties have not been optimized yet, suggesting that there is still room for improvement in the InAs/$InAs_{1-x}Sb_x$ T2SL minority carrier lifetime. Since the non-radiative recombination rate has now been significantly reduced, future studies can examine the tradeoff between radiative and non-radiative recombination, and sample

designs can be optimized to balance lowering the wave function overlap to decrease the radiative recombination rate with increasing the wave function overlap to increase the absorption coefficient.

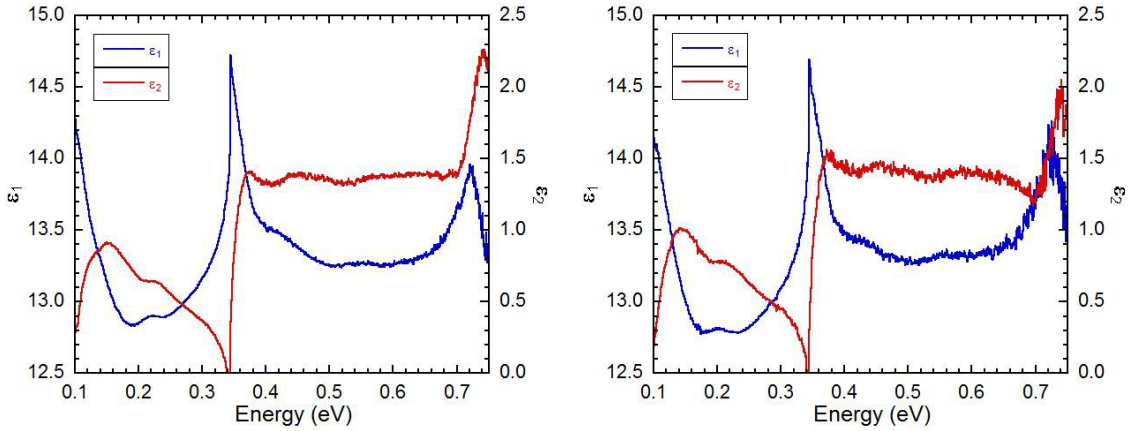

Figure 4.1 Dielectric constants obtained from modelling of ellipsometric data on (a) sample MBE 0218-1 (b) sample MBE 0218-2.

Ellipsometry measurements are performed utilizing a UV-visible ellipsometer with a range or an IR ellipsometer which, when used in conjunction, can measure from below 1 micron to above 40 microns. The modelling of ellipsometric data on for samples MBE 0218-1 and MBE 0218-2 are done as a three-layer system consisting of a GaSb substrate, a superlattice film, and a GaSb cap layer to obtain the complex dielectric function, $\varepsilon(E) = \varepsilon_1(E) + i\,\varepsilon_2(E)$, of the superlattice. The thicknesses of the substrate, superlattice layers and cap layer utilized in the ellipsometry modelling are the same as the thicknesses determined from XRD measurements. The complex dielectric function is obtained both with a point-by-point non-parametric fitting as well as a complete spectrum fitting algorithm. In the point-by-point fitting, the values of the dielectric constant are adjusted to fit the ellipsometric angles on a wavelength by wavelength basis while the complete spectrum technique uses an iterative Marquardt-Levenberg fitting algorithm to work with all ellipsometric data simultaneously. The results of ellipsometric modelling of the dielectric function for samples MBE 0218-1 and MBE 0218-2 are shown in Figure 4.1(a) and (b) respectively. Comparison of the dielectric constants of the superlattice samples to bulk InAs shows additional absorption features below the bandgap of InAs as indicated by a nonzero value of ε_2 from 0.1 to 0.35 eV.

4.2. Optical Properties and Band Offsets of InAs/InAsSb SLs (Johnson, Zhang, ASU)

Precise estimates of the conduction and valence band edge positions as a function of mole fraction for a given material typically rely on accurate knowledge of the materials bandgap bowing parameter. The bandgap bowing parameter of InAsSb varies considerably in the literature, so it is measured in this work using a 500 nm thick layer of lattice-matched $InAs_{0.911}Sb_{0.089}$ on GaSb. The bandgap of $InAs_{0.911}Sb_{0.089}$ is measured using photoluminescence spectroscopy at low temperature and spectroscopic ellipsometry at room temperature, and the bandgap bowing parameters that are inferred are used to deduce the conduction and valence band bowing parameters from photoluminescence and ellipsometry measurements of InAs/InAsSb superlattices.

Photoluminescence from the lattice-matched InAsSb sample is measured as a function of temperature (15 to 295 K) and pump power density (0.133 to 265 W·cm^{-2}). The bandgap energy is determined at each temperature using two methods, both of which are demonstrated using the 30 K photoluminescence spectra plotted in *Figure 4.2*. In the peak method, the bandgap energy (E_p) is identified as the photoluminescence peak energy minus kT/2 [110]. This method assumes an idealized parabolic band cutoff in the density of states of bulk material, ignoring the impact of localized states found near the continuum band edges in real material [111, 112]. In the photoluminescence first derivative method, the bandgap energy (E_g) is identified as the maximum of the first derivative of the photoluminescence spectra (shown in the *Figure 4.2* inset), which identifies the maximum change in the optical joint density of states and hence the energy at which the onset of optical transitions involving the continuum band edges occurs. Note that both methods identify the bandgap energy described by the perfectly sharp cutoff specified by the ideal parabolic band model.

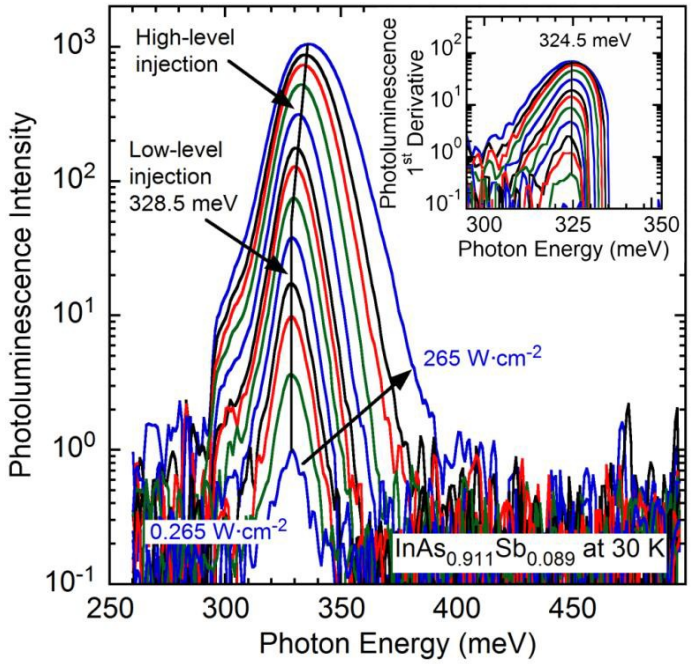

Figure 4.2 Photoluminescence spectra from lattice-matched InAs0.911Sb0.089 on GaSb at 30 K, measured using pump power densities ranging from 0.265 to 265 W·cm^{-2}. The photoluminescence peak position is independent pump power under low injection (0.265 to 2.65 W·cm^{-2}) and blue shifts under high injection (2.65 to 265 W·cm^{-2}). The position of the maximum of the first derivative spectra shown in the inset is independent of pump power for all injection levels.

Two injection level regimes are indicated in *Figure 4.2*; at high injection the photoluminescence peak blue shifts with increasing excitation density and at low injection the photoluminescence peak energy is independent of excitation density. When identifying the bandgap energy using the peak minus kT/2 method, the photoluminescence peak position is measured at low injection. For the 30 K measurements the bandgap energy (E_p = 327.2 meV) is given as the peak energy (328.5 meV) less kT/2 (1.3 meV). When identifying the bandgap energy using the first derivative maximum method, the analysis is insensitive to the injection level as it is associated with the underlying band structure instead of carrier occupation. For the 30 K measurements the bandgap energy (E_g = 324.5 meV) of the material is identified as the peak energy in the first derivative spectra of the photoluminescence. The significance of the first derivative maximum method is that it indicates the energy at which the product of the optical joint density of states and photon occupation number increases most rapidly. Since the optical joint density of states rapidly

increases at the onset of optical transitions involving the electron and hole continuum band edges (i.e. at the bandgap energy) and the occupation number decreases at a much lower rate, the first derivative peak position is at or very near the bandgap energy and is insensitive to excitation density as can be seen in the inset of *Figure 4.2*.

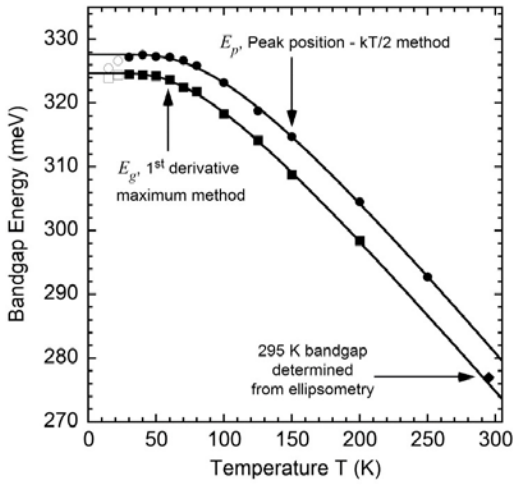

Figure 4.3 Bandgap energy of lattice-matched InAs0.911Sb0.089 on GaSb determined from the photoluminescence peak energy minus kT/2 (Ep, circles) and the first derivative maximum of the photoluminescence spectra (Eg, squares). An Einstein single oscillator model (solid line) is fit to the bandgap as a function of temperature. The absorption cutoff measured by spectroscopic ellipsometry at room temperature is also shown (diamond).

The $InAs_{0.911}Sb_{0.089}$ bandgap energies determined using the photoluminescence peak position minus kT/2 (E_p, shown by solid and open circles) and the first derivative maximum (E_g, shown by solid and open squares) are plotted as a function of temperature in *Figure 4.3*. Room temperature photoluminescence is observed, however the bandgap energy cannot be accurately identified as the photoluminescence peak occurs near 290 meV where there is a strong CO_2 absorption feature in the spectra. The Einstein single oscillator model [51] is fit to temperature dependence of the bandgaps identified using each method (E_p and E_g). The best fit 0 K bandgap energies, E_0, are 327.6 and 324.7 meV from which 0.903 and 0.939 eV low temperature bandgap bowing parameters are inferred. For both methods, the open circles and squares at 15 and 22 K are omitted from the fit as it is likely that the decrease in bandgap energy with decreasing temperature is only a result of a small degree of compositional inhomogeneity in the alloy.

The optical constants of the $InAs_{0.911}Sb_{0.089}$ layer are measured at room temperature over the 30 to 800 meV (40 to 1.55 μm wavelength) photon energy range using spectroscopic ellipsometry. The absorption coefficient of $InAs_{0.911}Sb_{0.089}$ presented in Figure 4.4 alongside its first derivative shows two distinct absorption features occurring at 225 and 277 meV. The 225 meV feature is the cutoff in the below bandgap absorption, which is the point at which absorption in the 500 nm thick layer is no longer observable. The 277 meV feature is onset of optical transitions involving the continuum band edges of the fundamental bandgap. The room temperature bandgap bowing parameter inferred from the bandgap absorption onset is 0.766 eV.

The advantage of the first derivative method is that it systematically identifies the bandgap energy for both emission and absorption measurements as it is sensitive to the underlying material band structure; note the agreement of photoluminescence and ellipsometry experiments shown in *Figure 4.3*. Therefore the InAs/InAsSb superlattice photoluminescence and ellipsometry results that follow are analyzed using the first derivative maximum method for determining ground state transition energies.

The InAsSb conduction and valence band edge positions are determined using a set of ten InAs/InAsSb superlattice samples. The room temperature ground state transition energies were determined from spectroscopic ellipsometry measurements previously published in reference[113]. The low temperature ground state transition energies are determined using photoluminescence measured at 12 K using a pump power density of 90 $W \cdot cm^{-2}$. The normalized photoluminescence spectra of samples A, B, E, and F are plotted in Figure 4.5 as a function of photon energy (lower horizontal axis) and photon wavelength (upper horizontal axis), which shows that the InAs/InAsSb superlattice miniband structure can emit and absorb photon wavelengths as long as 12 μm at low temperature. The peaks in the first derivative spectra of the photoluminescence are indicated in the figure with vertical dashed lines. The first derivative transition energy of sample D is not accurately distinguishable due to weak, noisy photoluminescence intensity.

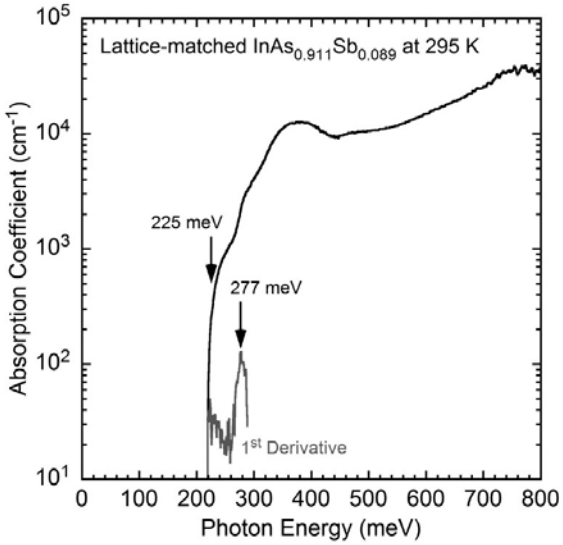

Figure 4.4 Absorption coefficient (black curve) of $InAs_{0.911}Sb_{0.089}$ and its first derivative (grey curve). Two absorption onsets are identified from two peaks in the first derivative, one at the onset of sample absorption (225 meV) and one at the bandgap energy (277 meV).

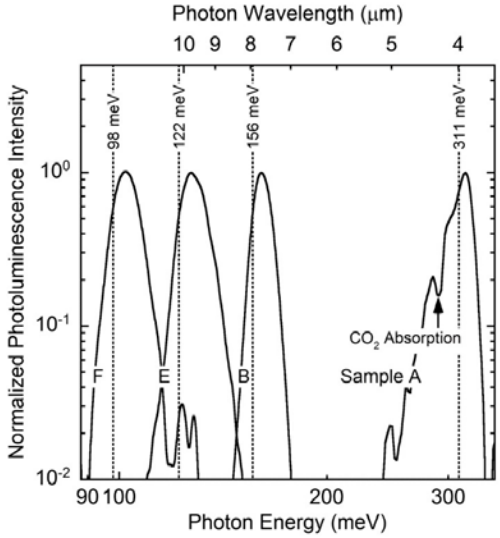

Figure 4.5 Normalized photoluminescence spectra of selected InAs/InAsSb superlattices (samples A, B, E, and F). The superlattice ground state transition energies indicated in the figure with vertical dashed lines are identified from the peaks in the first derivative spectra of the photoluminescence.

For the calculation of the superlattice miniband structure, the strained band offset between the $InAs_{1-x}Sb_x$ heavy hole valence band edge, $E_v(x)$, and the InAs heavy hole band edge, $E_v(0)$, is fit in a Kronig-Penney model[114, 115] to align each superlattice ground state transition to the transition energies determined at low and room temperature. The relative band offsets in the valence band, $\Delta E_v(x) = E_v(x) - E_v(0)$, determined at low and room temperature are plotted as a function of Sb mole fraction in Figure 4.6, where the unstrained data presented is determined by accounting for the effect of strain to the GaSb substrate [116]. The valence band edges of InAs and InSb, $E_v(0)$ and $E_v(1)$, are known [16, 116], and thus the valence band bowing parameter, b_v, is the only variable fit in the valence band bowing model in $\Delta E_v(x) = x\Delta E_v(1) - x(1 - x)b_v$.

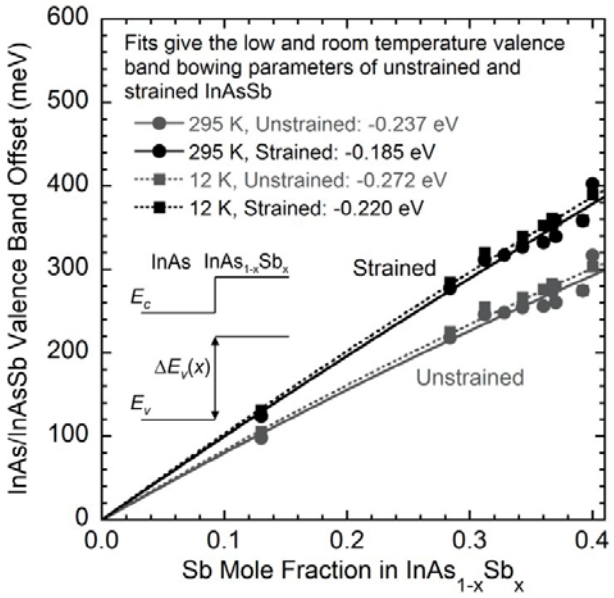

Figure 4.6 Heavy hole valence band offset of InAs1-xSbx relative to InAs, $\Delta E_v(x)$, plotted as a function of Sb mole fraction at 295 K (circles) and 12 K (squares). Solid and dotted lines represent bowing model fits to the unstrained (grey) and strained (black) band offset data.

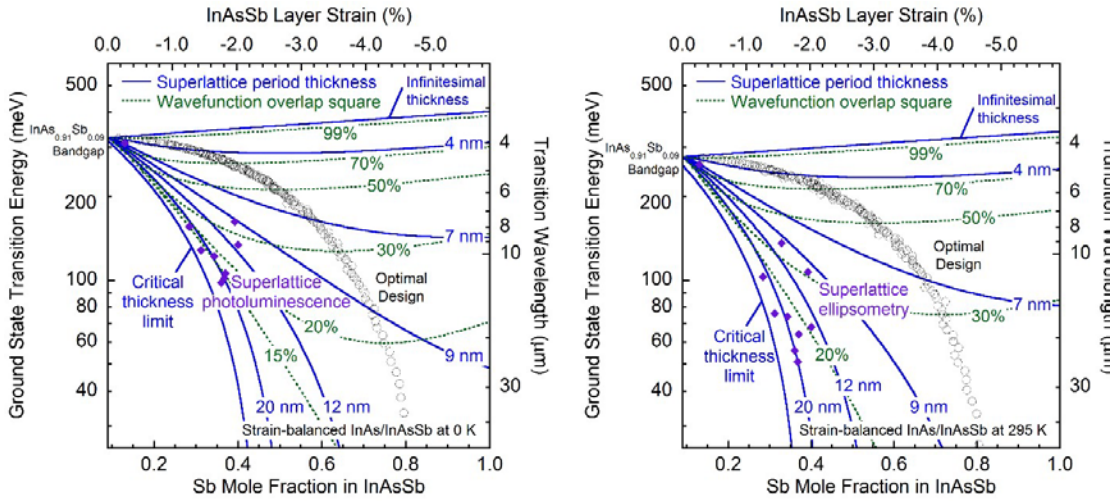

Figure 4.7 Ground state transition energy plotted as a function of the InAsSb layer mole fractions (layer strain upper horizontal axis) of the strain-balanced InAs/InAsSb type-II superlattices at 0 K (left) and 295 K (right). The solid lines are contours of constant superlattice period thickness that provide the ground state transition energy of the superlattice as a function of the alloy layer composition, and the largest period thickness that can be grown before the onset of relaxation of either of the individual InAs or InAsSb layers is labeled as the critical thickness limit. The dotted lines are contours of constant electron-hole wavefunction overlap squared expressed as a percentage. The minima in the wavefunction overlap contours provide the design with the optimal transition strength for a given transition energy shown by the open circles.

The valence band bowing parameters, b_v, are determined in Figure 4.6, as well as the corresponding bandgap bowing parameters, b_g, and conduction band bowing parameters, $b_c = b_v + b_g$. The 0.766 eV room temperature bandgap bowing parameter of InAsSb increases to 0.799 eV when the material is coherently strained on GaSb. The ellipsometry and photoluminescence measurements examine the strained band alignment of the InAs/InAsSb superlattice, and the bowing model fit to the room temperature band offset data results in the determination of the strained InAsSb valence band bowing parameter of -0.185 eV (solid black line). The effect of strain is removed from the data [116] to obtain the unstrained InAsSb valence band bowing parameter of -0.237 eV (solid gray line). Similar results are obtained at 12 K (dotted black and gray lines); the 0.939 eV low temperature bandgap bowing parameter of InAsSb increases to 0.972 eV when the material is coherently strained on GaSb, and valence band bowing parameters of -0.220 and -0.272 eV are ascertained for strained and unstrained material respectively.

These measurements of the InAsSb conduction and valence band edge positions are used in the Kronig-Penney model of the superlattice miniband structure to map the ground state transition energies and corresponding wavefunction overlaps of all conceivable strain-balanced InAs/InAsSb superlattice designs. The low and room temperature design spaces of the strain- balanced InAs/InAsSb superlattice are shown in the left- and right-side plots in Figure 4.7. For each plot, the ground state transition energy is plotted on the left-hand vertical axis (wavelength on the right-hand vertical axis), InAsSb layer composition is plotted on the lower horizontal axis (layer strain on the upper horizontal axis), and contours of constant period thickness are provided (solid lines). The designs of the ten InAs/InAsSb superlattice samples presented are shown with purple diamonds. The optimal design in terms of maximizing absorption strength of the superlattice will be the one which provides maximum wavefunction overlap [113]; by overlaying contours of constant wavefunction overlap square onto the figure (dotted lines), optimal superlattice designs are readily identified as a function of ground state transition energy appearing as minima in the wavefunction overlap square contours (circles).

As it would be highly desirable to compare the optimal design parameters of the strain-balanced InAs/InAsSb superlattice to those of other infrared superlattice systems, the design software is further utilized to determine the optimal designs of lattice-matched GaSb/InAsSb and strain-balanced InAs/GaInSb superlattices. Figure 16 shows the wavefunction overlap square as a function of ground state transition energy of optimally designed InAs/InAsSb (green lines), InAs/GaInSb (blue lines), and GaSb/InAsSb (red lines) superlattices. However, another important aspect of the design is the practicality of

strained layer growth as photoluminescence efficiency (optical quality) begins to degrade when the material is strained in excess of ±2% even if the layer is pseudomorphic. Therefore also plotted in Figure 16 are a set of practical optimal designs for the InAs/InAsSb and InAs/GaInSb superlattices which enforce the added constraint that the GaInSb layer strain is limited to -2.0% corresponding to an In mole fraction limit of 0.324 (blue dotted line), and that the InAsSb layer strain is limited to -2.0, -2.5, and -3.0% corresponding to Sb mole fraction limits of 0.385 (green dotted line), 0.460 (green dash-dot line), 0.537 (green dash-dash- dot line) respectively. No practical optimal design line is present for the lattice-matched GaSb/InAsSb superlattice as the structure is entirely unstrained.

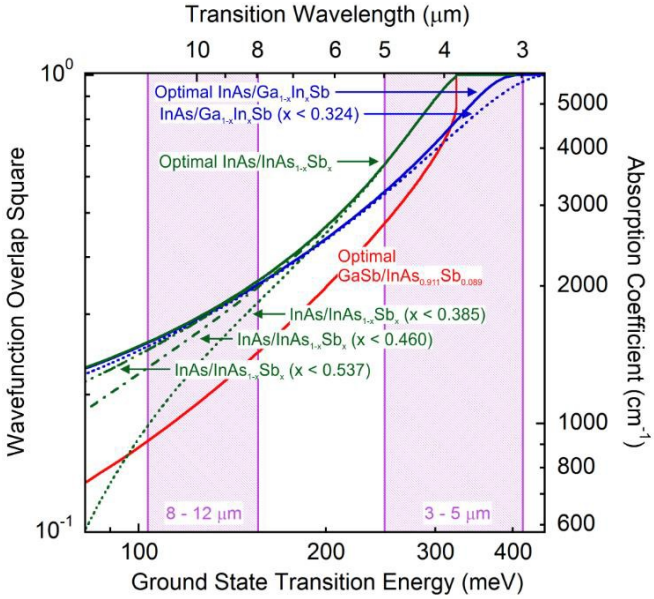

Figure 4.8 Optimal wavefunction overlap square plotted as a function of ground state transition energy for lattice- matched GaSb/InAsSb (red) and strain-balanced InAs/InAsSb (green) and InAs/GaInSb (blue) superlattice systems at 0 K. Solid lines represent the true optimal designs whereas dotted, dash-dot, and dash-dash-dot lines represent the practical optimal designs in which the In mole fraction in the GaInSb layers is limited to 0.324 and the Sb mole fraction in the InAsSb layers is limited to 0.385, 0.460, and 0.537. The absorption coefficient of the InAs/InAsSb superlattice is presented on the right-hand vertical axis.

The practical optimal designs for InAs/InAsSb follow the true optimal design throughout the 3-5 μm wavelength range and then begin to deviate once the optimal Sb mole fraction reaches the corresponding strain limited values. The InAs/InAsSb superlattice can be grown along the true optimal design curve over the full 3-5 μm wavelength window and outperforms both InAs/GaInSb and GaSb/InAsSb in this range. At longer wavelengths the wavefunction overlap of the optimal InAs/GaInSb and InAs/InAsSb superlattices are almost identical, though larger InAsSb layer strains are necessary for the InAs/InAsSb superlattice to maintain this level of wavefunction overlap. The practical optimal design criteria for the InAs/InAsSb superlattice are outlined.

4.3. Optical Properties of Type-II InAs/InAsSb superlattices (Johnson, Zhang, ASU)

The transition energies and design parameters of the strain-balanced InAs/InAsSb superlattice system are presented in Figure 4.7a (0 K) and 17b (295 K), which plot the ground state transition energy of the superlattice as a function of the InAsSb layer composition for 0 (infinitesimal), 4, 7, 9, 12, and 20 nm period thicknesses (solid blue curves). Also shown with a solid blue curve is a critical thickness limit [117], which provides a suggested maximum period thickness that can be utilized before the individual InAs or InAsSb layers themselves could begin to relax. Wavefunction overlap square contours are represented with dotted green curves which show that a digital alloy regime is formed between the bandgap energies of tensilely strained InAs on GaSb and lattice-matched InAsSb, within which the optimal design follows the infinitesimal (0 nm) period thickness design contour. Additionally, an extended wavelength regime is formed below the bandgap energy of lattice-matched InAsSb within which the optimal design follows the minima of the wavefunction overlap square contours (open circles).

The low and room temperature optimal designs in Figure 4.7 are compared so as to determine whether or not it is necessary to calculate the optimal design parameters as a function of temperature. In Figure 4.9, wavefunction overlap square is plotted as a function of ground state transition energy in the extended wavelength regime of the optimal InAs/InAsSb superlattice. The solid blue curve represents the low temperature optimal design from Figure 4.7a and the solid red curve represents the room temperature optimal design from Figure 4.7b. Next, the transition energies and wavefunction overlap square of the low temperature optimal design are calculated at an operating temperature 295 K, resulting in the dashed blue curve which closely follows the room temperature optimal design (red curve) with virtually no loss in wavefunction overlap.

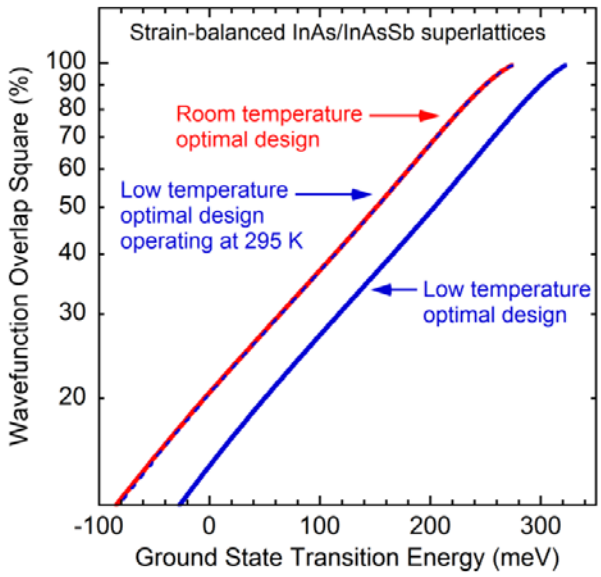

Figure 4.9 Wavefunction overlap square plotted as a function of the ground state transition energy of the strain-balanced InAs/InAsSb superlattice. Solid curves represent designs optimized at low temperature (blue) and at room temperature (red). The dashed blue curve represents the low temperature optimal design operating at 295 K.

These results indicate that the optimized InAs/InAsSb superlattice design parameters are not a strong function of temperature. This characteristic of the superlattice can be

understood by considering how temperature modifies the bulk band structure of the superlattice constituents. When the temperature is changed, the conduction bands of the two superlattice constituents generally shift in the same direction and often by roughly the same amount. As a result, the repeating potential in the conduction band is virtually unchanged; the electron minibands shift with the bulk band structure while the wavefunctions are essentially unaltered. The same is true of the hole minibands formed in the valence band, and thus what is ultimately observed is that the ground state transition energy primarily shifts with the bulk band structure while wavefunction overlap is unchanged. Therefore, it is only necessary to calculate the design space map of a superlattice at a single temperature in order to determine the optimal layer thicknesses and mole fractions as a function of wavefunction overlap. The ground state transition energy of the optimal design is the only parameter that is a strong function of temperature. The optimal design parameters of the InAs/InAsSb superlattice are given at key transition wavelengths in Table 4.1. In instances where the optimal design calls for very thick or thin layers or InAsSb strain in excess of -2%, practical design parameters which abide by practical growth constraints are also provided.

The optimal design criteria in Table 4.1 are utilized in the design and growth of one optimized mid-wave infrared strain-balanced InAs/InAsSb superlattice. The sample is composed of alternating InAs (2.16 nm) and $InAs_{0.802}Sb_{0.198}$ (1.51 nm) layers with a total thickness of 1 μm sandwiched between 10 nm thick AlSb confinement layers with a 10 nm thick GaSb cap. The sample is grown at 425 °C on a (100)-oriented GaSb substrate by molecular beam epitaxy using a 0.5 monolayer per second InAs growth rate and a constant 1.20 As/In flux ratio. The structural properties of the superlattice are measured using X-ray diffraction. The unintentional Sb in the InAs layers of the superlattice was not quantifiable due to the short period thickness of this sample, therefore an unintentional Sb mole fraction of 0.024 is assumed based on the unintentional Sb measured in other InAs/InAsSb superlattices grown under the similar conditions. The sample cross section is shown in the inset of Figure 19.

Table 4.1 Table 1. Optimal and practical design parameters for strain-balanced InAs/InAsSb, superlattices. Electron-hole wavefunction overlap square, absorption coefficient α_{SL}, and the superlattice constituent layer thicknesses and mole fractions are provided for several key detector wavelengths at low temperature (0 K) and at room temperature (295 K). When the optimal design calls for thicknesses less than 0.500 nm or strain exceeding -2%, an alternate set of practical design parameters are also provided which limit the minimum layer thickness to 0.500 nm and the maximum strain to -2%.

Transition wavelength (μm)		Optimal or practical	Wavefunction overlap square $\left\|\Psi_h^*\Psi_e\right\|^2$ (%)	Absorption coefficient α_{SL} (cm^{-1})	InAs thickness (nm)	InAsSb thickness (nm)	Sb mole fraction
at 0 K	at 295 K						
4.0	4.8	Optimal	94.6	4721	1.884	1.396	0.211
5.0	6.3	Optimal	66.3	3308	3.749	1.121	0.395
5.0	6.3	Practical	66.3	3308	3.748	1.162	0.384

8.0	12.3	Optimal	37.5	1871	5.780	1.160	0.550
8.0	12.1	Practical	34.8	1737	6.694	2.076	0.384
10.0	18.0	Optimal	31.3	1562	6.484	1.196	0.592
10.0	17.5	Practical	26.6	1327	8.465	2.625	0.384
12.0	26.2	Optimal	27.7	1382	6.970	1.220	0.620
12.0	25.1	Practical	21.2	1058	10.168	3.152	0.384
15.0	47.3	Optimal	24.5	1223	7.472	1.248	0.646
15.0	44.8	Practical	15.5	774	12.595	3.905	0.384

The superlattice design software is used to calculate the ground state transition energy of the superlattice at 305.9 meV (4.1 μm wavelength) at low temperature and 258.1 meV (4.8 μm wavelength) at room temperature, and the square of the electron-hole wavefunction overlap at the ground state is 94.3%. Spectroscopic ellipsometry is used to measure the room temperature absorption coefficient of the superlattice shown in Figure 4.10. The ground state transition energy (effective bandgap) of the superlattice is identified at the absorption coefficient first derivative maximum at 257 meV (within 0.5% of the calculated value of 258.1 meV), at which point the absorption coefficient increases rapidly to α_{SL} = 4750 cm^{-1}.

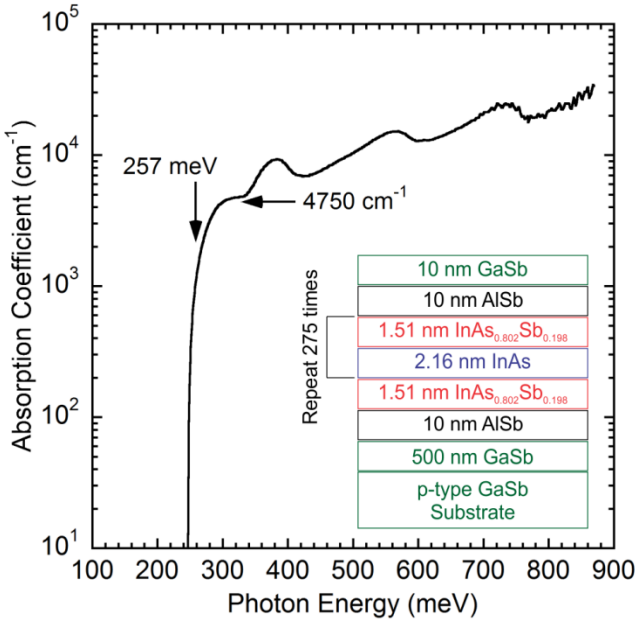

Figure 4.10 Absorption coefficient of strain-balanced InAs/InAsSb superlattice optimized for maximum absorption at ground state transition energy of 257 meV (4.8 μm wavelength). Inset shows ample cross section.

Figure 4.11 shows the absorption coefficient of strain-balanced InAs/InAsSb superlattices as a function of the wavefunction overlap squared. The data represented by open black circles and the power law fit given by the solid line is the same data in Ref. [118]. The solid blue circle shows the absorption coefficient of the optimized practical design in

Figure 19 at 94.3% wavefunction overlap square which agrees with the fitted line to within 1%.

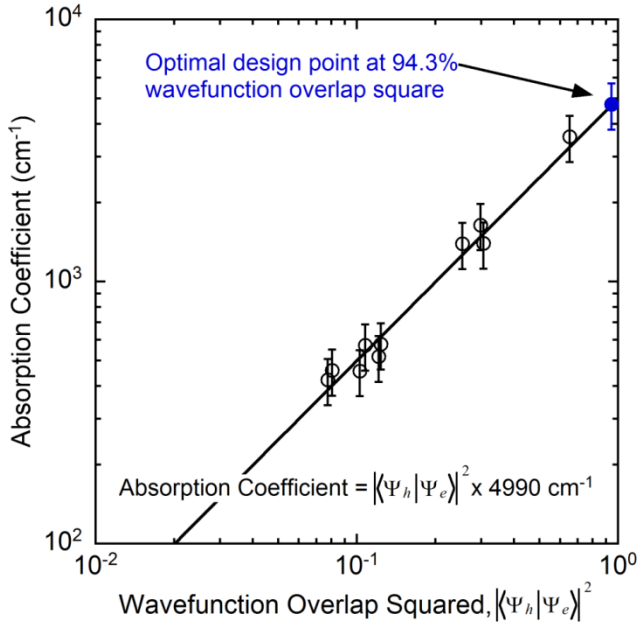

Figure 4.11 Ground state absorption coefficient as a function of the square of the electron-hole wavefunction overlap integral in strain-balanced InAs/InAsSb superlattices. The solid line shows the unity power law fit to the data from Ref. 58 (open black circles). The solid blue circle shows the optimized 4.8 μm wavelength optimized design with 94.3% wavefunction overlap square.

A Nicolet Instrument Corporation Magna-IR 760 Fourier transform infrared spectrometer is used to measure room temperature photoluminescence from the 1.0 μm thick optimal superlattice grown at 425 °C as well as a 0.5 μm thick bulk lattice-matched $InAs_{0.911}Sb_{0.089}$ sample grown at 430 °C[113]. The samples are excited using an 808 nm pump laser and 200 mW of laser power. The pump power density reaching the active region of each sample is 265 W·cm^{-2} which corresponds to an excitation density of 1×10^{25} cm^{-3}·s^{-1} in the superlattice and 2×10^{25} cm^{-3}·s^{-1} in the bulk $InAs_{0.911}Sb_{0.089}$ sample. The raw photoluminescence from the superlattice (dotted blue curve) and the bulk $InAs_{0.911}Sb_{0.089}$ layer (dotted green curve) are plotted as a function of photon energy (lower horizontal axis) and photon wavelength (upper horizontal axis) in Figure 4.12. The raw photoluminescence spectra exhibit an absorption feature near 290 meV due to the presence of CO_2 in the air which is removed in the solid blue and green curves by correcting the spectra for the optical throughput of the system.

The photoluminescence first derivative maximum is used to identify the room temperature bandgap energy of the bulk $InAs_{0.911}Sb_{0.089}$ sample at 275 meV, which closely agrees with the room temperature bandgap energy of 277 meV measured using spectroscopic ellipsometry[113]. Using the same analysis on the superlattice, the photoluminescence first derivative maximum identifies an effective bandgap of 249 meV, which likewise agrees with the 257 meV bandgap measured using spectroscopic ellipsometry in Figure 4.10. By integrating the photoluminescence spectra as a function of photon energy, a relative measure of the total optical output and general optical quality is obtained. The total integrated intensity of 1664 from the optimized superlattice is more than a factor of three greater than the integrated intensity of 507 from the bulk $InAs_{0.911}Sb_{0.089}$ sample which emits at a shorter wavelength. The superior optical quality of the superlattice is attributed to the high wavefunction overlap of the optimized design and the long minority carrier lifetimes inherent to this material system[9].

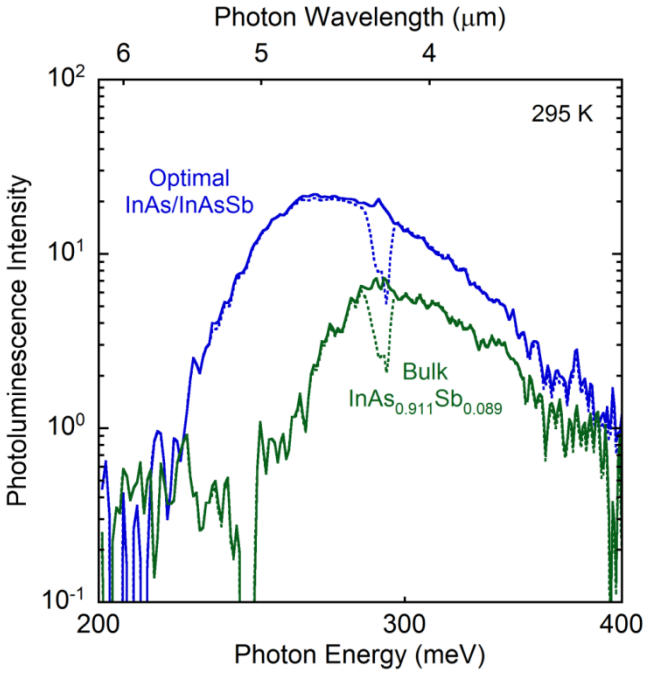

Figure 4.12 Room temperature photoluminescence from bulk lattice-matched $InAs_{0.911}Sb_{0.089}$ (green curves) and an InAs/InAsSb superlattice designed to provide optimal wavefunction overlap square at 4.8 μm wavelength (blue curves). Dotted curves show the raw photoluminescence spectra while solid curves show the spectra after correcting for the optical throughput of the system.

4.4. MOCVD-grown InAs-GaSb and InAs-InAsSb T2SL structures and devices (Dupuis, GT)

Previously in the earlier years of this program, the GT team developed growth conditions and strain management schemes that can minimize the strain accumulation in the epitaxial structures of InAs-GaSb and InAs-InAsSb type-II superlattices (T2SLs) on GaSb substrates grown by metalorganic chemical vapor deposition (MOCVD). Also, strain management approaches for T2SLs grown on InAs substrates were also studied and

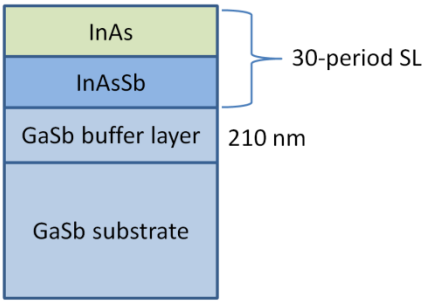

Figure 4.13: General structure of all the InAs/ InAsSb T2SL samples grown.

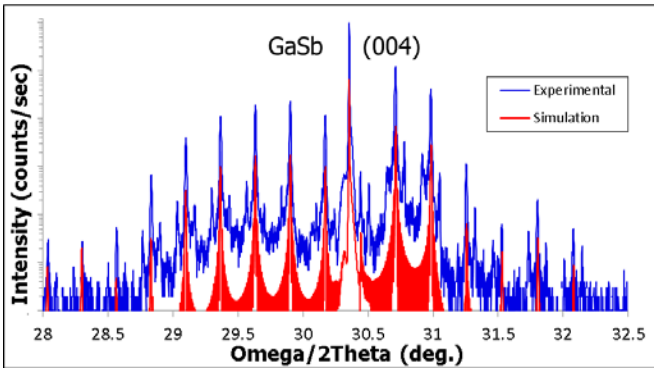

Figure 4.14: (004) XRD scan of 30-period InAs-InAsSb SL sample 3-2287 (blue) and simulation of the intended structure (red).

developed. *We then demonstrated the first MOCVD-grown InAs-GaSb and InAs-InAsSb T2SL structures and devices.*

The InAs-InAsSb T2SLs were grown at 100 Torr with a wafer rotation of 100 rpm. The carrier gas used is H_2 with the group III precursors being trimethylindium (TMIn) and triethylgallium (TEGa) and the group V precursors being trimethylantimony (TMSb) and arsine (AsH_3). A typical SL test structure is shown in Figure 4.13 with a 210 nm GaSb buffer layer on a GaSb (100) ± 0.04° substrate. Layer compositions and thicknesses were verified with (004) (Figure 4.17) and (113) X-ray diffraction (XRD) scans and the corresponding simulation. Additionally, atomic force microscopy (AFM) images were taken to measure surface roughness. Finally, transmission electron microscopy (TEM) images were taken to analyze the interfaces between layers.

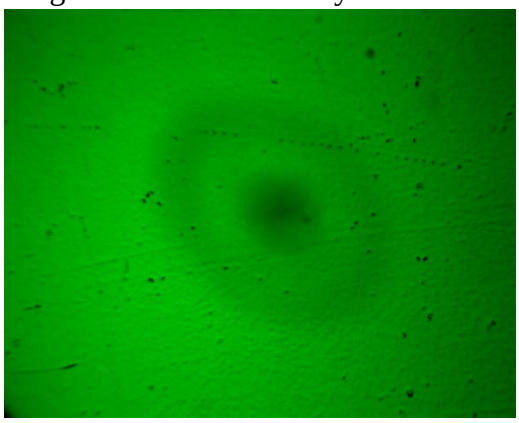

Figure 4.15 Optical microsopce image of 33% AlGaSb on GaSb wafer 3-2355.

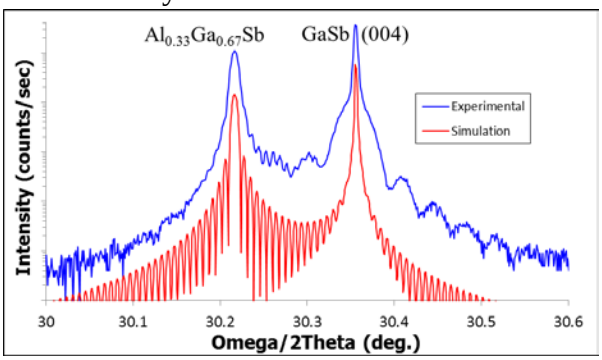

Figure 4.16 (004) XRD scan of 33% AlGaSb on GaSb wafer 3-2355 (blue) and simulation of the intended structure (red).

Figure 4.17: Bright Field TEM of cross-section of 33% AlGaSb with GaSb cap for wafer 3-2355.

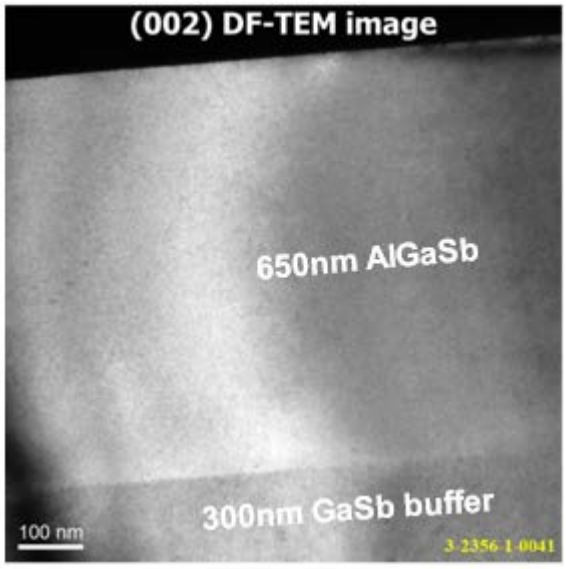

Figure 4.18: Dark Field TEM of cross-section of 36% AlGaSb without GaSb cap for wafer 3-2356.

As reported in Y4 activity, due to unstable growth process window of AlSb in MOCVD, we took an approach of growing AlGaSb and gradually increasing Al contents until the layer quality severely degraded. The maximum Al composition reached was about 38% per sample 3-2326. As shown in Figure 4.15, there were number of pits developed on this AlGaSb layer. A number of pits increased with Al composition. For instance, (004) XRD pattern as shown in Figure 4.16, verified the Al composition of AlGaSb layer was 33% with layer thickness of 640nm for sample 3-2355. The secondary Pendellösung fringes were pointing to a thin layer with thickness equivalent to that of GaSb buffer and, hence, suggested possibility of contamination of this buffer layer. For further analysis, SIMS measurement was performed for wafer 3-2319 having similar epi structure with that of 3-2355. From the SIMS data, it indicated high quantity of As and Al at the interface between GaSb buffer and GaSb wafer, while high concentration of C was observed within AlGaSb layer. So for any future run, it is important to recondition the MOCVD growth chamber to avoid these contaminations which are believed to initiate the crystallographic defects seen in Figure 4.15. Dr. Zuo at UIUC had performed transmission electron microscopy (TEM) analysis of two AlGaSb samples, i.e., 3-2355 and 3-2356 as shown in Figure 4.17 and Figure 4.18. Though the macroscopic defects observed via optical Nomarski microscope were not detected, there was no extended defect generated neither at the interface of AlGaSb and the rest of the layer nor in any epitaxially grown layers within the observation region. This implied that this AlGaSb could be employed as both top and bottom window layers sandwiching the T2SL.

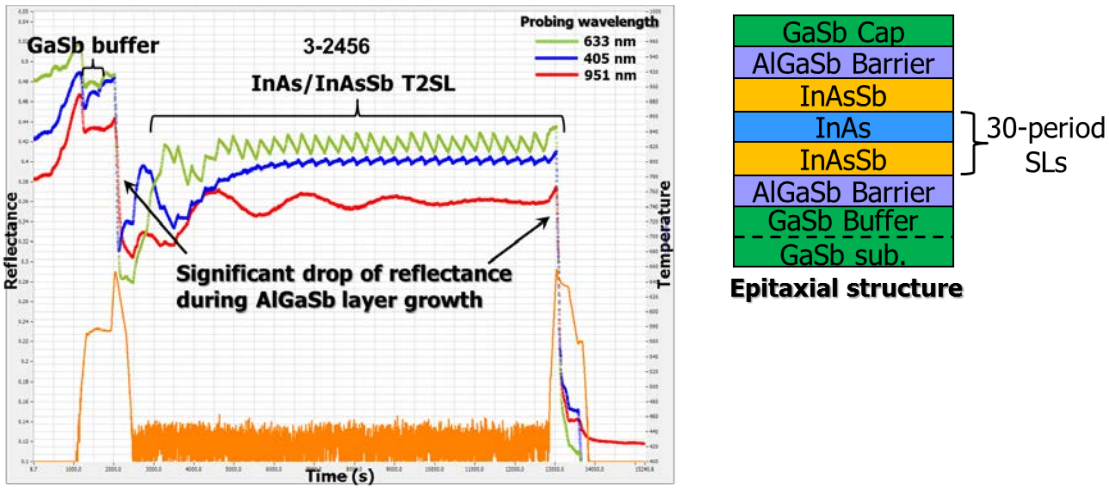

Figure 4.19 Reflectance (green, blue and red curves) and temperature profile (orange) of MOCVD grown InAs/InAsSb T2SL with 10 nm AlGaSb windows on GaSb wafer 3-2456 (left) including schematic drawing of target structure (right)

Number of runs were carried out to grow the T2SL structure with AlGaSb windows; however, all samples turned hazy with degraded surface morphology regardless of several optimization tries aiming to improve the surface morphology including varying growth parameters such as source supply rate, V/III, temperature, and pressure. We had decided to installed EpiTT monitoring system to help justifying surface morphology evolution, and sample surface temperature control. From the reflectance signal, we observed the poor surface degradation during the high temperature ramping in preparation for growing AlGaSb bottom layer and later introduced optimum supply of TMSb to prevent such

surface degradation. An example of EpiTT signal for the full MOCVD process for the attempt structure is shown in Figure 4.19. Due to narrow bandgap of grown materials, all 3 probing lights were strongly absorbed by the material and there was no optical interference to be observed except for that of 951nm which was visible up to total epitaxial layer thickness of approximately 600nm. Saw-teeth like scan during T2SL growth reflected the change of refractive index between InAs and InAsSb layers. There was a drop of reflectance during both AlGaSb windows due to surface degradation. The reflectance was recovered within the first 10 pairs of SL after the AlGaSb bottom window; however, it was not the case after the top window layer was grown. Compromised surface morphology and (004) XRD scan were observed for this sample. TEM analysis shown in *Figure 4.20*, indicated complete SL structure with number of treading dislocations and stacking faults. There were also number of voids formed in the GaSb layer. Since full SL structure was visible above the voids, it suggested that these voids were formed after SL growth and likely to be caused by thermal degradation during the top AlGaSb growth. However, the details of its mechanism are still unknown and required further investigation.

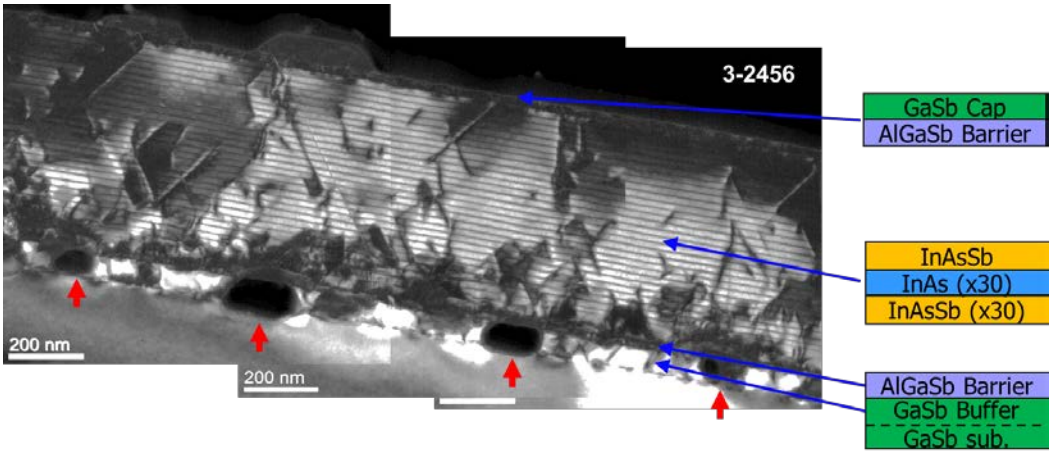

Figure 4.20 TEM of cross-section of InAs/InAsSb T2SL with 10 nm AlGaSb windows on GaSb wafer 3-2456. Red arrows indicate voids in the GaSb buffer layer.

In addition, we had investigated defect formation at the interface of GaSb buffer and GaSb wafer. As mentioned above, the contamination of As (~1%), and Al (~10%) including O (mid 1E18cm^{-3}) was the major concern for any T2SL of interest. We implemented EpiTT as well as reconditioning chamber step to minimize such contamination issue. As shown in the upper row of Figure 4.21, there was a slight decrease in reflectance with high density surface bumps and XRD fringes for a GaSb buffer grown during a typical MOCVD operation without proper cleaning and conditioning. In this case the shoulder peak on the higher angle side and fringes shown in (004) XRD confirmed the contamination of As in the GaSb buffer. When we introduced chamber cleaning and GaSb coating, the surface morphology degraded significantly as shown in the middle row of this figure. However, after optimizing the V/III ratio, i.e., increasing from 1.19 to 1.4, the reflectance stayed constant over the course of the GaSb buffer growth while surface defect was removed as well as the XRD fringes. We are planning to adopt this procedure for the next T2SL growth.

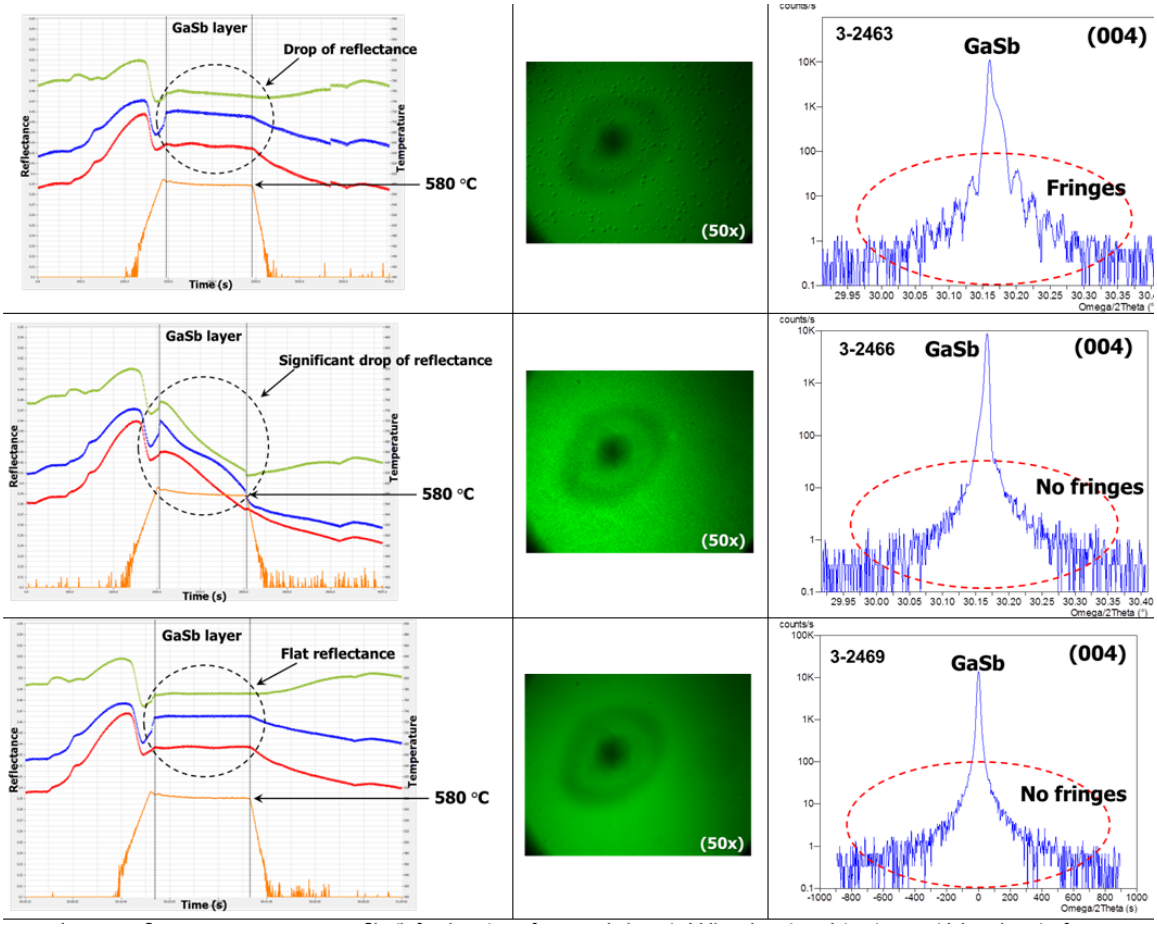

Figure 4.21 Reflectance & temperature profile (left column), surface morphology (middle column), and (004) XRD (right column) of GaSb buffer on GaSb wafer for before optimization (upper row), after platter cleaning & Sb coating (middle row), after V/III ratio optimization (lower row).

4.5. Structure of MOCVD-grown InAs/InAsSb T2SLs (Zuo, UIUC)

One part of this MURI project focused on MOCVD grown InAs/GaSb and InAs/InAsSb T2SL structures and devices. While MBE has been used as the major growth technology for T2SLs, it is of great benefit if these structures can be produced by MOCVD, which could enable lower-cost and higher-yield production of IR photodetectors. However, growth of the III-Sb-based materials, alloys, and T2SL structures by MOCVD is more challenging than by MBE[119, 120]. Therefore, there have been very few reports on the growth and characterization of InAs/GaSb and InAs/InAsSb T2SLs[121, 122]. The GT team has investigated the MOCVD growth and strain balancing of InAs/GaSb and InAs/InAsSb T2SLs on GaSb and InAs substrates, and demonstrated the first MOCVD-grown InAs-GaSb and InAs-InAsSb T2SL devices (Section 4.4). Here we report on the structure of MOCVD grown InAs/InAsSb T2SLs as determined by TEM and STEM.

Three samples were received from GT, samples 3-2497, 3-2498 and 3-2499. These samples were grown under the same growth conditions with different structures as

illustrated in Figure 4.22. For TEM imaging, cross-section samples were prepared by focused ion beam (FIB) milling, finishing the milling using low currents to minimize the ion-induced structural damage.

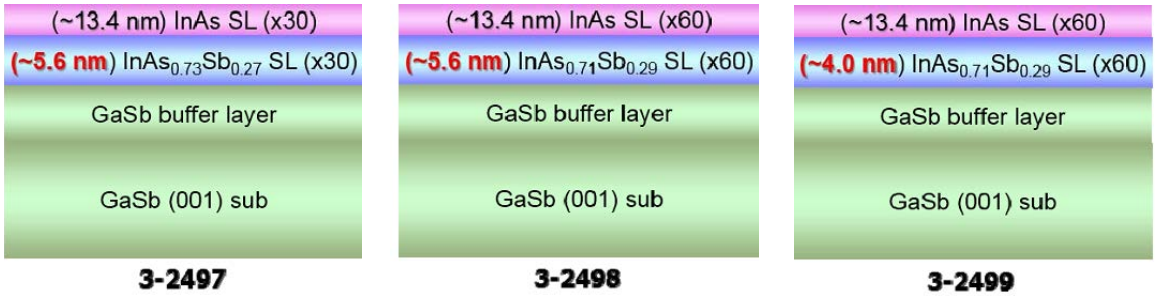

Figure 4.22 MOCVD grown InAs/InAsSb T2SLs for three samples received from GT.

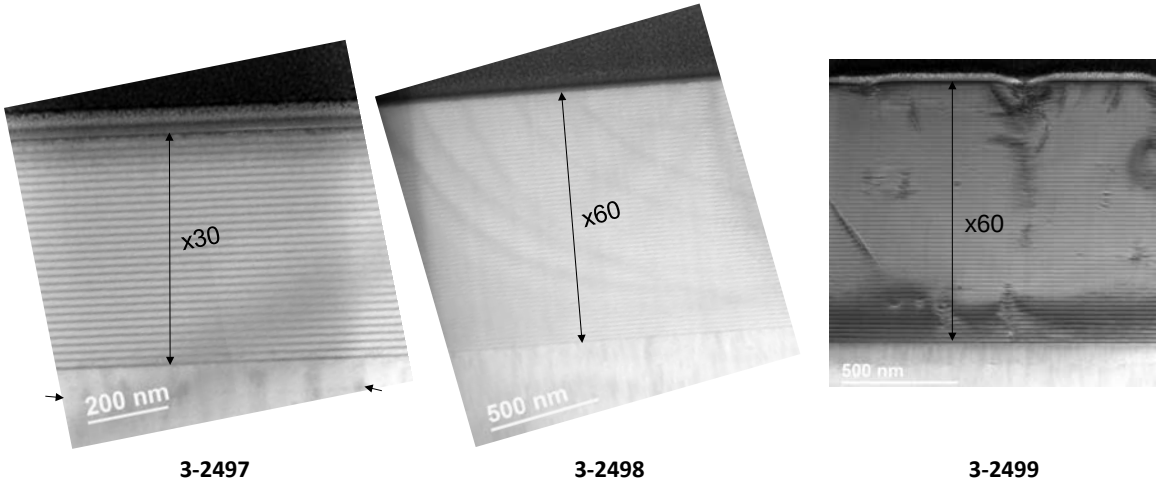

Figure 4.23 Bright-field images of three MOCVD grown InAs/InAsSb T2SLs. Samples 3-2497 and 3-2498 are largely free of defects. The curved lines in 3-2498 are bent contours due to bending of the prepared thin cross-sectional sample.

Figure 4.23 shows the bright-field images recorded under the systematic (002) diffraction condition for the three MOCVD samples. All three images show the periodic structure of the superlattice. While samples 3-2497 and 3-2498 are largely free of defects, large defects are observed throughout the thin-film, near the film-substrate interface as well as at the top of thin-film.

The formation of defects in sample 3-2499 is correlated with the roughness at the InAs/InAsSb film and GaSb buffer layer interface. Figure 4.24 examines the interface for three MOCVD samples. Compared to samples 3-2497 and 3-2498, the HREM image of sample 3-2499 indicates a rough interface, which is correlated with the roughness at the buffer layer and GaSb substrate interface. Thus, the preparation and quality of GaSb substrate is the determining factor here.

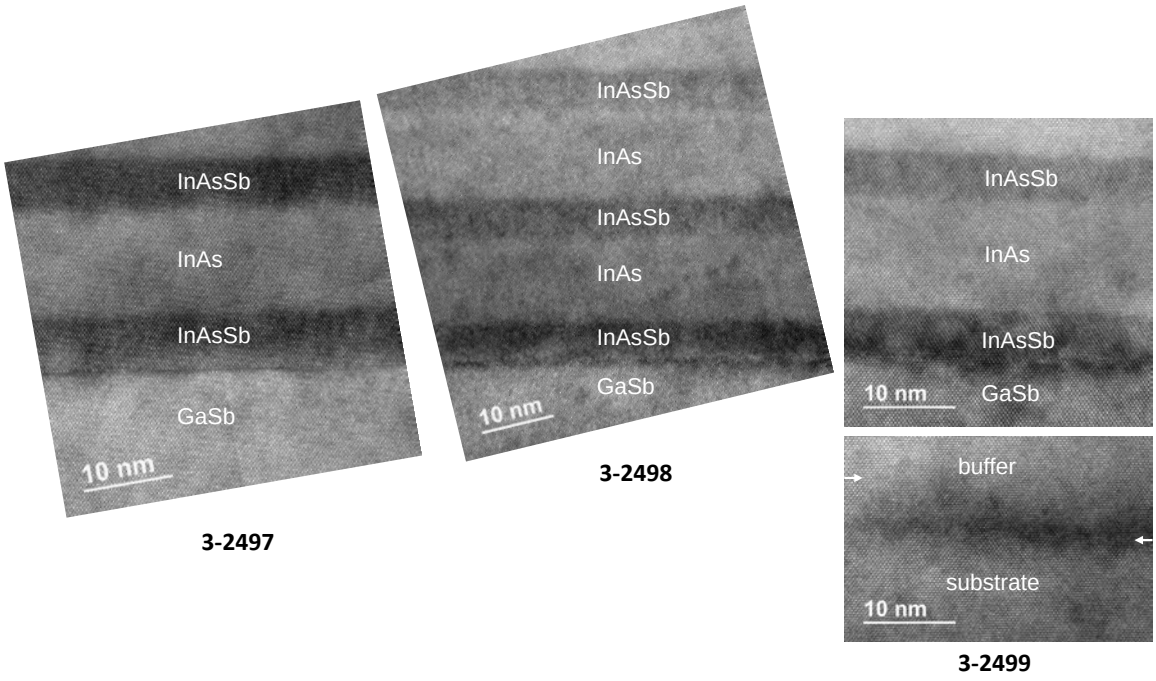

Figure 4.24 High resolution electron microscopy images of InAs/InAsSb film, buffer and substrate interface.

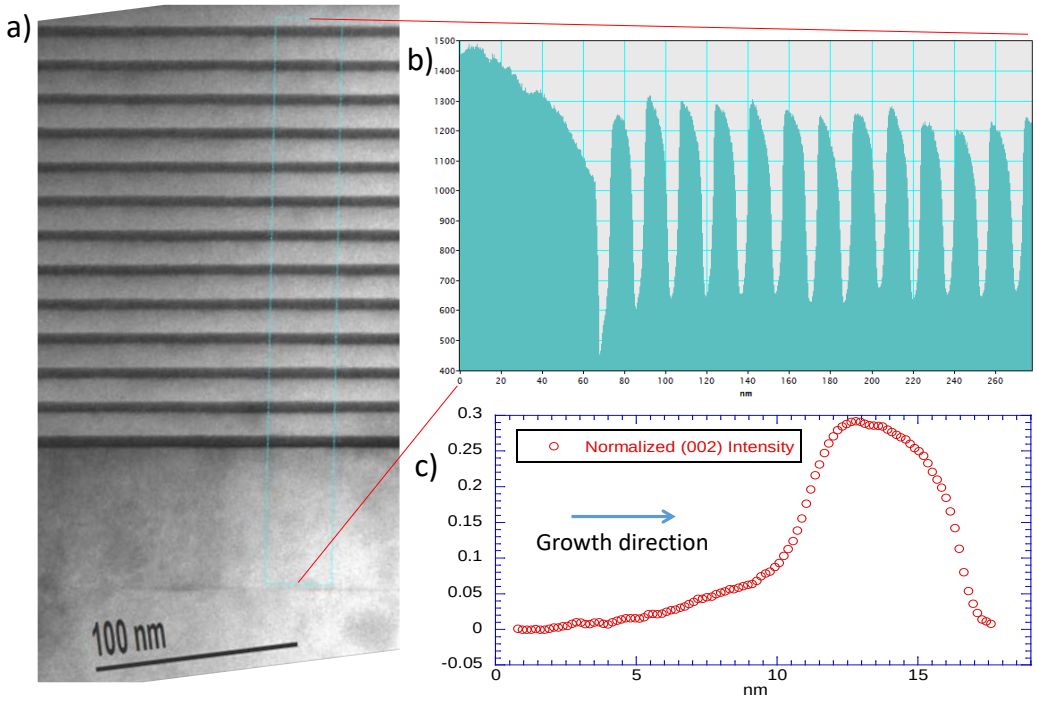

Figure 4.25 (002) dark-field (DF) imaging of InAs/InAsSb T2SL (sample 3-2498). a) as-recorded DF image, b) profile intensity taken from the boxed region in a). c) Normalized (002) intensity (1-I(002)/I_{max}), with the maximum of the normalized intensity taken as the nominal Sb concentration (0.29).

A typical (002) dark-field (DF) image of the MOCVD grown superlattices is shown in Figure 4.25(a). The structure factor of (002) is determined by the difference between atomic scattering at the cation and anion site, and thus gives rise a weak reflection whose intensity in this case is sensitive to the Sb concentration. Figure 4.25(b) shows the intensity profile extracted from the boxed region in Figure 4.25(a). In Figure 4.25(c), the intensity is inverted and normalized to the nominal concentration of the designed InAsSb layer. This approach is similar to the method used in Section 2.5 for the evaluation of Sb concentration distribution in the MBE grown InAs/InAsSb T2SL. The InAsSb layers appear darker than the InAs layers because of an increase in anion scattering due to Sb substitution. The presence of asymmetric Sb profiles on either side of the InAsSb layers is observed, which is different from that of MBE grown InAs/InAsSb T2SLs. In particular, we note a slow rise in Sb concentration in the InAs layer and relative abrupt drop of Sb in the InAsSb layer. The same profile is observed in all three MOCVD grown T2SLs.

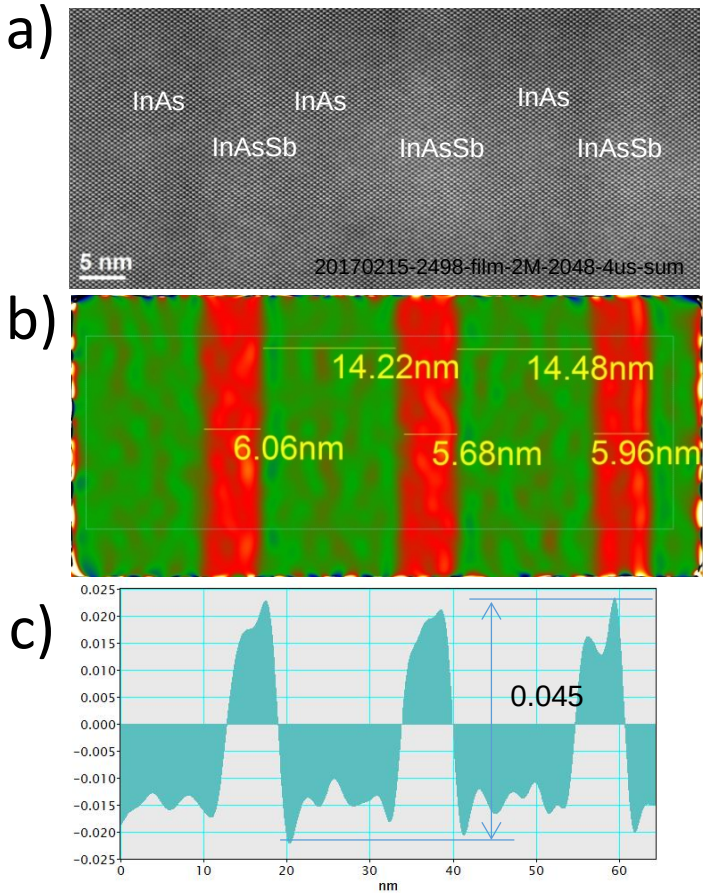

Figure 4.26 STEM analysis of strain in MOCVD grown InAs/InAsSb T2SL (Sample 3-2498). a) As-recorded HAADF-STEM image, b) strain (ε_{xx}) obtained using the method of GPA, c) Strain profile from the boxed region in b).

The strain in the MBE grown InAs/InAsSb T2SL is confirmed by HAADF-STEM and GPA analysis[123]. Figure 4.26 shows a typical example. The HAADF-STEM image was recorded using the probe aberration corrected JEOL 2200F installed at UIUC at 200 kV. The image was Fourier transformed and then analyzed by GPA. Distinctive positively and

negatively strained regions for InAsSb and InAS, respectively, are observed. The strain profile in Figure 4.26(c) shows the asymmetrical interface in agreement with the (002) DF image intensity analysis of Sb concentration.

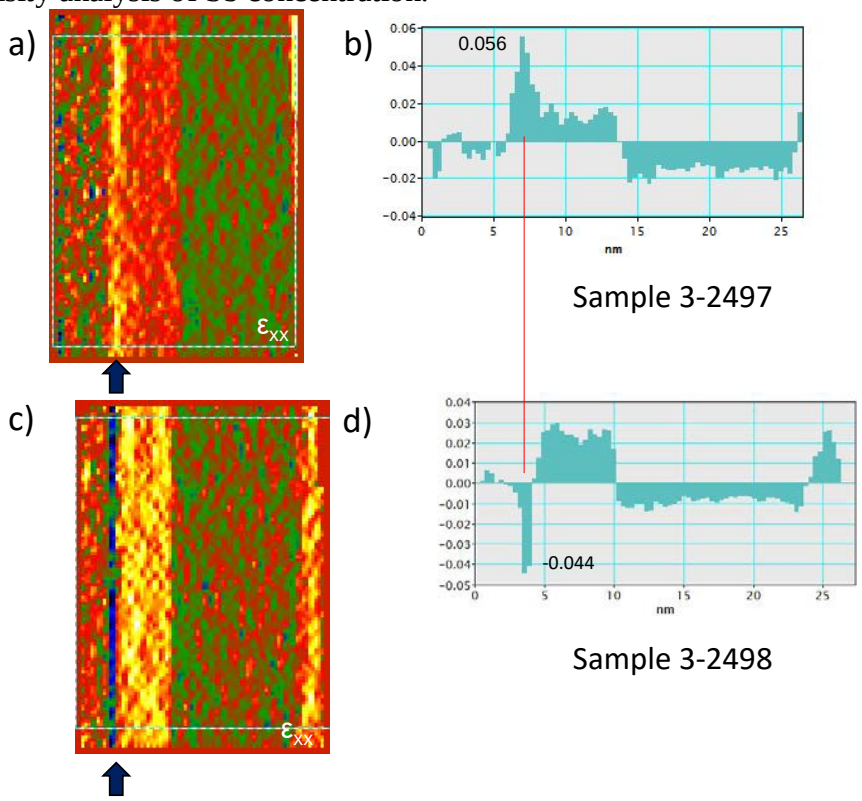

Figure 4.27 InSb and GaAs like buffer and film interfaces observed in Samples 3-2497 and 3-2498, respectively. a),c) strain maps obtained from as-recorded HAADF-STEM image, b, d) strain (ε_{xx}) profiles.

Two types of buffer and film interfaces are observed in the MOCVD grown T2SLs, one is InSb (in Sample 3-2497) and the other is GaAs like (in Sample 3-2498). One gives rise to positive interfacial strain, while the other gives negative strain. The amount of strain is less than pure InSb and GaAs, thus, certain amount of interfacial intermixing is present at the interface. The difference in the interfacial strain did not appear to lead to significant difference in structure, other than the strain.

4.6. Passivation of T2SLs using ammonium sulfide

One of the most important dark current mechanisms for fabricated photodiode mesas is the surface leakage current arising from both the abrupt termination of the T2SL at the sidewall of a device, as well as the native oxides, such as In_2O_3, and residual materials formed on the sidewall surfaces during processing. The termination of the lattice at the sidewall results in surface dangling bonds which pins the Fermi level above the conduction band at the surface. Native oxides formed during processing, and by-products of etching or mask materials, can also facilitate the this band bending and Fermi level pinning, if they are charged, or can act as trap states within the bandgap, increasing the trap-assisted

tunneling (TAT) current. The result is the formation of a depletion region under the surface, which must be eliminated to suppress the surface leakage current. Some of the methods used to remove the dangling bonds or reduce the band bending at the interface are:

1) Soaking the sample in aqueous solutions of ammonium sulfide ($(NH_4)_2S$), which reduces the amount of surface oxides and produces passivating sulfide compounds.
2) Low-temperature deposition of a thin layer of SiO_2, which has also resulted in a decrease in dark current densities and increase in device resistances.
3) Encapsulation by electrically neutral polyimide, which, in one case, resulted in an R0A product greater than 5300 Ω-cm^2 when combined with an effective dry etching recipe and a wide bandgap barrier in the depletion region.

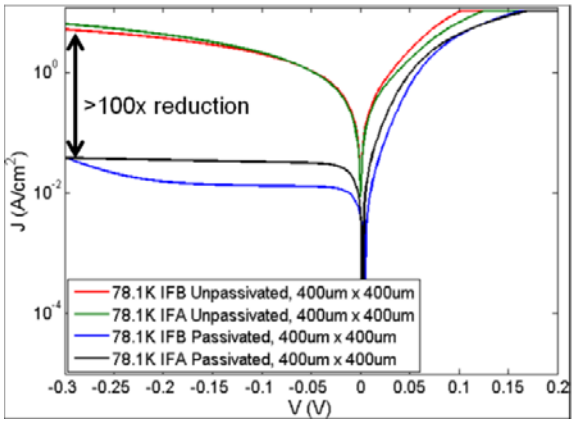

Figure 4.28 Unpassivated (upper) and passivated (lower) curves for IFA and IFB devices of size 400 µm x 400 µm. The passivated dark current densities are reduced by 2 orders of magnitude and the improvement of IFB over IFA in the reverse bias is clearly shown.

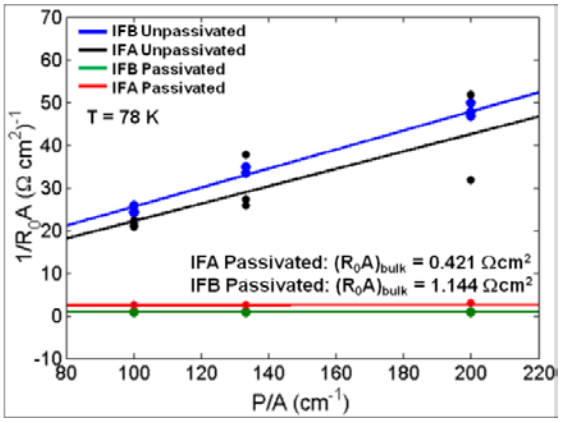

Figure 4.29 Plots of the inverse R_0A vs. the perimeter to area ratio (P/A) for both passivated (lower) and unpassivated (upper) IFA and IFB devices. Before passivation, a dependence of the R0A on device size can be seen, indicating surface leakage current. After, the slope of the best fit line is essentially zero, indicating little-to-no surface leakage current.

In the previous section, the electrical differences between samples with different light p-doping in the absorber region were discussed and it was shown that samples with slightly

higher absorber region p-doping had lower dark current densities. However, since the samples were unpassivated it is difficult to extract the bulk properties of the different samples. In this case, the same IFA and IFB devices tested in the previous section were passivated using an ammonium sulfide solution neutralized with HCl to a pH of 7.0 in order to observe their bulk electrical properties.

From Figure 4.22, it can be seen that there is a large difference between the unpassivated (upper) and passivated (lower) dark current densities at 78 K. In fact, at -0.3 V there is a dark current density reduction of approximately 2 orders of magnitude, indicating that the previously tested devices suffered greatly due to surface leakage currents. Passivation effectively quenches the surface leakage current, and allows direct comparison of the bulk dark current densities of our samples, demonstrating a reduced dark current density for the IFB devices (higher p-doping) when compared to the IFA devices, in reverse bias.

Passivation also allows for the extraction of the bulk R0A of the two different samples. Figure 4.23 plots the inverse of the R0A as a function of the perimeter to area ratio of tested devices. As mentioned previously, when unpassivated, the dark current density scales according to this ratio, with surface leakage current affecting smaller devices more dramatically than larger devices. This can be seen in the upper curves of Figure 4.23, where the best fit line has a large slope. The following equation shows that the slope of the best fit line corresponds to the inverse of the surface resistivity of the devices, while the y-intercept corresponds to the inverse of the bulk R_0A value:

$$\frac{1}{R_0A} = \frac{1}{(R_0A)_{bulk}} + \frac{1}{\rho_{surface}}\frac{P}{A} \qquad (10)$$

The performance of the unpassivated devices is reduced drastically due to surface leakage currents, which results in a low surface resistivity (large slope). However, after passivation the slope is reduced to nearly zero (very high surface resistivity) due to the elimination of trap states and dangling bonds on the device surface, indicating that the performance of each device is affected only by the bulk properties of the sample. When looking at the passivated curves, the best fit for the IFB devices is the lower of the two, meaning it has a larger bulk R_0A, which is to be expected given the larger absorber region p-doping. Thus, not only is it important to consider the effect of the interfacial layers on the device performance, but it is also important to optimize the light p-doping in the absorber region so as to maximize the electrical performance while sacrificing very little performance optically. However, in order to achieve the maximum electrical performance, an effective surface passivation scheme is necessary. Though ammonium sulfide works initially, it has a long-term degradation problem which will reduce the device performance to below its initial, unpassivated state if left untreated. The possible combination of ammonium sulfide and SiO_2 or polyimide will be explored to determine if a physical encapsulation layer would preserve the surface passivation effects of the ammonium sulfide over time.

5. Evaluation of Defect Reduction Approaches and Device Applications

5.1. Interfacial effect and large optical tunable range (Chuang and Wasserman, UIUC)

Interfacial (IF) layers in InAs-GaSb T2SL structures, either unintentionally formed or intentionally grown, are present at each of the InAs-GaSb heterojunctions. Because InAs and GaSb do not share a common element, these IF layers are typically InSb-like or GaAs-like, depending on the growth techniques and conditions, atomic segregation and diffusion, or by intentional control. IF layers are commonly used for strain balance, yet they also have a significant effect on T2SL optical properties. Our theoretical model, based on the 8-band **k.p** method, predicts a significant shift of the T2SL effective band gap due to the IF effect. Researchers have recently demonstrated a blue-shift of the band gap due to GaAs IF control. Here we show that detectors with InSb IF control have 10-times reduction of dark current and simultaneous improvement of quantum efficiency, despite having a 2 μm longer cutoff wavelength than non-IF control samples. We designed two samples with identical InAs/GaSb layer structure designed for 11 μm cutoff wavelength, one of which was grown with intentional sub-monolayer (ML) InSb interfaces and the other with no intentional IF control, in order to experimentally compare the effects of the IF layers on device performance. We include both InSb- and GaAs-type IF layers in our model to study their effect. Due to the large lattice mismatch to the GaSb substrate, InSb and GaAs IF layers have large biaxial compressive and tensile strain, respectively. The large strain causes the conduction and heavy-hole band edge to shift significantly, as shown in Figure 5.1. Thus, the IF layers introduce a strong perturbation to the superlattice eigen-energies and the effective band gap. Figure 5.2 plots the superlattice absorption spectra with different types and thicknesses of interfaces, calculated based on the 8-band **k.p** band structure model developed in this MURI by the UIUC team. The InSb and GaAs IF layers cause a significant red-shift and blue-shift of the cutoff wavelength, respectively. Our modelling also predicts the simultaneous improvement of the cutoff wavelength and absorption strength with InSb interface control, effects which cannot be simultaneously achieved via conventional well-width engineering.

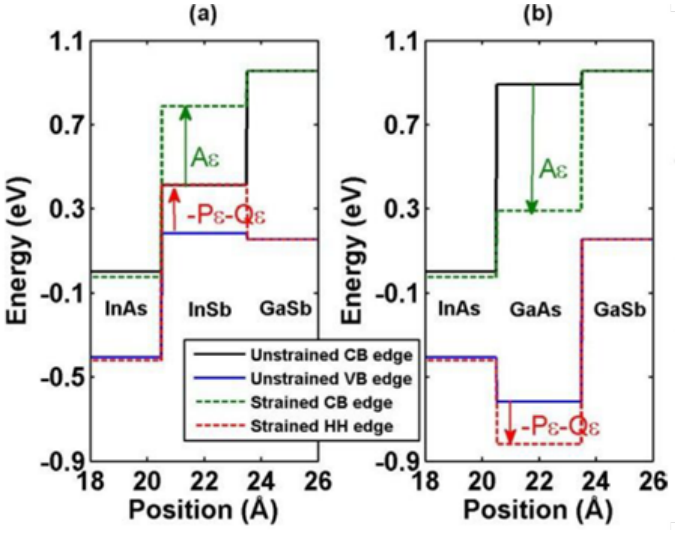

Figure 5.1 Bandedge alignment of the InAs/GaSb heterojunction when including interfacial layers of: (a) InSb type and (b) GaAs type. Solid lines are conduction (black)

and valence (blue) bandedges for unstrained bulk. Dashed lines are conduction (green) and heavy-hole (red) bandedge for strained bulk.

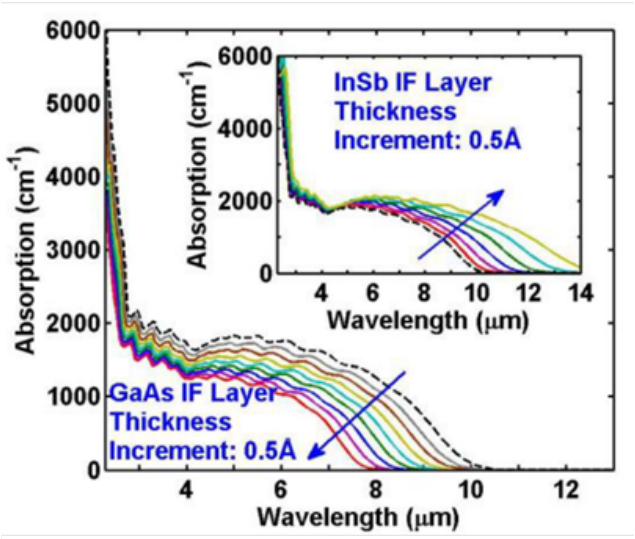

Figure 5.2 Absorption spectra for an InAs/GaSb 44 Å/21 Å superlattice with forced GaAs IF layer and InSb IF layer (inset). The black dashed lines in both cases represent zero IF layer thickness.

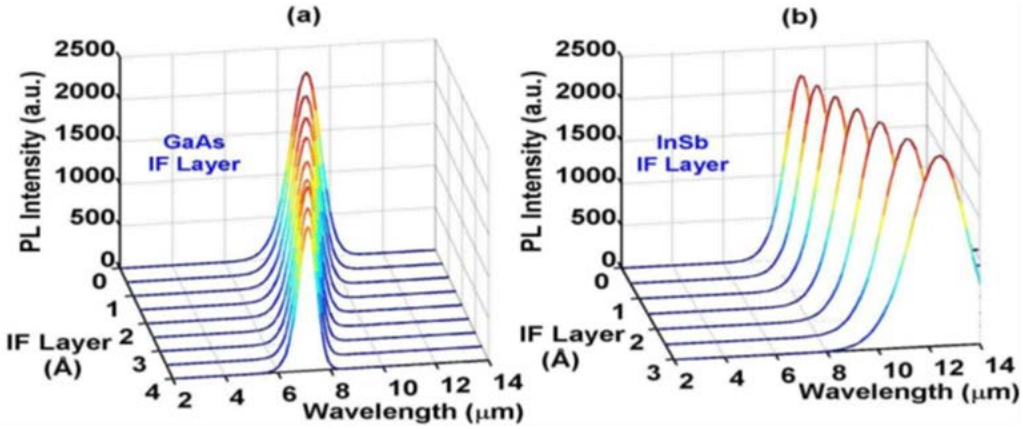

Figure 5.3 Modeled photoluminescence (PL) spectra with different interfacial (IF) layer thicknesses in an InAs/GaSb 44 Å /21 Å T2SL. The PL peak has a red-shift with thicker InSb IF layer while a blue-shift with thicker GaAs IF layer.

We include actual IF layers in our model to study their effect on optical properties. IF layers are forced at the heterojunction while the thickness of one superlattice period remains the same. Assuming pure InSb IF layers can be intentionally grown in between the InAs and GaSb layers, the VB states in the T2SL are shifted to higher energies since the VB edge in InSb is much higher than the VB edges in both InAs and GaSb, as shown in Figure 5.1. The change in the CB state energies is small compared to the change in the VB state energies because the CB edge in InSb is still in between the CB edges in InAs and GaSb. As a result, the InSb IF layer shrinks the effective bandgap and increases the transition wavelength. Such effects can be observed from the red-shift of the absorption cutoff and the PL peak, shown in Figure 5.2 and Figure 5.3, respectively. Due to the large

biaxial tensile strain in GaAs on GaSb substrate, optical properties are affected in the opposite way compared to InSb IF layers.

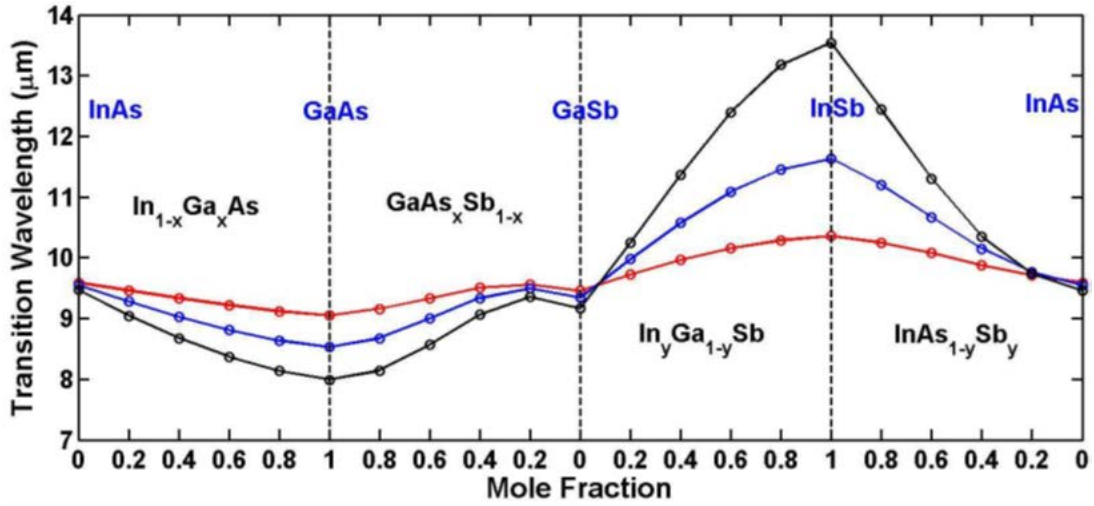

Figure 5.4 Transition wavelength as a function of the interfacial (IF) layer mole composition. Ternary IF layers of 1Å (red), 2 Å (blue), and 3 Å (black), are forced in an InAs/GaSb 44 Å/21 Å superlattice

There is normally a trade-off between the cutoff wavelength and the absorption strength when designing a T2SL, but the InSb IF layers are able to simultaneously increase both properties, as shown in Figure 5.3. The absorption coefficient increases with InSb IF layer thickness because it improves the wavefunction overlap between electrons and holes. It is easier for electrons to tunnel through the interface, and the hole-confining regions are effectively wider.

As a result, the InSb IF layer becomes a preferable region for electrons and holes to recombine. In reality, GaAs or even ternary and quaternary compound IF layers can also unintentionally form or be forced to form during the crystal growth of the InAs/GaSb T2SL. We model the bandedge transition wavelength in InAs/GaSb T2SLs when forcing ternary IF layers of all four possible types (seen in Figure 5.4). The ternary compounds reduce the range the cutoff wavelength shifts when compared to pure InSb or GaAs IF layers, and the mole fraction serves as another degree of freedom for strain balancing and crystal quality optimization. A wide tunable range of optical properties can be achieved by controlling the both the composition and the thickness of the IF layers.

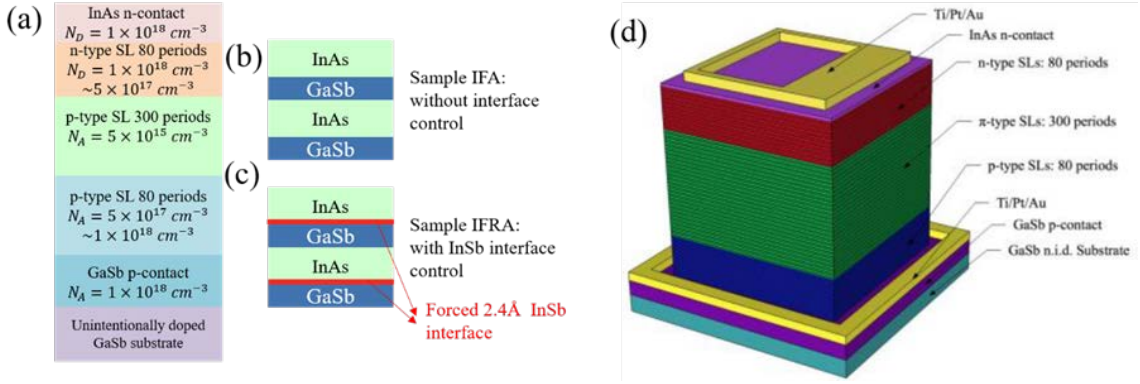

Figure 5.5 (a) Designed layer structure for type-II superlattice etectors and a single period of T2SL structure (b) IFA (without interface control and (c) IFRA (with interface control). (d) Device schematic.

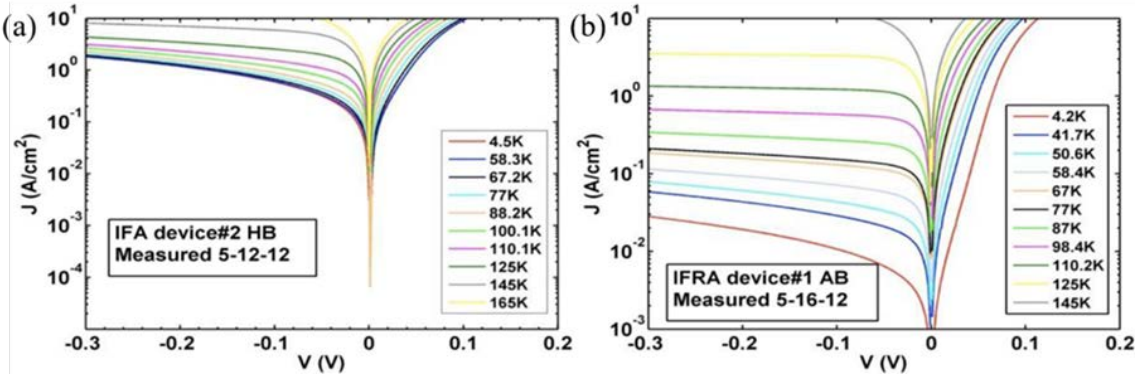

Figure 5.6 Measured temperature-dependent dark current densities for IFA (left) and IFRA (right) devices. Below 110 K, IFRA dark current densities are lower than those of IFA, an indication of improved electrical performance due to defect reduction despite the longer cutoff wavelength.

In the second year of the program, two devices were designed, modelled and grown (labelled as IFA and IFRA) with the same InAs/GaSb (15ML/8ML, 45Å/24Å) layer structure designed to operate up to 11 μm, with sample IFA grown without specific interfacial control, and sample IFRA grown with InSb interface control, as shown in Figure 5.5.

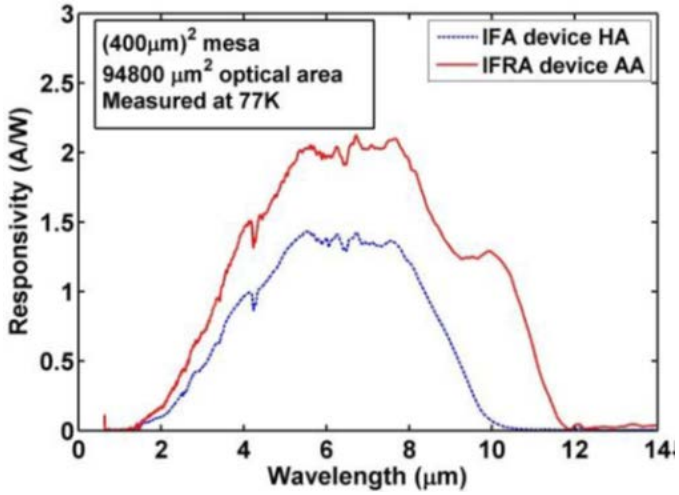

Figure 5.7 Measured responsivity spectra of IFA (blue) and IFRA (red) devices. IFRA, despite having a 2 μm longer cutoff wavelength, has larger responsivity values over all wavelengths, when compared to IFA, indicating the effectiveness of interface control as a method for not only strain compensation, but improved T2SL optical performance.

The device structures consist of 300 periods of lightly *p*-doped superlattice absorber regions sandwiched between 80 periods of *p*-doped and 80 periods of *n*-doped superlattices, as shown in Figure 5.5(d). The device mesas are formed by inductively-coupled plasma reactive-ion etching. The dark current densities of T2SL detectors

fabricated using samples IFA and IFRA are measured at a range of temperatures, from approximately 4 K to 165 K, as shown in Figure 5.6. We expect that for sample IFRA, the compressive strain in the forced InSb interfacial layers will compensate for the slight tensile strain in the InAs layers. Better strain balance is expected to produce a smaller defect density and a longer minority carrier lifetime, which can suppress both the diffusion and generation-recombination dark current. The results show an order of magnitude reduction of the dark current density in reverse bias for the IFRA devices when compared to the IFA devices, despite the 2 μm longer cutoff wavelength.

The photoresponse spectra of the IFRA and IFA devices are obtained using a Bomem DA8 Fourier-Transform Infrared (FTIR) Spectrometer. The device photoresponse is calibrated using a Mikron M305 black-body source at 1000 °C and a lock-in technique, from which the device responsivity and quantum efficiency spectra are obtained, as shown in Figure 5.7. By forcing the IF layers (sample IFRA), the device cutoff wavelength increases by almost 2 μm. Simultaneously, the responsivity and quantum efficiency both increase, which agrees well with our theoretical predictions. The introduced InSb interfacial layers not only reduce the effective band gap but also enhanced the electron and hole wavefunction overlap, thus increasing the transition strength. With conventional well-width engineering, T2SL quantum efficiency and responsivity are sacrificed in order to obtain longer cutoff wavelengths. However, our results in Figure 5.7 demonstrate that this trade-off can be avoided by interface control, which confirms our theory for the interfacial effect.

5.2.Absorber region light *p*-doping to improve device performance

The doping in the many-period absorber region of a T2SL is an important factor that contributes to the device performance and must be considered carefully when designing a structure. As it turns out, it is more beneficial to grow T2SLs on a *p*-type GaSb substrate in the *n*-on-*p* configuration, where the absorber region is lightly *p*-doped, forming a *p*+-*p*-*n*+ diode. Looking at the growth direction energy band structures of typical InAs/GaSb or InAs/InGaSb superlattices, the effective mass of holes are much heavier than that of the electrons, making them harder to collect. Thus, it is desirable to have electrons as the minority carriers in the absorber region, hence the light *p*-doping, which results in not only better vertical transport properties but a further reduction in Auger recombination rates with only a minimal decrease in the wavelength dependent absorption coefficient due to the introduction of extra holes in the valence band (VB) and no change in cutoff wavelength. Devices were fabricated and tested using the samples IFA (mentioned previously) and IFB. The only difference between the two samples (both without intentional interfacial layer control) is that the absorber region *p*-doping for IFB (1.0×10^{16} cm^{-3}) is slightly higher than that of IFA (5.0×10^{15} cm^{-3}). This slight increase for IFB should lead to better electrical properties (reduced dark current in the reverse bias and higher R0A) with only a minimal sacrifice in optical performance. Figure 5.8 plots the dark current densities for three different sized IFA (dashed) and IFB (solid) devices at a temperature of 4.5 K: 400 μm x 400 μm (a), 300 μm x 300 μm (b), and 200 μm x 200 μm (c). As these devices are unpassivated, the dark current density should scale according to mesa size, increasing as the device sizes shrink and the perimeter to area (P/A) ratios increase. However, the key finding is that in all cases, IFB has a smaller dark current

density than IFA, indicating better electrical performance, which can be attributed to the larger *p*-doping in the superlattice absorber region.

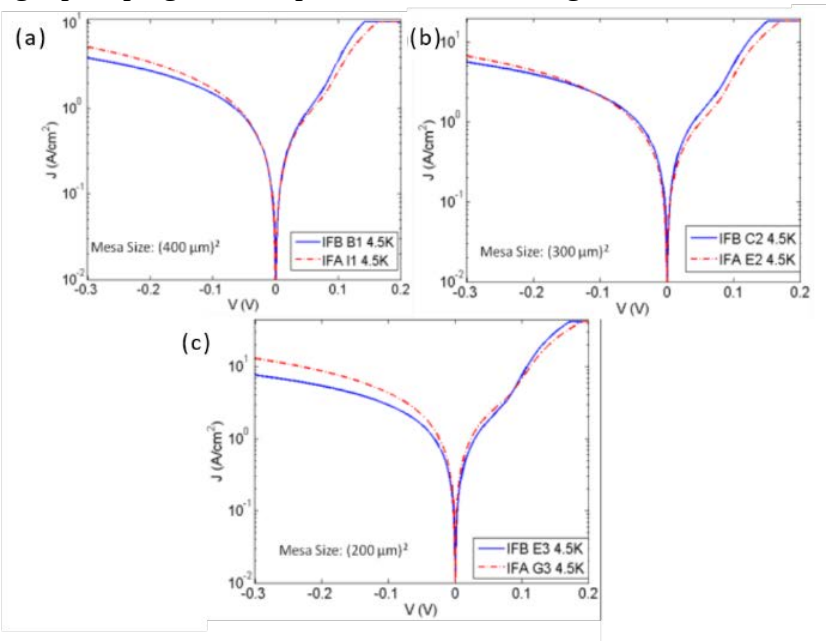

Figure 5.8 Dark current densities for 3 different sized devices, (a) 400 µm x 400 µm, (b) 300 µm x 300 µm, and (c) 200 µm x 200 µm, using samples IFA (dashed) and IFB (solid). As expected, IFB has better electrical properties due to its slightly higher absorber region p-doping.

Figure 5.9 Fig. 13: Responsivity curves for 3 different sized devices, (a) 400 µm x 400 µm, (b) 300 µm x 300 µm, and (c) 200 µm x 200 µm, using samples IFA (dashed) and IFB (solid). The slightly higher p-doping for IFB sacrifices optical performance for better electrical performance (Figure 5.5).

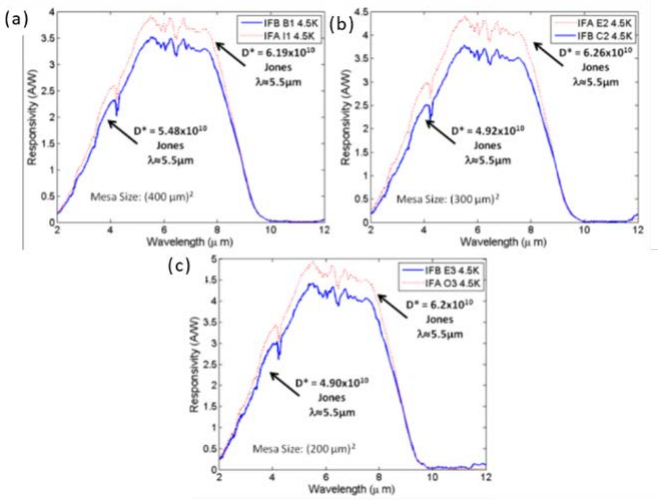

The optical performance of the two samples also followed the expected trend. *Figure 5.9* plots the absolute responsivity of IFA (dashed) and IFB (solid) devices for three different sizes: 400 µm x 400 µm (a), 300 µm x 300 µm (b), and 200 µm x 200 µm (c). These curves were measured in a Bomem DA-8 FTIR and calibrated using a spike filter at 4.845 µm. In each case the responsivity and specific detectivity of the higher *p*-doped IFB devices were less than that of the IFA devices, as predicted, and no change in cutoff wavelength was observed between the two different samples. In addition to the modelling, electrical, and optical characterization of the interface-controlled samples, we also performed electron beam induced current (EBIC) measurements of these samples. The results from this work will be presented in the EBIC portion of the report.

5.3. Electron Beam Induced Current Measurements of T2SL Materials

A significant portion of the UT/UIUC group's efforts over the course of the MURI were geared towards the development and utilization of a low temperature electron beam induced current (EBIC) measurement system for probing the carrier dynamics of T2SL devices. In the first year of the program, a setup for low-temperature EBIC measurements was established with the help of the Frederick Seitz Material Research Laboratory at the University of Illinois at Urbana-Champaign. The setup utilizes a JEOL 6060LV SEM fitted with a helium-cooled thermal stage, allowing for measurements down to temperatures around 6 K. A highly sensitive current amplifier allows for the generation of quality EBIC images as a direct result of specimen current generated by the electron beam of the SEM, which provides useful information about the carrier transport properties of our devices. Using this setup we were able to observe defect structures in T2SL samples: Figure 5.10 shows images taken from an undoped InAs/InAs1-xSbx T2SL structure with electronically active defects being identified through contrast analysis.

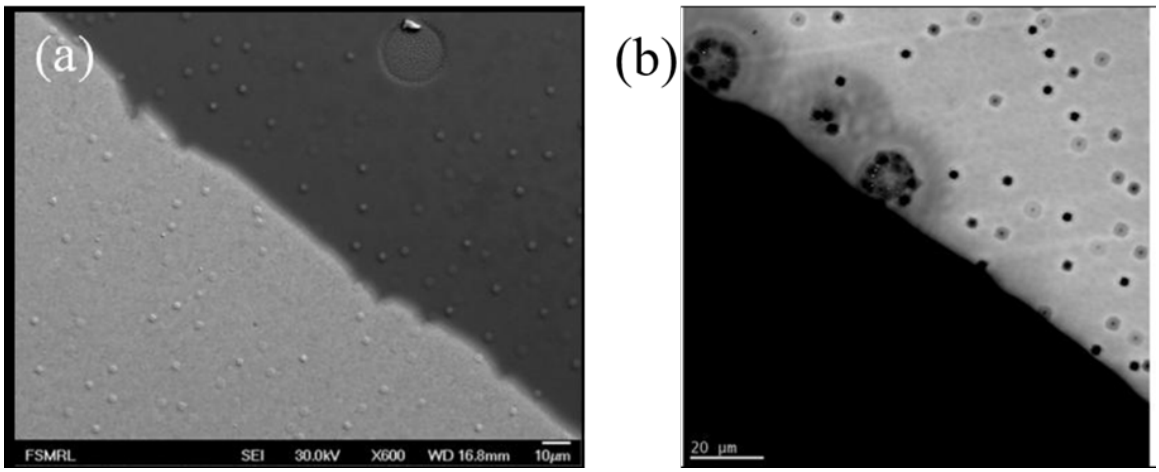

Figure 5.10 (a) SEM and (b) electron beam induced current (EBIC) images of the top surface of an InAs/InAs$_{1-x}$Sb$_x$ SL taken at 6 K. Visible in both images are a number of round aberrations, due to threading dislocations within the structure.

In the first year of the program, we also began preparations for cross-sectional EBIC analysis in order to extract the minority carrier diffusion properties within T2SL detector samples[124]. While some initial EBIC images have been taken of detector sidewalls, further improvements in the experimental setup are required in order to ensure that the surface of the sample is normal to the electron beam. Additionally, modeling of the electron beam incidence will need CASINO software in order to extract useful information from the EBIC images.

In addition, the first year of the program saw progress towards the development of a deep-level transient spectroscopy (DLTS) measurement process, utilizing a Boonton 7200 capacitance meter. By analyzing the changing capacitance of a T2SL device with respect to pulsed bias voltage, we will be able to extract information about trap states created by surface and bulk defects.

5.4. EBIC Analysis of IF Series Samples

The first EBIC performed by our group focused on the interfacial T2SL samples designed at UIUC and grown via MBE by IQE. Data were obtained for three samples, IFA, IFB, and IFRA, each previously described. Detector samples were fabricated with an inductively coupled plasma dry etch, metal deposition and liftoff process, then cleaved through the mesa and mounted vertically in an SEM especially equipped with a closed cycle helium stage and electrical contacts to measure the current response of the devices when subjected to an electron beam. The beam was then scanned across the exposed junctions of the devices and the magnitude of the induced current used to form images, which are then compared to the images generated by the backscattered electrons of the SEM. Analysis of the images yielded response curves based on the electron beam's position relative to the growth direction of the samples.

An accurate model is essential for extracting useful data from EBIC measurements. Substantive comparisons of the diffusion characteristics of the IFA and IFRA samples required enhancements to the standard modeling techniques for the EBIC experiment[125]. An extension to the existing theory was required to properly model the behavior of the EBIC signal, which is generated by separation of electron-hole pairs generated by the high energy electrons accelerated in the SEM. The existing model, which was published by Bonard and Ganière[126] and heavily based on diffusion theory established by Donolato[127], deals with the EBIC behavior of a p-n junction. However, in our modeling efforts we found that this theory as written could not explain the asymmetric nature of our data (see *Figure 5.12*). To model our data, we extended our theory to include the effects of recombination in the lightly p-doped absorber region. Our treatment expands the altered solution of the diffusion equation shown by Donolato with an additional material layer representing the lightly doped absorption region with a distinct set of diffusion properties, and a boundary condition at its edge to ensure a continuous collection probability distribution, φ. The equation for φ for a carrier generated at (x, z) in a p+-π-n+ structure is then given as:

$$\varphi(x,\mathrm{z}) = \frac{1}{\pi}\int dk \frac{2s}{k^2+s_o^2} \times [\cos(kz) + s_o \sin(kz)] \times \begin{cases} exp\left(x\sqrt{k^2 + L_{n^+}^{-2}}\right) & x < 0 \\ exp\left(-x\sqrt{k^2 + L_p^{-2}}\right) & 0 \le x \le d_N \\ exp\left(-x\sqrt{k^2 + L_{p^+}^{-2}} - d_N\sqrt{k^2 + L_p^{-2}}\right) & x \ge d_N \end{cases} \quad (11)$$

where s_o is the surface recombination velocity, d_N is the width of the π-region, and L is the local minority carrier diffusion length. The two dimensional carrier collection probability φ, based on this solution is shown in *Figure 5.11*. Of particular interest is the region in the middle, which exhibits an asymmetric behavior similar to what was observed in the EBIC data of Fig. 5.12.

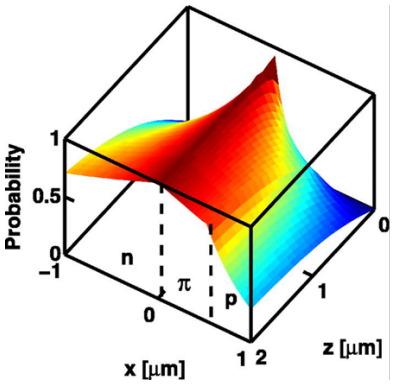

Figure 5.11 Probability of carrier capture within the photodetector device. The x axis represents the growth direction, and z axis represents the distance from the cleaved surface of the device. The calculation results are obtained from an extension of existing theory established by Donolato[127]..

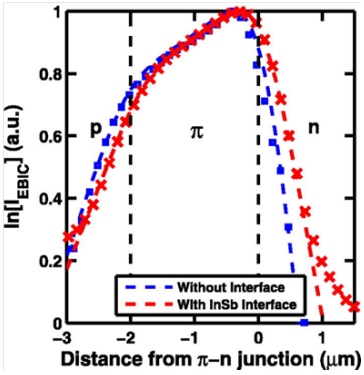

Figure 5.12 Comparison of EBIC data (squares, crosses) and modeled fits (dashed lines) for the IFA (blue) and IFRA (red) samples. The vertical lines indicate boundaries between doped regions.

Figure 5.12 shows the measured EBIC data from the IF series samples IFA and IFRA, along with our theoretical fits to the data. Table 5.1 shows the parameters used to obtain the fits. We observed a significant improvement in the vertical diffusion length (from 500 nm to 900 nm), and thus the minority carrier lifetime (from 48.4 ns to 157 ns) of the holes in the *n*-region due to the interfacial treatment. A slight improvement for the minority electrons in the *p*-doped region was also noticed, but the margin of improvement was much smaller -- 1.7 to 2 μm and 50.8 to 70.3 ns for diffusion length and lifetime, respectively. We used a very large value for diffusion length, 60 μm, for the π-doped region to represent the presence of a weak electric field enhancing carrier collection. The reason for improvement is believed to be reduction of strain-induced defects and better control of the switching between InAs/GaSb layers due to a forced deposition of InSb. Since the GaSb layer is used for confinement of the hole energy states in the T2SL configuration, we suspect that the use of the interfacial layers helps to mitigate defects cause by the deposition of GaSb directly onto InAs, for example, by diffusion of Ga across the interface or antisite defects near the interface. The electrical and optical improvements mentioned earlier in the report lend further credibility to this result. More importantly, however, is our demonstration of a successful EBIC experiment involving a T2SL sample with a lightly-doped absorber region appropriate for a photodetector device, and the successful application of theory to model the change in structure.

Table 5.1 List of material parameters used to fit the EBIC data of the IFA and IFRA samples designed by UIUC and grown by IQE

Quantity	Symbol	IFA	IFRA
Minority diff. length (n)	L_h	0.5 μm	0.9 μm
Minority lifetime (n)	τ_h	48.4 ns	157 ns
Hole mobility	μ_h	100 cm^2/Vs	100 cm^2/Vs
Surface recombination – diffusion ratio (n)	S_h/D_h	1000 cm^{-1}	1000 cm^{-1}
Minority diff. length (p)	L_e	1.7 μm	2 μm
Minority lifetime (p)	τ_e	50.8 ns	70.3 ns
Electron mobility	μ_e	1100 cm^2/Vs	1100 cm^2/Vs
Minority diff. length (π)	L_j	60 μm	60 μm
Surface recombination – diffusion ratio (p)	S_e/D_e	400 cm^{-1}	400 cm^{-1}

5.5. EBIC Study of Mid-Wave Ga-Free T2SLs in nBn Detector Samples

Following our demonstration of EBIC as a powerful tool for the characterization of pn-junction T2SL samples with controlled interfaces, we moved forward to apply this technique to characterization of T2SL detectors in an nBn configuration. In particular, we focused on the EBIC study of InAs/InAsSb superlattices in mid-wave IR detectors with nBn detector architectures. As with previous results, we carried out these studies with a JEOL 7000F scanning electron microscope equipped with a helium cryogenic cooling stage, which enabled us to collect temperature-based EBIC data with samples fabricated with electrical contacts. While most initial nBn detector studies have focused on InAs/GaInSb T2SLs for MWIR and LWIR applications, there has been growing interest in Ga-free InAs/InAsSb T2SL structures. Such devices have demonstrated reduced dark currents[128] and longer minority carrier lifetimes, hypothesized to result from the absence of native defects associated with GaSb[105]. As we demonstrated previously for p-i-n design T2SL detectors,[125] EBIC is a useful technique for characterizing carrier transport, particularly in samples intended for use in detector elements or arrays where excited carriers can be collected via electrical contacts. In the EBIC technique, a high energy electron beam is focused on the surface of a sample to generate excess carriers, which can be measured as an electrical current. *Figure 5.13* contains simple schematics of both the sample bandstructure and the EBIC experiment.

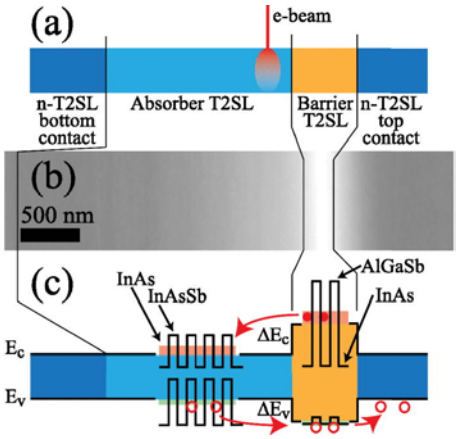

Figure 5.13 (a) Schematic of the EBIC experiment. The electron beam strikes the cleaved surface of the detector at a normal incidence, creating a localized area of excess electron-hole pairs. (b) Representative EBIC image oriented with the epitaxial growth direction from left to right, with guide lines showing the spacing of the detector regions. Image brightness corresponds to measured current as a function of beam position. Image taken at a beam energy of 15 keV and at a device temperature of 6 K. (c) Illustrative band diagram, not to scale. Carriers generated in the barrier layer can easily contribute to EBIC current, whereas a small valence band offset (ΔEV) in the barrier can impede the transport of minority carriers generated in the absorber region.

In this effort, we demonstrated the utility of the EBIC technique for characterization of an nBn detector based on a Ga-free, InAs/InAsSb T2SL absorber region. We also demonstrated that the EBIC analysis can be supplemented with time-resolved photoluminescence (TRPL) characterization of the same sample. This allows the minority carrier lifetime to be measured independently from the minority carrier diffusion length. By combining both measurements on the same device, the minority carrier diffusion coefficient in the growth direction (i.e., the vertical diffusivity) is obtained. The detector structures are characterized by photoluminescence (PL) spectroscopy and TRPL, photoresponse spectroscopy, and beam energy dependent EBIC, providing a comprehensive experimental characterization of both the devices' optical properties and the nonequilibrium carrier dynamics in the T2SL absorber.

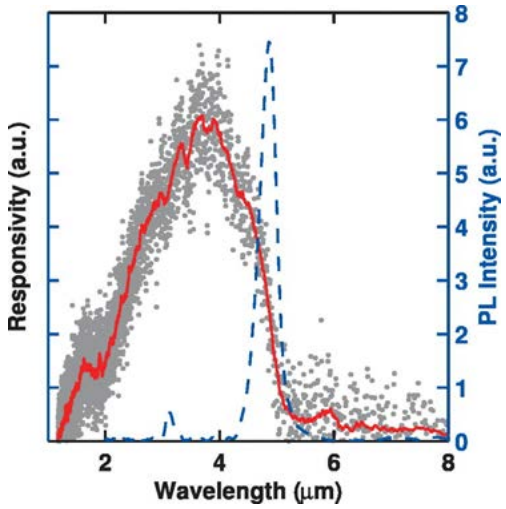

Figure 5.14 Uncalibrated responsivity (left axis) and PL (right axis) spectra of the nBn detector taken via Fourier transform spectroscopy. The raw responsivity data (points) are shown along with a smoothed average (solid line), and the PL spectrum (dashed line) is overlaid for comparison. Measurements were taken at 77 K with a 0.35 V bias applied to the detector for the responsivity spectrum.

The sample used for measurements was grown via molecular beam epitaxy on an undoped GaSb substrate. The epitaxial layers consist of a 500 nm GaSb buffer, a 950 nm

n-type T2SL bottom contact layer, a 2.4 µm (256 periods) InAs/InAsSb T2SL absorber layer, the wide-bandgap superlattice barrier layer, and a T2SL top n-type contact layer. The T2SL absorber structure used was 49 Å InAs/45 Å $InAs_{0.81}Sb_{0.19}$, resulting in a superlattice bandgap of 5.5 µm. The bottom contact was created using 950 nm (101 periods) of the same T2SL structure as the absorber, doped n-type using Si to 1×10^{18} cm^{-3}. Similarly, the top contact was formed with 96 nm (10 periods) of the absorber T2SL structure followed by 30 nm of bulk InAs. The top contact was uniformly doped n-type at 1×10^{18} cm^{-3} also using Si. The barrier layer consisted of 20 periods of a 29.3 Å InAs/21.7 Å AlGaSb superlattice. Devices were formed by etching mesas down to the bottom contact layer using a standard lithography and chemical wet etch process, followed by deposition of Ti/Pt/Au metal contacts.

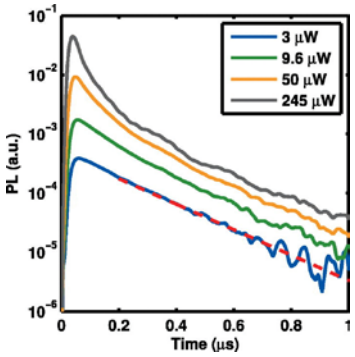

Figure 5.15 Time resolved photoluminescence data obtained from the nBn detector sample at 16 K, for a range of optical pumping powers. The fit used to extract carrier lifetime (dashed line) from the 3 µW injection curve is shown for comparison.

The optical responsivities of the fabricated detectors were measured via Fourier transform infrared spectroscopy (FTIR). Uncalibrated spectra of the device were taken using a Bomem DA-8 FTIR instrument with a global source and CaF_2 beam splitter, and a Stanford Research Systems SR570 current preamplifier to measure the photocurrent of the device. *Figure 5.14* shows the resulting responsivity spectrum of a fabricated detector cooled with liquid nitrogen to 77 K at a bias of 0.35 V, with both the raw data (grey) and a smoothed interpolation (red) plotted. Note that forward bias on the device refers to a positive voltage applied to the bottom n-contact. *Figure 5.14* also shows PL spectrum taken at 77 K for comparison. The PL data were acquired using a Bruker V80v FTIR operating in amplitude modulation step-scan mode. For the PL measurement, the sample was mounted in a cryostat behind a ZnSe window and excited using a 980 nm diode laser pulsed at 45 kHz and incident at −45° through a quartz window. The excited PL was collected at +45°, collimated via a Ge lens (which blocks the pump laser) and fed to the FTIR. The response of the internal FTIR MCT detector is taken to an external lock-in amplifier and returned to the FTIR for processing. From the collected PL spectra, we observe strong emission from our sample at a wavelength just under 5 µm, in good agreement with the cut-off wavelength of our detectors observed in the responsivity data.

TRPL measurements were carried out using a 1064 nm pump laser with a 4 ns pulse width and 1 kHz repetition rate. The sample was housed in a closed-cycle He cryostat for temperature control and excited with a range of optical powers. The resulting emission was collected by a fast MCT detector and recorded with a high speed oscilloscope. The various transient curves are plotted in Figure 5.15 for a sample temperature of 16 K. The minority carrier lifetime was obtained from these curves by fitting the 3 µW data with a single exponential decay function. The model fits the portion of the TRPL curve after t = 200 ns,

corresponding to non-degenerate carrier concentrations expected in normal operation of the nBn photodetector. From this measurement, the hole lifetime in the absorber region was estimated to be 200 ns. As can be seen from the slopes of the higher excitation power data in Fig. 5.15, similar hole lifetimes are obtained for increasing pump pulse energies when fitted at low carrier concentrations (t > 200 ns). While our measured lifetime is lower than that observed in studies of state-of-the-art InAs/InAsSb T2SLs[129], they are well within the bounds of reasonable performance observed in the literature[3].

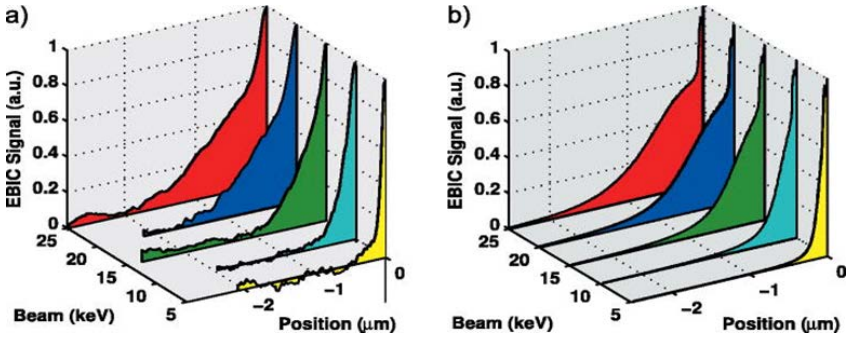

Figure 5.16 Fig. 22: EBIC signals plotted versus beam position on the sample (right horizontal axis, peak signal corresponding to x = 0, with positive x direction indicating the direction of growth) as well as beam energy in keV (left horizontal axis). (a) Experimental data collected at 6 K in an SEM for the cleaved nBn detector, with the sample oriented with the exposed side wall normal to the beam. (b) Theoretical simulation of the EBIC signal for the sample used to extract minority carrier diffusion length and surface recombination parameters.

EBIC measurements were taken at various electron beam energies, ranging from 5 keV to 25 keV at a probe current of 1 nA. The EBIC data for various beam energies at a fixed temperature of 6 K, as well as the corresponding modeled fits are shown in Figure 5.16. The data exhibit a maximum in signal near the top contact of the device, defined as x = 0, with a drop-off in signal as the beam moves away from this point, through the absorber, and towards the substrate. With increasing beam energies, a shoulder appears in the EBIC data, beginning at beam positions corresponding to the absorber/barrier interface and decaying as the beam position moves towards the bottom contact. Using the standard Bonard and Ganière[126] method to fit the data, we were unable to replicate the obtained EBIC signal without introducing a thin artificial region of unrealistically high surface recombination and low diffusion length. The unique shape of the nBn detector EBIC profiles (sharp peak with a shoulder appearing at increasing beam energies) suggests that the collection efficiency of minority carriers generated in the absorber layer is less than unity, since the rise in signal outside of the peak (in the shoulder) does not trend towards the global maximum. This is likely due to the presence of a relatively small minority carrier potential barrier due to valence band mismatch between the absorber and barrier layers. To account for this, we modeled our EBIC results using two separate contributions to EBIC current. Using Monte Carlo simulations[130], we extracted the distribution of energy absorbed from inelastic collisions of electrons (i) within the barrier layer and (ii) within the absorber region for each position and energy of the electron beam. These absorbed energy distributions represent electron-hole pairs (EHPs) generated (i) directly in the higher band gap barrier layer, which are swept away by the electric field in the barrier region to create

drift current and (ii) holes generated in the absorber region, which must diffuse to the top contact, across the small potential barrier at the absorber/barrier interface. The first current contribution (drift) dominates the EBIC signal when the electron beam spot is within or near the barrier layer and leads to the peaks (at $x = 0$) observed in the data. The second current contribution (diffusion) is responsible for the shoulder observed in the absorber region of the nBn detector.

We combined the modeled drift current signal with the traditional diffusion current from EHPs generated in the absorber layer, via a weighted sum, to reconstruct the total EBIC current. The ratio of diffusion current to drift was determined to be 0.35 via empirical comparison of the modeled signals' shoulder heights to the data. It is worthwhile to mention that in the typical application of an nBn detector, the wide gap of the barrier layer provides enough selectivity to ignore photogenerated carriers within it. In the EBIC measurements, where the electrons used to generate current have much higher energy and are focused at a very small beam spot, we cannot ignore such a contribution to current, even when we are primarily concerned with the behavior of carriers in the absorber region. For this reason, the barrier band gap is not observed in the optical data presented in *Figure 5.14*.

The resulting modeled data, obtained from the Monte Carlo simulations combined with our drift/diffusion model of carrier collection, are shown in Figure 5.16(b) alongside the experimental data (Figure 5.16(a)). We note that the theoretical data follow the same trend as the experimental data, with a narrow peak followed by a shoulder, whose signal decays with increasing distance from the top contact. Additionally, by using the same diffusion length and surface recombination velocities for each beam energy in the model, we were able to replicate the beam energy dependence of the data, obtaining close fits to each set of experimental data by only changing the carrier generation profile due to beam energy (obtained by Monte Carlo simulations).

From the data in Figure 5.16, we were able to extract a hole diffusion length in the absorber region of 750 nm and a surface recombination to diffusivity ratio of 10^6 cm^{-1} at $T = 6$ K. Based on the fit of the surface recombination to diffusivity ratio, we estimate a surface recombination velocity of 3×10^4 cm/s. The surface recombination parameter becomes increasingly less sensitive as its value grows larger and this value is an estimate of the lower bound for the true surface recombination velocity. Nonetheless, the large surface recombination velocity of our result compared to previous modeling done on comparable InAs/GaSb T2SL pn junction photodiodes[131] suggests a strong contribution to the effective carrier lifetime by the unpassivated surface of the InAs/InAsSb T2SL. This suggests that device fabrication methods which avoid etching below the barrier layers should be used to optimize device performance. In conjunction with the lifetime measured via TRPL, we estimate a hole diffusivity of 3×10^{-2} cm^2/s. Using Einstein's relation, a hole mobility of 60 cm^2/V s is estimated. This value is an order of magnitude larger than the vertical hole transport reported recently for InAs/GaSb T2SLs,[129] suggesting that the issue of hopping transport for holes in our Ga-free T2SL is less severe than for holes in an InAs/GaSb T2SL.

In this thrust we have demonstrated minority carrier diffusion length and lifetime characterization using EBIC and TRPL for an nBn device structure utilizing a type-II InAs/InAsSb superlattice absorber layer. By studying the dependence of the EBIC data on

the electron beam energy, we were able to characterize the sample's surface recombination characteristics as well as the minority carrier diffusion length. When combined with the lifetime via TRPL data, we were able to additionally determine the hole vertical mobility and diffusivity, providing a comprehensive picture of device performance and excited carrier dynamics in Ga-free nBn T2SL detectors.

5.6. Modification of EBIC for Improved Parameter Extraction (Wasserman, UIUC)

In principle, the extremely small electron beam spot size of EBIC offers the potential for spatially-resolved information of material parameters in active devices. This technique has been applied over the past decades to characterize electronic and opto-electronic devices, providing valuable information on the electronic properties of the device material [127, 132]. In comparison to the closely related XBIC[133] and LBIC[134] measurements (x-ray- and laser- beam induced current, respectively), EBIC offers more accurate material parameter extraction for materials with short diffusion lengths[135] as well as straightforward integration with scanning electron microscopes. In practice, however, the EBIC technique has limitations. Material parameters are most typically extracted by fitting the experimentally obtained EBIC data to a model which uses numerical techniques (Monte Carlo simulations) to determine the carrier generation profile[130], combined with an analytical model of carrier collection[126, 132, 136], which together give a predicted current vs. position plot for the device under test. Analytical integration of the product of the carrier generation profile and the carrier collection probability, however, requires the use of analytical fits to the carrier generation profile, fits which do not accurately reflect the numerical simulations, resulting in a loss of spatial resolution for the modelled EBIC, and poorer fits to the data. In addition, the most frequent examples of EBIC modelling fit normalized experimental data and modelled results (with fitting parameters of diffusion length L and surface recombination velocity to diffusivity ratio, S/D) for a range of electron beam energies[137 126, 132]. By normalizing both experimental and modelled data, these approaches look to fit only the shape of the EBIC signal, and omit valuable information obtained from the relative magnitude of the EBIC signal as a function of beam currents and energies. This results in uncertainty in the extracted parameters, with broad ranges of L and S/D offering similar fits to the experimental data, and thus weakening the significance of the extracted data. For EBIC measurements on bulk materials and large areas or cross-sections with weak surface recombination and long diffusion lengths, these uncertainties are minimized, but this is not the case for more complicated devices, having shorter active regions, multiple material layers, and/or significant surface recombination. By retaining both the shape and the magnitude of the EBIC signal, improvements to the fit of the EBIC data, as well as improvements to the uncertainty in the extracted data, can be achieved. In addition, the comparison of excited EHP densities (which can be obtained from the beam energy and current) and the magnitude of the collected current can provide additional insight into carrier dynamics in devices, potentially offering the opportunity to observe transitions where carrier lifetimes are changing as a function of excess carrier concentration[138]. Thus, it is conceivable that a new approach to EBIC modelling, which takes into account not only the shape of the EBIC data, but also its relative magnitude, would offer the potential to realize the full capability of EBIC.

One example of the more complex devices mentioned above are the subject of this MURI, the strained layer superlattices (SLS) such as InAs/GaSb, InAs/InAsSb and

InGaAs/InAsSb, which have attracted significant interests over past decades due to their potentially superior performance in detecting mid-wave or long-wave infrared (MWIR or LWIR) light[1, 9, 139-142]. Compared to the already commercialized state-of-the-art mercury cadmium telluride (MCT) detectors or quantum well infrared photodetectors (QWIPs), SLS detectors have competitive advantages such as a theoretically higher operating temperature, a suppression of Auger recombination, and an ability to control the detectors' effective bandgaps by engineering layer thicknesses in a binary system of ternary or quaternary alloys[1, 141]. However, the theoretically superior performance of SLS detectors has yet to be demonstrated experimentally or commercially, with material defects and growth imperfections considered as the major limiting factors for these infrared detector material systems[3, 143, 144]. Improving the material quality of SLS's requires techniques to characterize and understand the carrier dynamics of this material. However, characterizing material quality, and understanding the effect of material quality on device operation, for the narrow effective bandgap SLS's, often consisting of hundreds of alternating layers of alternating group V materials, and the potential concerns regarding intermixing, strain, and defect formation, requires a multi-pronged approach. Invaluable information can be gleaned from electron microscopy and optical and electronic material and device characterization techniques. In addition, various techniques are already being utilized for measuring the minority carrier lifetime of SLS's [9, 129]. However, there is no viable technique reported so far to measure the vertical mobility, which is the other most important parameter for SLS detectors. EBIC offers a potential approach for characterizing both material quality and device operation, measuring the minority carrier diffusion characteristics of SLS materials, and has been utilized as a valuable supplemental characterization tool for understanding material quality, for instance in InAs/GaSb SLS detectors as a function of interfacial layers [125] and for the promising Ga-free InAs/InAsSb T2LS material system[145]. The latter SLS material system has attracted growing interest resulting from demonstrated reductions in dark currents and longer minority carrier lifetimes compared to the early versions of SLS detectors employing the InAs/GaSb material system, hypothesized to result from the absence of native defects associated with Ga-associated defects in the GaSb layers[9, 10, 129]. Recently, the introduction of Gallium into the InAs layer of InAs/InAsSb SLS's, has been proposed as a possible improvement to SLS detector active region design, and has been experimentally shown to improve the detector absorption coefficient due to increased overlap of electron and hole states in the superlattice[146]. In addition, the InGaAs/InAsSb SLS material system, when compared to the Ga-free InAs/InAsSb material system, are theoretically expected to show higher vertical hole mobility due to reduced hole effective mass. However, the diffusion length and vertical carrier mobility in these SLS structures, key parameters for understanding carrier dynamics and potential device performance in the material system, have yet to be investigated.

In this thrust, we investigate the effect of Ga content in In(Ga)As/InAsSb SLS detector devices using a combination of time-resolved photoluminescence (TRPL) and EBIC measurements, leveraging a new approach to EBIC parameter extraction. We demonstrated that the previous approaches to EBIC modeling leave uncertainty in the fitting parameters for SLS materials, and we introduced a new numerical approach to EBIC modeling which improves the spatial resolution of our model and reduces the uncertainty in our extracted fitting parameters, modeling not only the EBIC lineshape as a function of position, but the

magnitude of the EBIC response. We use the latter to better understand the effects of nonequilibrium carrier concentration on the minority carrier transport properties, and discuss the limitations of EBIC associated with changes in minority carrier lifetime at higher nonequilibrium carrier concentrations. We apply our developed numerical EBIC modeling technique to understand the behavior of our In(Ga)As/InAsSb SLS's and discuss the agreement and discrepancies between our developed model and experimental results. The extracted fitting parameters are compared to those extracted using external quantum efficiency measurements performed on the same material with good agreement.

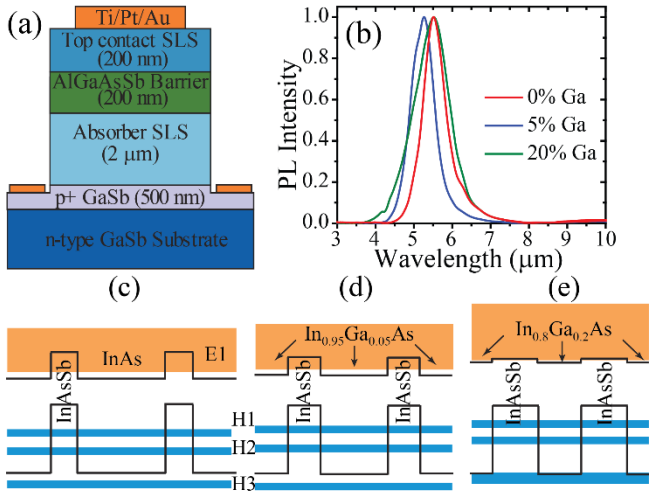

Figure 5.17 Fig. 23. (a) Schematic of the layer structure and device geometry of the tested SLS infrared detectors, (b) normalized photoluminescence (PL) spectra of all three detectors at 80 K, showing similar cut-off wavelengths for each of the three designs. Conduction and valence band profile along with electron and hole minibands for two periods of the (c) InAs/InAs$_{0.65}$Sb$_{0.35}$, (d) In$_{0.95}$Ga$_{0.05}$As/InAs$_{0.65}$Sb$_{0.35}$ and (e) In$_{0.80}$Ga$_{0.20}$As/InAs$_{0.65}$Sb$_{0.35}$ SLSs used for the absorber regions.

Three In(Ga)As/InAsSb based nBn infrared photodetectors, grown by molecular beam epitaxy (MBE) on GaSb substrates, were investigated in this work. From the bottom to top, our devices consist of a GaSb buffer layer, a 2μm n-type SLS absorption layer (n-doped 2×10^{16} cm^{-3}), an undoped 200nm AlGaAsSb electron-blocking barrier layer, and a 200nm n-type SLS top contact (n-doped 2×10^{16} cm^{-3}). The three different SLS designs are: 17ML InAs/5.5ML InAs$_{0.65}$Sb$_{0.35}$ (0% Gallium content), 13ML In$_{0.95}$Ga$_{0.05}$As/6.5ML InAs$_{0.65}$Sb$_{0.35}$ (5% Gallium content), and 8.5ML In$_{0.80}$Ga$_{0.20}$As/9ML InAs$_{0.65}$Sb$_{0.35}$ (20% Gallium content), each designed to be strain balanced and also to have similar effective bandgaps. Figure 5.17(a) shows the schematic of the layer structure and device geometry of the SLS devices investigated in this work, while Figs. 5.17(c), (d), and (e) show the band diagram of two periods of the InAs/InAsSb, In$_{0.95}$Ga$_{0.05}$As/InAsSb, and In$_{0.80}$Ga$_{0.20}$As/InAsSb designs, respectively.

Samples were initially characterized with a Bruker v80V Fourier transform infrared (FTIR) spectrometer, using mid-IR photoluminescence (PL) spectroscopy in an amplitude modulation step-scan experiment. Figure 5.17(b) shows the low temperature (80K) PL spectra for each sample, indicating similar cut-off wavelengths for the three SLSs detectors investigated in this work. The same samples were also characterized using temperature

dependent time-resolved photoluminescence (TRPL). Here, the as-grown samples were pumped with a Q-switched diode-pumped laser emitting ~1ns pulses at λ=1064nm, with 10kHz repetition rate and varying pulse energies (controlled by neutral density filters at the laser output). The light emitted from the samples is collected with a parabolic mirror, and focused onto a high-speed MCT detector (Kolmar Technologies) using a Ge lens (which also serves, along with a low-pass 3.6μm filter, to block the scattered pump laser light). The output of the MCT detector is collected using a 14-bit LeCroy oscilloscope and the tail of the PL emission for all pulse energies is modeled using a single-exponential fit in order to extract the low-injection minority carrier lifetime[108]. TRPL data is collected from all samples for temperatures from 80K to 200K.

The EBIC measurements were carried out on detector devices whose growth is described above, fabricated into mesa structures with solid, continuous metal contact pads, as shown in Fig. 5.17(a). For the EBIC measurements, the fabricated devices are cleaved through the top contact and mesa, and then mounted in the chamber of a JEOL 7000F scanning electron microscope (SEM) such that the cleaved surface is positioned normal to the SEM's electron beam (Fig. 24(a)). The sample substrate is grounded to the SEM mount, and the top and bottom contacts to the detector are wire-bonded to ceramic stand-offs, connected to BNC cables. The current collected across top and bottom contacts of the device is amplified using a Stanford Research SR570 preamplifier connected via electrical feedthroughs in the SEM. The output of the pre-amplifier is fed into the SEM DigiScan control software and a "current image" of the sample is generated. It is important to note that this current image includes not only the EBIC signal, but also a DC dark current from the sample. This dark current (measured in the EBIC image as the current far from the collection junction) is removed from the final EBIC signal with a uniform background subtraction. The remaining EBIC image is averaged (parallel to the growth plane, along the y-direction of Fig. 5.18(a)) to produce an EBIC profile as a function of beam position in the growth direction. Each device is measured at temperatures from 80K to 200K with beam energies ranging from 10 keV to 30 keV in 5 keV increments. The experimental EBIC profile is compared to the modeled profile, which allows for an extraction of the minority carrier diffusion length, *L*, and the surface recombination velocity to diffusivity ratio, *S/D*.

Our EBIC data is compared to values for the vertical hole mobility extracted from external quantum efficiency (EQE) measurements. First, the EQE of fully reticulated single element detectors at different temperatures was measured[147] following a standard radiometric characterization technique described in Ref. [108]. The variation of the theoretically expected quantum efficiency with the diffusion length (L_h) for the same set of detectors was analytically calculated as described in Ref. [143], using the experimentally determined absorption coefficient from the detector materials, measured using the technique described in Ref.[148]. The diffusion length values at different temperatures were then extracted by fitting the experimental EQE data points at corresponding temperatures.

The power of the EBIC technique is somewhat offset by the significant modeling required to extract meaningful values from the experimental data. The EBIC signal, for a given electron beam position on the cleaved surface, is proportional to the minority carrier collection efficiency of the device junction. In the idealized picture of EBIC, an extremely narrow electron beam acts as a point source generator of electron hole pairs (EHPs), and

thus for each beam position one can assume a singular collection efficiency. In reality, the small spot size, high energy beam of electrons scatters upon reaching the material surface, and thus results in an EHP generation volume extending both laterally from the beam position (x, along the growth direction and y, along the growth plane) and into the sample (z, depth from cleaved surface). Figure 5.18(a) shows the orientation of the electron beam on the SLS infrared detector. We define the probability of collection ($\varphi(x,y,z)$), as the probability that a hole generated at point (x,z) will diffuse to the detector junction and be collected as a photocurrent. The collection probability for EHPs generated at different x positions (for the same position of the electron beam, x_o) will vary, depending on their relative proximity to the junction. The EHPs' probability of collection will also vary as a function of depth into the sample (z), due to surface recombination effects. Finally, $\varphi(x,y,z)$ can also depend on y, for EBIC measurements close to detector mesa sidewalls, on samples with metal aperture contacts, or for samples with inhomogeneous defect densities (on a length scale on the order of the width of the carrier generation volume). The efficiency of collection, $\eta(x_o)$, is effectively a measure of the EBIC current generated by a the EHP generation distribution associated with a beam position x_o, and can be calculated by taking the volume integral of the product of the probability of collection, $\varphi(x,z)$, and the electron hole pair (EHP) generation function, $g_{E_b}(x-x_o,y,z)\left[\frac{\text{EHP}}{\text{s-cm}^3}\right]$, where the "$E_b$" subscript indicates the fact that our EHP distribution depends on the electron beam energy. The solid metal contact pads, the location of our EBIC measurement (far from the mesa sidewalls), and the fact that we see consistent EBIC signals across the lateral range (y-direction) of the sample cross-sections, enables us to approximate the probability of collection in our measurement as having no y-dependence, such that we can integrate our three-dimensional (3D) generation function to give a two-dimensional (2D) generation function $h_{E_b}(x-x_o,z)=\int_{-\infty}^{\infty} g_{E_b}(x-x_o,y,z)dy$. For a sample using metal contacts with apertures for light transmission, or with defect spacing on the order of the width of the generation function, the full 3D generation function would need to be used. At each beam position (x_o), we solve the integral

$$\eta_{E_b}(x_o) = \int_{-\infty}^{+\infty} dx \int_0^{\infty} h_{E_b}(x-x_o,z)\,\varphi(x,z)\,dz \qquad (12)$$

where $x=0$ denotes the position of the collection junction (at the barrier/absorber interface) and $z=0$ the cleaved surface of the device. The 2D generation function $h_{E_b}(x-x_o,z)$ is determined numerically using CASINO Monte Carlo software simulations for each position (x_o) across the growth direction of the device, while the probability of collection, $\varphi(x,z)$, can be derived from the diffusion equation.

In previous approaches to EBIC modeling, the normalized 2D carrier generation function $h_{E_b}(x-x_o,z)$, is analytically expressed as shown in Equation (12).

$$h_{E_b}(x,z) = \frac{1}{H}\exp\left(-\frac{x^2}{\sigma_1^2}\right) z^2 \exp\left(-\frac{z}{\sigma_2}\right) \qquad (13)$$

where H is the normalization factor, σ_1 represents the spread of the generation profile in the x direction, and σ_2 the spread of the profile in the z direction (both of which have empirical dependence on beam energy). Eq. (13) is used to fit the normalized Monte-Carlo simulated generation distribution, with the fitting performed in the x and z directions

separately. Figure 5.18(b) and (c) show the Monte Carlo-simulated EHP generation profiles in the *x* and *z* directions, respectively, for incident electron beam energies of 10 keV and 15 keV, for the electron beam impinging at $x_o = 1$ μm (with $x = 0$ again being the barrier/absorber interface). The analytical fitting functions ($h_{E_b}(x - x_o, z)$) for each beam energy are plotted as dashed lines in Figure 5.18(b, c). Comparison between the numerically simulated generation distribution and the analytical fitting functions show good agreement in the *z* direction, into the sample. However, the analytical expression for the *x*-dependence (along the growth direction) of the generation profile does not accurately capture the strength of EHP generation near the position of the incident electron beam (x_o). To quantify this, we compare the percentage of EHPs generated within the range $x_o \pm 40nm$ for both the analytical and numerical generation distributions as a function of beam energy. At low beam energies (10keV), the two approaches are similar (62% vs. 61%), but as beam energy increases, the analytical approach diverges from our numerical results: 37% vs. 30%, 27% vs. 19%, 21% vs. 13% and 17% vs. 10% (numerical vs. analytical) for 15, 20, 25, and 30 keV beam energies, respectively. In addition, the normalization of the beam profiles removes the ability to model the relative amplitude of the EBIC signal as a function of beam energy and current.

Once the generation distribution is calculated, the diffusion equation, describing the transport of beam-generated minority carriers, is used to determine the probability of collection, $\varphi(x, z)$. Originally, this expression was derived for EBIC modeling of bulk p-n junction diode devices[149, 150, 132] and later also used to model SLS p-n junction detectors[126]. The probability of collection expression for SLS nBn detectors must be adjusted somewhat, and is given below in Eq. (13)(a-d):

$$\varphi(x,z) = \frac{2S_h}{\pi D_h}\int_0^\infty e^{x\sqrt{k^2+\left(\frac{1}{L_h}\right)^2}} \frac{\cos(kz) + \frac{1}{kD_h}S_h \sin(kz)}{k^2 + \left(\frac{S_h}{D_h}\right)^2} dk;\ -0.4 < x < -0.2\ \mu\text{m} \qquad (14)(a)$$

$$\varphi(x,z) = 1;\ -0.2 < x < 0\ \mu\text{m} \qquad (14)(b)$$

$$\varphi(x,z) = \frac{2S_h}{\pi D_h}\int_0^\infty e^{-x\sqrt{k^2+\left(\frac{1}{L_h}\right)^2}} \frac{\cos(kz) + \frac{1}{kD_h}S_h \sin(kz)}{k^2 + \left(\frac{S_h}{D_h}\right)^2} dk;\ 0 < x < 2\ \mu\text{m} \qquad (14)(c)$$

$$\varphi(x,z) = 0;\ x > 2\ \mu\text{m} \qquad (14)(d)$$

As can be seen in the above expressions, the $\varphi(x, z)$ expression, once integrated over *k*, depends entirely on the minority (hole) carrier diffusion length, L_h, and the surface recombination velocity to diffusivity ratio, S_h/D_h. Here the *k's* denote discrete solutions to the transcendental equation governing the z-dependence of the probability of collection, which for thick materials ($z \gg L$) become continuous, resulting in the integrals of Eq. (14) , as detailed in Ref. [126]. In Figure 5.18(d-f), we show contour plots of the probability of collection in our SLS structures for various L_h and S_h/D_h combinations: $L_h = 0.5\ \mu m$ and $S_h/D_h = 1\ \mu\text{m}^{-1}$, $L_h = 0.5$ μm and $S_h/D_h = 10\ \mu\text{m}^{-1}$, and $L_h = 1$ μm and $S_h/D_h = 1\ \mu\text{m}^{-1}$, respectively. From these plots one can clearly see the effect of higher S_h/D_h values, significantly reducing the probability of collection at the cleaved surface ($z = 0$ μm), as more of the generated EHPs recombine via surface states before they can be

collected. As expected, increases in L_h broaden the probability of collection towards the substrate.

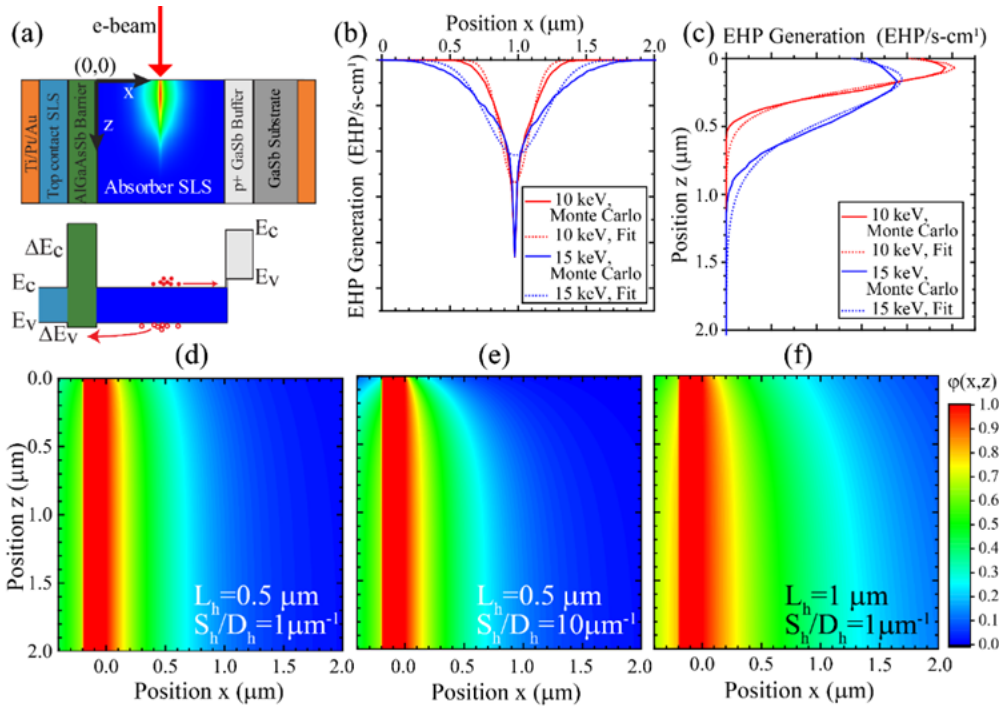

Figure 5.18 (a) EBIC experimental configuration with contour plot of generation distribution superimposed over absorber region. Also shown is a band-structure schematic of the detector samples studied. The Monte Carlo simulation (solid) of, and analytical fit (dashed) to, the excited carrier generation distribution created by the electron beam (10keV-red and 15keV-blue) of a scanning electron microscope (SEM) plotted as a function of the position in the (b) x-direction, integrated in y *and* z *and (c) z-direction, integrated over* x *and* y*. The modeled probability of collection for an nBn detector plotted for (d)* $L_h = 0.5\ \mu m$ *and* $S_h/D_h = 1\ \mu m^{-1}$*, (e)* $L_h = 0.5\ \mu m$ *and* $S_h/D_h = 10\ \mu m^{-1}$*, and (f)* $L_h = 1\ \mu m$ *and* $S_h/D_h = 1\ \mu m^{-1}$*, showing the effect of each variable on the probability of collection.*

As described in Eq. (12) above, the integral of the product of the 2D EHP generation function, $h_{E_b}(x - x_o, z)$, and the probability of collection, $\varphi(x, z)$, over the *x*-*z* plane, returns the efficiency of collection, $\eta(x_o)$. The use of the analytical expression for the EHP generation function given in Eq. (12) and the probability of collection expressions derived from the diffusion equation shown in Eqs. (9), allows for an analytical expression to be derived for the collection efficiency $\eta_{E_b}(x_o)$,[126] significantly simplifying the EBIC modeling process. However, because both the EHP generation function and the probability of collection are typically normalized, the resulting $\eta_{E_b}(x_o)$ does not reflect the relative changes in $\eta_{E_b}(x_o)$ with changing beam energy and current. In addition, as mentioned earlier, while the analytical expressions for generation distribution allow for a final analytical expression for $\eta_{E_b}(x_o)$, they do not offer an entirely accurate picture of the actual EHP generation distribution, especially in the lateral (x and y) directions. This can

lead to weaker fits to the data, and thus slightly more uncertainty in the extracted values for L_h and S_h/D_h.

With the rapid recent increases in computational speed and power, an analytical approach to EBIC modeling may no longer be the only suitable technique for parameter extraction. To demonstrate this, we developed a technique for our EBIC modeling which leverages a numerical approach to solve Eq. 7. Our Monte Carlo simulations effectively return a volumetric distribution of EHP generation, $h_{E_b}(x_i - x_o, z_j)$, for some number of incident high energy electrons (*N*, typically in the 10's of thousands). Using the recorded beam current (I_{beam}, measured by a Faraday cup) for each beam energy, we can determine the EHP generation rate as a function of position, $G_{EHP}(x_i - x_o, z_j) = \frac{h_{E_b}(x_i - x_o, z_j) I_{beam}}{Ne}$ [EHPs/s], where *e* is the charge of an electron. Using this Monte Carlo-simulated generation distribution, as opposed to the analytical fit of Eq. (13), we can perform a numerical integration by dividing our device into discrete differential volumes and summing the current contributed to the total EBIC signal from each of these differential volumes (Eq. (14)(a)), which we can use to determine the EBIC current ($i_{E_b}(x_o)$) and normalized EBIC current ($I_{E_b}(x_o)$) as a function of position (Eq. (14)(b)):

$$\eta_{E_b}(x_o) = \sum_{i=-\infty}^{+\infty} \Delta\tilde{x}_i \sum_{j=0}^{+\infty} h_{E_b}(x_i - x_o, z_j)\, \varphi(x_i, z_j)\, \Delta z_j \qquad (15)(a)$$

$$I_{10keV}(x_o) = \frac{\eta_{10keV}(x_o) I_{beam}(10keV)}{NA_{mod}} = \frac{i_{10keV}(x_o)}{A_{mod}} \quad , \quad where\ I_{10keV}(x = 0) = 1 \qquad (15)(b)$$

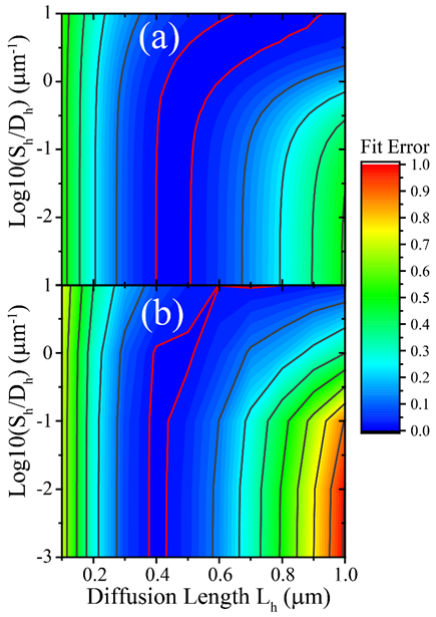

Figure 5.19 Contour plot of the normalized fit error between the low beam energy experimental data and modeled EBIC data obtained using (a) analytical and (b) numerical integration approaches as a function of the fitting parameters L_h and S_h/D_h. The experimental data used comes from the InAs/InAsSb SLS device at 120 K. The calculated fit error for each approach, (a) analytical and (b) numerical integration, is normalized to the same value. In the plots above, we use the maximum calculated fit error of the numerical integration approach (b) across the parameter space investigated (the axes of our contour plots), as our normalization constant. Red lines show normalized SSE=0.02, for comparison of fit uncertainty.

The fitting process then begins by looking at the lowest energy electron beam data. For our initial fitting, we normalize both our modeled and experimental data such that $I_{10keV}(x_o = 0) = 1$, using scaling factors A_{mod} and $A_{exp}(10\text{keV})$, respectively. We evaluate the numerical sum in Eq. (15)(a), and the scaling of Eq. (15)(b), for a range of L_h and S_h/D_h values, and then measure the fit error by summing the square of the deviation of our modeled current to the experimental current. Figure 5.19 shows the contour plot

generated from this fitting process for both the analytical (Figure 5.19(a)) integration and the numerical (Fig. 5.19(b)) summation approaches, in this case using our data from the InAs/InAsSb SLS device at 120 K as representative data.

A number of features can be observed from the comparison offered by Figure 5.19. First, we see that the effect of the S_h/D_h parameter on our fit quality is minimal, particularly for low S_h/D_h values ($< 0.1\mu m^{-1}$). This is to be expected, as once the surface recombination is slower than the diffusion of carriers toward the junction (effectively the carrier lifetime τ_p), one would not expect surface recombination to have a significant quantitative effect on the model. In addition, we do observe a narrower range of our fit quality when we utilize the numerical integration technique, suggesting at least a slight reduction in the uncertainty of the extracted L_h term, presumably a result of the improved spatial resolution offered by employing the raw output of our Monte Carlo simulations, as opposed to the analytical fit to this simulation.

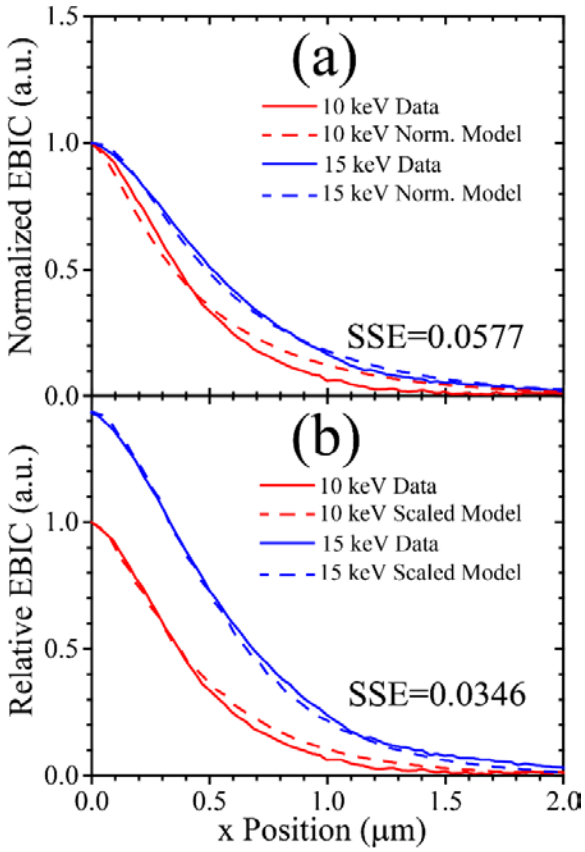

Figure 5.20 Experimental and modeled EBIC data for InAs/InAsSb detector device at 120 K for beam energies of 10 keV and 15 keV. (a) Experimental data (solid) and modeled fit using analytical expression for h_(E_b) (x̃-x_o,z̃) *(dashed), with experimental and modeled data normalized for each beam energy. (b) Experimental data (solid) and modeled fit using numerical expression for* h_(E_b) (x̃_i-x_o,z̃_j) *(dashed), with modeled and experimental data for 15 keV is scaled by A_mod and A_Exp, respectively, which were determined by fitting to the 10 keV data. The averaged fit error (SSE) for each approach is shown in each plot.*

Once the best fit for the L_h and S_h/D_h parameters are obtained for the low energy electron beams, we model the higher beam energies by inserting the L_h and S_h/D_h, extracted for low beam energies, into the expression for $\varphi(x_i, z_j)$, and now using generation distribution, $h_{E_{b>15keV}}(x_i - x_o, z_j)$ obtained for the higher beam energy, and the beam current measured for the higher beam energy conditions, we calculate the new EBIC curve. For a beam energy of 20keV, this would appear as:

$$I_{20keV}(x_o) = \frac{\eta_{20keV}(x_o) I_{beam}(20keV)}{NA_{mod} I_{beam}(10keV)}, where\ now\ I_{20keV}(x_o = 0) \neq 1 \quad (16)$$

The result of this approach is an EBIC curve scaled in amplitude (due to the changes in I_{beam} and $\eta_{E_b>15keV}$), with only slight changes in EBIC profile shape resulting from the change in the carrier generation distribution at higher beam energies. The immediate and clear benefit of this approach is the ability to model not only the change in the EBIC profile, but the amplitude as well. Figure 5.20(a) shows, for 10 keV and 15 keV beam energies, the comparison of our normalized experimental data to the normalized EBIC model using the analytical fit to the carrier generation profile. Thus for the data of Figure 5.20(a), we scale both our modeled and experimental $I_{E_b}(x)$ such that, once again, $I_{10keV}(x_o = 0) = I_{15keV}(x_o = 0) = 1$, and in doing so lose any information regarding the relative strengths of the EBIC signals. In Figure 5.20 (b), however, we show the comparison of modeled and experimental data using our numerical approach (Eq. (16)). Here, the experimental data is scaled by the very same factor as our 10 keV data, $A_{exp}(10\text{keV})$, while the scaling of our modeled data uses both the same factor as our 10 keV model, A_{mod}, as well as the additional scaling coming from the change in the beam current. Thus, the change in the magnitude of the modeled EBIC profile results from measurable experimental parameters (beam energy and current), more accurately reflecting the change in experimental parameters with increasing beam energy. The advantage of this approach can be clearly seen in Figure 5.20(b), where we observe excellent fits to both the shape and magnitude of the EBIC profile. As is indicated in Figure 5.20, our averaged sum of squared error (SSE) for the 10 keV and 15 keV data improves from 0.0577 to 0.0346 using our numerical EBIC approach. At higher beam energies, the normalized EBIC model will give better fits, for reasons discussed later.

Our approach to EBIC modeling not only offers improved fitting to the experimental data with decreased uncertainty in the extracted values of L and S/D, but also allows us to predict the amplitude of the EBIC signal for increasing beam energies, as we can see in Figure 5.20(b). This will provide us with additional valuable data points for understanding EBIC measurements of our samples. Below we discuss the results from the samples investigated, and benefits and challenges of the EBIC modeling technique described above.

5.7. Comparison of EQE and EBIC approaches (Wasserman, UIUC)

While the results from the EBIC measurement provide diffusion lengths for our devices as a function of temperature, a more holistic understanding of minority carrier transport is achieved when the extracted diffusion lengths are combined with minority carrier lifetimes (τ_p), allowing for the calculation of the hole diffusivity (D_h) and, using the Einstein relation, minority carrier vertical mobility (μ_h):

$$D_h = {L_h^2}/{\tau_p} \quad , \quad \mu_h = qD_h/kT \quad (17)$$

Time-dependent photoluminescence (TRPL) spectroscopy allows for the measurement of the minority carrier lifetime in the low injection regime, where typical IR detectors operate. The full expression for carrier lifetime in a SLS is most accurately expressed as[129]:

$$\tau^{-1} = \frac{(n_o+\delta n)}{\tau_{po}(n_o+\delta n)+\tau_{no}\delta n} + B(n_o+\delta n) + C_n(n_o+\delta n)^2 \qquad (18)$$

Where δn is the excess carrier concentration, τ_{po} and τ_{no} are the minority and majority carrier Shockley-Read-Hall (SRH) lifetimes, B is the bulk radiative coefficient, and C_n is the Auger recombination coefficient. For low injection, $\delta n \ll n_o$, and lightly doped material ($n_o < 2.5\times10^{15}$ cm^{-3}), the minority carrier lifetime is dominated by the contributions from SRH and radiative recombination, and can be described by a single value for lifetime (independent of excess carrier concentration). Recent result have demonstrated that for more highly doped material ($n_o > 2.5\times10^{15}$ cm^{-3}), the low injection lifetime is dominated by Auger recombination, though the resulting TRPL data can still be fitted with a single exponential[151]. Figure 5.21 shows the TRPL results from all of our samples for temperatures of 80K, 120K, 160K, and 200K, using a single-exponential fit to the tail of the TRPL data, from which we can extract the temperature dependent carrier lifetime. From this data we observe decreasing carrier lifetimes with increasing Ga content of our samples, with the 0% Ga sample showing a factor of 2 or greater lifetime than the 20% Ga sample across the entire temperature range investigated. All samples display similar decreases in minority carrier lifetimes as a function of temperature, an indication that the extracted carrier lifetime is an Auger-limited lifetime, as opposed to resulting from SRH recombination, as would be expected at our intended doping concentrations of $n_o = 2\times10^{16}$ cm^{-3}. [108] The observed decrease in carrier lifetime with increased Ga concentration, in a more lightly doped SLS, could indicate the presence of additional defects associated with Ga in our SLS's. Alternatively, the decrease in lifetime with increasing Ga could result from the increased overlap between electron and hole wavefunctions in the InGaAs/InAsSb SLS material system[152], and thus shorter radiative recombination times. However, low-injection lifetimes in our material system, as discussed above, are most likely Auger-limited. Thus, from the lifetime data alone, it cannot be said that the presence of Ga either introduces non-radiative recombination centers or improves radiative lifetimes in the SLS structure. The decrease in lifetime as a function of Ga content is more likely a result of changes in the Auger lifetime of our highly doped samples, an effect we will discuss below.

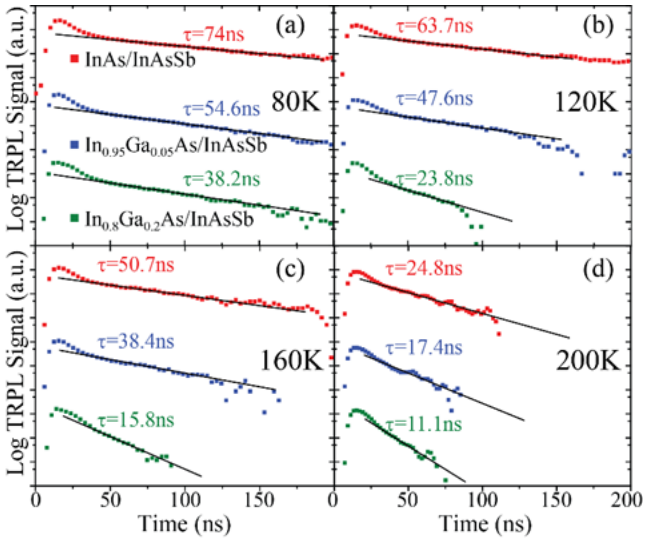

Figure 5.21 FIG. 27: Time-resolved photoluminescence (TRPL) signals (scatter) from InAs/InAs$_{0.35}$Sb$_{0.65}$ (red), In$_{0.95}$Ga$_{0.05}$As/InAs$_{0.35}$Sb$_{0.65}$ (blue), and In$_{0.80}$Ga$_{0.20}$As/InAs$_{0.35}$Sb$_{0.65}$ (green), detector samples at (a) 80K, (b) 120K, (c) 160K, and (d) 200K, with exponential fittings (solid lines) and the extracted low-injection carrier lifetimes shown for each temperature and sample.

Extracting our temperature dependent lifetime from the TRPL measurements (Fig. 5.21(a)), and our temperature-dependent diffusion length from the numerical model of the EBIC measurement (Fig. 5.22(b)), we are able to measure the vertical hole mobility for each of the SLS samples as a function of temperature. Figure 5.22(c) shows the resulting temperature dependent vertical hole mobility for all three of our samples, where the uncertainty shown in our data is determined using the $SSE < 0.02$ metric depicted in Fig. 5.19.

In a separate analysis, the hole diffusion lengths for the same set of samples were determined by fitting the experimental external quantum efficiency (EQE) of the detectors to the theoretically expected EQE at temperatures in the same range (80 -200K). The EQE experimental approach is detailed in Ref. [144], and requires careful absorption and reflection measurements with a (spatially and spectrally) well-calibrated IR light source, and accurate current measurements, which when combined with an analytical model, allow for the extraction of the minority carrier diffusion length. Using those values of L_h and the TRPL lifetime values, another set of values for the vertical hole mobility was obtained. We compare these results in Figure 5.22 and both approaches show vertical hole mobilities

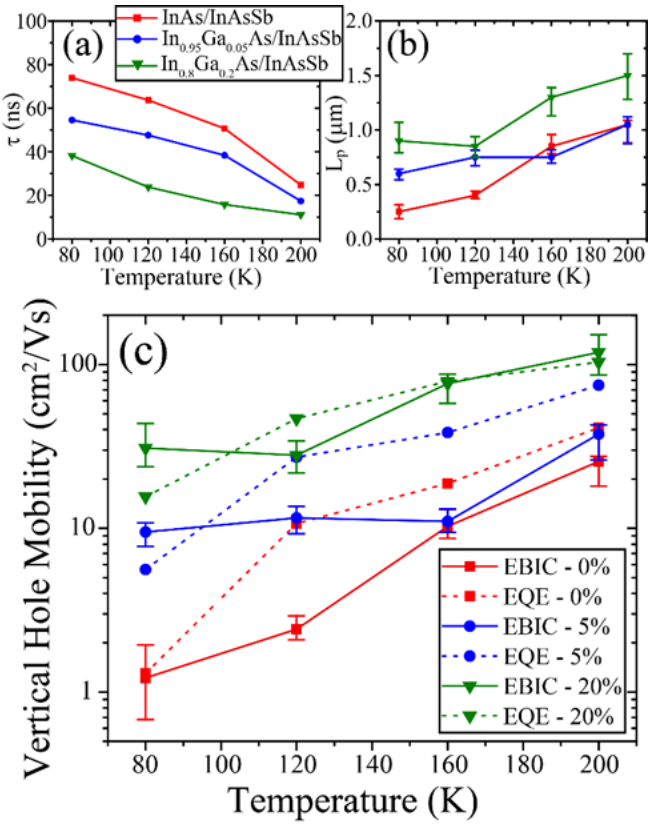

Figure 5.22 FIG.28. (a) Plot of minority carrier lifetimes at low injection levels as a function of temperature for the InAs/InAsSb (red), $In_{0.95}Ga_{0.05}As/InAsSb$ (blue), and $In_{0.80}Ga_{0.20}As/InAsSb$ (green) samples. (b) Extracted minority carrier diffusion lengths (L_h) for InAs/InAsSb (red), $In_{0.95}Ga_{0.05}As/InAsSb$ (blue), and $In_{0.80}Ga_{0.20}As/InAsSb$ (green) samples. (c) Vertical hole mobility for both InAs/InAsSb (red), $In_{0.95}Ga_{0.05}As/InAsSb$ (blue), and $In_{0.80}Ga_{0.20}As/InAsSb$ (green) samples, as determined by EBIC (solid) and EQE (dashed) techniques.

increasing as a function of temperature. In addition, both the EQE and EBIC techniques show increasing mobility, at all temperatures, for increasing Ga content in the SLS samples. Finally, we also observe a significantly stronger temperature dependence for the 0% Ga SLS sample (a factor of ~20) than the 5% and 20% Ga samples (factors of 4 and 5, respectively) across the T=80K to T=200K range of temperatures investigated.

The increase in vertical carrier mobility with increasing Ga content can be understood by recalling that a primary benefit of the addition of Ga to the InAs layers of an InAs/InAsSb SLS is the increase in the wavefunction overlap between electron and hole states in the SLS[152]. This overlap is caused not only by the weaker quantization of the states in the conduction band (due to the decrease in conduction band offset between the InAsSb and the In(Ga)As), but also from the decrease in thickness of the In(Ga)As barriers between the hole states in the InAsSb, which allows increased extension of hole states into the In(Ga)As hole barriers (which for the 20% Ga sample are only 8.5ML thick), and thus improved vertical transport. Band structure calculations of the vertical hole effective mass indicated that the effective mass decreased from $2.97m_o$ to $1.49\ m_o$ as the gallium composition was increased from 0 to 20%. These calculations do not take into account intersubband scattering effects[153], which could explain the discrepancy between the expected change in mobility and the actual change.

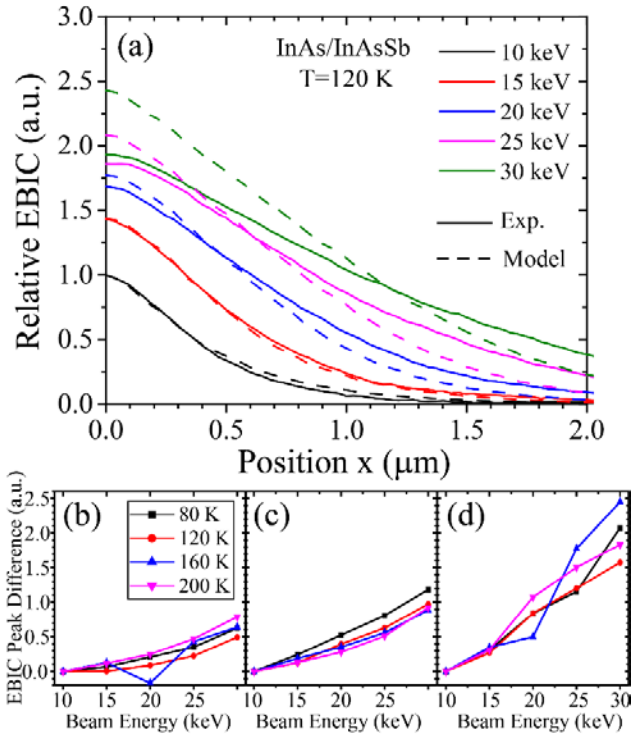

Figure 5.23 29. (a) Experimental (solid) and modeled (dashed) EBIC profiles for InAs/InAsSb SLS at T=120K as a function of beam energy. Difference between modeled and experimental beam current at the SLS junction ($x = 0$) for the (b) InAs/InAsSb and (c) $In_{0.95}Ga_{0.05}As$/InAsSb, and (d) $In_{0.80}Ga_{0.20}As$/InAsSb SLS's as a function of beam energy for all temperatures investigated.

Previous approaches to EBIC modeling searches for the optimized fitting parameters (L and S/D) which most accurately fit the EBIC profiles (lineshapes) for all beam energies. The argument for this approach is that at higher beam energies, the carrier generation volume probes deeper into the device, essentially providing a variation in the effective depth of the average EHP generated. Finding the optimized fitting parameters for all beam energies is thus argued to offer the ability to extract a more accurate S/D value. However, for many material systems, large variations in the S/D value have little to no effect on the accuracy of the fit to EBIC data, as can clearly be observed in Fig. 5.19. In fact, for the normalized EBIC fittings, many different combinations of L and S/D values can produce very similar EBIC profiles, with a greater uncertainty in the extracted diffusion length. At the same time, by focusing solely on the EBIC profile, it is possible that this technique discards valuable information which could be extracted from the relative

magnitudes of the EBIC profiles. Using our scaled EBIC fittings, however, not only do we decrease the uncertainty in extracted L_h and S_h/D_h for a given experimental condition, we are able to use the relative magnitude of our modeled EBIC signal to obtain improved fits and qualitative information regarding the performance of our devices as a function of excess carrier concentration.

Figure 5.23(a) shows the scaled fits to our EBIC data for the 0% Ga SLS sample at 120K for all of the beam energies investigated in this work, in addition to the 10 and 15 keV data already presented in Figure 5.20(b). The fits to our experimental data become progressively poorer as we move to higher beam energies. We can understand this effect by returning to our expression for carrier-dependent lifetime in Eq. (18), which indicates that for higher carrier concentrations, we would expect a decrease in the average lifetime of excited carriers due to increased Auger recombination, regardless of whether our SLS minority carrier lifetime is Auger- or SRH-limited at low excess carrier concentrations. A higher beam energy results in not only a broader carrier generation distribution, but also significantly higher carrier concentration (which is also affected by beam current). Thus, it would be expected that as we increase beam energy (and/or current), we would observe an increased deviation from our EBIC model (which we fit to the low beam energy data).

In fact, the deviation from our fit offers qualitative information regarding the carriers effectively "lost" to increased recombination rates (Auger) in our experiment. Figure 5.23(b), (c), and (d) show the difference between our scaled experimental and modeled EBIC signal at the SLS junction ($x = 0$) for the samples studied in this work. A largely monotonic increase in the deviation is observed for all samples at all temperatures (with the exception of one outlier data point: the 160K, 20keV data for the InAs/InAsSb SLS). In addition, we observe a weaker increase in the difference between our model and our data for the 0% Ga SLS than for the 5% Ga SLS, and significantly weaker than the 20% Ga SLS, whose experimental EBIC signal is far smaller than that predicted by our model. These results suggest that the effects of additional, carrier concentration-dependent, recombination mechanisms are correlated with increasing Ga content in our SLS structures. As Auger recombination is known to be quenched by increased quantization of charge carriers, the stronger signature of Auger recombination observed with increasing Ga content could be attributed to the decreasing conduction band offset and thus weaker quantization of conduction band electrons with increasing Ga content. Measuring the change in the difference between the modeled and experimental EBIC signal provides only a qualitative measure of the change in carrier lifetime. Future efforts will attempt to develop a quantitative understanding of this measure using samples with a clear transition between SRH and Auger limited lifetimes.

Previous approaches to EBIC modeling thus not only miss valuable information obtained from the relative magnitudes of the EBIC signal and model, but potentially could result in inaccurate parameter extraction. These approaches attempt to fit EBIC data from all beam energies simultaneously, including the higher beam energy data, where carrier lifetimes can be very different than for lower beam energy excitation. While this approach may be sufficiently accurate for materials with long diffusion lengths and relatively constant carrier lifetimes (small Auger coefficients), for materials with shorter diffusion lengths and larger Auger coefficients (such as narrow bandgap semiconductors), the fit to the data then may not accurately reflect the device parameters for typical operating

conditions (low excess carrier concentration). Though our improved EBIC modeling technique is thus far only able to extract qualitative information regarding the behavior of our devices as a function of carrier concentration, future efforts will look to develop a more quantitative approach to understand the effects of beam energy (and/or current) on the EBIC profiles of our narrow bandgap materials. In particular, we will look to investigate beam energy dependence of devices as a function of background doping. In doing so, we will look to observe the transition between SRH- and Auger-limited lifetimes, either by control of beam energy or doping, and use this data to develop quantitative modeling techniques to extract device parameters as a function of excess carrier concentration.

In the final year of this program we developed a technique for modeling electron beam induced current measurements which offers improved fitting to experimental data, lower uncertainty in parameter extraction, and qualitative information on carrier dynamics as a function of carrier concentration. Our approach utilizes Monte Carlo-simulated carrier generation distributions combined with an expression for carrier diffusion modified for the devices investigated, with a numerical integration to obtain a modeled EBIC profile which more accurately fits our experimental data. We use the modified EBIC model to extract minority carrier diffusion length and the surface recombination velocity to diffusivity ratio for In(Ga)As/InAsSb strained-layer superlattice detectors with 0, 5, and 20% Ga content. Though we use the presented technique to measure vertical hole mobility in narrow bandgap SLS materials with nBn detector architectures and diffusion dominated transport, our approach could well be adapted for lateral mobility studies (plan view) or for studying alternative material systems and/or detector architectures, with adjustments to the probability of collection expression (Eqn. (14)) and our Monte Carlo simulation parameters. Together with time-resolved photoluminescence (TRPL) measurements, we use our EBIC technique to extract the temperature dependent mobility of our samples. We observe increasing hole mobility as a function of the temperature, and higher mobilities for the InGaAs/InAsSb devices than the InAs/InAsSb device at all temperatures. In addition, we compare the deviation of our modeled EBIC response from the experimental data, and use this discrepancy to qualitatively understand the effect of additional recombination mechanisms, or changes in the existing recombination rates, in our samples. The In(Ga)As/InAsSb SLS material system provides the opportunity to investigate the effects of electron/hole wavefunction overlap in narrow bandgap materials by control of Ga content in the In(Ga)As layers. The extracted temperature dependent mobility and beam-energy dependent current amplitudes for our samples are discussed using the framework of wavefunction overlap and carrier quantization, and offer an understanding of the effects of bandstructure design on carrier dynamics in the SLS material system. The presented work offers an approach to electron beam induced current measurements and parameter extraction with improved fitting of the experimental data, lower uncertainty and the potential for measuring device properties as a function of injection regime. While in this work we investigate narrow bandgap SLS materials, the approach presented is applicable to the investigation of a wide range of semiconductor-based electronic and optoelectronic devices.

5.8. InSb interfacial treatment improves the strain balance and reduces large strain fluctuations in the InAs/GaSb T2SL (Zuo, UIUC)

We investigated the structural effects of the interfacial treatment using a thin layer of InSb in the InAs/GaSb SLs. The composition and strain of the SLs with and without the interfacial treatment were studied by atomic resolution STEM and EELS. By correlating composition with strain, we found that the interfacial treatment reduces the amount of GaAs bonds at the Sb-Ga-As-In interfaces and leads to a symmetric interface strain profile and reduces large strain fluctuations near the interface.

Two InAs/GaSb T2SLs are studied here; both were grown by MBE at IQE (Bethlehem, PA). They are named as sample A (IFA, with no interfacial treatment) and sample B (IFRA, with interfacial treatment). These samples were characterized by EBIC in Section 5.4. Both samples consist of a 500 nm thick p-doped GaSb bottom electrode grown on the GaSb substrate, and the InAs/GaSb T2SLs on top of the GaSb. The T2SLs are designed to achieve the cutoff wavelength of about 11 μm. It is comprised of 4.5 nm InAs and 2.4 nm GaSb, which is repeated for 80 periods for a p-doped superlattice, followed by 300 periods of an absorber region, and 80 periods of an n-doped superlattice. For sample B with interfacial treatment, a thin InSb layer (~ 2.4 Å) was intentionally forced on top of the GaSb layer before growing InAs.

The specimen for the cross-sectional STEM observation was prepared by mechanical polishing, followed by Ar ion milling at 3.0 and 2.0 kV at the glancing angle of 6˚ for electron transparency. HAADF imaging, using a Nion UltraSTEM, which is equipped with a spherical aberration corrector, was operated at 100 kV to obtain atomic resolution images of InAs/GaSb T2SLs and to perform EELS (electron energy loss spectroscopy) analysis. The atomic resolution images were later used to measure strain on the atomic scale. The convergence semi-angle of the electron beam of 31 mrad, and the detector cutoff angles of 86-200 mrad were used for HAADF imaging. EELS data were acquired using the Gatan Enfina EELS installed on the Nion UltraSTEM. The spectra covered the energy loss signals for every element in the InAs/GaSb T2SLs.

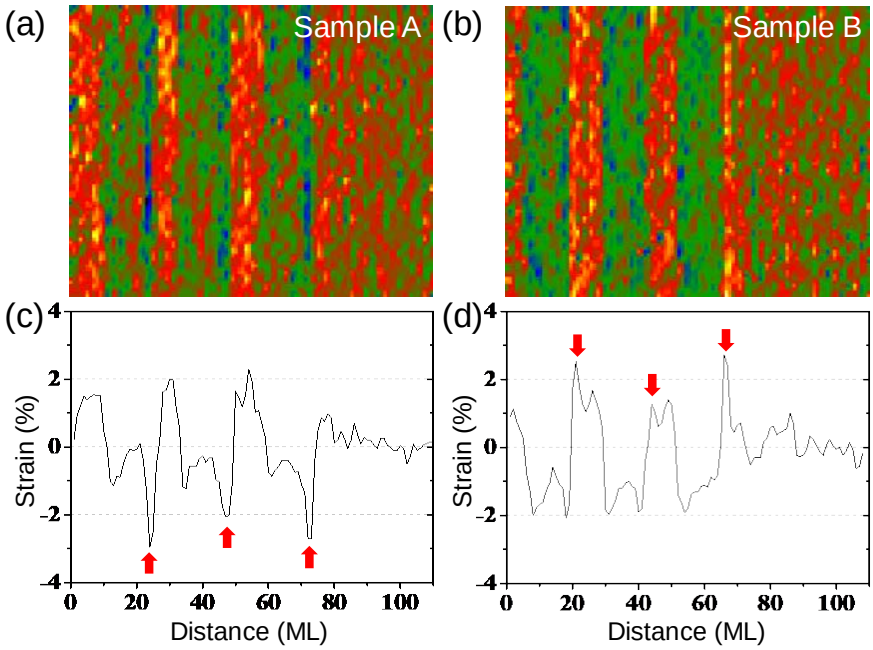

Figure 5.24 Strain maps of sample (a) A (IFA) and (b) B (IFRA), obtained by averaging strain maps from cation and anion sub-lattices. Corresponding averaged strain profiles for sample (c) A and (d) B are shown.

To quantify the HAADF images, we constructed separate cation and anion lattice images using the peak separation method described in Ref. [39]. Briefly, in this technique, each dumbbell feature in the recorded HAADF image along the [110] direction is fitted with two Gaussian peaks, resulting in separate fitted images for cation and anion lattices. By subtracting fitted image consisted of only anions or cations from the original image, separate images with cations or anions can be obtained. Since this method leaves only one type of atomic columns, whose intensity is not affected by the neighboring atomic columns, precise measurements of atomic column positions can be successfully made. The positions of every atomic column in cation and anion sub-lattices are located by the correlation based technique based on template matching (TeMA).[56] The detailed procedure of peak separation method and strain mapping using TeMA is explained in elsewhere.[39]

Figure 5.24(a) and (b) shows the strain maps of sample IFA and IFRA, respectively. These are the representative stain maps obtained by averaging the strain maps from cation and anion lattices (Strain maps for separate sub-lattices are discussed later in Figure 5.25). The strain profiles along the growth direction also plotted in Figure 5.24(c) and (d). The strain measured here is based on the out-of-lattice mismatch between the film and the reference, a GaSb bottom electrode, expressed by $\varepsilon^{\perp} = (a_f^{\perp} - a_{GaSb})/\, a_{GaSb}$, where $a_f^{\perp}$ and a_{GaSb} are the out-of-plane lattice constant of the deposited film and the bulk lattice constant of GaSb, respectively. From the equation $a_f^{\perp} = a_f(1 - 2\nu_f/(1 - \nu_f))\varepsilon_f^{\parallel}$, where a_f, ν_f are the bulk lattice constant of the film and Poisson ratio and $\varepsilon_f^{\parallel}$ is in-plane strain of the film, the out-of-lattice constants of stoichiometric InAs, GaSb, GaAs, and InSb epitaxially grown on GaSb are found to be 6.0174, 6.0959, 5.2429, and 6.8978 Å, corresponding to the strain values ($\varepsilon^{\perp}$) of -1.29, 0, -13.99, and 13.15 %, respectively.

The strain value in the nominal GaSb inside the superlattice of sample IFA (Figure 5.24(a)) is positive with the maximum strain of ~ 2 % although the stoichiometric GaSb grown on GaSb should have zero strain. Since As segregation into GaSb leads to smaller lattice constant than that of bulk GaSb, we concluded that the positive strain value in the nominal GaSb results from In segregation during MBE growth. At interfaces between InAs and GaSb, negative strain values are found. The strain at InAs-on-GaSb interfaces, in particular, is more negative than that at GaSb-on-InAs interfaces (see red arrows in Figure 5.24(c)). The negative strain arises from the short chemical bonding distance, which indicates the interfacial bonds of low atomic number elements. Therefore, the more negative strain at InAs-on-GaSb interfaces represent that these interfaces contain a larger amount of Ga-As bonds than GaSb-on-InAs interfaces, resulting in asymmetric interfacial strain.

The strain distribution in sample IFRA (Figure 5.24(b)) shows several features that are different compared to that in sample IFA. The strain profile inside the nominal GaSb is altered by the insertion of thin forced InSb layer whose location is indicated by the red arrows in Figure 5.24(d). Due to a relatively large lattice constant of InSb, the stain near the top of the nominal GaSb shows the positive strain peak, which is distinctly different from sample A, where the positive strain is peaked in the middle of the nominal GaSb with

gradual decrease as it grows. Another interesting feature in the strain map of sample B is the removal of large negative strain peak (~ -3 %) near InAs-on-GaSb interfaces, indicating the reduction of the amount of Ga-As bonds.

Lastly, we performed monolayer-by-monolayer strain analysis on the strain maps. Figure 5.25 shows sub-lattice strain maps for sample IFA and IFRA and averaged strain profiles along the out-of-plane direction, obtained using separate sub-lattice images in Fig. 2. The strain variation (σ) in each monolayer is partially attributed to the measurement precision. We calibrated the measurement precision by using the standard deviation of the measured strain in the GaSb bottom electrode, which has a uniform composition and gives the measured σ at ~ 3 pm . The statistical analysis of strain in each monolayers allows a measurement of strain fluctuations, where the abnormally large strain deviations from the average strain can be detected. Specifically, we have marked these monolayers contain strain values lying outside 3σ from the mean strain and marked by white circles in strain maps and red dots in strain profiles. The detailed procedure for this method is presented elsewhere.[154] For statistics, two regions (I and II) from sample IFA and two regions (III and IV) from sample IFRA are examined.

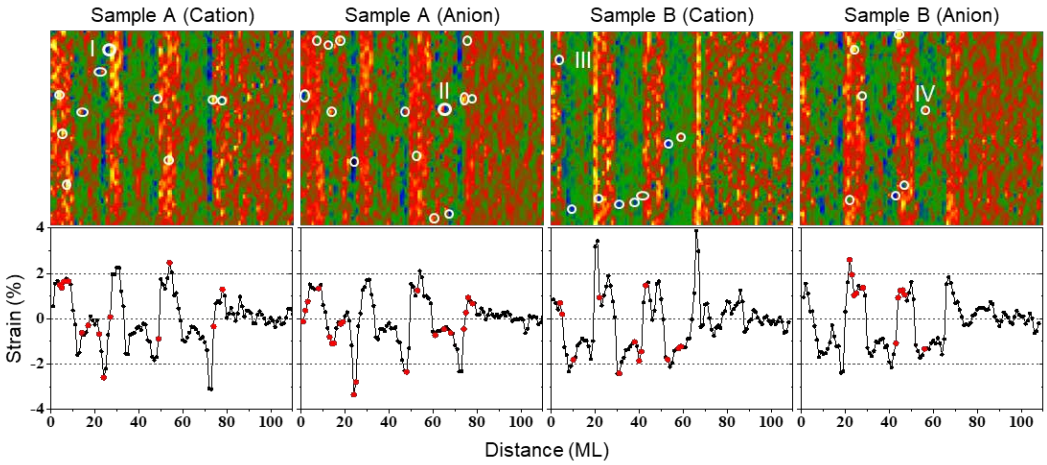

Figure 5.25 Strain maps and averaged strain profiles from cation and anion sub-lattice images of sample A (IFA) and B (IFRA). The white circles in each strain map and red dots in each strain profile indicate where the large strain deviation is detected.

The number of locations with large atomic displacements in sample IFA are 10 and 14 from anion and cation sub-lattices, respectively, while 8 and 7 are identified from anion and cation sub-lattices in sample IFRA within the same field-of-view as sample IFA. These result indicates that interface engineering helps to reduce the concentration of large strain fluctuations from the point defects in T2SLs.

Previous studies have identified that the device performance of InAs/GaSb T2SLs is largely limited by short minority carrier lifetime, which is due to the Shockley-Read-Hall recombination mediated by native defects.[3, 100, 155] Using the same T2SLs studied in this work, Zuo *et al.*[125] previously reported that the InSb-like interface formation at InAs-on-GaSb interfaces significantly enhances the minority carrier lifetime and subsequently lowers the dark current level.

The above strain analysis confirms that interface engineering successfully reduced the amount of Ga-As bonds near InAs-on-GaSb interfaces and resulted in a symmetric strain profile across interfaces. Interface engineering also improves the strain uniformity in both InAs and GaSb, which is evidenced by smaller standard deviation of strain values in each constituent layer of sample IFRA. In particular, the strain uniformity in the nominal InAs of sample IFRA is significantly improved by > 0.2 %, which can be verified as uniform green color in the strain map of sample IFRA (see Figure 5.24(b)).

References

1. D. L. Smith and C. Mailhiot, Journal of applied physics **62** (6), 2545-2548 (1987).
2. C. H. Grein, M. E. Flatte and H. Ehrenreich, Proc. of 3rd Int. Symp. on LWIR Detectors & Arrays: Physics & Apps III, 211 (1995).
3. B. C. Connelly, G. D. Metcalfe, H. Shen and M. Wraback, Applied physics letters **97** (25), 251117 (2010).
4. W. Walukiewicz, MRS Proceedings **148**, 137 (1989).
5. W. Walukiewicz, Physical Review B **37** (9), 4760-4763 (1988).
6. Y. H. Zhang, Applied Physics Letters **66** (2), 118-120 (1995).
7. D. Lackner, O. J. Pitts, M. Steger, A. Yang, M. L. W. Thewalt and S. P. Watkins, Applied Physics Letters **95** (8), 081906 (2009).
8. O. O. Cellek, H. Li, X.-M. Shen, Z. Lin, E. H. Steenbergen, D. Ding, S. Liu, Q. Zhang, H. S. Kim, J. Fan, M. J. DiNezza, W. H. G. Dettlaff, P. T. Webster, Z. He, J.-J. Li, S. R. Johnson, D. J. Smith and Y.-H. Zhang, presented at the SPIE Defense, Security, and Sensing, 2012 (unpublished).
9. E. H. Steenbergen, B. C. Connelly, G. D. Metcalfe, H. Shen, M. Wraback, D. Lubyshev, Y. Qiu, J. M. Fastenau, A. W. K. Liu, S. Elhamri, O. O. Cellek and Y. H. Zhang, Applied Physics Letters **99** (25), 251110 (2011).
10. Y. Aytac, B. V. Olson, J. K. Kim, E. A. Shaner, S. D. Hawkins, J. F. Klem, M. E. Flatté and T. F. Boggess, Applied Physics Letters **105** (2), 022107 (2014).
11. P. Tang, M. J. Pullin, S. J. Chung, C. C. Phillips, R. A. Stradling, A. G. Norman, Y. B. Li and L. Hart, Semiconductor Science and Technology **10** (8), 1177 (1995).
12. D. E. Eastman and J. L. Freeouf, Physical Review Letters **34** (26), 1624-1627 (1975).
13. A. Prins, A. Adams and S. Sweeney, in *Semiconductor Research: Experimental Techniques*, edited by A. Patane and N. Balkan (Springer Berlin Heidelberg, Berlin, Heidelberg, 2012), pp. 171-195.
14. R.-D. Hong, D. W. Jenkins, S. Y. Ren and J. D. Dow, Physical Review B **38** (17), 12549-12555 (1988).
15. X. Liu, M.-E. Pistol, L. Samuelson, S. Schwetlick and W. Seifert, Applied Physics Letters **56** (15), 1451-1453 (1990).
16. I. Vurgaftman, J. R. Meyer and L. R. Ram-Mohan, Journal of Applied Physics **89** (11), 5815-5875 (2001).
17. E. H. Steenbergen, O. O. Cellek, D. Lubyshev, Y. Qiu, J. M. Fastenau, A. W. K. Liu and Y.-H. Zhang, presented at the SPIE OPTO, 2012 (unpublished).
18. H. Li, S. Liu, O. O. Cellek, D. Ding, X.-M. Shen, E. H. Steenbergen, J. Fan, Z. Lin, Z.-Y. He, Q. Zhang, P. T. Webster, S. R. Johnson, L. Ouyang, D. J. Smith and Y.-H. Zhang, Journal of Crystal Growth **378**, 145-149 (2013).
19. W. B. Daniels, M. Lipp, D. Strachan, D. Winters and Z.-H. Yu, in *Proceedings of the XIII AIRAPT International Conference on High Pressure Science and Technology*, edited by S. A. K. (1992), pp. 809–811.
20. A. F. Phillips, S. J. Sweeney, A. R. Adams and P. J. A. Thijs, IEEE Journal of Selected Topics in Quantum Electronics **5** (3), 401-412 (1999).
21. E. K. Plyler, J. Res. Natl. Bur. Stand. **48**, 281 (1952).
22. P. E. Van Camp, V. E. Van Doren and J. T. Devreese, Physical Review B **41** (3), 1598-1602 (1990).
23. I. E. Itskevich, S. G. Lyapin, I. A. Troyan, P. C. Klipstein, L. Eaves, P. C. Main and M. Henini, Physical Review B **58** (8), R4250-R4253 (1998).

24. M. I. Daunov, I. K. Kamilov, S. F. Gabibov and A. B. Magomedov, physica status solidi (b) **235** (2), 297-301 (2003).
25. W. Feng, Y. Wang, J. Wang, W. K. Ge, Q. Huang and J. M. Zhou, Applied Physics Letters **72** (12), 1463-1465 (1998).
26. C. Xiren, Z. Yi, Z. Liang, Q. Zhen, X. Qingqing, X. Zhicheng, G. Shaoling, C. Jianxin, H. Li and S. Jun, Japanese Journal of Applied Physics **53** (8), 082201 (2014).
27. J. L. Pankove, *Optical Processes in Semiconductors* (Dover, New York, 1971).
28. Y. Meng, H. Kim, J.-L. Rouviére, D. Isheim, D. N. Seidman and J.-M. Zuo, Journal of applied physics **116** (1), 013513 (2014).
29. S. Hendricks and E. Teller, The Journal of Chemical Physics **10**, 147 (1942).
30. E. E. Fullerton, I. K. Schuller, H. Vanderstraeten and Y. Bruynseraede, Physical Review B **45**, 9292-9310 (1992).
31. R. Magri and A. Zunger, Physical Review B **65**, 165302 (2002).
32. K. Mahalingam, H. J. Haugan, G. J. Brown and K. G. Eyink, Ultramicroscopy **127**, 70-75 (2013).
33. K. Mahalingam, H. J. Haugan, G. J. Brown and A. J. Aronow, Applied Physics Letters **103**, 211605 (2013).
34. Y. Ashuach, Y. Kauffmann, D. Isheim, Y. Amouyal, D. N. Seidman and E. Zolotoyabko, Applied Physics Letters **100** (24), 241604 (2012).
35. X. Sauvage, L. Renaud, B. Deconihout, D. Blavette, D. H. Ping and K. Hono, Acta Materialia **49** (3), 389-394 (2001).
36. M. Müller, D. W. Saxey, G. D. W. Smith and B. Gault, Ultramicroscopy **111** (6), 487-492 (2011).
37. O. Dehaese, X. Wallart and F. Mollot, Applied Physics Letters **66**, 52 (1995).
38. R. Magri and A. Zunger, Physical Review B **65** (16), 165302 (2002).
39. H. Kim, Y. Meng, J.-L. Rouviére and J.-M. Zuo, Micron **92**, 6-12 (2017).
40. J. Chung, G. Lian and L. Rabenberg, Ieee Electron Device Letters **31** (8), 854-856 (2010).
41. J. M. Zuo, A. B. Shah, H. Kim, Y. F. Meng, W. P. Gao and J. L. Rouviere, Ultramicroscopy **136**, 50-60 (2014).
42. J. M. Zuo and J. C. H. Spence, *Advanced Transmission Electron Microscopy, Imaging and Diffraction in Nanoscience*. (Springer, New York, 2017).
43. J. J. Peters, R. Beanland, M. Alexe, J. W. Cockburn, D. G. Revin, S. Y. Zhang and A. M. Sanchez, Ultramicroscopy **157**, 91-97 (2015).
44. H. Kim, Y. Meng, J.-L. Rouviére, D. Isheim, D. N. Seidman and J.-M. Zuo, Journal of applied physics **113** (10), 103511 (2013).
45. H. L. Xin and D. A. Muller, Journal of Electron Microscopy **58** (3), 157-165 (2009).
46. A. Y. Borisevich, A. R. Lupini and S. J. Pennycook, Proc. Natl. Acad. Sci. U. S. A. **103** (9), 3044-3048 (2006).
47. L. Muratov, S. Little, Y. Yang, B. R. Cooper, T. H. Myers and J. M. Wills, Physical Review B **64** (3), 035206 (2001).
48. J. Shen, S. Y. Ren and J. D. Dow, Physical Review B **46** (11), 6938 (1992).
49. J. Lu, E. Luna, T. Aoki, E. H. Steenbergen, Y.-H. Zhang and D. J. Smith, Journal of Applied Physics **119** (9), 095702 (2016).
50. M. Hÿtch, E. Snoeck and R. Kilaas, Ultramicroscopy **74** (3), 131-146 (1998).
51. P. A. Doyle and P. S. Turner, Acta Crystallographica Section a-Crystal Physics Diffraction Theoretical and General Crystallography **A 24**, 390-& (1968).
52. K. Muraki, S. Fukatsu, Y. Shiraki and R. Ito, Applied Physics Letters **61** (5), 557-559 (1992).
53. D. Lackner, O. Pitts, M. Steger, A. Yang, M. Thewalt and S. Watkins, Applied Physics Letters **95** (8), 081906 (2009).

54. M. Wood, K. Kanedy, F. Lopez, M. Weimer, J. Klem, S. Hawkins, E. Shaner and J. Kim, Journal of Crystal Growth **425**, 110-114 (2015).
55. C. Wang, D. J. Smith, S. Tobin, T. Parodos, J. Zhao, Y. Chang and S. Sivananthan, Journal of Vacuum Science & Technology A: Vacuum, Surfaces, and Films **24** (4), 995-1000 (2006).
56. J.-M. Zuo, A. B. Shah, H. Kim, Y. Meng, W. Gao and J.-L. Rouviére, Ultramicroscopy **136**, 50-60 (2014).
57. R. Pérez and P. Gumbsch, Acta Materialia **48** (18–19), 4517-4530 (2000).
58. L. B. Freund and S. Suresh, *Thin film materials: stress, defect formation and surface evolution*. (Cambridge University Press, 2004).
59. I. Vurgaftman, J. Meyer and L. Ram-Mohan, Journal of applied physics **89** (11), 5815-5875 (2001).
60. J. Lu, E. Luna, T. Aoki, E. H. Steenbergen, Y.-H. Zhang and D. J. Smith, Journal of Applied Physics **119** (9), 095702 (2016).
61. M. Wang, D. Collins, T. McGill, R. Grant and R. Feenstra, Journal of Vacuum Science & Technology B **13** (4), 1689-1693 (1995).
62. J. Steinshnider, J. Harper, M. Weimer, C. H. Lin, S. S. Pei and D. H. Chow, Physical Review Letters **85** (21), 4562-4565 (2000).
63. V. Virkkala, V. Havu, F. Tuomisto and M. J. Puska, Physical Review B **86** (14), 144101 (2012).
64. E. G. Seebauer and M. C. Kratzer, Materials Science and Engineering: R: Reports **55** (3), 57-149 (2006).
65. X. Sang, E. D. Grimley, C. Niu, D. L. Irving and J. M. LeBeau, Applied Physics Letters **106** (6), 061913 (2015).
66. H. Kim, J. Y. Zhang, S. Raghavan and S. Stemmer, Physical Review X **6** (4), 041063 (2016).
67. B. Olson, E. A. Shaner, J. K. Kim, J. F. Klem, S. D. Hawkins, M. Flatté and T. Boggess, Applied Physics Letters **103** (5), 052106 (2013).
68. S. Krishnamurthy and Z.-G. Yu, Applied Physics Letters **110** (2), 021113 (2017).
69. Y. Lin, D. Wang, D. Donetsky, L. Shterengas, G. Kipshidze, G. Belenky, S. P. Svensson, W. L. Sarney and H. S. Hier, Journal of electronic materials **42** (5), 918 (2013).
70. P. F. Fewster, *X-ray scattering from semiconductors* 2nd ed. (Imperial College Press, London, 2003).
71. K. Matney and M. S. Goorsky, Journal of Crystal Growth **148** (4), 327-335 (1995).
72. P. M. Petroff, A. C. Gossard, W. Wiegmann and A. Savage, Journal of Crystal Growth **44** (1), 5-13 (1978).
73. H. Cerva and H. Oppolzer, Applied Physics A **57** (5), 377-383 (1993).
74. K. Kanedy, F. Lopez, M. R. Wood, C. F. Gmachl, M. Weimer, J. F. Klem, S. D. Hawkins, E. A. Shaner and J. K. Kim, Applied Physics Letters **112** (4), 042105 (2018).
75. Z.-Y. Lin, S. Liu, E. H. Steenbergen and Y.-H. Zhang, Applied Physics Letters **107** (20), 201107 (2015).
76. J. B. Khurgin, Y. Dikmelik, P. Q. Liu, A. J. Hoffman, M. D. Escarra, K. J. Franz and C. F. Gmachl, Applied Physics Letters **94** (9), 091101 (2009).
77. F. Lopez, Ph.D Texas A&M University, College Station, 2015.
78. K. M. Kanedy, Ph.D Texas A&M University, College Station, 2016.
79. M. R. Wood, K. Kanedy, F. Lopez, M. Weimer, J. F. Klem, S. D. Hawkins, E. A. Shaner and J. K. Kim, Journal of Crystal Growth **425**, 110-114 (2015).
80. J. D. Steinshnider, M. B. Weimer and M. C. Hanna, in *Spontaneous Ordering in Semiconductor Alloys*, edited by A. Mascarenhas (Springer US, Boston, MA, 2002), pp. 273-282.

81. T. L. Hill, *Statistical Mechanics: Principles and Selected Applications* (McGraw-Hill, New York, 1956).
82. M. R. Wood, Ph.D Texas A&M University, College Station, 2017.
83. A. G. Norman, in *Spontaneous Ordering in Semiconductor Alloys*, edited by A. Mascarenhas (Springer US, Boston, MA, 2002), pp. 45-97.
84. J. Steinshnider, J. Harper, M. Weimer, C. H. Lin, S. S. Pei and D. H. Chow, Physical Review Letters **85** (21), 4562-4565 (2000).
85. S. P. Svensson, W. L. Sarney, H. Hier, Y. Lin, D. Wang, D. Donetsky, L. Shterengas, G. Kipshidze and G. Belenky, Physical Review B **86** (24), 245205 (2012).
86. W. L. Sarney, S. P. Svensson, Y. Lin, D. Donetsky, L. Shterengas, G. Kipshidze and G. Belenky, Journal of Applied Physics **119** (21), 215704 (2016).
87. Q. Chen, H. Liu, H.-S. Kim, Y. Liu, M. Yang, N. Yue, G. Ren, K. Zhu, S. Liu, N.-G. Park and Y. Zhang, Physical Review X **6** (3), 031042 (2016).
88. H. Liu, Y. Zhang, E. H. Steenbergen, S. Liu, Z. Lin, Y.-H. Zhang, J. Kim, M.-H. Ji, T. Detchprohm, R. D. Dupuis, J. K. Kim, S. D. Hawkins and J. F. Klem, Physical Review Applied **8** (3), 034028 (2017).
89. J. Wang, Y. Zhang and L.-W. Wang, Physical Review B **92** (4), 045211 (2015).
90. L. W. Wang, Applied Physics Letters **78** (11), 1565-1567 (2001).
91. J. Wang and Y. Zhang, Journal of Applied Physics **116** (21), 214301 (2014).
92. A. D. Prins, M. K. Lewis, Z. L. Bushell, S. J. Sweeney, S. Liu and Y.-H. Zhang, Applied Physics Letters **106** (17), 171111 (2015).
93. Y. Zhang and J. Wang, Bulletin of the American Physical Society **59 (http://meetings.aps.org/link/BAPS.2014.MAR.B44.3)** (2014).
94. N. F. Mott and R. W. Gurney, *Electronic processes in ionic crystals*. (Oxford University Press, London, 1940).
95. S. T. Pantelides, Review of Modern Physics **50**, 797-858 (1978).
96. P.-F. Qiao, S. Mou and S. L. Chuang, Opt. Express **20** (3), 2319-2334 (2012).
97. J. V. Li, C. J. Hill, J. Mumolo, S. Gunapala, S. Mou and S.-L. Chuang, Applied Physics Letters **93** (16), 163505 (2008).
98. D. R. Rhiger, Journal of Electronic Materials **40** (8), 1815-1822 (2011).
99. G. Belenky, G. Kipshidze, D. Donetsky, S. P. Svensson, W. L. Sarney, H. Hier, L. Shterengas, D. Wang and Y. Lin, presented at the SPIE Defense, Security, and Sensing, 2011 (unpublished).
100. D. Donetsky, S. P. Svensson, L. E. Vorobjev and G. Belenky, Applied Physics Letters **95** (21), 212104 (2009).
101. J. Pellegrino and R. DeWames, presented at the SPIE Defense, Security, and Sensing, 2009 (unpublished).
102. S. Bandara, P. Maloney, N. Baril, J. Pellegrino and M. Tidrow, Infrared Physics & Technology **54** (3), 263-266 (2011).
103. B. C. Connelly, G. D. Metcalfe, H. Shen and M. Wraback, presented at the SPIE Optical Engineering + Applications, 2011 (unpublished).
104. S. P. Svensson, D. Donetsky, D. Wang, P. Maloney and G. Belenky, presented at the SPIE Defense, Security, and Sensing, 2010 (unpublished).
105. S. P. Svensson, D. Donetsky, D. Wang, H. Hier, F. J. Crowne and G. Belenky, Journal of Crystal Growth **334** (1), 103-107 (2011).
106. S. Bandara, P. G. Maloney, N. Baril, J. G. Pellegrino and M. Z. Tidrow, 2011 (unpublished).
107. J. R. Dixon and J. M. Ellis, Physical Review **123** (5), 1560-1566 (1961).
108. J. D. Vincent, *Fundamentals of Infrared Detector Operation and Testing*. (Wiley, New York, 1990).

109. C. M. Ciesla, B. N. Murdin, C. R. Pidgeon, R. A. Stradling, C. C. Phillips, M. Livingstone, I. Galbraith, D. A. Jaroszynski, C. J. G. M. Langerak, P. J. P. Tang and M. J. Pullin, Journal of Applied Physics **80** (5), 2994-2997 (1996).
110. E. F. Schubert, *Light-Emitting Diodes*. (Cambridge University Press, New York, 2007).
111. F. Urbach, Physical Review **92** (5), 1324-1324 (1953).
112. S. R. Johnson and T. Tiedje, Journal of Applied Physics **78** (9), 5609-5613 (1995).
113. P. T. Webster, N. A. Riordan, S. Liu, E. H. Steenbergen, R. A. Synowicki, Y. H. Zhang and S. R. Johnson, Journal of Applied Physics **118** (24), 245706 (2015).
114. H.-S. Cho and P. R. Prucnal, Physical Review B **36** (6), 3237-3242 (1987).
115. S.-h. Pan and S.-m. Feng, Physical Review B **44** (11), 5668-5671 (1991).
116. S. L. Chuang, *Physics of Optoelectronic Devices*. (Wiley, New York, 1995).
117. J. W. Matthews and A. E. Blakeslee, Journal of Crystal Growth **27**, 118-125 (1974).
118. P. T. Webster, N. A. Riordan, S. Liu, E. H. Steenbergen, R. A. Synowicki, Y. H. Zhang and S. R. Johnson, Applied Physics Letters **106** (6), 061907 (2015).
119. R. M. Biefeld, Materials Science and Engineering: R: Reports **36** (4), 105-142 (2002).
120. A. Aardvark, N. J. Mason and P. J. Walker, Progress in Crystal Growth and Characterization of Materials **35** (2), 207-241 (1997).
121. G. R. Booker, P. C. Klipstein, M. Lakrimi, S. Lyapin, N. J. Mason, R. J. Nicholas, T. Y. Seong, D. M. Symons, T. A. Vaughan and P. J. Walker, Journal of Crystal Growth **145** (1), 778-785 (1994).
122. Y. K. Su, C. L. Lin, S. M. Chen, J. R. Chang and D. H. Jaw, Journal of Applied Physics **81** (11), 7529-7532 (1997).
123. M. J. Hytch, E. Snoeck and R. Kilaas, Ultramicroscopy **74** (3), 131-146 (1998).
124. D. Zuo, Univ. of Illinois, , 2011.
125. D. Zuo, P. Qiao, D. Wasserman and S. Lien Chuang, Applied Physics Letters **102** (14), 141107 (2013).
126. J.-M. Bonard and J.-D. Ganière, Journal of Applied Physics **79** (9), 6987-6994 (1996).
127. C. Donolato, Journal of Applied Physics **76** (2), 959-966 (1994).
128. H. S. Kim, O. O. Cellek, Z.-Y. Lin, Z.-Y. He, X.-H. Zhao, S. Liu, H. Li and Y. H. Zhang, Applied Physics Letters **101** (16), 161114 (2012).
129. B. V. Olson, E. A. Shaner, J. K. Kim, J. F. Klem, S. D. Hawkins, M. E. Flatté and T. F. Boggess, Applied Physics Letters **103** (5), 052106 (2013).
130. D. Dominique, C. A. Réal, J. Dany, T. Xavier, A. Vincent and G. Raynald, Scanning **29** (3), 92-101 (2007).
131. J. V. Li, S. L. Chuang, E. Aifer and E. M. Jackson, Applied Physics Letters **90** (22), 223503 (2007).
132. C. Donolato, Solid-State Electronics **25** (11), 1077-1081 (1982).
133. O. F. Vyvenko, T. Buonassisi, A. A. Istratov, H. Hieslmair, A. C. Thompson, R. Schindler and E. R. Weber, Journal of Applied Physics **91** (6), 3614-3617 (2002).
134. J. Bajaj and W. E. Tennant, Journal of Crystal Growth **103** (1), 170-178 (1990).
135. V. I. Orlov, O. V. Feklisova and E. B. Yakimov, Solid State Phenomena **205-206**, 142-147 (2014).
136. H. J. Leamy, Journal of Applied Physics **53** (6), R51-R80 (1982).
137. K. L. Luke, O. von Roos and L. j. Cheng, Journal of Applied Physics **57** (6), 1978-1984 (1985).
138. O. Marcelot, S. I. Maximenko and P. Magnan, IEEE Transactions on Electron Devices **61** (7), 2437-2442 (2014).
139. E. R. Youngdale, J. R. Meyer, C. A. Hoffman, F. J. Bartoli, C. H. Grein, P. M. Young, H. Ehrenreich, R. H. Miles and D. H. Chow, Applied physics letters **64** (23), 3160-3162 (1994).

140. C. H. Grein, M. E. Flatté, J. T. Olesberg, S. A. Anson, L. Zhang and T. F. Boggess, Journal of Applied Physics **92** (12), 7311-7316 (2002).
141. H. Haugan, F. Szmulowicz, G. Brown and K. Mahalingam, Journal of applied physics **96**, 2580 (2004).
142. C. H. Grein, J. Garland and M. E. Flatté, Journal of Electronic Materials **38** (8), 1800-1804 (2009).
143. E. H. Steenbergen, K. Nunna, L. Ouyang, B. Ullrich, D. L. Huffaker, D. J. Smith and Y.-H. Zhang, Journal of Vacuum Science & Technology B **30** (2), 02B107 (2011).
144. O. Klin, N. Snapi, Y. Cohen and E. Weiss, Journal of Crystal Growth **425**, 54-59 (2015).
145. D. Zuo, R. Liu, D. Wasserman, J. Mabon, Z.-Y. He, S. Liu, Y.-H. Zhang, E. A. Kadlec, B. V. Olson and E. A. Shaner, Applied Physics Letters **106** (7), 071107 (2015).
146. I. Vurgaftman, G. Belenky, Y. Lin, D. Donetsky, L. Shterengas, G. Kipshidze, W. L. Sarney and S. P. Svensson, Applied Physics Letters **108** (22), 222101 (2016).
147. G. Ariyawansa, C. J. Reyner, J. M. Duran, J. D. Reding, J. E. Scheihing and E. H. Steenbergen, Applied Physics Letters **109** (2), 021112 (2016).
148. G. Ariyawansa, E. Steenbergen, L. J. Bissell, J. M. Duran, J. E. Scheihing and M. T. Eismann, presented at the SPIE Defense + Security, 2014 (unpublished).
149. F. Berz and H. K. Kuiken, Solid-State Electronics **19** (6), 437-445 (1976).
150. M. Watanabe, G. Actor and H. C. Gatos, IEEE Transactions on Electron Devices **24** (9), 1172-1177 (1977).
151. E. A. Kadlec, B. V. Olson, M. D. Goldflam, J. K. Kim, J. F. Klem, S. D. Hawkins, W. T. Coon, M. A. Cavaliere, A. Tauke-Pedretti, T. R. Fortune, C. T. Harris and E. A. Shaner, Applied Physics Letters **109** (26), 261105 (2016).
152. G. Ariyawansa, J. M. Duran, C. J. Reyner, E. H. Steenbergen, N. Yoon, D. Wasserman and J. E. Scheihing, presented at the SPIE Defense + Security, 2017 (unpublished).
153. D. Z. Ting, A. Soibel and S. D. Gunapala, Applied Physics Letters **108** (18), 183504 (2016).
154. H. Kim, Y. Meng, J.-H. Kwon, J.-L. Rouviére and J. M. Zuo, IUCrJ **5** (1) (2018).
155. D. Donetsky, G. Belenky, S. Svensson and S. Suchalkin, Applied Physics Letters **97** (5), 052108 (2010).